2-P(mix)

CR 114297
AVAILABLE TO THE PUBLIC

RTG/SCIENCE INSTRUMENT RADIATION INTERACTIONS STUDY FOR DEEP SPACE PROBES

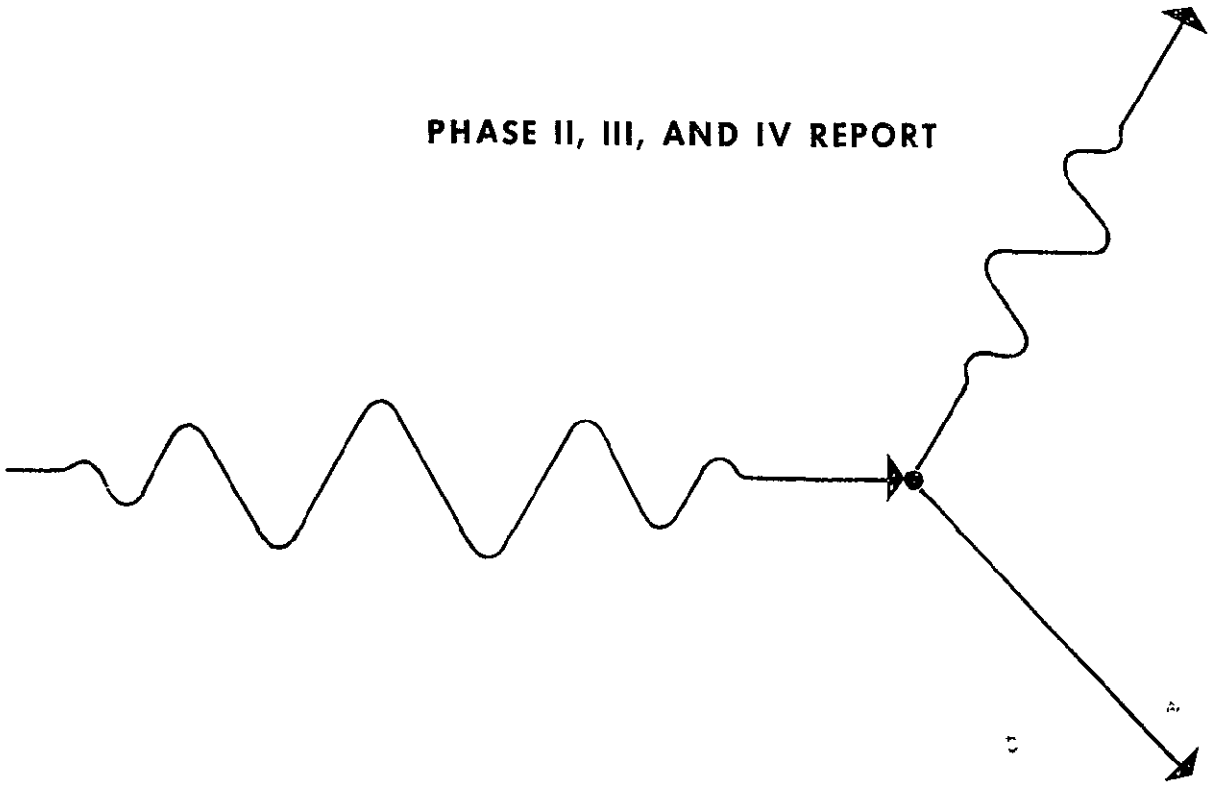

PHASE II, III, AND IV REPORT

PREPARED FOR NASA AMES RESEARCH CENTER

MOFFET FIELD, CALIFORNIA

CONTRACT NO. NAS 2—5222

TRW SYSTEMS GROUP

PHASE II, III, & IV

RTG/SCIENCE INSTRUMENT RADIATION INTERACTIONS FOR DEEP SPACE PROBES

NAS 2-5222

SUBMITTED TO:

NATIONAL AERONAUTICS AND SPACE ADMINISTRATION
AMES RESEARCH CENTER
MOFFETT FIELD, CALIFORNIA

31 January 1971

Approved by: R. Kaminskas
R. A. Kaminskas,
Program Manager

Approved by: I. R. Jones
I. R. Jones, Manager
Nuclear Systems Department

Prepared by:

R. A. Kaminskas
J. S. Brunhouse
K. T. Hartwig

TRW SYSTEMS GROUP
REDONDO BEACH, CALIFORNIA
90278

RTG/SCIENCE INSTRUMENT RADIATION INTERACTIONS FOR

DEEP SPACE PROBES

TABLE OF CONTENTS

Page

1.0 INTRODUCTION

Pioneer F and G are spacecraft designed to obtain precursory scientific information beyond the orbit of Mars with the following emphases:

- Investigation of the interplanetary medium.
- Determination of the nature of the asteroid belt, both scientifically and as a hazard to space flight.
- Exploration of Jupiter and its environment.

A secondary objective is to develop the technology for long duration flights to the outer planets.

A Jupiter launch opportunity occurs approximately once every 13 months. The nominal launch periods for Pioneer F and G spacecraft occur during February and March of 1972 and March and April of 1973, respectively. The Pioneer F launch window is 30 minutes a day on any one of 18 consecutive days, which results in a large number of potential launch trajectories. The trip time to Jupiter varies between 645 and 795 days, depending upon the launch date and time in the launch window when the launch occurs. After Jupiter flyby, the Pioneer F spacecraft will escape the solar system. The Pioneer G mission trajectories have not as yet been developed but are expected to be different from the trajectory of Pioneer F.

Each Pioneer F/G spacecraft uses four SNAP-19 radioisotope thermoelectric generators (RTG's) as electrical power generators and approximately eleven radioisotope heater units (RHU's) as heat sources for thermal control of various spacecraft subsystems. The RTG's and the RHU's use plutonium-238 dioxide as the fuel, in the form of a plutonia molybdenum cermet (PMC). The fuel, besides generating heat by emitting alpha particles, also generates gamma and neutron radiation. This radiation escapes the fuel capsule walls and is a source of interference and potential radiation damage to a number of subsystems carried in the payload of the spacecraft.

The instruments on board the Pioneer F/G spacecraft will carry the following experiments and measurement systems during its voyage:

- A plasma probe to measure electrons and ions.

- A magnetic field experiment to measure the spectrum of the field changes as well as the absolute value of the field.
- Cosmic ray composition and Jovian trapped radiation experiments to measure the radiation flux spectra, and to identify the specific nuclear species of particles with atomic numbers up to oxygen.
- An ultraviolet photometry experiment to measure the intensity of ultraviolet radiation.
- An imaging photometry and polarimetry experiment for zodiacal light mapping, Jupiter polarimetry, and Jupiter imaging.
- A Jovian thermal structure experiment to measure the net thermal energy flux from Jupiter.
- A meteoroid/asteroid astronomy experiment to measure the sizes, velocities, concentrations, and orbits of meteroids and asteroids.

The RTG radiation provides a constant background for the radiation sensitive elements of the instruments and could, in fact, completely subordinate the space radiation which is being measured. To determine the extent and significance of this interference to the science instruments and their objectives, a RTG/Science Instrument Interactions for Deep Space Probes program was commenced at TRW Systems during February, 1969, under NASA Ames Research Center sponsorship (Contract NAS 2-5222). This program consists of five phases.

Phase I was conducted prior to the time the decision was made to use RTG's on the Pioneer F/G spacecraft. The study combined an analytical and experimental approach and was directed towards investigation of RTG radiation effects on typical spacecraft instrument systems found in deep space missions. The study included a survey of over one hundred instruments carried on board various spacecraft, selection of the 26 most frequently used radiation detectors for experimental evaluation with the RTG radiation, and tests of these radiation detectors using a SNAP-27 fuel capsule as the radiation source. The Phase I results, which indicated that the Pioneer F/G spacecraft mission would not be severely jeopardized due to the RTG's, played an important role in the selection of RTG's for use with the Pioneer F/G mission. The Phase I results are summarized in RTG/Science Instrument Radiation Interactions Study for Deep Space Probes, Phase I Report (Reference 1).

Phase II of the program extended the study to the investigation of radiation effects on instrument systems specifically for the Pioneer F/G spacecraft. Also, to verify the Phase I results, Pioneer F/G experimenters were invited to come to TRW test facility and perform radiation interference tests with their instruments using the SNAP-27 as the radiation source. Almost every investigator who suspected a potential radiation interference problem came to TRW and performed tests during the Phase II effort. In general, the results of Phase I were verified as applied to the Pioneer F/G mission. It was found that the spacecraft could attain most of its scientific objectives requiring only approximately 2.5 lbs. of shielding for one detector system.

As the work progressed, the requirements for the radiation measurements became more refined. Thus, it became necessary to produce a better simulation of the RTG radiation environment in the Pioneer spacecraft than it was possible to attain with the SNAP-27 fuel capsule. The SNAP-27 used for the Phase I and II radiation testing was a bare capsule while the SNAP-19 RTG's used on the Pioneer spacecraft also consist of a graphite heat shield and thermoelectric materials surrounding the fuel capsules. In addition, the fuel form was different. The SNAP-27 fuel capsule contains plutonium dioxide microspheres while the SNAP-19 is fueled with plutonia molybdenum cermet and provides much more self absorption. Further, the instruments were located in the spacecraft where the structure and electronic equipment provide considerable scattering and absorption of radiation.

Phases III and IV of the program were initiated to obtain an accurate simulation of the radiation environment in the Pioneer F/G spacecraft. This was accomplished by construction of a mass mockup of the Pioneer spacecraft which simulates the physical size and radiation scattering of the real spacecraft. The SNAP-19 RTG radiation was simulated using a set of radioisotope sources which provided considerable flexibility that could not be obtained any other way. For example, it was easily possible to change the fuel age by adjusting the source strength of one of the sources or to change the spectrum to represent radiation emission from a solid solution cermet or plutonia molybdenum cermet fuel form. The Pioneer F/G spacecraft mockup and the simulated RTG radiation sources were extensively used during Phases III and IV of this program and proved to be extremely valuable tools for various radiation measurements.

Phase V of this program is designed primarily for radiation measurements dealing with prototype Pioneer radiation interference testing and will be reported separately in a later report.

This report covers the work performed during Phases II, III and IV. It is presented in eight sections. Section 2 is a review of program objectives and a summary of the major tasks that were completed in Phases II, III, and IV. Section 3 gives a brief description of the Pioneer F/G mission and spacecraft, describes the Pioneer F/G instruments and assesses the the effect of RTG radiation on each instrument. Section 4 describes the RTG and RHU fuel and their measured and computed radiation fields. Section 5 describes the Pioneer F/G spacecraft and radiation mockup design and construction. Section 6 describes the results of tests conducted to evaluate the effectiveness of various radiation shields. Section 7 gives the radiation doses to the spacecraft subsystems and discusses its effect on various electronic components. Section 8 presents conclusions and recommendations for further studies.

This report covers the work performed during the time period between June 1969 through January 1971. During this period, the radiation environment stipulated for the Pioneer F/G spacecraft underwent a number of significant changes. For instance, in the beginning it was thought that the neutron emission from the RTG fuel was in the order of 22,000 neutrons/second per gram of Pu-238. Later this number was revised to 5,000 neutrons/second per gram and then to approximately 9,000 neutrons/second per gram. The prototype SNAP-19 RTG's finally had a neutron output in excess of 30,000 neutrons/second per gram. Likewise, the RTG fuel form changed from plutonium dioxide microspheres to solid solution cermet and finally to a plutonia molybdenum cermet. These changes affected the radiation flux and spectrum emitted from the RTG's and changed the radiation environments at the spacecraft. Since various tasks and studies described in this report were performed at various times, in many cases they used different assumptions about the radiation emitted from the RTG's. Care has been taken to assure that these assumptions have been clearly stated for all studies that have been performed during the course of this program and are described in this report.

2.0 PROGRAM OBJECTIVES AND TASKS

The RTG/Science Instrument Radiation Interactions study was designed to provide the experimenters using scientific instruments onboard RTG-powered spacecraft with basic data to assess the radiation interference caused by the radiation emanating from the RTG. The program had a dual purpose:

- To provide data for an immediate requirement concerning the RTG radiation interference with science instruments for the Pioneer F/G spacecraft mission.
- To provide data to assess RTG radiation interference with science instruments for future scientific spacecraft missions.

To satisfy these objectives a five phase program was performed. Phase I began in February, 1969, and was completed in July, 1969. It was concerned primarily with the study and measurement of radiation interference with a variety of radiation sensitive detectors and elements applicable for Pioneer F/G spacecraft as well as other future RTG-powered spacecraft missions. The results of Phase I study are summarized in a report "RTG/Science Instrument Interactions for Deep Space Probes" Phase I Final Report. Phase II was started in July, 1969, and completed in February, 1970. It was designed to study the radiation interference specifically for Pioneer F/G instruments. Phase III was started in December, 1969, and completed in August, 1970. Phase III was an extension of the basic Phase II effort aimed at providing an accurate and versatile simulation of the Pioneer F/G radiation environment for radiation interference testing using a mass mockup of the Pioneer F/G spacecraft and simulated SNAP-19 RTG radiation sources. Phase IV included a task to perform a trade-off study to determine the relative benefits that can be gained in reducing the RTG and RHU radiation interference with science instruments by:

- Limiting the impurities in the RTG and RHU fuel and/or
- Selectively stacking the fuel discs in the SNAP-19 fuel capsule so that fuel discs which emit less radiation are placed at one end of the fuel capsule to minimize the radiation output in the direction of the spacecraft.

The results of this task are described in a report entitled "RTG Radiation Cleanliness Study", 16 August 1970. Phase IV also extended the time period for tests with the Pioneer F/G spacecraft mockup to the time that the Pioneer prototype becomes available for radiation interference tests (February 1971).

Phase V is concerned with tests of the SNAP-19 RTG's and Pioneer prototype spacecraft. At the time of writing of this report, Phase V is still in progress and will be reported separately.

The following sections summarize the tasks that appear in the work statements for Phase II, III, and IV. It is also indicated where, in this report, the results of each task are described.

2.1 Phase I

A review of scientific instruments commonly carried in spacecraft was performed and the elements of the instruments most susceptible to the RTG radiation were identified. These elements, which included semiconductor detectors, plastic scintillators, CsI scintillators and a number of other radiation detectors were exposed to a SNAP-27 fuel capsule assembly. The resultant spectral response of each detector was determined along with the effects of various separation distances, capsule orientations, and different shielding materials and thicknesses. A detailed analysis of the nuclear radiation emitted from the SNAP-27 fuel capsule was also performed, including the effect of fuel form age on the source spectrum. The results of this work were reported in the Phase I report.

2.2 Phase II Task Summary

2.2.1 Pioneer F/G Instrument Performance Study (Task 1.1)

The purpose of this task was to perform a detailed study of science instruments selected for Pioneer F/G mission and evaluate the radiation response of each major component of the instrument. This effort was coordinated through NASA/ARC, the TRW Pioneer F/G Project Office, and individual experimenters to obtain up-to-date design and functional information about the experiments. The instrument operation in the RTG radiation environments was assessed. For those instruments that were affected by radiation, countermeasure techniques to reduce the radiation interference were explored.

A description of the Pioneer F/G experiments and how they are affected by the RTG radiation is included in Section 3.

2.2.2 Update Phase I Test Data for Pioneer F/G Mission (Task 1.2)

Since all radiation detector response testing in Phase I was performed using a SNAP-27 fuel capsule, while the Pioneer F/G instruments will be in a SNAP-19 radiation environment, it became necessary to find means to correct the Phase I experimental data and correlate the response of the instruments to the real environment. The objective of this task was to provide means to update the Phase I data to take into account the differences between SNAP-27 fuel capsule and the SNAP-19 RTG's radiation flux, spectra, and the differences in the orientation of the RTG with respect to the detectors. This task was accomplished by simulating the SNAP-27 radiation emission on a digital computer and computing the radiation spectrum and photon flux around it. Then a tandem pair of SNAP-19 RTG's were simulated and the spectrum and flux similarly computed. The ratio of the SNAP-19 to the SNAP-27 fuel capsule spectra provided a basis for correcting the radiation detector response obtained with the SNAP-27 to correspond to SNAP-19. Using a ratio of the two spectra tended to cancel out some of the errors caused by inaccuracies in source radiation spectrum and absorption coefficients. A detailed description of the analysis and calculations that were performed under this task are included in Sections 4.2 and 4.3.

2.2.3 Recommendations for Spacecraft Modifications (Task 1.3)

This task consisted of an analysis of the radiation fields at the instrument locations and determination of the optimum spacecraft arrangement to minimize the interference of RTG radiation with science instruments. In particular, the study included investigation of:

- The effect of RTG orientation on the radiation field in the instrument compartment.
- Selection of optimum shielding for the RTG's and/or the experiments.
- Determination of optimum RTG boom length.
- Determination of RTG and instrument orientation and/or position on the spacecraft.

The results of this work are given in Section 6. In general, however, this task was started late relative to the Pioneer F/G program so that the basic design of the spacecraft had been completed and could not be influenced to improve the radiation environment for the experimenters. Section 8 deals with the object of this task and makes recommendations and suggestions on the approach to be followed for future RTG-powered spacecraft. By optimizing the spacecraft layout from radiation interference point of view, the radiation flux and interference with science instruments may be greatly reduced.

2.2.4 Experiment Design (Task 1.4)

This task consisted of the following activities:

- Design and construction of test fixtures, detector containers, shields, cables, etc.
- Testing, check-out, and calibration of radiation detector electronic subsystems and components.
- Design and preparation of test procedures.

Discussion of the work performed under this task appears as appropriate throughout the report rather than as a separate section.

2.2.5 Cooperative Test Program to Test Science Instruments (Task 2.1)

This task was established to provide the Pioneer F/G experimenters with an opportunity to test their instruments with the SNAP-27 fuel capsule. All experimenters were notified that the SNAP-27, RTG/Science Instrument Interaction Test Facility, technical assistance, and laboratory instrumentation was available at TRW at no cost to the experimenters. Five experimental groups took advantage of this offer, and tested their instruments at TRW with the SNAP-27 fuel capusle. These were:

1. GSFC/McDonald
2. University of Iowa/Van Allen
3. University of Chicago/Simpson
4. USC/Judge
5. NASA ARC/Wolfe

The results of the tests are given in Section 3.3.

2.2.6 Countermeasure Investigation (Task 2.2)

This task was initiated to obtain supplementary data for the purpose of evaluating the effectiveness of countermeasure techniques. This task was an extension of Phase I effort and included the evaluation of additional absorbers and absorber thicknesses. Also, a more detailed study of the coincidence effects produced by the SNAP-27 radiation in semiconductor detectors was performed.

The absorption data obtained during this task is presented in Section 6.2. The study of coincidence effects is summarized in Section 6.3.

2.2.7 Spectral Measurements (Task 2.3)

This task was established to perform, in cooperation with JPL, accurate SNAP-27 gamma ray spectral measurements using a germanium semiconductor detector. The results are presented in Section 4.4.

2.3 Phase III Task Summary

2.3.1 RTG Source Mockup (Task 1.1)

This task was for the design and construction of two radioisotope source mockups to simulate the gamma radiation spectra and fluxes produced by SNAP-19 RTG's and Pioneer F/G RHU's at fuel ages of one and four years. The neutron flux from one pair of RTG's using a Pu-Be neutron source was also simulated. A detailed description of the simulated sources and associated data are presented in Section 5.2.

2.3.2 Spacecraft Mockup (Task 1.2)

This task comprised the design and construction of a Pioneer F/G spacecraft mockup simulating the mass properties and distribution of a Pioneer F/G spacecraft including:

- A spacecraft structure constructed of materials having radiation absorption and scattering properties similar to Pioneer F/G.
- Mockups of electronic and other equipment simulating the radiation scattering and absorption of the actual equipment.
- Provisions for mounting the RTG and RHU source mockups.

A detailed description of the mockup is presented in Section 5.1.

2.3.3 Radiation Mapping (Task 1.3)

This task included measurements of the gamma radiation fields within the spacecraft science instrument compartment. Direct and scattered radiation were measured as well. Data obtained in this task are presented in Section 6.1.

2.3.4 Radiation Shielding (Task 1.4)

This task was originally designed to include the following items:

- Obtain prototype science instruments from Pioneer F/G experimenters and/or simulate the critical part of these experiments with laboratory radiation detectors.
- Design minimum weight shields for shielding the radiation-sensitive elements of the science instruments from the RTG and RHU radiation.
- Construct the shields and experimentally verify their effectiveness on the spacecraft mockup.

However, discussions with the experimenters revealed that the objective could be better accomplished by making directional radiation flux measurements with a highly collimated radiation detector system. It was agreed with ARC personnel to perform these directional flux measurements instead of experimentally investigating various shield configurations. Description of the test equipment, experimental procedures, and the results are included in Section 6.1.

2.3.5 Cooperative Test Program (Task 1.5)

This task included providing the spacecraft mockup and technical support to the Pioneer F/G experimenters for testing of radiation interference to their instruments in the TRW RTG/Science Instrument Interaction Test Facility.

2.3.6 Radiation Effects Analysis (Task 2.0)

The purpose of this part of the program was to compute the integral radiation doses for various spacecraft subsystems as a function of time and to determine the effects of this radiation on the electronic and other components of the spacecraft. This part of the program consisted of several tasks described in the following paragraphs.

2.3.7 Radiation Field Determination (Task 2.1)

This task consisted of calculating the radiation fields around each pair of RTG's and around RHU's. The calculations, as specified by the work statement, were based on:

- Neutron radiation only (Because gamma radiation is insignificant)
- Approximation of radiation fluxes by $1/r^2$
- A NASA-ARC-supplied model of space radiation and Jovian radiation belts

A detailed description of work performed in this task is presented in Section 7.1.

2.3.8 Radiation Effects Determination (Task 2.2)

This task included the following subtasks:

- Radiation Effects Bibliography

  A bibliography of radiation effects documents pertinent to the Pioneer mission was compiled.

- Materials and Parts Lists

  A list of all materials and parts to be used on the spacecraft science instruments was prepared.

- Radiation Threshold and Damage Level Determination

  The radiation threshold and damage to the science instrument parts and materials was determined as a function of exposure.

- Determination of Problem Areas

  The damage level data was compared to the Pioneer radiation field levels and the Ames ARC was notified of any problem areas via the the monthly progress reports.

- Consulting Services

  Science experimenters were provided consulting services for solving nuclear radiation damage problems and selecting radiation resistant components.

The work performed under these subtasks is summarized in Sections 7.2 and 7.3.

2.4 PHASE IV TASK SUMMARY

2.4.1 RTG Radiation Cleanliness Study (Task 1.0)

This task was established to perform a trade-off study and determine the relative benefits that could be gained by reducing the RTG and RHU radiation interference with science instruments by limiting the impurities in the RTG and RHU fuel. Recommendations were made on the advantages to be gained by the Pioneer F/G experimenters relating to the following:

- Reduction of the neutron emission by using oxygen-18 depleted oxygen in PuO_2 as well as limiting other neutron producing impurities.
- Reduction of gamma ray emission by limiting plutonium-236 and other impurities.
- Selectively stacking the fuel discs in the SNAP-19 fuel capsules to minimize the radiation in the direction of the Pioneer F/G spacecraft by placing the discs with lower gamma ray emission at the end facing the spacecraft.

If such fuel disc stacking was found to be beneficial in reducing radiation levels at the spacecraft, recommend how this can be accomplished. The maximum permissible neutron flux, gamma ray flux and spectrum for the SNAP-19 RTG's was also recommended.

All work performed under this task was reported in a separate report "RTG Radiation Cleanliness Study" dated 16 August 1970.

2.4.2 Continue Cooperative Test Program (Task 2.0)

The Phase III cooperative test program (2.3.5) was extended to January, 1971.

2.4.3 RTG Age Simulation (Task 3.0)

This task was designed to provide a method to change the apparent age of the RTG for spacecraft radiation tests. This was accomplished by augmenting the RTG radiation with radioisotopic sources to produce spectra simulating fuel ages of approximately 2, 4, and 6 years.

This task is still in progress and a summary of the work will be included in the Phase V Final Report.

3.0 PIONEER F/G MISSION

3.1 MISSION DESCRIPTION

The Pioneer F/G mission will be man's first venture beyond the orbit of Mars into the outer solar system. These spacecraft will be the first to penetrate the asteroid belt and to reconnoiter the planet Jupiter. Pioneer F will be launched in late February or early March 1972, with the trip to Jupiter taking from 645 to 795 days. Pioneer G will be launched in April 1973, with a comparable trip time. Unlike earlier Mariner planetary missions, specific dates for planetary encounters by the Pioneers will not be established prior to launch. This will give greater flexibility to trajectory planning for such long missions.

The Pioneer F mission trajectory is shown in Figure 3-1. After a trip of more than half-a-billion miles to Jupiter, each craft will pass the planet with the period of maximum scientific interest covering about 100 hours. Closest approach is planned to be about 100,000 miles.

3.1.1 Gathering of Interplanetary Space Data

One goal of the mission is to assess hazards in deep space and to develop technology and operations experience for the Grand Tour missions to the outer planets - Jupiter, Saturn, Uranus, Neptune and Pluto - planned for the late 1970s.

The Pioneer F/G spacecraft will spend six months to a year passing through the asteroid belt which circles the Sun from 180 million to 330 million miles out. The spacecraft will carry instrumentation to measure the size, density, and velocity of the asteroids. The intensity and polarization of sunlight reflected from asteroids and cosmic dust (zodiacal light) will be measured to allow calculations of overall quantities of cosmic debris.

The experiments will identify the elements making up cosmic radiation and measure speed and direction of these particles within the heliosphere. They will also measure cosmic ray particles outside the heliosphere if its boundary is reached before the limits of spacecraft communications.

After Jupiter enounter, the Pioneers will continue into deep space. Their trajectories will be dependent on the final aim point near Jupiter

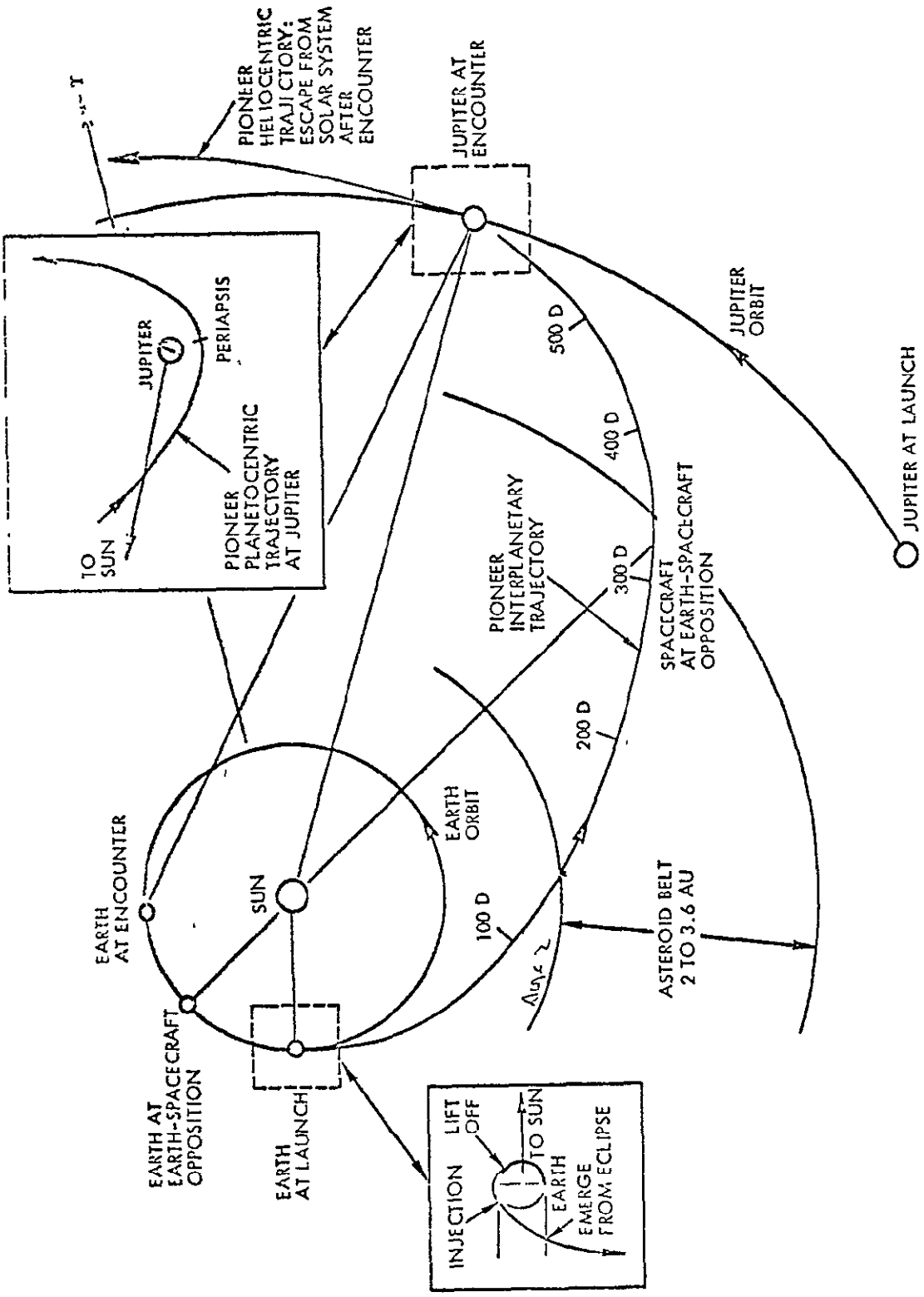

Figure 3-1. Pioneer F MIssion (1972 Launch)

selected for each spacecraft. The trajectory of Pioneer F will take it on a course away from the Sun until it escapes the solar system beyond the orbit of Pluto. It will be the first man-made object to do so. Pioneer G's trajectory could make it the first spacecraft to depart the ecliptic plane. It would travel back in toward the Sun, passing millions of miles above the north poles of the inner planets.

Figure 3-2 shows the predicted plasma density in interplantary space as a function of distance from the sun. Figures 3-3 and 3-4 show the predicted gamma ray and high-energy particle fluxes, respectively. Pioneer spacecraft will actually measure these fields and particles in the interplanetary space.

3.1.2 Gathering of Jupiter Data

Jupiter has a mass some 318 times that of Earth and its period of rotation is about ten hours. Scientists hope to gather clues as to why a planet with a diameter 11 times that of Earth rotates more than twice as fast as Earth.

Jupiter has 12 moons, including three, Io, Ganymede and Callistro, which are larger than Earth's moon. The Jovian atmosphere is made up of hydrogen with minor amounts of methane and ammonia and probably helium. Earth-based studies of Jupiter have not yet revealed whether the surface of the planet is solid, liquid or gas. The surface is hidden by a dense layer of clouds which forms slate blue and salmon pink bands around the planet.

Within these bands a huge Red Spot was detected some 300 years ago. It drifts very slowly about the same latitude but it floats relatively rapidly in longitude. In the last 200 years the Red Spot has circled the planet three times relative to other features. Thus the Red Spot, a major feature of Jupiter, is of major scientific interest.

The planet is believed to be the only planet in our solar system which radiates more energy than it absorbs from the Sun. Current measurements indicate about twice as much. If these observations are correct, they show that Jupiter has a very dynamic interior and may have processes at work which are similar to a star's such as our Sun. Jupiter periodically emits huge surges of radio noise. It appears to have a magnetic field of its own,

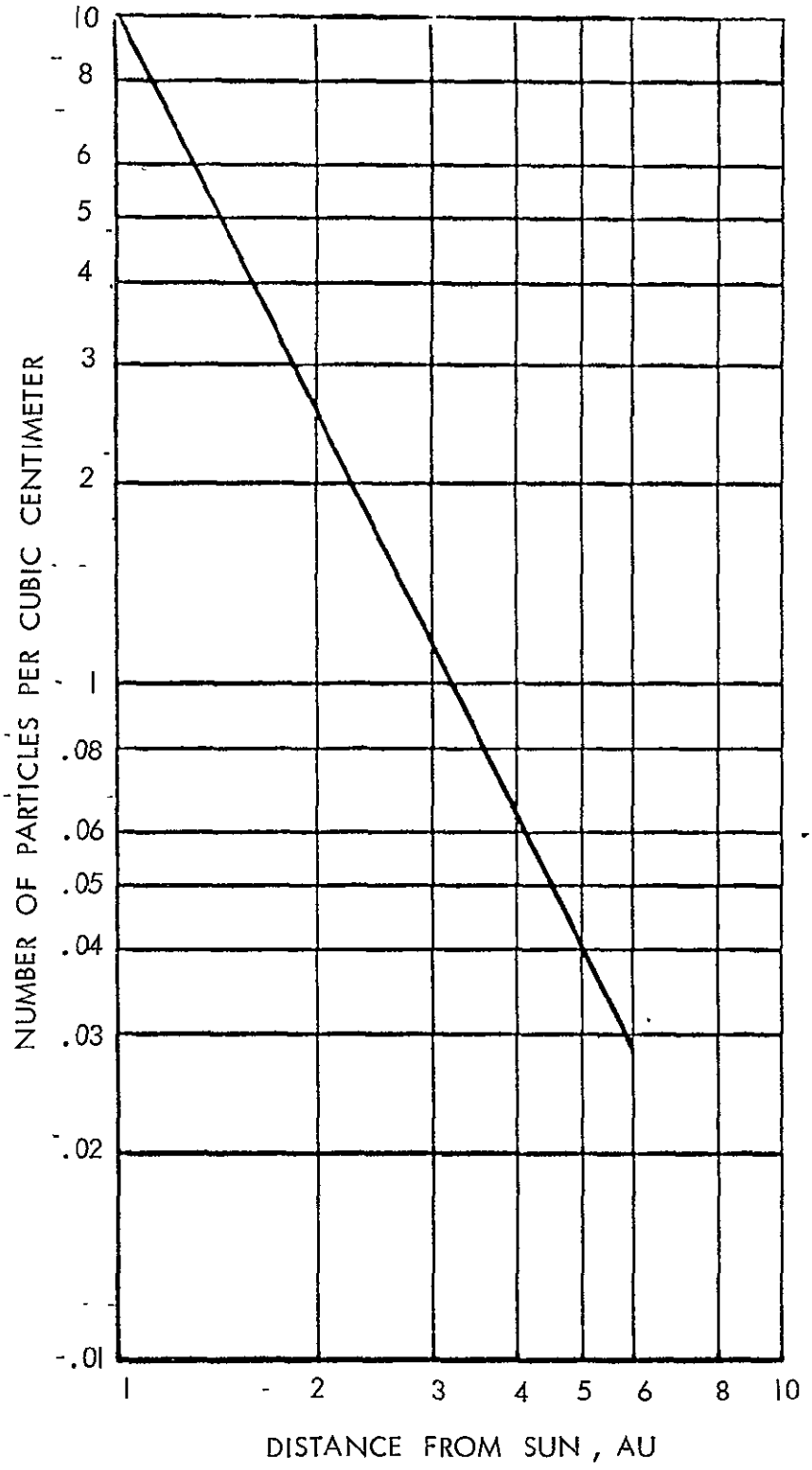

Figure 3-2. Nominal Plasma Density in Interplanetary Space

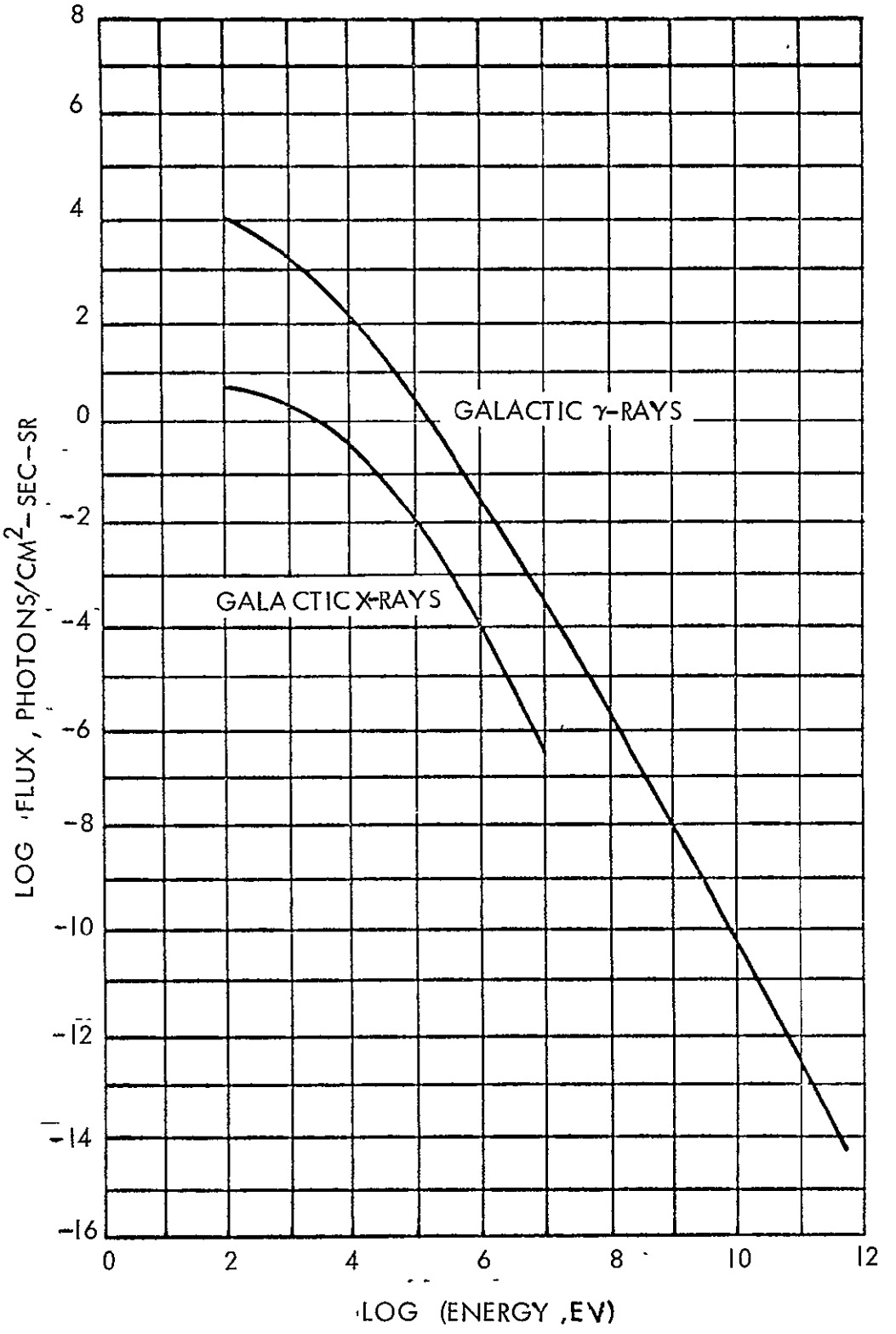

Figure 3-3. X- and γ-Ray Fluxes

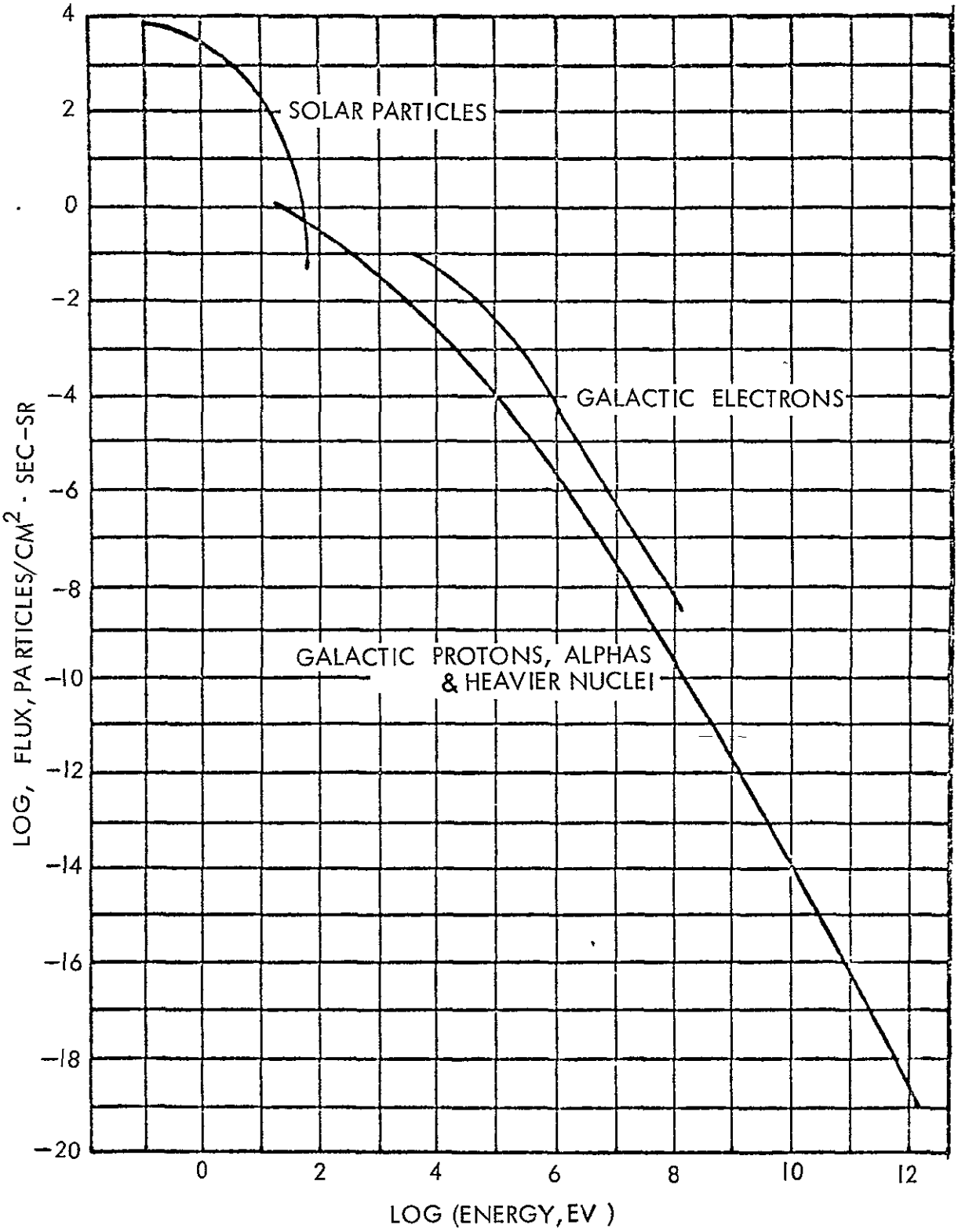

Figure 3-4. High-Energy Particle Flux

similar in shape to Earth's but far stronger, and radiation belts an estimated one million times more intense than Earth's. A model of the predicted trapped radiation zones for Jupiter is shown in Figure 3-5.

Near Jupiter, the Pioneers are instrumented to gather information on a number of unknowns surrounding the planet. In addition, scientists will perform a celestial mechanics experiment and a radio-occultation experiment by analyzing the radio signals from the Pioneers just before and just after they pass behind for about one hour as viewed from Earth. Data returned by the Pioneers during the period of closest approach to the planet will be used in studies of the composition and dynamics of the Jovian atmosphere, its cloud structure and its interaction with the interplanetary medium. Instruments aboard the Pioneers will measure Jupiter's radiation belts and determine the strength of its magnetic field. They will try to determine the mechanism producing the planet's massive radio emissions and measure the planet's internal source of energy. The infrared radiometer should provide data to analyze the thermal balance of Jupiter from several different angles and establish whether the planet does have an unusual internal source of energy.

Scientists also will study Jupiter's bow shock wave created by the solar wind striking the planet's magnetic field and they will gather data on the temperature and composition of Jupiter's upper atmosphere and look for hot spots in the atmosphere.

Also to be studied are possible auroral regions near both poles and levels of heat radiation from the dark side of the planet.

A versatile instrument, an imaging photopolarimeter, will take images of Jupiter which can be used to obtain photographs of the planet. The instrument will have been used earlier in interplanetary space to measure zodiacal light and changes in light reflected by the planet indicating characteristics of Jupiter's surface.

The camera-like device will use the spin of a Pioneer to scan the planet in narrow strips in both red and blue light. Investigators will put the elements together to make composite pictures of the planet. It may be possible to superimpose elements taken with the red and blue filters to make color pictures of the planet. At closest approach (about 100,000 miles) the planet's image will span about 40 degrees of the frame. Taking pictures in strips three-tenths-of-a-degree wide, the camera will complete a picture every 25 to 50 minutes.

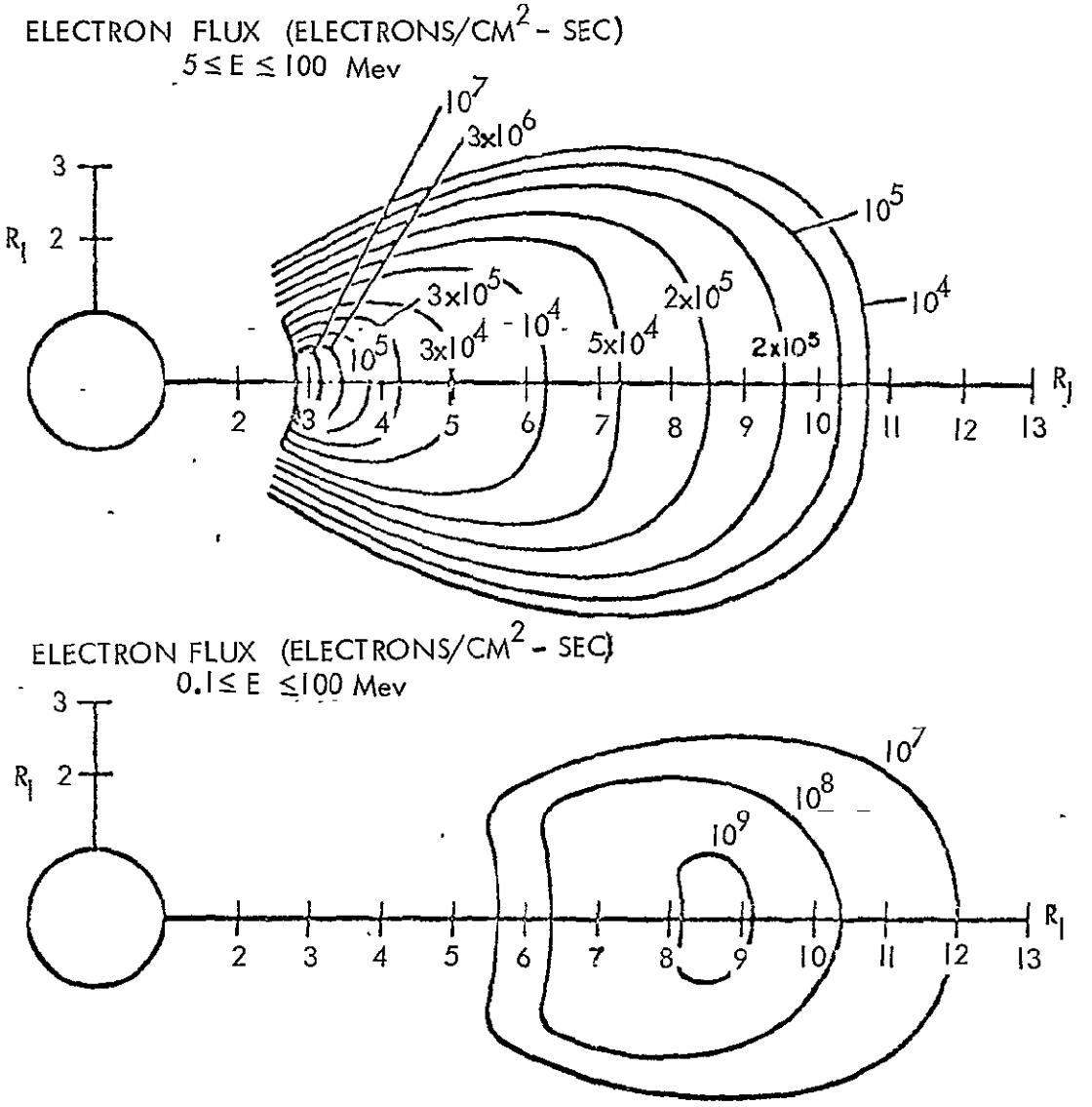

Figure 3-5. Jupiter Trapped Radiation Zones

3.2 SPACECRAFT

3.2.1 Spacecraft Description

Pioneers F and G will be identical spacecraft weighing about 550 pounds apiece and carrying 60 pounds of scientific instruments. Each will be capable of performing 13 scientific experiments in space including photographing Jupiter with better detail than can be obtained with Earth-based telescopes.

The Pioneers will be powered by four radioisotope thermoelectric generators producing a total of 120 watts of electric power. The spacecraft will be stabilized in space by spinning at five revolutions-per-minute in the plane of the Earth's orbit so that a nine-foot-diameter directional radio antenna is pointed constantly at Earth.

Figure 3-6 shows an artist's conception of the Pioneer F/G spacecraft in flight. Figure 3-7 shows the actual Pioneer F structural test model after completion of vibration tests. The RTG's (simulated) and the magnetometer are in the undeployed (launch) positions.

3.2.2 Launch Vehicles

The Pioneers will be launched from the Kennedy Space Center, Cape Kennedy Complex 36B,on a direct ascent trajectory by Atlas-Centaur launch vehicles mounted with a TE 364-4 solid-fuel third stage, (a larger version of the retro motor used in the Surveyor soft lunar landing spacecraft of 1966-8). An Atlas-Centaur vehicle for a Pioneer mission is about 129 feet high and 10 feet in diameter. The booster is the 1-1/2 stage Atlas SLV-3C which has an overall thrust of 420,000 pounds. The upper stage is the 30-foot Centaur vehicle with a thrust of 30,000 pounds. At third stage cut-off, the Pioneers will have a velocity of about 32,400 miles-per-hour (47,350 feet-per-second), believed the fastest a man-made object has ever traveled in space.

3.3 PIONEER F/G INSTRUMENTS

The Pioneer spacecraft will perform thirteen scientific experiments which will make a broad study of a number of interplanetary phenomena, possible hazards of flying through the asteroid belt, the Sun's influence on interplanetary space and the penetration of galactic cosmic radiation into the solar system.

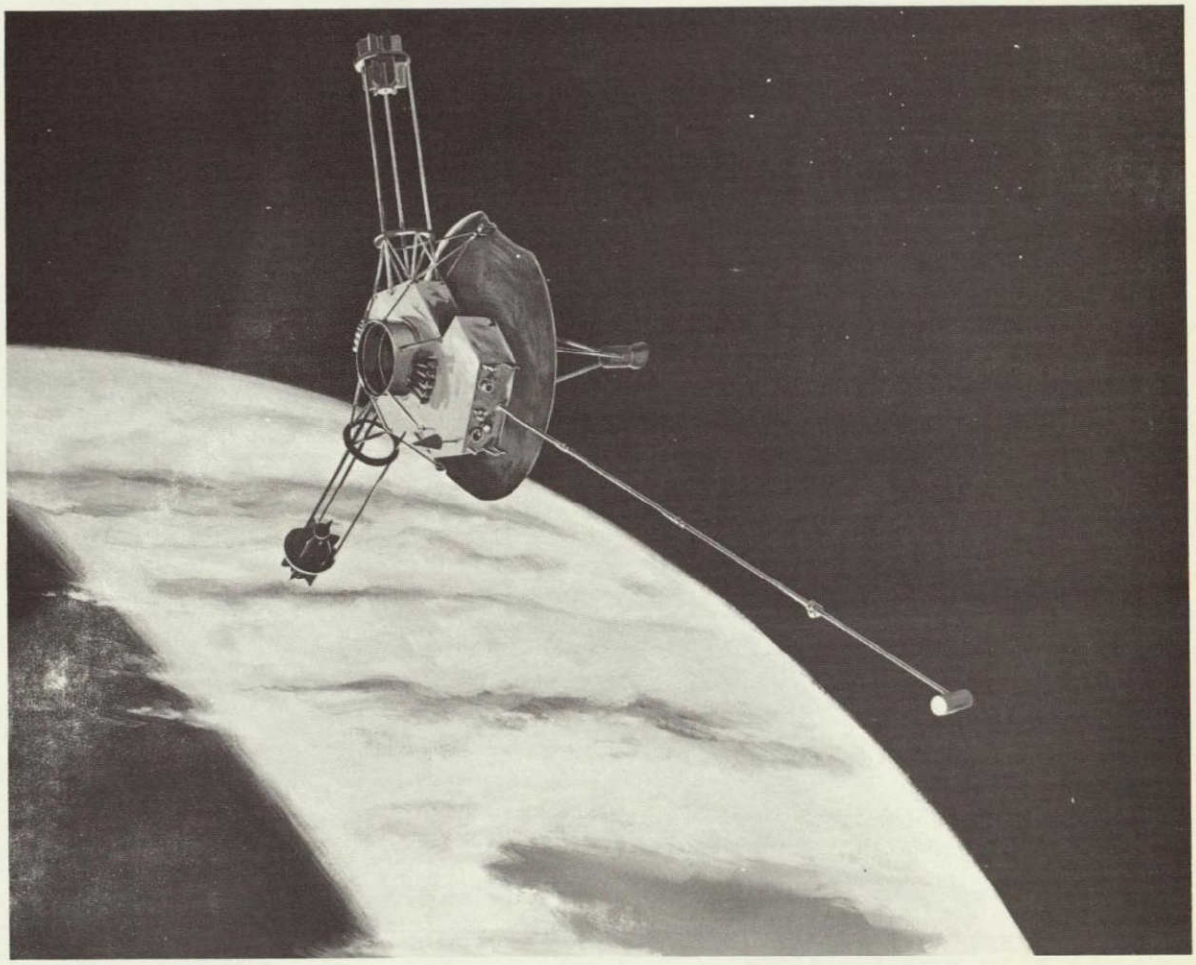

Figure 3-6. Artist's Conception of Pioneer F at Jupiter Encounter

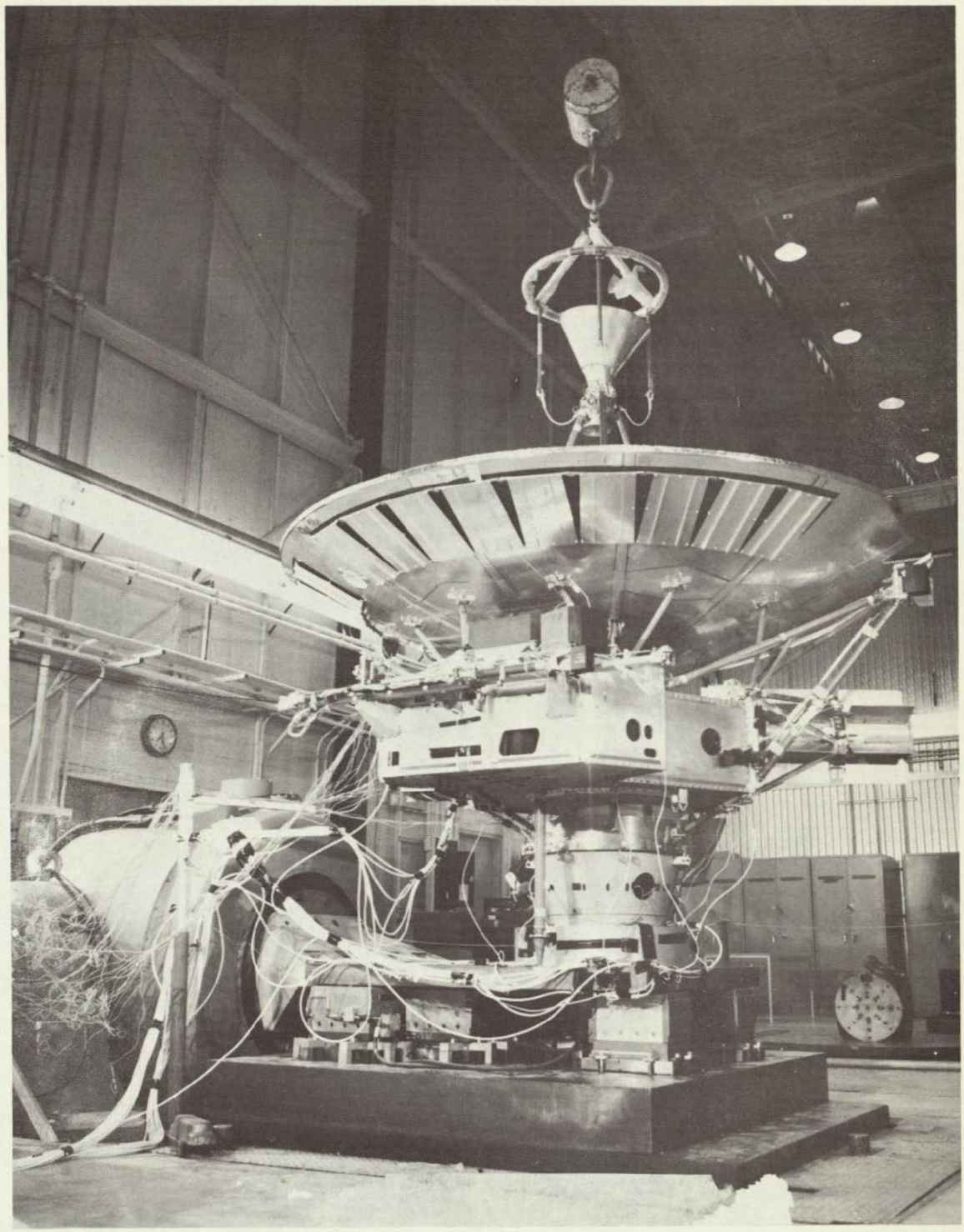

Figure 3-7. Structural Model of Pioneer F Spacecraft after Completion of Vibration Test

Following is a brief description of the scientific instruments which comprise the Pioneer F/G scientific payload. The effect of RTG radiation on each of these instruments is indicated.

3.3.1 Plasma Probe (ARC/Dr. John H. Wolfe)

3.3.1.1 Description

The plasma probe consists of two concentric quasispherical electrostatic analyzers. It is designed to measure 1 ev to 500 ev electrons in 15 energy steps and 100 ev to 8 kev ions in 32 or 64 energy steps.

The various energy ranges are selected by stepping the high voltage on the analyzer plates. This is performed twice per spacecraft revolution for bit rates higher than 256 bits/sec. Detector A is sensitive to electron fluxes as low as 5×10^3 electrons/cm^2-sec-sr. The detecting elements for Detector A are 27 continuous channel multipliers. These are symmetrically located around the exit aperture of the analyzer. Each multiplier is then sensitive to a different portion of the angular distribution of the particles at the entrance aperture in a plane perpendicular to the detector plane of symmetry. The zero angle view direction is parallel to the spacecraft spin axis and the largest angle setting is approximately ± 50 degrees. The angular view in the symmetry plane is 2.4 degrees. As the spacecraft rotates, this 100 x 2.4 degree fan scans about the spin axis. At 512n bits/sec each spacecraft revolution is divided into approximately 20n sampling sectors for $n \geq 1$. The solar wind flow direction can be determined with an accuracy of 2 to 3 degrees when the flow is within ± 50 degrees of the spacecraft spin axis and better than 1 degree when the flow is within ± 40 degrees of the spin axis.

Detector B is different from Detector A in that the detecting elements are five electrometer targets. It is basically an analog device and extends the dynamic range of the total instrument. Its minimum sensitivity is 10^{-14} amp.

The instrument operates in two basic modes. Maximum flux mode (MFM) and a high data rate full scan mode (FSM). In the MFM all sensors of both detectors measure the flux for one-half spacecraft revolution at a fixed analyzer plate voltage. The peak flux is determined. The integrated flux from each Detector A sensor and the samples from the Detector B targets,

along with a measurement of the roll index at each peak, are stored and transmitted at the next half revolution while new data are taken at the next energy step.

The FSM enables generation of high resolution contour plots of the complete plasma angular distribution as a function of energy by stepping the voltage once per revolution.

3.3.1.2 Effect of RTG Radiation

A prototype plasma probe instrument was tested with the SNAP-27 fuel capsule at TRW. The test results indicated that the background produced by the RTG radiation will be in the order of 10 to 30 counts per second in each channeltron. These count rates are considered to be conservative because the tests were conducted with the instrument located in a vacuum chamber where radiation scattering from the walls contributed to the count rate. For most of the time the signal levels are anticipated to be considerably higher than the RTG background. However, at very low plasma densities in the interplanetary space the signal is expected to be of the same magnitude as the RTG induced background making the RTG radiation a potential source of interference.

3.3.2 Magnetic Fields (JPL/Dr. Edward J. Smith)

3.3.2.1 Description

This experiment consists of a vector helium magnetometer designed to operate in seven ranges from ± 2.5 gamma to ± 10 gauss. The instrument will measure the spectrum of the field changes as well as the absolute value of the field in three frequency bands:

0.1 to 1.0 Hz
1 to 3 Hz
3 to 10 Hz

The helium magnetometer operates on the principle that the metastable helium atom states separate into magnetically split energy levels whose separation is proportional to the ambient field. These levels are populated by optical pumping in the infrared (1.08 $m\mu$) and de-excited by the application of a 100 MHz RF signal. The instrument consists of a helium lamp, a polarizer,

a helium absorption cell, an RF excitation supply, an IR detector, and a set of tri-axial coils.

RF excitation (100 MHz) is applied simultaneously to the lamp and absorption cell. The 1.08 mμ radiation from the lamp is circularly polarized and focused on the cell. A rotating magnetic field is applied to the cell, producing a variation in the transparency of the gas which depends on the direction of the magnetic field. The IR detector output is then a sinusoid at twice the frequency of the rotating field. When an ambient field is present the IR detector output contains a component at the rotating field frequency. This component is used to generate three direct currents which are applied to the field coils to null the ambient field. The measurement of these currents yield the magnitude and direction of the field.

The instrument will be mounted on a long boom twenty feet from the spacecraft center, to be as far as possible from the spacecraft body to minimize magnetic field interference from the spacecraft body.

3.3.2.2 Effect of RTG Radiation

Analysis of the helium magnetometer indicates that there is no reason to suspect any effect on the operation of the instrument due to RTG or RHU radiation. One RHU will be mounted on the magnetometer.

3.3.3 Cosmic Ray Composition and Jovian Trapped Radiation (University of Chicago/Dr. John A. Simpson)

3.3.3.1 Description

This experiment will identify specific nuclear species with atomic numbers up to oxygen in an energy range from less than 1 Mev to more than 200 Mev/nucleon. It will also permit the study of electrons E>0.4 Mev.

The instrument consists of three detector systems:

Charged Particle Telescope. The charged particle telescope consists of five Li-drifted silicon solid state detectors, and a CsI crystal in a linear array. A plastic scintillator detector forms a cylindrical guard defining the entrance aperture. A photomultiplier tube detects the scintillations from the plastic scintillator detector. A photodiode is used to detect scintillations from the CsI detector.

The specie of each particle and energy for each event are determined from the particle range and the energy loss in each detector. This is accom-

plished by measuring coincidences between adjacent detectors and performing 256-channel pulse height analyses on the detector outputs.

"Egg". The "egg" is a lead-encased AuSi solid state detector operated in the current mode. This detector will respond to energetic (Mev) electrons at fluxes up to 5×10^{11} (cm^{-2} sec^{-1}). The lead shield acts as a converter to produce low energy electrons and photons that are measured in the detector. It also stops protons E<50 Mev and low energy primary electrons. The instrument is designed to operate in the Jovian radiation belts.

Fission Detector. This detector determines the flux of high energy protons in the Jovian belt by measuring the fission fragments resulting from proton-induced fission in thorium-232. The fission fragments are detected with AuSi solid state detectors. The instrument will determine the intensity of protons E>50 Mev and discriminates against high electron background.

3.3.3.2 Effect of RTG Radiation

A part of the University of Chicago charged particle experiment had to be redesigned in order to operate in the RTG radiation environment. Originally the experiment used a relatively large charged particle telescope consisting of five detectors, a CsI crystal and a plastic scintillator anti-coincidence shield. Tests conducted with a prototype system using a SNAP-27 fuel capsule indicated that the detectors were subordinated by RTG radiation making it impossible to perform measurements of low energy (E <2 Mev) space electrons and protons. As a result the function of analyzing electrons and protons was dropped from the main telescope. An additional small telescope using very thin semiconductor detectors, which are virtually insensitive to gamma radiation, was added to the system. This telescope performs measurements of protons in the energy range of approximately 400 kev to 9.0 Mev. Electron measurements have been sacrificed altogether because of excessive background produced by the RTG gamma radiation.

3.3.4 Jovian Charged Particles (University of Iowa/Dr. James A. Van Allen)

3.3.4.1 Description

The purpose of this experiment is to make an exploratory survey of the intensity, spectra, and angular distribution of energetic electrons (E >40 kev) and protons (E >0.2 Mev) in the magnetosphere of Jupiter. The instrument consists of a coincidence telescope comprised of three miniature Geiger tubes.

Shielding is placed between the elements of the telescope as well as the entrance aperture to define the energy and specie sensitivity of the various element combinations. All other areas of detectors are heavily shielded ($\geq$7 gm/cm^2) to minimize unwanted counts due to penetrating particles. The singles rates E1, E2, and E3 from each tube are read out as well as the double coincidence rate E12 and triple coincidence rate E123.

3.3.4.2 Effect of RTG Radiation

A provisional prototype detector assembly was brought to TRW and tested with the SNAP-27 fuel capsule radiation on July 14 and 15, 1969.

Test data, after correcting for differences in gamma ray flux between the SNAP-27 fuel capsule and SNAP-19 RTG's indicated:

- The single Geiger-Mueller tube counting rate was 0.4 counts/sec (expected galactic cosmic ray rate: 0.2 count/sec),
- The two-tube coincidence rate was 0.15 count/sec (expected galactic cosmic ray rate: 0.007 count/rate, and the
- Three tube (triangular array) coincidence rate was <0.0001 count/sec (expected galactic cosmic ray rate: 0.0002 count/sec).

J. A. Van Allen, the Principal investigator for this experiment, concluded in a letter to Charles F. Hall, Pioneer Project Office, ARC, dated 12 August 1969, that:

- There will be mildly prejudicial effect on the secondary objectives of measuring the galactic cosmic ray gradient and weak solar particle events.
- There will be a trivial effect on the primary objectives of studying the Jovian radiation belts.
- No adverse radiation effects on circuit components are anticipated.
- The potential virtues of RTG's for providing ample power for extended missions beyond the Jupiter encounter far outweigh the slight radiation background that they will cause.

3.3.5 Cosmic Ray Energy Spectra (GSFC/Dr. Frank B. McDonald)

3.3.5.1 Description

The experiment will obtain data to perform studies of the spectra and distribution of:

- Galactic and solar protons — $0.05 < E < 800$ Mev
- Galactic and solar helium — $1 < E < 600$ Mev/nucleon
- Galactic and solar electrons — $0.05 < E < 5$ Mev
- Li, Be, B, C, N, O, F, Ne, and their isotopic composition — $6 < E < 200$ Mev/nucleon

The instrument consists of two charged particle telescopes:

High Energy Telescope (HET). This telescope consists of three solid state detectors and measures protons and alpha particle fluxes between 100 and 800 Mev/nucleon. The specie and energy of the particle are determined by its energy loss (dE/dx) in the central detector. This is performed with a four level integral pulse height analyzer. The outer two detectors define the telescope geometry.

Medium Energy Telescope (MET). This telescope consists of nine stacked solid state detectors. The energy loss (dE/dx), range, and total energy of particles stopping in the stack (4.5 to 50 Mev/nucleon) are determined. This is accomplished with three 256 channel pulse height analyzers. These three analyzers are time shared between seven of the nine telescope elements. The time sharing gives priority to events which occur infrequently. Charge resolution as well as electron measurements are performed.

3.3.5.2 Effect of RTG Radiation

The sensitivity of cosmic ray energy spectra experiment for measurements of electrons and protons in the energy range of 50 kev will be reduced. Dr. McDonald estimated that 25% of the total scientific value of the experiment would be lost due to RTG gamma radiation. As a result a 2.4-pound shield was incorporated into the detection system to attenuate the RTG radiation to acceptable levels for electron and proton measurements during quiescent times of solar activity. Even with this shielding there is some doubt whether measurements of 50 kev electrons will be possible. It may be found necessary to raise the minimum energy threshold to a higher value.

3.3.6 Jupiter Trapped Radiation (University of California - San Diego/ Dr. R. Walker Fillius)

3.3.6.1 Description

The Jupiter trapped radiation experiment will determine the flux and

angular distribution of high energy charged particles. The following species and energy ranges will be studied.

- Protons — 1 to 250 Mev in five energy intervals
- Alpha Particles — 7 to 25 Mev
- Electrons — 0.3 to >8.5 Mev in five energy intervals

The experiment will also determine the total particle flux for:

- Electrons and Protons — E > 10 kev
- Electrons — E > 1 Mev
- Protons — E > 450 Mev

The instrumentation consists essentially of four detector systems:

Cerenkov Counter - Electrons 1 to 100 Mev. This detector operates on the principle that a particle moving through a medium at a velocity faster than the velocity of light causes the emission of light in the forward direction. The radiator medium will probably be an organic liquid such as alcohol sealed in a lucite container. Light from the radiator will be detected by a photomultiplier tube which will convert the light into electrical pulses whose energy height, up to an electron energy whose range is the length of the radiator, is approximately proportional to the incident electron energy. Two pulse height discriminators separate the energies into two intervals E >2.5 Mev and E >8 Mev. The pulse mode is operable for electron fluxes up to 10^5 per cm^2-sec-ster . The DC current from the photomultiplier mode is also monitored. For large electron fluxes, this current yields the flux of electrons with E >1.5 Mev.

Solid State Detector - Protons 1 to 12 Mev, Alpha Particles 6 to 25 Mev. This device is a thin (100-micron depletion depth) solid state detector. The output pulses are examined with three discrimination levels. These detect protons of 1 to 12 Mev, protons of 1.5 to 6 Mev, and alpha particles of 6 to 25 Mev. Because the detector is thin and the discriminator levels are high, the detector is relatively insensitive to electrons.

Solid State Telescope - Protons 20 to 300 Mev. The telescope consists of two 500-micron-thick solid state detector. The telescope is shielded from the back with 19 gm/cm^2 of gold and from the sides with 8.5 gm/cm^2 of brass.

Discrimination levels are set on the rear detector defining energy thresholds at 20 and 90 Mev. Coincidence is required with the output of the front detector to define the entrance aperture. Pulses from the front detector are also counted in a separate channel to monitor the random coincidence rate.

Low Energy Scintillator - Electron >10 kev, Protons >100 kev. This detector consists of a plastic scintillator (1 mil thick)-photomultiplier tube combination designed to measure large fluxes of low energy particles. No specie discrimination is attempted. The photomultiplier anode current is logarithmically converted to a digital word to provide the main output. An auxiliary channel counts pulses greater than 100 kev to give an indication of the pulse height distribution. The dynamic range is 2×10^{-2} to 2×10^{4} ergs.

3.3.6.2 Effect of RTG Radiation. Calculations indicate that the effect of RTG radiation will be negligible since all the detectors are designed to measure high energy particles and very high fluxes as compared to the gamma ray flux produced by the RTG's.

3.3.7 Ultraviolet Photometry (U.S.C./Dr. Darrell L. Judge)

3.3.7.1 Description

The extreme ultraviolet (XUV) filter photometer experiment measures the intensity of ultraviolet radiation at the spectral lines of He I(584 Å), He II(303Å) and Lα(1216 Å). Incoming radiation is collimated and is incident on an aluminum filter with a band pass of 200 - 800 Å. Photons passing through the filter are collected by a lithium fluoride photocathode, which emits photoelectrons. Photoelectrons are also liberated from the front face of the filter predominantly by Lyman alpha radiation. Measurements of the three spectral lines of interest are accomplished by the use of two separate channeltron detectors and their associated pulse-handling circuits. In one channel, photoelectrons produced in the photocathode are electrostatically focused into the funnel-shaped cup of a channeltron multiplier. This channel, which monitors radiation in the filter pass band, is used to observe the 584 Å and 303 Å lines. The other channel, which also uses a channeltron multiplier, monitors photoelectrons released from the leading edge of the aluminum filter.

The charge pulse produced at the anode of each channeltron is amplified and shaped by a charge-sensitive amplifier. The resulting pulse is fed to a fixed dead-time discriminator, which is biased to reject noise and which also delivers standard pulses to the digital data-handling electronics.

3.3.7.2 Effect of RTG Radiation. A breadboard detector system was tested at TRW with the SNAP-27 fuel capsule in February, 1970. The test was described in a letter from Arnold Welch, USC/Project Engineer to Charles F. Hall, Pioneer Project Office, ARC, dated 12 June 1970.

In this test, the field of view limiter (FVL) for the XUV photometer, plus one Bendix continuous channel multiplier (CCM), type 4028C (S/N 9076049) was subjected to the RTG radiation. The CCM collected electrons through the hole nearest the cone end of the FVL. This detector assembly was placed inside the glass bell jar of a vacuum system, and operated at a pressure of 1.8×10^{-6} torr. The FVL did not contain the 1500 Å aluminum thin film filter or the lithium fluoride photocathode. The front end of the CCM was operated at +170 V, and the anode at +3700 V. Pulse counting equipment was used to monitor the output count rates from the CCM.

The fuel capsule was placed 2.7 meters away from, perpendicular to, and in the same plane as, the FVL.

For the above conditions, the results were:

a) When no fuel capsule was present, the count rate was <1 count/sec.

b) With the fuel capsule, the count rate was 24 counts/sec.

c) With a 0.090-in type 6061 aluminum shield between the FVL and the fuel capsule, the count rate was 23 counts/sec.

d) With a 0.25-in lead shield between the FVL and the fuel capsule, the count rate was 8.3 counts/sec.

e) With a 0.7 millicurie source of cobalt-60 placed a distance of 6-in from the FVL, the count rate was 150 counts/sec.

Conclusions:

No problems are anticipated as a result of the XUV experiment operating in the fields of the four RTG's being considered for the Pioneer Jupiter missions. The expected background count rate for each channel, for the RTGs in their deployed positions, is 12 counts/sec.

3.3.8 Imaging Photometry and Polarimetry (University of Arizona/ Dr. Thomas Gehrels)

3.3.8.1 Description

The Imaging Photometry Polarimetry (IPP) experiment performs three basic measurements:

- Zodiacal light mapping to study asteroidal matter, light scattered from the Jupiter atmosphere and the Galilean satellites.
- Jupiter polarimetry to study gas above the clouds and cloud particles.
- Jupiter imaging in two colors with 140 km resolution.

These measurements are performed with one instrument. A rotatable disk at the telescope focus carries four field stop apertures for the three operating modes and a calibration mode. Radiation passes through the field stop and is collimated onto a Wollastan prism. This prism spatially separates the radiation into two polarization components. Each component passes through a fiber optics bundle to a dichroic filter. Radiation reflected from this filter falls in the bandpass from 3900 to 4900 Å, and is detected by channeltron photomultipliers. Radiation transmitted through the dichroic filter is further passed through a bandpass filter which defines a 5800 to 7000 Å spectral bandpass. This is then also detected by a channeltron photomultiplier. Radiation is therefore analyzed in two colors and two components of polarization.

Two stepping motors are used, one changes the field stops and the second permits the viewing direction to be changed.

3.3.8.2 Effect of RTG Radiation

A review of the instrument revealed no reason to suspect that the RTG radiation will have an effect on its performance and/or operation.

3.3.9 Jovian Infrared Thermal Structure (Cal. Tech./Dr. Guido Munch)

3.3.9.1 Description

The main purpose of the experiment is to measure the net thermal energy flux from Jupiter. The instrument is a radiometer consisting of a Cassegrainian telescope and two thermopile detectors. Two reflecting filter elements define the two spectral bandwidths, i.e.,

Channel 1	14 to 25 microns	MgO reflector
Channel 2	29 to 50 microns	TiO_2 and BaF_2 reflectors

The radiometer measures temperatures between 80° and 180°K.

The radiation detectors are thin film bismuth-antimony thermopiles evaporated on an extremely thin aluminum oxide film which is supported by an annular saphire disc. Each detector has five bismuth-antimony junctions connected in series. The "hot" junction is fabricated by joining the bismuth and antimony bars together with a thin gold bar and blackening. A cold sink for the couple is provided by relatively wide gold bars connecting the couple in series.

Radiation is absorbed by the "hot junction" producing, by the Seebeck effect, a potential difference between the "cold" and "hot" junctions. The current produced is modulated by the spacecraft spin. This is then amplified, demodulated, digitized, and multiplexed to the telemetry.

3.3.9.2 Effect of RTG Radiation

Review of the instrument revealed no reason to suspect that the RTG radiation will have an effect on its operation or performance.

3.3.10 Meteoroid/Asteroid Astronomy (G.E./Dr. Robert K. Soberman)

3.3.10.1 Description

This instrument uses a Sisyphus optical detection system to measure meteoroid and asteroid concentrations and orbits on the Pioneer F/G missions through the asteroid belts to Jupiter. Meteoroid or asteroid size and velocity are determined by measurement of the reflected or scattered solar radiation from the object. The passage of the body is measured by three independent non-imaging optical subsystems. The optics use four 8-inch Cassegrainian telescopes, each coupled to a photomultiplier.

3.3.10.2 Effect of RTG Radiation

GE information for the Pioneer metroroid/asteroid astronomy experiment states that the experiment is quite immune to radiation and that even large fluxes of charged particles, such as caused by the solar events, will have a negligible affect. Thus there is no reason to anticipate any problems due to radiation produced by the RTGs.

3.3.11 Meteoroid Detection (NASA LRC/William H. Kinard)

This experiment uses externally mounted meteoroid penetration detectors. No effect due to RTG radiation is anticipated on this experiment.

3.3.12 S-Band Occultation (JPL/Dr. Arvydas J. Kliore)

This experiment will use the spacecraft radio transmitter. The radio signals from the Pioneers will be analyzed on Earth just before and just after Jupiter eclipse. No effect due to RTG radiation is anticipated.

3.3.13 Celestial Mechanics (JPL/Dr. John D. Anderson)

Earth-based Deep Space Network Doppler radar will be used to monitor the spacecraft and determine celestial mechanics. There will be no effect due to RTG radiation on this experiment.

4.0 PIONEER F/G RADIATION FIELDS AND EFFECTS

A detailed discussion of the nuclear environment created by plutonium-238 fuel was reported in reference 4-1. This section summarizes these results and also provides updated data applicable to the SNAP-19 RTG's to be used on the Pioneer spacecraft.

4.1 RTG RADIATION CHARACTERISTICS

The RTG fuel capsule produces heat by absorbing the radiation produced by the plutonium radioisotope fuel. The heat is derived mainly from alpha particles of 5.49 Mev (72%) and 5.45 Mev (≈28%). These alpha particles, however, are contained within the fuel capsule by the capsule walls and do not contribute to the nuclear environment around the scientific instruments.

The RTG fuel also produces other types of radiation,

- Neutrons from spontaneous fission of plutonium, (α,n) reactions with light elements, and neutron multiplication.
- Gamma radiation from impurities present in the fuel and gamma emission which accompanies alpha decay of plutonium-238.
- X-rays and beta particles which accompany some of the nuclear reactions in the plutonium fuel decay chains.

The neutrons and gamma rays largely escape the capsule to produce the nuclear environment around the spacecraft. The X-rays and beta particles do not interfere with the scientific instruments because they are absorbed within the fuel and/or the fuel capsule walls. Any bremsstrahlung produced in the beta ray absorption process contributes a very small amount of the total radiation.

The potential interference to the scientific instruments caused by gamma radiation will be quite significant while the interference caused by neutron emission, with one exception, will be small. Radiation damage to electronic components, on the other hand, is primarily due to neutron radiation.

4.1.1 Pioneer RTG and RHU Fuel

The SNAP-19 RTG fuel capsules for the Pioneer F/G Spacecraft contain 635 to 640 thermal watts of plutonium-238 fuel per RTG. There are four RTG's on each Pioneer F/G spacecraft. The fuel for each RTG consists of a stack of 17 plutonium-238 dioxide molybdenum cermet (PMC) pucks. Each stack is 3.9 inches high and 2.1 inches in diameter and is contained in a cylindrical fuel capsule consisting of a Ta-10W liner, a T-111 strength member, and a Pt-20Rh cladding.

The RHU's produce one thermal watt from the same fuel form as the RTG's. The fuel is contained in a small capsule consisting of the same materials as the RTG capsules.

The majority of the work performed under this program assumed solid solution cermet fuel (SSC), which was the baseline design at the time of the work. This fuel consists of molybdenum-coated PuO_2-ThO_2 solid solution ceramic particles pressed to form cermet pucks. About August, 1970, the fuel form for the SNAP-19 and RHU's was changed from SSC to PMC. This fuel consists of PuO_2 particles coated with 17.0 $^{+2.0}_{-1.0}$ weight percent molybdenum. Pucks are formed by hot pressing, typically at 13,500 psi and 1700°C for 10 min. Nominal compositions, density, and power densities of fuel forms are shown in Table 4-1

Table 4-1. Characteristics of Cermet Fuel Forms

	SSC	PMC
Plutonium, w/o	67.5	73
Thorium, w/o	6.5	--
Molybdenum, w/o	16	17
Oxygen, w/o	10	10
Density, gm/cc	10.4	10.2-10.4
Power Density, watts/cc	$\geq$3.2	3.2-3.5

Typical compositions of the plutonia ceramic before coating with shown in Table 4.2 together with actual formulas (calculated) demonstrating the deviation from stoichiometric $Pu_{1.00}O_{2.00}$.

Table 4-2. Chemical Analyses on Sized $^{238}PuO_2$ Feed Powder

Lot No.	Element, W/O				Calculated Formula
	Pu	Th	U	O	
27	87.4	0.20	0.59	11.75	$(Pu_{0.991}Th_{0.002}U_{0.007})\ O_{1.98}$
28	87.2	0.18	0.63	11.66	$(Pu_{0.990}Th_{0.002}U_{0.008})\ O_{1.97}$
33	87.1	0.17	0.68	11.76	$(Pu_{0.990}Th_{0.002}U_{0.008})\ O_{1.99}$
35	87.3	0.21	0.65	11.96	$(Pu_{0.990}Th_{0.002}U_{0.008})\ O_{2.02}$
36	87.7	0.21	0.76	11.68	$(Pu_{0.989}Th_{0.002}U_{0.009})\ O_{1.96}$

Plutonium compositions for typical lots of RTG fuel are given in Table 4-3.

Table 4-3. Isotopic Distribution of Plutonium Isotopes used in PMC Fabrication, Weight Percent

Isotope	Lot 1	Lot 2	Lot 3
238	80.0	79.6	79.5
239	15.76	16.1	16.3
240	2.77	2.8	2.8
241	1.01	1.0	1.0
242	0.368	0.40	0.34
236	0.00010	0.00011	0.00011

The level of impurity elements present in the molybdenum-coated plutonium dioxide particles are analyzed and limited to 0.31 weight percent total, with the stipulation that individual elements shall be reported if they exceed certain limits. Table 4-4 gives these limits together with actual analyses of four typical batches of particles.

Table 4-4. Impurity Analysis of Molybdenum-Coated Plutonium Dioxide Particles, ppm

Element	Batch No.				Limit	
	33	34	35	36	SSC	PMC
Al	< 50	< 50	< 66	< 85	400	400
Ca	<250	<250	<250	<250	500	500
Co	ND	ND	ND	< 28	250	250
Cr	< 50	< 50	< 50	< 78	350	350
Cu	150	< 52	< 50	50	300	300
Fe	280	303	198	282	350	500
Mg	< 50	< 50	< 50	< 50	50	50
Na	ND	ND	ND	ND	200	250
Ni	< 50	< 50	< 50	< 50	150	200
Si	50	< 50	< 50	< 78	300	300
Ba	< 50	< 50	< 50	< 50	-	-
Mn	< 50	< 50	< 50	< 50	-	-
Pb	< 50	ND	ND	< 50	-	-
Zn	150	ND	ND	ND	-	-
Sn	ND	ND	ND	ND	-	-

ND = Not Detected

4.1.2 Neutron Radiation from the Fuel

4.1.2.1 Neutron Generation

Neutron radiation in PuO_2 radioisotope fuel is produced in three different ways: spontaneous fission of plutonium, (α,n) reactions with light elements, and neutron multiplication. Spontaneous fission produces on the order of 3×10^3 neutrons/sec-gram of Pu. The (α,n) reaction produces 1.9×10^4 neutrons/sec-gram of PuO_2 in a normal (i.e., non-cermet) plutonium dioxide fuel. Thus the total emission (without neutron multiplication) is on the order of 2.2×10^4 neutron/sec-gram of PuO_2 fuel. This fission neutron energy spectrum for plutonium fuel is shown in Figure 4-1.

Neutrons produced by the (α,n) reaction are primarily due to alpha particles striking oxygen-18 and oxygen-17 isotopes contained in PuO_2. Although the natural abundance oxygen-17 and oxygen-18 is quite low, 0.037

and 0.204 percent, respectively, their high cross sections for (α,n) reactions make them by far the largest contributors to the total neutron output with the maximum cross sections for the ^{17}O (α,n) reaction being about 10% of that for the ^{18}O (α,n) reaction. The neutron yield in PuO_2 bearing naturally occurring oxygen is 1.9 x 10^4 neutrons/sec-gram of Pu. The neutron spectrum produced by the $^{18}O(\alpha,n)^{21}Ne$ reactions is given in Figure 4-2. Neutron yields for (α,n) reactions with other elements are given in Table 4-5 and Table 4-6 lists the threshold energy for several (α,n) and (α,p) reactions.

It can be seen that a (α,n) reaction also occurs by alpha particles striking fluorine atoms. Residual fluorine (0.3%) appears in the SSC and PMC fuel forms from the process used to coat PuO_2 with molybdenum hexafluoride before fabrication of the fuel discs.

The solid solution cermet fuel form has a higher oxygen content per gram of plutonium because it contains about ten percent of ThO_2, thus the neutron output should be approximately 10% higher per gram of

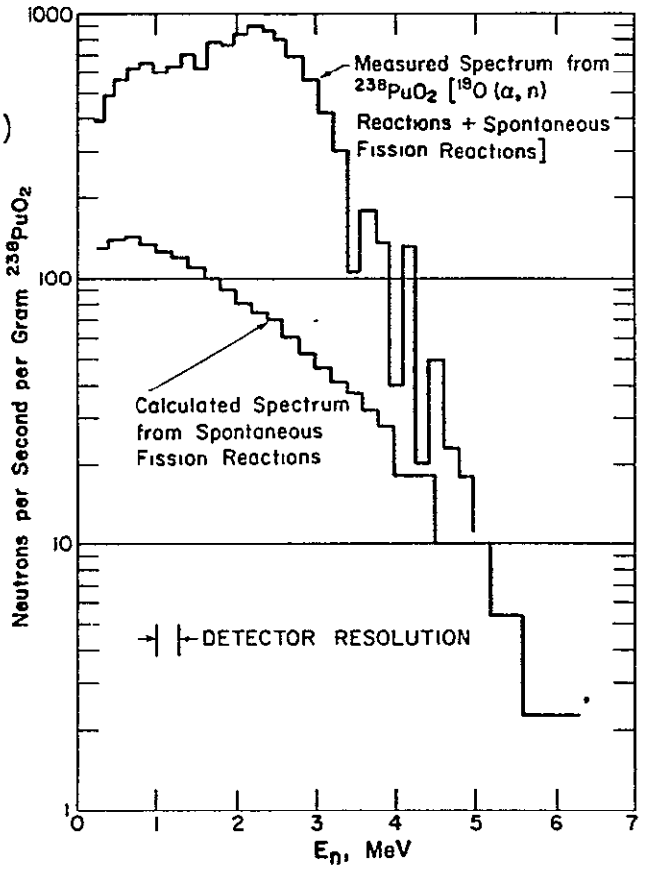

Figure 4-1. Plutonium-238 Dioxide Neutron Spectrum Components. (Ref. 4-2)

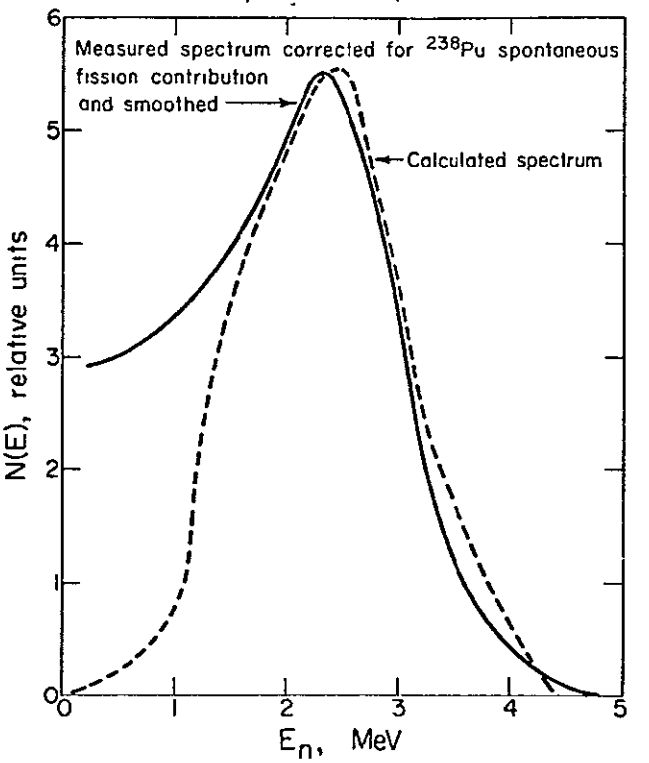

Figure 4-2. Neutron Spectrum Produced by Plutonium-238 alphas in ^{18}O (α,n) ^{21}Ne reactions. (Ref. 4-2)

Table 4-5. Neutron Yields from (α,n) Reactions of Plutonium-238

Element	n/sec/g Pu per 1 ppm	Element	n/sec/g Pu per 1 ppm
Li	4.6	Na	2.2
Be	133	Mg	2.1
B	41	Al	1.0
C	0.2	Si	0.2
N	0	P	< 0.3
O*	0.1	S	< 0.3
F	18		

*Normal Oxygen

Table 4-6. (α,n) and (α,p) Reactions Occurring in RTG Fuels

Nuclide	Natural Abundance %	Reaction	Threshold Energy, Mev
Carbon-12	98.89	α,n	11.35
Carbon-12	1.11	α,n	0
Nitrogen-14	99.63	α,n	6.10
Nitrogen-15	0.37	α,n	8.15
Nitrogen-14	99.63	α,p	1.54
Oxygen-16	99.759	α,n	15.19
Oxygen-17	0.037	α,n	0
Oxygen-18	0.204	α,n	0.86
Fluorine-19	100	α,n	3.10
Fluorine-19	100	α,p	0

plutonium than for pure PuO_2 such as used in PMC or microsphere fuel form.

A study conducted at Mound Laboratory (reference 4-3) reveals that the neutron multiplication for the SNAP-19 RTG fuel capsules in the geometry used by the Pioneer F/G spacecraft will be negligibly small, however, neutron multiplication within each capsule is not negligible. Measurements performed at Mound Laboratory with prototype SNAP-19 fuel capsules show that the neutron multiplication accounts for approximately 24 percent increase in neutron emission from each capsule.

The neutron multiplication for Pioneer capsule PF-2, the ratio of neutrons from neutron induced fission to all other neutrons, is

$$\frac{0.23}{1-0.23} = 0.30 \text{ or } 30\%.$$

This value is in agreement with a calculated value of 30%.

4.1.2.2 Emission Rates

In order to reduce the neutron output from the RTG's, oxygen gas, enriched to 99.98% oxygen-16, was used to form the dioxide during calcination of the oxalate. This resulted in a ten-fold reduction in the abundance of oxygen-17 and oxygen-18 over the natural state which should reduce the neutron emission due to (α,n) reactions to 1.7×10^3 neutrons/sec-gram of Pu-238. Thus the total neutron emission from the Pioneer RTG and RHU fuel was anticipated to be approximately 5×10^3 neutron/sec-gram of Pu-238. Since at the time of this work, a SNAP-19 RTG was expected to contain approximately 2300 grams of solid solution cermet fuel, (675 thermal watts at 0.31 watts/gram) and the SSC fuel contains 67.5 percent of plutonium, the total neutron output was calculated to be 7.5×10^6 neutrons/sec per RTG, or 1.5×10^7 neutrons/sec per pair of RTG's. Most of the work performed under Phase III of the RTG/Science Instrument Interactions Program, which included assessment of radiation interference with science instruments and radiation damage to electronic components, was based on this neutron emission rate. The neutron output per RHU was anticipated to be approximately 1000 neutrons/sec.

Later communications with Mound personnel indicated that measurements of the neutron emission from plutonium-238 PMC fuel samples yielded considerably higher flux than was initially anticipated, in the order of 3×10^4 neutrons/sec-gram of Pu-238. The corresponding neutron emission rates with neutron multiplication included would be on the order of 9×10^7 neutrons/sec for a pair of SNAP-19 RTG's and 6000 neutrons/sec per RHU, or approximately six times higher than originally anticipated.*

4.1.2.3 SNAP-19 Neutron Spectrum

In November, 1970, the neutron energy spectrum for Pioneer capsule PF-2 was determined at Mound Laboratory. A single stilbene crystal, fast neutron spectrometer and a long counter were used for the measurement. The capsule was removed from its calorimeter container and positioned in a stainless steel and aluminum support. Two blowers, directed at the capsule, were used for cooling. The capsule detector separation was 94 cm. The capsule and detector were located 156 cm above the floor, and the nearest wall was 145 cm from the capsule. A paraffin-filled shadow shield was used to determine the room scattered neutron background.

This spectrum is shown in Figure 4-3. Uncertainties shown are $\pm$ one standard deviation and are from counting statistics only. The datum point at 0.5 Mev was determined from a difference measurement using both the stilbene and long counter data. The rest of the spectrum was determined from the stilbene data. This spectrum is composed of neutrons from the

---

*The actual measurements of neutron emission from the first SNAP-19 prototype fuel capsule performed around November, 1969, yielded 4.5×10^4 neutron/second-gram of Pu-238 and a total neutron output of 5.17×10^7 neutrons/sec for the completed fuel capsule. The fuel for the second capsule had 3.73×10^4 neutron/second-gram of Pu-238 and a total output of 4.26×10^7 neutrons/sec from the complete fuel capsule. It is anticipated that as the fuel production technique is refined the neutron output for the Pioneer F/G flight units will be less than 3×10^4 neutrons/second-gram of Pu-238 or a total output of 3.4×10^7 neutrons/sec from each fuel capsule. Note that the neutron output is expressed per gram of Pu-238. Since plutonium used in the fuel capsule contains 79 percent Pu-238, while the remainder consists of other plutonium isotopes, the neutron emission rates should be multiplied by 0.79 to obtain neutron emission per gram of plutonium. Also the SSC and PMC contain 67.5 and 73 percent of plutonium, respectively, thus the neutron emission given in terms of neutrons/second-gram of Pu-238 should be multiplied by 0.532 and 0.576 to convert to neutron output per gram of fuel.

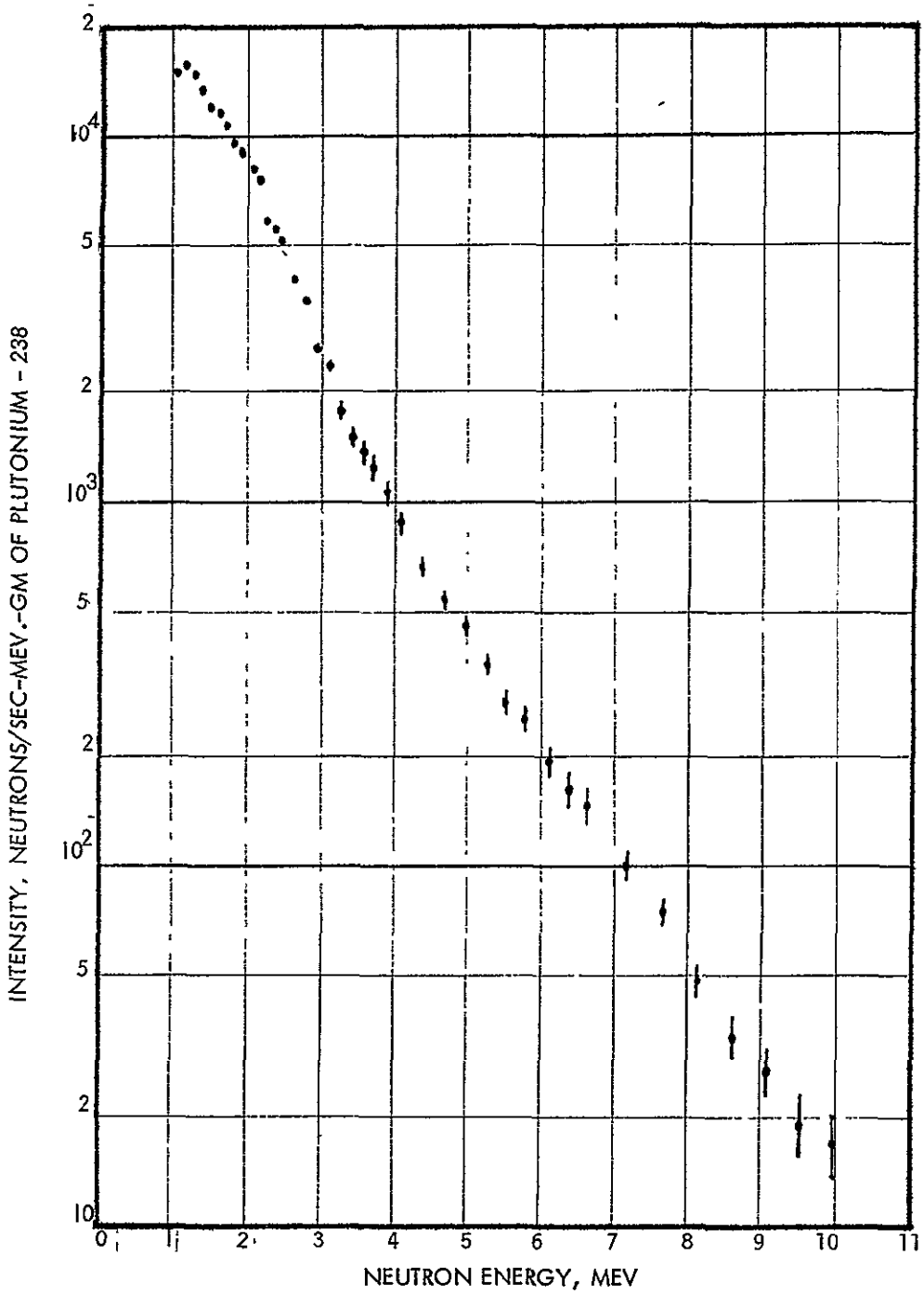

Figure 4-3. Neutron Energy Spectrum of Pioneer Capsule PF-2

following sources: spontaneous fission of plutonium-238 (7%), neutron induced fission of plutonium-238 (23%),(α,n) reaction with oxygen (7%), and (α,n) reactions with elements other than oxygen, the principal such element being fluorine - 63%.

4.1.3 Effect of Neutron Radiation on Operation of Scientific Instruments

Neutron radiation may cause damage to electronic components and interfere with the operation of Pioneer F/G science instruments. Neutron damage to electronic components is reported in Section 7. Interference of neutrons with the science instruments was studied during Phases I and II of the RTG/Science Instrument Interactions Program. With one exception, the interfence on science instruments due to neutrons was found to be small compared to the effects caused by gamma radiation. It was determined that only the fission detector used in University of Chicago charged particle experiment will be significantly affected by the neutrons.

4.1.3.1 University of Chicago Charged Particle Experiment

This detector is used to determine the high energy proton flux in the Jovian radiation belt by measuring the fission fragments resulting from proton-induced fission in a thorium-232 foil. The fission fragments are detected by a pair of AuSi solid state detectors. The instrument will determine the flux of protons with energies greater than 50 Mev and will be capable of discriminating against high energy electrons and other particles.

The thorium-232 foil used in the charged particle experiment is 0.004-in thick. It has a neutron-induced fission cross section on the order of 0.15 barn for neutrons with energy in the range of 1.5 to 6.5 Mev. The proton induced fission cross section is approximately 0.75 barn for protons with $E \geq 25$ Mev. Calculation shows that there will be 4×10^{-5} fissions produced in the fission foil per neutron striking it.

Figure 4-4 shows the neutron isoflux around the Pioneer F/G Spacecraft. Values on the left are based on a 5×10^{3} neutron/sec emission rate. To correct this to the measured Pioneer emission rate, the values on the left must be multiplied by six. The results are shown on the right. At the time of this work, it was planned to locate three RHU's in each of three thruster cluster assemblies and two in the Sun sensor. However, instead of the two RHU's in the Sun sensor it is now planned to locate one in the magnetometer and probably only one in the Sun sensor.

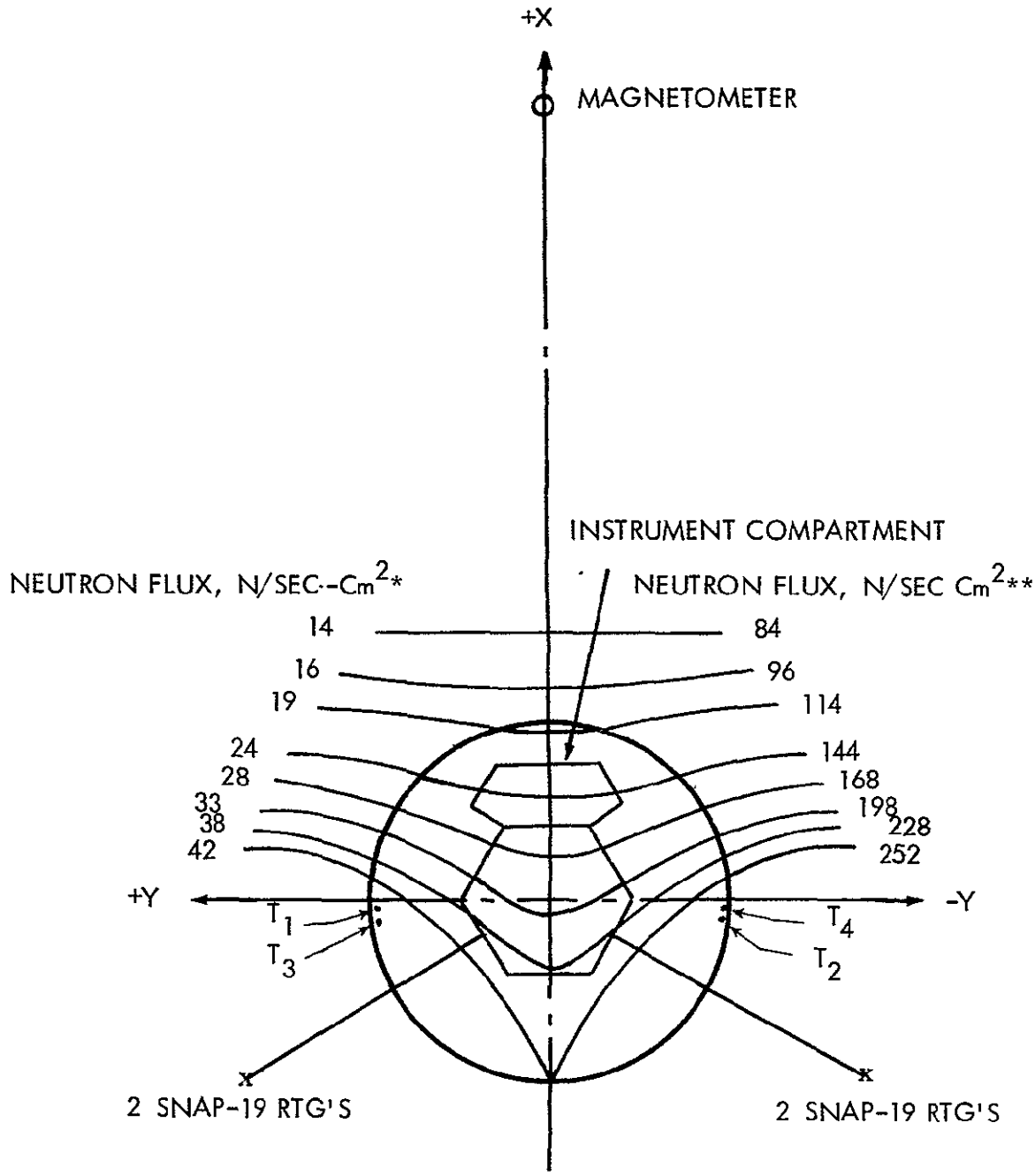

* BASED ON 5×10^3 NEUTRONS/SEC-GRAM OF PU-238.

** BASED ON 3×10^4 NEUTRONS/SEC-GRAM OF PU-238.

Figure 4-4. Neutron Isoflux Plot for Pioneer F/G Spacecraft

The effect of this change is negligible because of the large distance between the magnetometer (extended on an 20-foot long boom) and the instrument compartment. T_1, T_2, etc., indicate locations of the RHU's.

Table 4-7 gives the calculated neutron flux at the University of Chicago instrument location showing the relative contributions of the RTG's and the RHU's. For a 600-day mission this neutron flux represents a fluence of 1.2×10^9 to 7.2×10^9 neutrons/cm^2. For a 850-day mission the fluence at the science instrument will be 1.8×10^9 to 10.8×10^9 neutrons/cm^2. Since the anticipated neutron flux is approximately 20 to 120 n/sec cm^2 with E >1.5 Mev, there will be approximately 1 to 6×10^{-3} fissions/cm^2-sec induced in the foil. This fission rate is equivalent to the fission rate produced by a proton flux of about 0.5 to 3.0 protons/cm^2-sec with $E \geq 25$ Mev. This calculation is in agreement with test data obtained by J. J. O'Gallagher and S. Tejero of the University of Chicago during tests conducted at TRW, October 21-24, 1969, using a prototype fission detector system and a SNAP-27 fuel capsule as the radiation source.

The constant neutron background induced by the RTG's will affect the sensitivity of the fission detector to high energy protons (> 50 Mev) within the Jovian radiation belt. If compared to an estimated 10 events/day due to cosmic radiation, 0.6 events/sec due to solar flare (12 November 1968) and an anticipated maximum of 4200 events/sec for a hypothetical Jovian proton belt (assuming 10^3 x Earth proton belt of differential spectrum $J(E)\ E^{-4}$), a background of 0.5 to 3.0 counts/sec is a significant disadvantage in observing solar protons or determining the boundaries of radiation belts.

4.1.3.2 Silicon Semiconductor Detectors

Some concern has been expressed over the possibility of (n,α) and (n,p) reactions producing spurious counts in the silicon semiconductor detectors that are used in several experiments carried on board the Pioneer spacecraft. Tests conducted with the SNAP-27 fuel capsule have failed to detect any events in the presence of gamma radiation (even after considerable shielding) that could be attributed to the (n,α) and (n,p) reactions. Table 4-8 gives the expected neutron flux and spectrum at the instrument compartment location as a function of energy together with the cross sections for (n,α) and (n,p) reactions and the events due to these reactions

Table 4-7. Calculations of Neutron Flux for University of Chicago Instrument Assuming no Shielding

Neutron Source	Fuel Weight, Grams	Neutron Emission Rate, n/sec	Source to Instrument Distance, Inches	Neutron Flux at Detector, n/sec-cm^2
T_1	3	3×10^3	53.3	1.3×10^{-2}
	3	18×10^3	53.3	7.8×10^{-2}
T_2	3	3×10^3	89.9	0.5×10^{-2}
	3	18×10^3	89.9	3.0×10^{-2}
T_3	2	2×10^3	56.8	0.7×10^{-2}
	2	12×10^3	56.8	4.2×10^{-2}
T_4	3	3×10^3	87.2	0.5×10^{-2}
	3	18×10^3	87.2	3.0×10^{-2}
Total RHU's	11	11×10^3	--	3.0×10^{-2}
	11	66×10^3		18.0×10^{-2}
+Y RTG	4600	1.5×10^7	112	14.9
	4600	9.0×10^7	112	89.4
-Y RTG	4600	1.5×10^7	141	9.3
	4600	9.0×10^7	141	55.8
Total RTG's	9200	3.0×10^7	--	24.2
	9200	18.0×10^7		145.2

for a silicon semiconductor detector 1 mm thick and 1 cm^2 in. area.

Table 4-8 indicates that the proton and alpha production rates due to (n,p) and (n,α) reactions in a 1-mm thick detector are 0.31×10^{-3} and 0.13×10^{-3} particles/sec-cm^2, respectively. Thus in a large (4.9 cm^2 x 1.5 mm thick) University of Chicago charged particle telescope detector, the total expected count rate due to neutron reactions with silicon-28 will be on the order of 0.003 counts/sec assuming 5×10^3 neutrons/sec gram of Pu-238 or 0.018 counts per second assuming 3×10^4 neutrons/sec-gram of Pu-238. The counts produced by gamma radiation from the RTG's in a

similar detector (with the discriminator set at 0.5 Mev) will be on the order of 100 counts/sec. Thus it is seen that charged particles produced by neutron reactions with silicon contribute very little to the interference.

Table 4-8. Charged Particle Yields in 1 cm^2 by 1 mm Semiconductor Detector Due to Neutron Reactions with Silicon-28

Neutron Energy Interval, Mev	Flux at Instrument Compartment, n/cm^2-sec *	(n,p) Cross Section, mb	(n,α) Cross Section, mb	Number of Protons Produced/sec x 10^{-3}	Number of Alphas Produced/sec x 10^{-3}
0-1	7.2				
1-2	7.2				
2-3	7.2				
3-4	2.6	-	-	-	-
4-5	0.45	10	-	0.02	-
5-6	0.20	50	10	0.04	0.01
6-7	0.10	230	75	0.11	0.03
7-8	0.05	400	210	0.09	0.04
8-10	0.025	350	300**	0.04	0.04
10-12	0.005	350	300**	0.01	0.01
12-14	-	300	60**	-	-
Total	∿25			0.31	0.13

*Assuming 5 x 10^3 neutrons/sec-gram of Pu-238

**Estimated

4.1.4 Gamma Radiation from the Fuel

Most of the gamma radiation from RTG and RHU fuel comes from two distinct sources: gamma-emitting impurities contained in the fuel and gamma emission which accompanies alpha decay of plutonium-238. The gamma flux and spectrum changes significantly with the fuel age. For fuel ages less than one year, the predominant source is gamma emission which accompanies alpha decay of plutonium-238. However, spontaneous fission, fission products, (α,n) reactions, and other sources are also contributing factors. For older fuel, daughters of plutonium-236, which is an impurity present in

trace quantities in the fuel, become the main contributors of gamma radiation. The calculated gamma ray spectra for RTG and RHU fuel of several fuel ages are given in Table 4-9.

4.1.4.1 SNAP-19 Gamma Radiation

The gamma ray spectrum of Pioneer fueled capsule PF-2 was measured at Mound Laboratory in November, 1970, using a 30 cc Ge(Li) gamma ray detector. The capsule was contained in a 0.615 cm thick Type 304 stainless steel calorimetry can which was placed in a bucket of water for cooling. The distance from the source axis to the surface of the detector was 100 cm. To correct for the attenuation of the calorimetry can and bucket of water, measurements were performed on an identical can and bucket of water to determine the transmission through these materials. Figure 4-5 shows the measured transmission and the calculated values determined by using the thickness of each absorber and the published linear attenuation coefficients for that material. The values from this curve were used to correct the intensity of full energy peaks given in Table 4-10 so that they represent the emission through the clad over 4 π.

Table 4-10 also gives the origin of the listed photon when this information is known. Photons are present from alpha particle reactions with nitrogen-14, oxygen-17, oxygen-18, and fluorine-19. Radioactive nuclides other than plutonium-238 present are plutonium-239, bismuth-212, and thallium-208. In addition, neutron capture by hydrogen in the water surrounding the source gives rise to the 2223 kev photon. This photon will be absent when there is no hydrogenous material near the source.

In addition to the gamma rays listed in Table 4-10, gamma rays of energy greater than 2650 kev were observed up to an energy of 6135 kev with the Ge(Li) spectrometer. These photons arise from thermal neutron capture in the various materials surrounding the plutonium. Their intensity is enhanced by the thermalizing water bath in which the source was counted. Gamma rays were observed at 4220, 4406, 4795, 5920 and 6018 kev from thermal neutron capture in iron; 4795, 5621 and 6132 kev from (n,γ) reactions on aluminum; 6132 kev from the $^{16}O(n,\gamma)^{17}O$ reaction; and 3441, 3848, 5009, 5520 and 6112 kev of unknown origin. Since the Ge(Li) detector's efficiency has not been measured above 3500 kev, intensities for these peaks are not given.

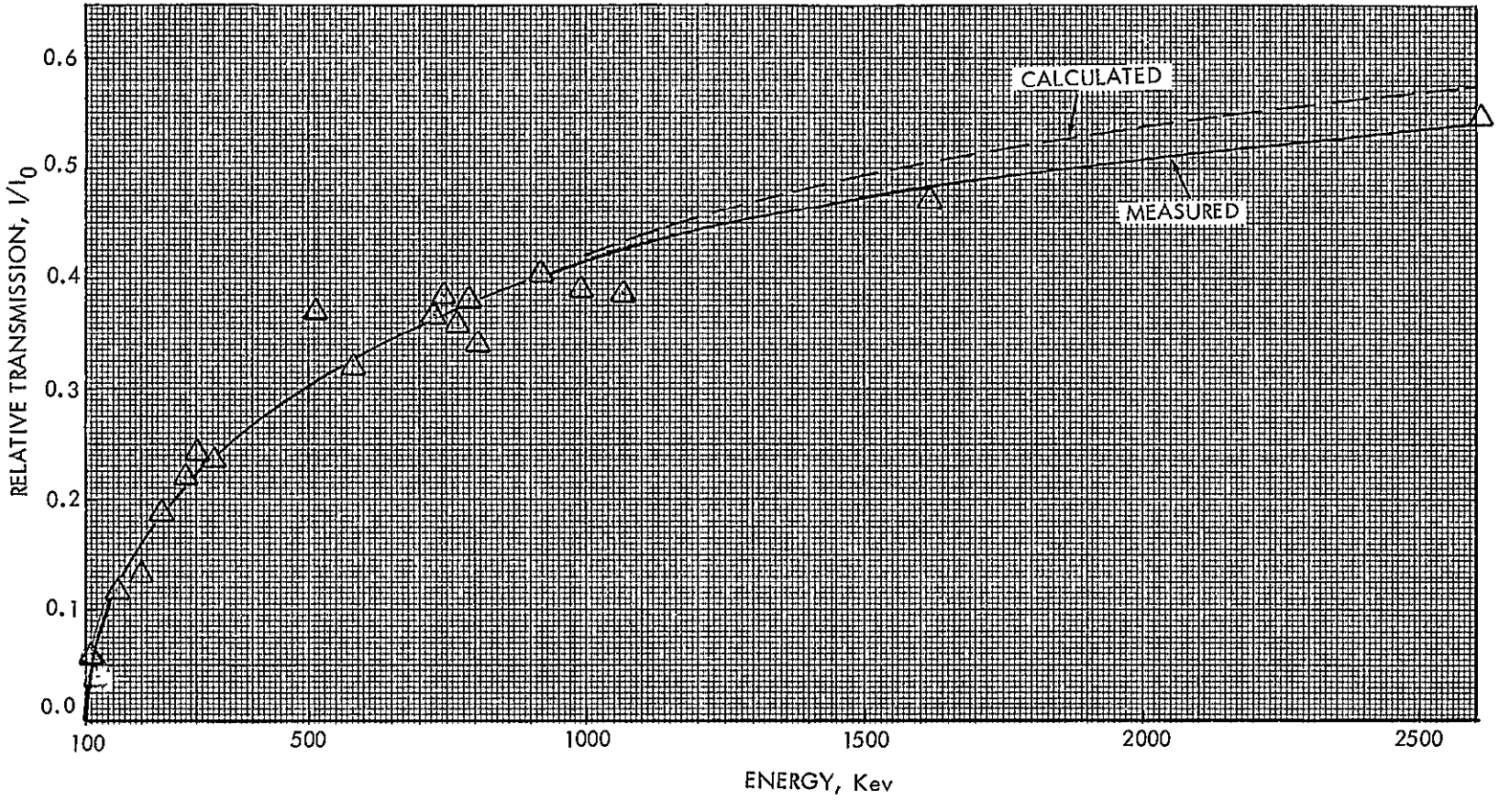

Figure 4-5. Relative Transmissibility through 0.615-cm. Thick Type 304 Stainless Steel Calorimeter Can, 8-cm. Water, and Galvanized Steel Bucket

Table 4-9. Calculated Gamma Photon Intensities in RTG Fuel Decay, Photons/Sec-Gm of Plutonium-238

Energy, kev	Origin	Fuel Age			
		0 Yrs	1 Yr	5 Yrs	10 Yrs
17	^{234}U X-Ray	8.3×10^{10}	8.2×10^{10}	7.9×10^{10}	7.7×10^{10}
43	^{238}Pu	2.4×10^{8}	2.4×10^{8}	2.3×10^{8}	2.2×10^{8}
99.8	^{238}Pu	5.1×10^{7}	5.0×10^{7}	4.9×10^{7}	4.7×10^{7}
115	^{212}Pb	--	2.1×10^{3}	2.5×10^{4}	4.4×10^{4}
153	^{238}Pu	6.4×10^{6}	6.3×10^{6}	6.1×10^{6}	5.9×10^{6}
203	^{238}Pu	2.5×10^{4}	2.5×10^{4}	2.4×10^{4}	2.3×10^{4}
239	^{212}Pb	--	1.4×10^{4}	1.7×10^{5}	3.0×10^{5}
241	^{224}Ra	--	1.1×10^{4}	1.4×10^{5}	2.4×10^{6}
277	^{208}Tl	--	7.8×10^{2}	9.2×10^{3}	1.6×10^{4}
300	^{212}Pb	--	9.8×10^{2}	1.2×10^{4}	2.1×10^{4}
511	^{208}Tl	--	2.5×10^{3}	3.0×10^{4}	5.3×10^{4}
583	^{208}Tl	--	9.4×10^{3}	1.1×10^{5}	2.0×10^{5}
727	^{212}Bi	--	1.4×10^{3}	1.6×10^{4}	2.9×10^{4}
743	^{238}Pu	5.7×10^{4}	5.7×10^{4}	5.5×10^{4}	5.3×10^{4}
767	^{238}Pu	2.2×10^{5}	2.2×10^{5}	2.1×10^{5}	2.0×10^{5}
785	^{212}Bi	--	2.2×10^{2}	2.6×10^{3}	4.6×10^{3}
810	^{238}Pu	$<6 \times 10^{3}$	$<6 \times 10^{3}$	$<6 \times 10^{3}$	$<6 \times 10^{3}$
860	^{208}Tl	--	1.3×10^{3}	1.6×10^{4}	2.8×10^{4}
865	$^{16}N(\alpha,p)$	Variable*			
1075	^{212}Bi	--	1.2×10^{2}	1.5×10^{3}	2.6×10^{3}
1620	^{212}Bi	--	3.5×10^{2}	4.2×10^{3}	7.4×10^{3}
2614	^{208}Tl	--	1.1×10^{4}	1.3×10^{5}	2.3×10^{6}

*Depends upon the nitrogen content

Table 4-10. Measured Gamma Ray Spectrum for Pioneer Capsule PF-2

Energy, kev	Origin	Intensity, Photons/W/sec
351	$^{18}O(\alpha,n\gamma)^{21}Ne$	366
414	^{235}Pu	275
511	^{208}Tl, Annihilation	5204
583	^{208}Tl	2204
597		1555
693	$^{56}Fe(n,\gamma)^{57}Fe$	1348
708	(^{238}Pu)	350
727	^{212}Bi	722
743	^{238}Pu	7185
767	^{238}Pu	32643
787	^{238}Pu	5125
808	^{238}Pu	1413
834	(^{18}F $[n,\gamma]^{20}F$)	239
849	^{232}Pu, $^{56}Fe(n,n')^{56}Fe$	3706
869	$^{14}N(\alpha,p\gamma)^{17}O$	263
883	^{238}Pu, $^{19}F(\alpha,n\gamma)^{22}Na$	2388
894		
927	^{238}Pu	985
942	^{238}Pu	991
1001	^{238}Pu	1818
1042	^{238}Pu	491
1223	($^{35}Cl[n,n']^{35}Cl$)	141
1237	$^{56}Fe(n,n')^{56}Fe$	618
1263	$^{56}Fe(n,\gamma)^{57}Fe$	77
1275	$^{19}F(\alpha,p\gamma)^{22}Ne$	4823
1401	$^{18}O(\alpha,n\gamma)^{21}Ne$	230
1435		305
1528		465
1555		84
1621	^{212}Bi, $^{17}O(\alpha,n\gamma)^{20}Ne$	504
1779	^{28}Al	253
2083		358
2224*	$^{1}H(n,\gamma)^{2}H$	11816
2440	$^{19}O(\alpha,n\gamma)^{21}Ne$	125
2614	^{208}Tl	9474

*Neutron activation of water surrounding the source

A 7.62-cm diameter by 7.62-cm high NaI(Tl) gamma-ray detector was used also to observe high energy photons up to 12 Mev. In addition to the high energy gamma rays mentioned previously, peaks were also observed at 7585 kev (believed to be a composite of the 7640 kev and 7540 kev peaks due to neutron capture by iron and molybdenum, respectively); an 8390 kev peak due to neutron capture by molybdenum; and an unidentified peak at 9640 kev.

In summary, the pulse height spectrum, full energy intensities, impurities and daughter products noted here in the energy range of zero to 2700 kev are normal for a plutonium heat source of this size. The high energy gamma rays produced by thermal neutron reactions are enhanced by the thermalizing action of the water bath. All of these high energy gamma rays except those arising from iron can be attributed to materials presented in the Pioneer capsule itself. The origin of the iron-produced gamma rays most likely arise from the stainless steel calorimetry can in which the capsule was counted.

4.1.4.2 Reduction of Gamma Radiation

Plutonium-236 is present in the fuel in quantities of only 1.0 to 1.2 ppm of Pu. However, the plutonium-236 decay chain produces a large number of daughter nuclides which emit gamma radiation. The decay chain is shown below in Figure 4-6.

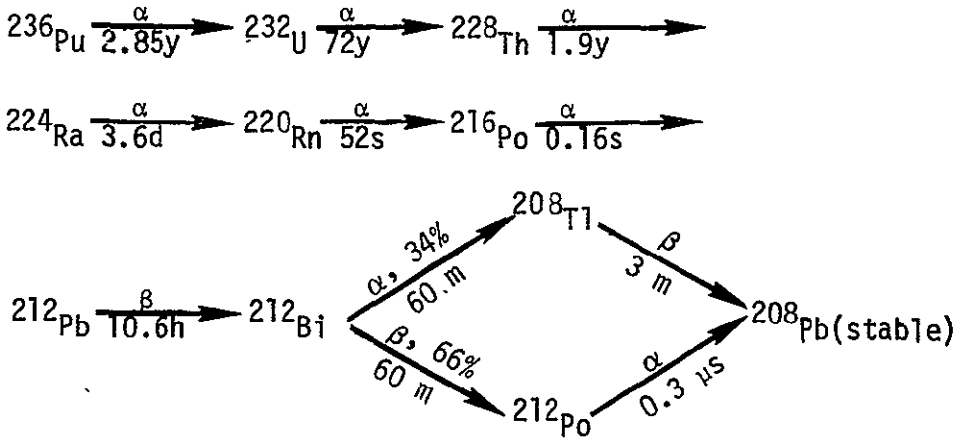

Figure 4-6. Plutonium-236 Decay Chain

The rate-controlling step in the sequence is uranium-232, but because uranium-232 does not contribute significantly to the gamma emission, the rate controlling step for the gamma-emitting daughter is the 1.91 year growth of thorium-228. The amount of gamma activity increases with time and reaches a maximum in 18 years.

The only way to decrease the gamma ray emission from the plutonium fuel is to decrease the amount of the plutonium-236 impurity. From the discussions held with the AEC personnel, it appears that it is not currently practical to purify the fuel to reduce the plutonium-236 content below approximately 1.2 ppm.

It is possible, however, after initial chemical separation, to store the fuel and let the plutonium-236 decay in activity. Plutonium-236 decays to uranium-232 with a half life of 2.85 years, then uranium-232 decays to thorium-228 with a half life of 72 years. After the storage period the fuel can be reprocessed and uranium-232 as well as thorium-228 and its daughters removed by chemical means thus decreasing the amount of plutonium-236 that remains in the fuel. The resultant reduction in gamma radiation for a four-year storage period is illustrated in Figure 4-7. The reduction in gamma ray emission at fuel age of 2, 4, 6, and 18 years after uranium-232 and thorium-228 removal for several storage times after initial processing are given in Table 4-11. The gamma ray emission rate is expressed in percent of emission rate of fuel with no uranium-232 and thorium-228 removal.

Two ways are available for making plutonium-238 with low plutonium-236 contents: $^{237}Np(n,\gamma)^{238}Np\ (\beta)^{238}Pu$ and $^{241}Am(n,\gamma)^{242}\ Am(\beta)^{242}Cm(\alpha)\ ^{238}Pu$ (reference 4-4). Pilot irradiations of both routes for the production of plutonium-238 have been made in both the Richland and Savannah River production reactors (reference 4-5). From the neptunium-237 irradiations, the plutonium-236/plutonium-238 ratio will be <0.3 ppm and from the american-241 irradiation, which requires several years of cooling for the decay of the curium-242, the ratio will be <0.1 ppm.

4.1.5 Effect of Gamma Radiation on Operation of Scientific Instruments

Gamma radiation can produce two types of effects on the electronic subsystems associated with the scientific instruments:

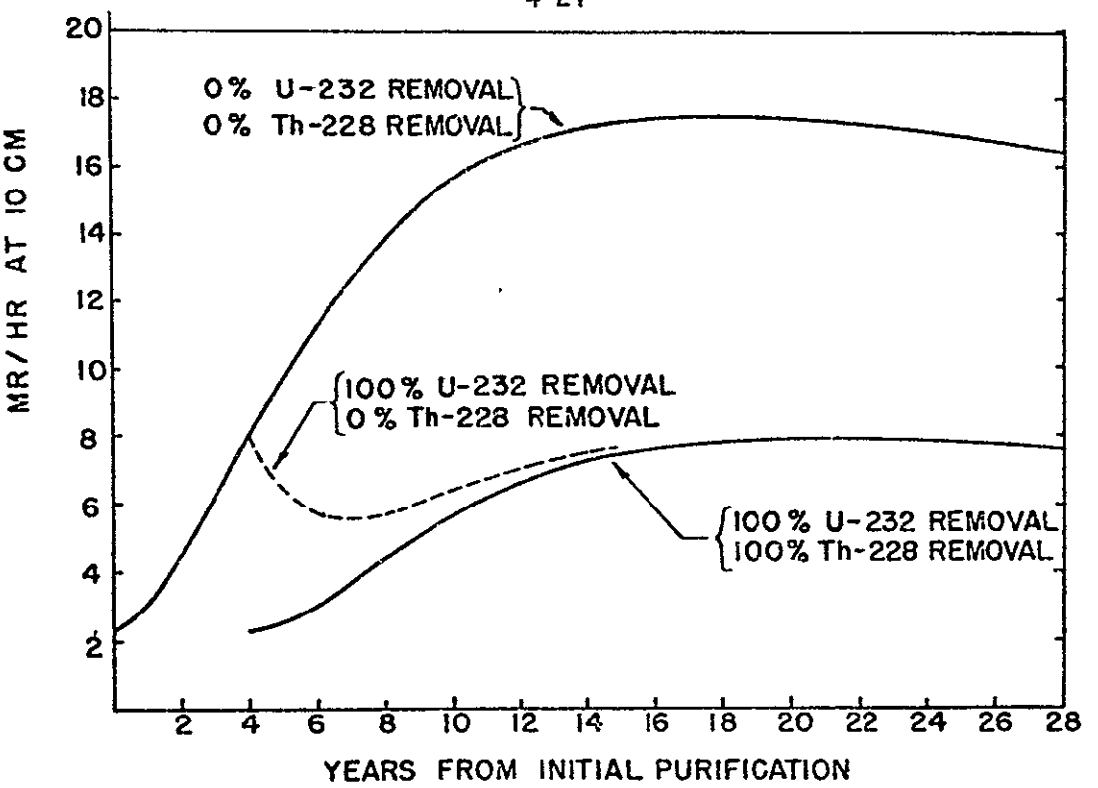

Figure 4-7. Gamma Dose Rate from 20-Grams 90% Plutonium-238 + 1.2 ppm Plutonium-236 contained in 0.030-inch Tantalum

Table 4-11. Gamma Ray Emission Rate from ^{238}Pu Fuel as a Function of Time that ^{236}Pu is Allowed to Decay Before ^{232}U and ^{228}Th Removal for Several Fuel Ages (Expressed in Percent of Gamma Emission of Fuel with no ^{232}U and ^{228}Th removal)

Time that ^{236}Pu is Allowed to Decay Before Reprocessing, Years	Fuel Age, Years after Reprocessing			
	2	4	6	18
0	100	100	100	100
1	90	84	83	81
2	81	73	69	66
3	75	64	59	55
4	71	57	51	46
5	67	51	45	39
6	64	46	41	34
7	61	43	38	30

- Radiation damage
- Active interference with the operation of various elements of the electronic systems

The radiation damage aspect due to gamma radiation on spacecraft components was investigated during Phase III of the RTG/Science Instrument Interactions program. The total gamma ionizing dose for the Pioneer F/G experiment payload was found to be only 1.6×10^3 rads (C). This dose is too small to have a noticeable effect even on the most sensitive elements in the payload such as crystal oscillators.

However, the active interference caused by gamma radiation is quite significant in the Pioneer Spacecraft. There are several instruments designed to measure relatively low energy space radiation (50 kev and above) such as electrons and protons. These instruments incorporate radiation detectors which are sensitive to the gamma radiation produced by the RTG fuel. Tests conducted during phases I, II & III of the RTG/Science Instrument Interactions Program indicate that the majority of interference comes from the 2.62 Mev thallium-208 gammas and several gamma energies concentrated between 0.7 and 0.9 Mev. Although there are numerous gammas with energies below 0.7 Mev, most of them are attenuated due to self absorption in the fuel, the capsule walls, and the RTG outer structure so that only a small fraction escapes. The computed ratio of number of gamma escaping the SNAP-19 RTG to the gammas generated in the fuel is given in Figure 4-8 for two SNAP-19 RTG's positioned in tandem. The emitted gamma ray flux is along a line going through the center of the RTG's and at 20 degrees to the longitudinal axis. This angle approximately corresponds to the position of the scientific experiments in relation to the RTG's on the Pioneer F/G Spacecraft.

The assessment of radiation interference with scientific instruments indicates that University of Chicago/Simpson and GSFC/McDonald experiments will be most severly affected by the RTG gamma radiation. A smaller effect will be seen by University of Iowa/Van Allen experiment. This assessment is based on tests conducted with a SNAP-27 fuel capsule which, at the time it was manufactured, contained on the order of one part per million of plutonium-236. The fuel was 2.5 to 3 years old at the time measurements were performed.

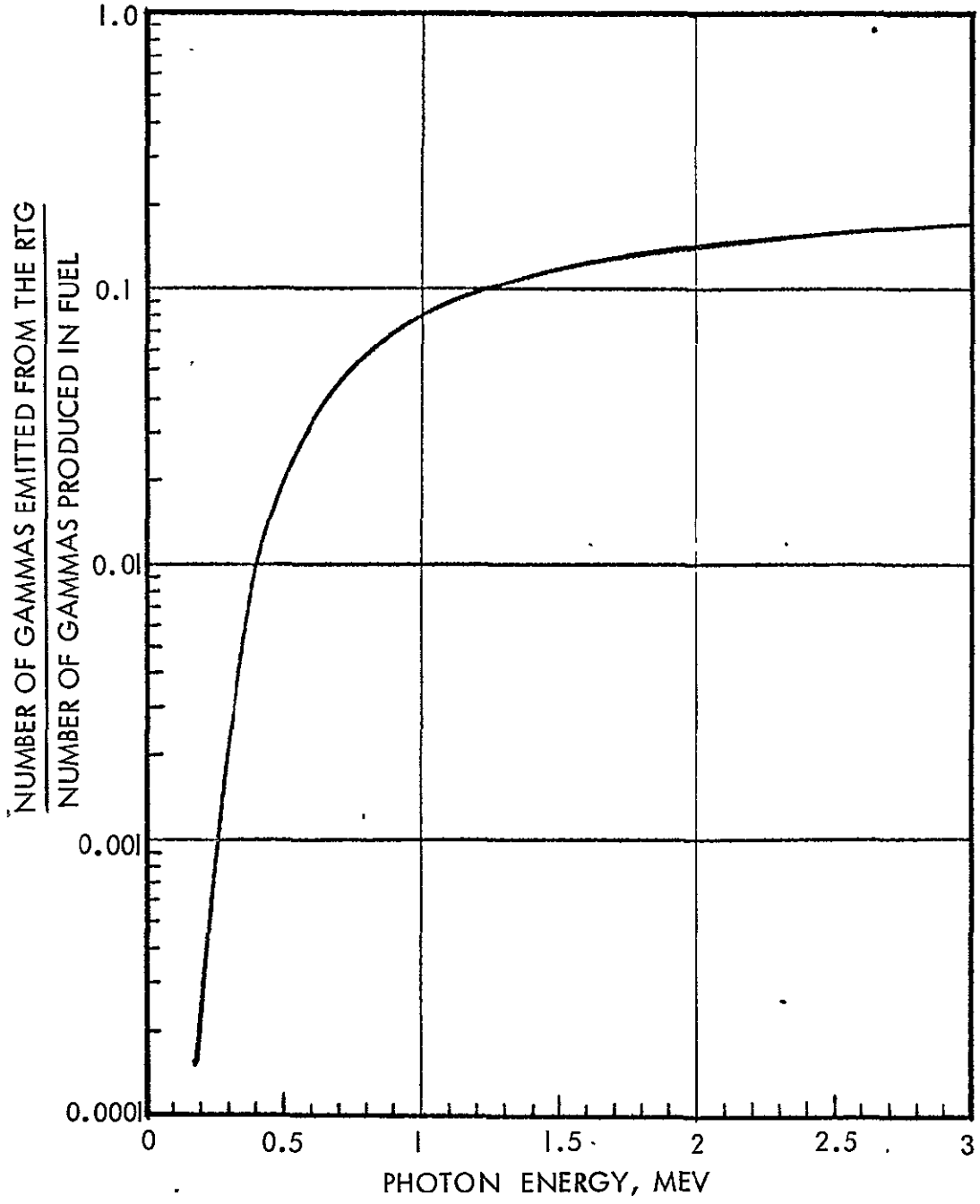

Figure 4-8. Ratio of Number of Gamma Escaping the RTG to Number of Gammas Produced in the Fuel for a Pair of SNAP-19 RTG's at 20° to the Longitudinal Axis.

The sensitivity of GSFC/McDonald's experiment for measurements of electrons and protons in the energy range of 50 kev to 2 Mev will be reduced. Dr. McDonald estimated that 25% of the total scientific value of the experiment would be lost due to RTG gamma radiation. As a result, a 2.4-pound shield was incorporated in the detection system to attenuate the RTG radiation to acceptable levels for electron and proton measurements during quiescent times of solar activity. Even with this shielding there is some doubt whether measurement of 50-kev electrons will be possible. It may be found necessary to raise the minimum energy threshold to a higher value.

A part of the University of Chicago charged particle experiment had to be redesigned in order to operate in the RTG radiation environment. Originally the experiment used a relatively large charged particle telescope consisting of five detectors, a CsI crystal and a plastic scintillator anticoincidence shield. Tests conducted with a prototype system using a SNAP-27 fuel capsule indicated that the detectors were subordinated by the RTG radiation, making it impossible to perform measurements of low energy ($E < 2$ Mev) space electrons and protons. As a result, the function of analyzing electrons and protons was dropped from the main telescope. An additional small telescope using very thin semiconductor detectors which are virtually insensitive to gamma radiation was added to the system. This telescope performs measurements of protons in the energy range of approximately 400 kev to 9.0 Mev. Electron measurements have been sacrificed altogether because of excessive background produced by the RTG gamma radiation.

4.2 Computed Radiation Fields

There are significant differences between the design of the SNAP-27 fuel capsule which was used for the majority of radiation interference measurements during this program and the SNAP-19 RTG's. The differences affect the flux and the spectra of the gamma ray field. The SNAP-27 fuel capsule is 15.60 inches long and has an outside diameter of 2.519 inches. Its thermal output is approximately 1480 watts. The fuel consists of PuO_2 microspheres loaded into a long hollow tube and encapsulated in several layers of superalloy. The thickness of the fuel annulus is 0.467 inch.

The one tandem pair of SNAP-19 RTG's have a thermal output of about 1350 watts. The SNAP-19 fuel consists of a cermet containing PuO_2 and molybdenum metal as discussed in Section 4.1. Each of the two cylindrical fuel capsules have hemispherical ends and are approximately 4 1/2 inches long by 2 1/2 inches in diameter. Each fuel capsule is surrounded by a graphite reentry heat shield approximately 0.5 inch thick. The graphite is in turn surrounded radially by thermoelectric modules and a magnesium alloy generator structure.

Because the additional layers of metal and graphite close to the SNAP-19 fuel capsules modify the gamma ray leakage and spectra outside the assemblies, one cannot merely multiply the gamma ray levels around SNAP-27 by the ratio of the power levels (0.911) to determine the spectrum and fluxes around a pair of SNAP-19's. The amount of variation in the gamma radiation field depends on the angular displacement with respect to the longitudinal axis of the RTG. In addition, the field depends upon the shape and density of the heat source capsules themselves. The SNAP-27 has a foam superalloy region at the bottom of the capsule which adds considerably more attenuation than is present in a direction away from the side of the capsule.

4.2.1 Comparison of SNAP-27 and SNAP-19 RTG Radiation Fields

In order to determine the differences in the gamma radiation fields of the SNAP-27 and SNAP-19's RTG's, the spectra and dose rates were calculated at several locations outside both the SNAP-27 fuel capsule and a pair of SNAP-19 RTG's at a distance of 8 feet from the center of each assembly. The calculations were performed with the QAD P-5 point kernel code (Ref. 4-6) obtained from the Radiation Shielding Information Center and originally developed at Los Alamos Scientific Laboratory and modified at Aerojet General, NASA, and ORNL. The gamma-ray source spectrum was divided into 13 energy groups and the buildup factor for each group was calculated using energy dependent polynominal coefficients supplied as input and obtained from Ref. 4-7. The buildup factor and gamma ray attenuation depend on gamma ray energy, and the number of mean free paths between the different source regions into which the source is divided. The code calculates the path length through each region described by the

input parameters, computes the attenuation and buildup factor for each path from each small source region, and integrates over the volume of the source to give the spectrum. It also can apply an energy dependent response function to convert the flux spectra to dose rates, heating rates, etc.

Table 4-12 shows the total flux at each point together with a breakdown of the percentage of the total flux contributed by the gamma rays in each energy group. The souce spectrum used for all the computations is given in Reference 4-1 for two-year-old fuel having 1.2 ppm of plutonium-236. For these calculations the SNAP-19 was assumed to have oxide fuel rather than cermet fuel. Both capsules contain materials with high atomic numbers and the thermoelements of SNAP-19 also consist primarily of lead telluride. Thus most of the data were computed with lead buildup factors. However, for SNAP-27 the average atomic number of the superalloy container is much closer to that for iron, so additional computations were made using iron buildup factors. The results show that replacing the buildup factors for a SNAP-27 with those for iron increases the flux by a factor ranging from 1.26 (along midplane) to 1.46 (along axis).

Table 4-13 shows the ratio of the gamma ray flux in each energy group for SNAP-19 to that for SNAP-27. It is obvious that at eight feet from the sources the low energy gamma rays are very much more prominent for the SNAP-27 midplane than for the SNAP-19 at 20°. However, on the axis of SNAP-27 fuel capsule and at 20° to the axis of a pair of SNAP 19's, a relatively good match exists in spectra and total flux at just about all energies. Most of the Pioneer F/G scientific instrumentation will be approximately 20° relative to the RTG's. It appears therefore, that measurements made on the axis of a SNAP-27 capusle provide a reasonably good match of the environment to be expected at the location of the Pioneer scientific instrumentation.

Table 4-12. Calculated SNAP-27 Fuel Capsule and Tandem SNAP-19 RTG Gamma Ray Spectra (Photons/cm^2-sec), Eight Feet from the Sources*

Group	Mean Energy, Mev	SNAP-27 (Mid-plane**)	Percent in Group	SNAP-19 (20°**)	Percent in Group	SNAP-27 (On-axis**)	Percent in Group	SNAP-27 (Mid-plane***)	Percent in Group
1	0.050	2.145/1*	1.078	1.141/-13	5.7/-12	3.38/-18	3.4/-16	2.584/1	1.0511
2	0.100	1.123/3	56.461	2.468/-1	0.195	2.702/-1	0.312	1.365/3	55.53
3	0.150	2.367/2	11.90	8.654/-2	0.068	1.337/-2	0.015	2.953/2	12.012
4	0.200	2.175/1	1.094	1.933/-1	0.15	1.083/-1	0.125	2.760/1	1.123
5	0.800	4.197/2	21.101	7.505/1	59.281	5.293/1	61.112	5.820/2	23.674
6	1.00	3.395/1	1.707	7.475/0	5.904	4.098/0	5.750	4.335/1	1.763
7	1.50	7.732/0	0.389	2.313/0	1.827	1.431/0	1.652	8.997/0	0.366
8	2.00	5.036/0	0.253	1.739/0	1.374	1.044/0	1.206	5.623/0	0.229
9	2.50	1.187/2	5.968	3.895/1	30.766	2.550/1	29.446	1.303/2	5.300
10	3.00	1.143/0	0.058	4.367/-1	0.345	2.53/-1	0.292	1.243/0	0.051
11	4.00	2.114/-1	0.011	8.225/-2	0.065	4.653/-2	0.054	2.281/-1	0.009
12	5.00	1.067/-1	0.005	4.112/-2	0.033	2.288/-2	0.062	1.137/-1	0.005
13	6.00	5.210/-2	0.003	1.993/-2	0.016	1.089/-2	0.013	5.459/-2	0.002
Total flux		1.989/3	100	1.266/2	100	8.660/1	100	2.486/3	100
Mean E, Mev		0.4255		1.374		1.335		0.423	
Mean Buildup Factor		1.128		1.558		1.407		1.410	

*2.145/1 = 2.145×10^1
**Lead Buildup Factors
***Iron Buildup Factors

Table 4-13. Ratios of Gamma Ray Spectra (Photons/cm^2-sec) for SNAP-27 Fuel Capsule and SNAP-19 RTG's at Different Locations Eight Feet from the Sources

Group	Mean Energy, Mev	SNAP-19 (20°)/ SNAP-27 (Mid Plane)	SNAP-19 (20^0)/ SNAP-27 (0^0)
1	0.050	5.3×10^{-13}	3.38×10^{-4}
2	0.100	2.2×10^{-4}	0.913
3	0.150	3.7×10^{-4}	6.473
4	0.200	8.89×10^{-3}	1.785
5	0.800	0.179	1.418
6	1.00	0.220	1.501
7	1.50	0.299	1.616
8	2.00	0.345	1.666
9	2.50	0.328	1.527
10	3.00	0.382	1.726
11	4.00	0.389	1.768
12	5.00	0.385	1.805
13	6.00	0.383	1.8301
Total	--	0.0636	1.462

4.2.2 Effect of Orientation

A more explicit indication of the significance of RTG orientation is shown in Table 4-14 and Figure 4-9. For SNAP-19 the intensity of the gamma rays with energies above 0.5 Mev first decreases with angle and then increases to values higher in the midplane than on the axis. For low energy gamma rays the highest values are actually on the axis. For SNAP-27 the gamma ray intensity increases with the angle from the axis for all energies.

Table 4-14. Effects of RTG Orientation on Calculated Gamma Ray Flux at 8 Feet from Source Center*, photons/cm^2-sec.

SNAP-19 (Lead buildup factors)		Energy Level			
Angle from Axis, °	Total	0.10 Mev	0.15 Mev	0.8 Mev	2.6 Mev
0	1.003/2	6.20/-1	1.61/-1	5.94/1	3.073/1
5	8.609/1	5.00/-1	1.305/-1	5.04/1	2.706/1
10	9.247/1	4.32/-1	1.16/-1	5.37/1	2.94/1
15	1.067/2	3.43/-1	9.685/-2	6.25/1	3.338/1
20	1.266/2	2.468/-1	8.655/-2	7.505/1	3.895/1
25	1.468/2	1.59/-1	8.33/-2	8.814/1	4.43/1
30	1.622/2	9.319/-2	9.08/-2	9.857/1	4.799/1
90	2.52/2	3.234/-5	1.325/-1	1.649/2	6.354/1
SNAP-27 (Iron buildup factors)					
0	1.346/2	4.194/-1	2.644/-2	9.143/1	3.117/1
20	5.183/2	1.757/1	1.852/1	3.437/2	9.436/1
90	2.486/3	1.365/3	2.953/2	5.82/2	1.303/2

*1.003/2 = 1.003×10^2

4.2.3 Effect of Graphite and Thermoelectric Elements on SNAP-19 Fluxes

The effect of the SNAP-19 outer thermoelement region and the inner graphite regions on gamma ray intensities was determined by setting the density of each one of these regions to zero and repeating several QAD runs. The results are summarized in Table 4-15 which lists the dose rates and total fluxes at 8 feet from the center of a tandem SNAP-19 assembly on the axis, at 20° to the axis, and on the midplane. The thermoelements were assumed to be a hollow cylinder around the capsules. Hence, they have no effect on dose rate on the axis. The thermoelements and graphite together reduce the dose rate from the fuel capsule by a factor as high as 1.9, though the effect on low energy gamma ray fluxes is considerably greater.

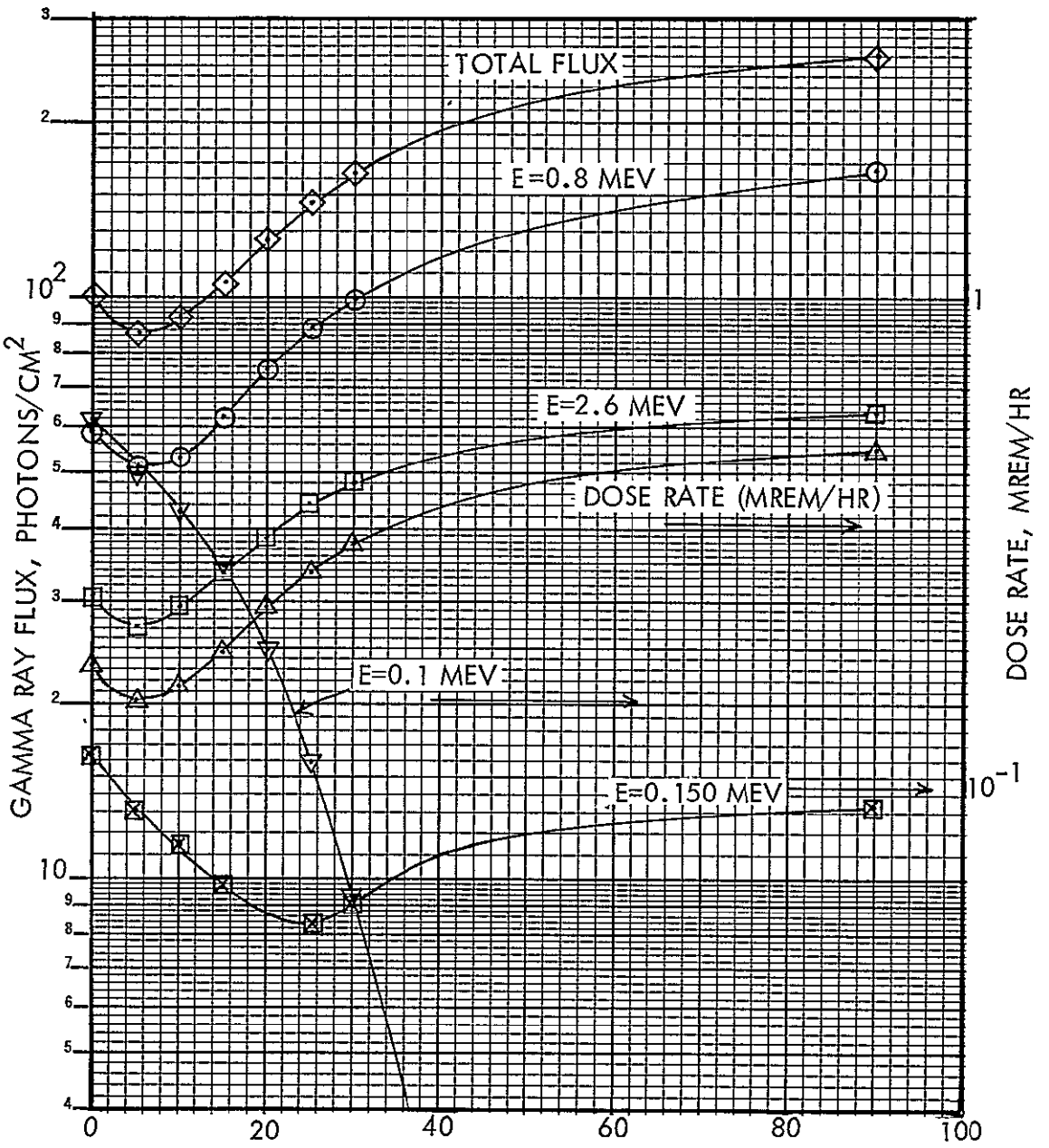

Figure 4-9. Computed Gamma Ray Flux As a Function of Angle from the Centerline of a Tandem SNAP-19 (at 8 feet from Tandem Center - Lead Buildup Factors)

Table 4-15. Effect of Graphite and Thermoelectric Element Regions on Calculated SNAP-19 Gamma Ray Fluxes and Dose Rates at 8 Feet from the Source.

Angle from Axis, °	Complete RTG		No Thermoelements		No Thermoelements or Graphite	
	Flux, photons cm^2-sec	Dose Rate, mrem/hr	Flux, photons cm^2-sec	Dose Rate, mrem/hr	Flux, photons cm^2-sec	Dose Rate, mrem/hr
0	100	0.232	100	0.232	130.7	0.292
10	92.5	0.216	112.7	0.266	--	--
20	126.6	0.295	173.9	0.400	253.8	0.561
30	162.2	0.374	219.5	0.497	--	--
90	252	0.557	398.1	0.792	491.3	0.932

*Lead buildup factor

4.2.4 Correlation of SNAP-27 Measurements with the Pioneer SNAP-19 Environment

Almost all of the Phase I measurements (Ref. 4-1) were made with the detectors located in the horizontal midplane of the SNAP-27 capsule. Later in the program, when the SNAP-19 RTG's were selected for the Pioneer mission it became clear that there are very significant differences between the SNAP-27 spectrum to which the instruments were exposed and that which the calculations indicate will be present at the instrument compartment of the spacecraft. Thus the response of the detectors should be adjusted by the energy dependent flux ratios for SNAP-19 RTG's at 20° to the SNAP-27 fuel capsule horizontal midplane given in Table 4-13.

Thus, the counts in a detector caused by the 2.62 Mev gammas from SNAP-27 at midplane would be reduced by a factor of 0.328 to correspond to counts produced by a tandem SNAP-19 RTG. In the same way, the counts produced by 0.76 Mev gammas by the SNAP-27 would be reduced by a factor of 0.179 for SNAP-19's.

Since two pair of RTG's are used on Pioneer F/G, the counts obtained at a distance of 9 feet from the SNAP-27 at midplane may be multiplied by a factor of 0.37 to obtain a conservative estimate of the counts for the entire spectrum at the Pioneer instrument compartment.

4.2.5 Dose Rates Compared to Fluxes and Measurements

Often the radiation levels around radioisotope sources are expressed in terms of dose rates rather than spectra. Partly this is the result of interest in determining the biological hazards to persons near the sources and partly because dose rates are, in general, easier to measure than spectra. Unfortunately, dose rates can be quite misleading since they may vary in a quite different manner from photon fluxes as a function of energy and of position around an RTG. Table 4-16 shows the calculated fractions of the total flux and of the total dose rate at 8 feet from a SNAP-27 contributed by each of the thirteen gamma ray energy groups employed in the QAD calculations. The higher energy gamma rays contribute very much more to the dose rate than their percentage in the spectra. In evaluating radiation interactions with scientific instrumentation one clearly cannot use dose rates.

Dose rates do, however, provide a convenient means for evaluation of the computational techniques because flux measurements cannot be directly compared to measured spectra without rather complicated unfolding of the spectrometer output to produce a "free field" spectrum. Measurements were made of the gamma ray dose rate as a function of distance from the SNAP-27 both on the axis and in the midplane using a calibrated Victoreen 440RF health physics type dosimeter. These measurements are compared to preliminary SNAP-27 calculations in Figure 4-10. There is good agreement between the measured and predicted ratios of the radial dose rates to the ones on the axis. However, to obtain a true comparison, the calculated values would have to be modified to account for the age of the fuel which was very close to three years old at the time of these measurements rather than the two years used in the calculations.

Table 4-16. Computed Dose Rates and Fluxes as a Function of Energy in the SNAP-27 Mid-plane at 8 Feet.

Group	Energy Mev	Percent of total flux	Percent of total dose rate
1	0.05	1.078	0.192
2	0.100	56.461	11.817
3	0.150	11.90	4.258
4	0.200	1.094	0.561
5	0.800	21.101	45.60
6	1.00	1.707	4.425
7	1.50	0.389	1.380
8	2.00	0.253	1.101
9	2.50	5.968	30.229
10	3.00	0.158	0.334
11	4.00	0.011	0.0739
12	5.00	0.005	0.046
13	6.00	0.003	0.0255

Total flux is 1.989×10^3 photons/cm^2/sec and total dose is 1.47 mrem/hr.

4.3 Correction of Phase I Test Data to Pioneer F/G Mission

A number of assumptions were made at the beginning of the program concerning the gamma radiation levels around the SNAP-27 fuel capsule and how this radiation level would compare with that from the Pioneer RTGs. The assumptions, discussed in detail in Reference 4-1, included the following:

1. The spectrum outside all plutonium-238 dioxide heat sources would be quite similar.
2. The geometric attenuation from relatively small isotopic sources would vary with distance, r, as $1/r^2$.
3. Facility influence would be minimal.
4. Neutron effects on the scientific instruments would be unimportant.

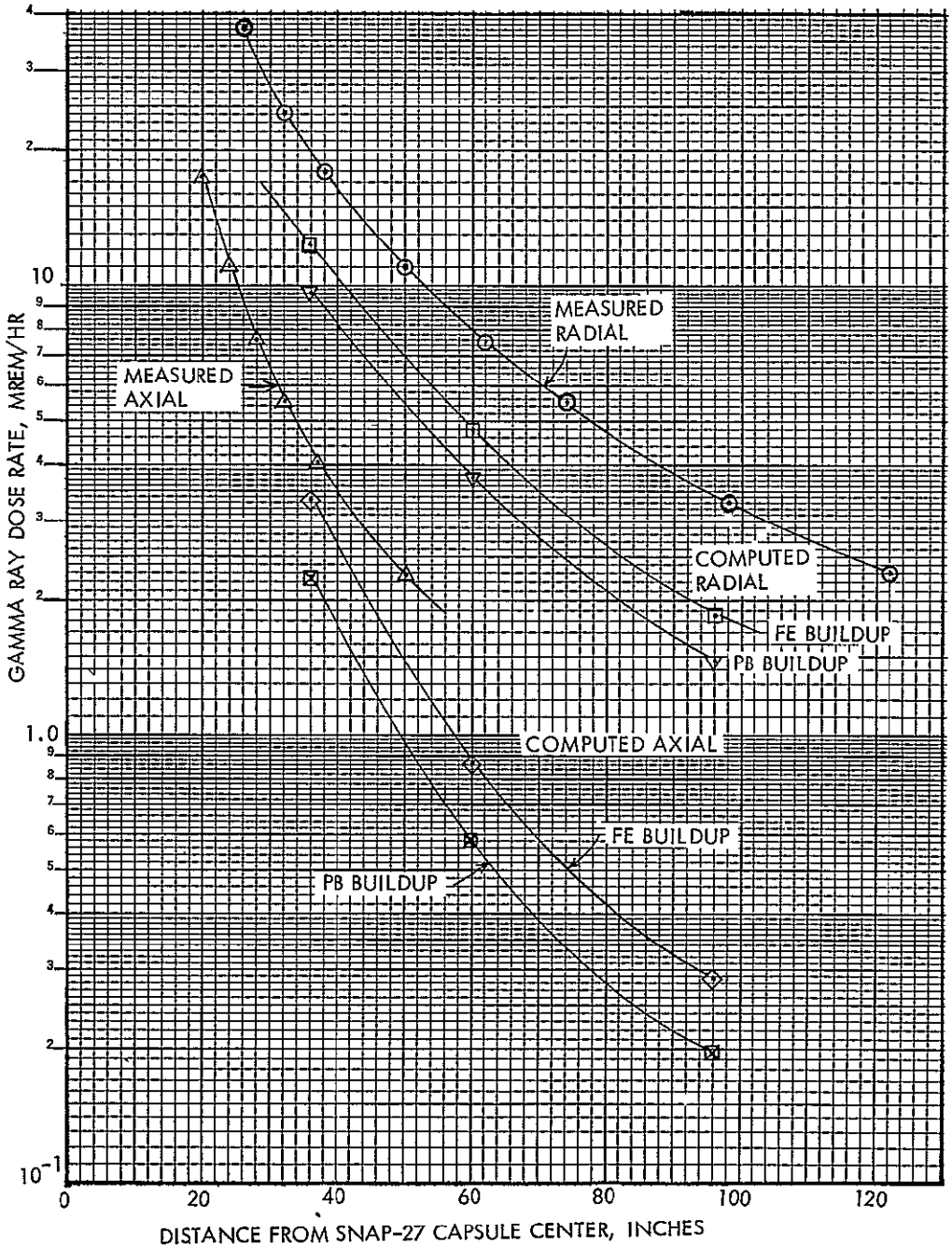

Figure 4-10. Gamma Dose Rates vs. Distance From the Center of a SNAP-27 Capsule

Thus, it appeared that measurements of the response of a variety of scientific instruments could be made with the SNAP-27 fuel capsule assembly at convenient locations as determined by good counting statistics and that these results could be readily adjusted by correcting for the differences in distances form the source on the spacecraft and in the test facility. The details of the Pioneer spacecraft RTG design had not at that time been finalized. Since the original calculations of the gamma ray levels in the vicinity of SNAP-27 had been hand calculations employing line sources it was deemed necessary that these be repeated with a more detailed computer code, QAD P-5, using as much of the previously generated source strength information as possible but describing the actual source geometry. The same techniques and source terms were then employed to compute the gamma ray spectrum in the vicinity of the SNAP-19 RTG's which had meanwhile been selected for the Pioneer spacecraft. There are a number of fairly obvious differences between the SNAP-27 fuel capsule and SNAP-19 RTG, which produce significant differences in the radiation spectra for the two. These differences were described in considerable detail in Section 4.2.

4.3.1 Computed Gamma Radiation Levels

As the spacecraft became better defined, the expected radiation levels as a function of distance from the RTG's were calculated and correlated with the known instrument locations on board the spacecraft with the RTG's oriented in the as-designed configuration. Using QAD, calculations were made of the SNAP-27 gamma ray intensities at a variety of locations with regard to the capsule including along the longitudinal axis as well as in the capsule midplane. The spectrum at the Pioneer instrument locations was then compared to the computed SNAP-27 position dependent spectra to get correlation factors for scientific instrument responses.

Figures 4-11 and 4-12 show the calculated gamma ray environment in the vicinity of the SNAP-27 fuel capsule in the radial and axial directions. The OAD, P-5 (ref. 4-6) calculations assumed iron buildup factors and the source strength from Reference 4-1. It can be seen that there is a substantial difference both in the magnitude of the fluxes and in the spectral

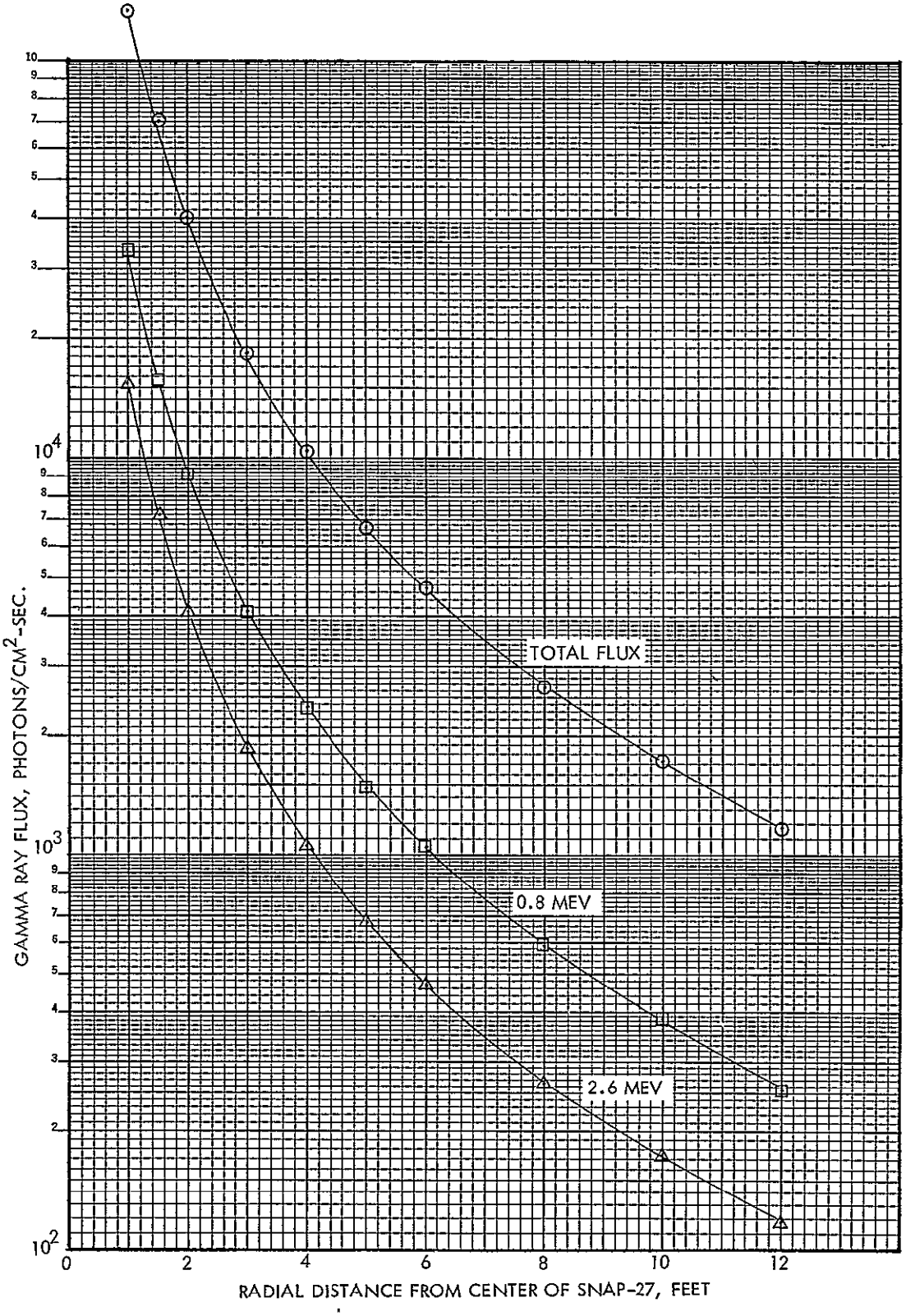

Figure 4-11. Calculated Total, 2.6 Mev. and 0.8 Mev Gamma Ray Fluxes as a Function of Radial Distance from the SNAP-27 Fuel Capsule.

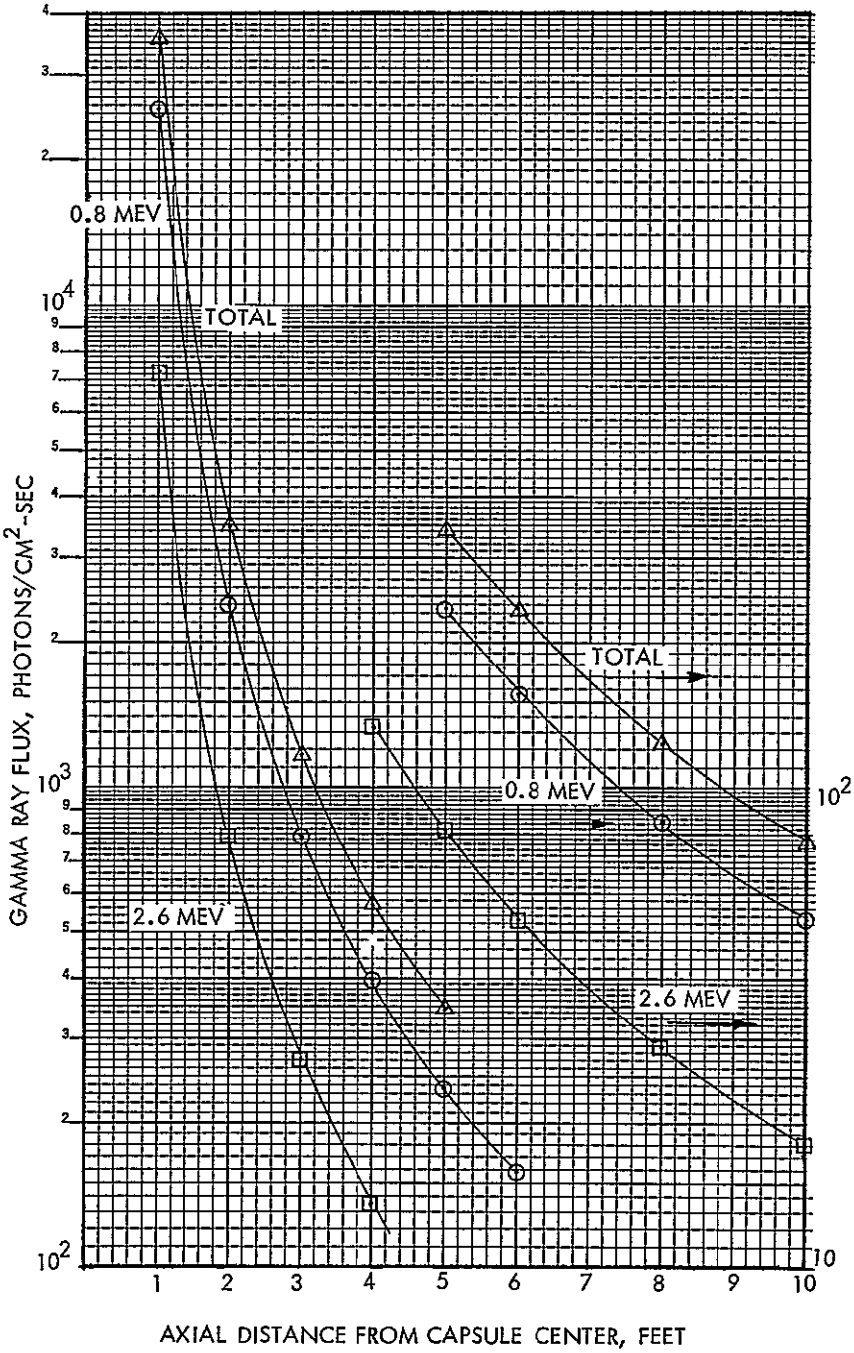

Figure 4-12. Calculated Total, 2.6 and 0.8 Mev Gamma Flux as a Function of Axial Distance from SNAP-27 Center.

shape on the axis of the SNAP-27 FCA as compared to the horizontal midplane. There is also a much faster decrease in intensity with increasing distance from the FCA in the axial direction than in the radial direction.

One check on the validity of the computations is provided by the data shown in Figure 4-13, which compares predicted and measured gamma ray dose rates around the FCA. These calculations assumed three year old fuel since the capsule was three years old at the time the measurements were made. (Compare to Figure 4-10 which assumed two year old fuel). The experimental data were obtained with a Victoreen 440 RF health-physics type dosimeter and include all facility produced background such as scattering or secondary gamma rays from inelastic scattering or neutron capture. The facility component should be more important as one moves away from the fuel capsule, especially axially, since the direct dose rate decrreases while the facility contribution increases as one gets closer to the floor and walls.

The excellent agreement between predicted and measured values close to the fuel capsule with the measurements decreasing more slowly with increased distance than predicted indicated the accuracy of the QAD computations and the assumed source strengths. The calculated dose rates do not include any "background". To a first approximation the differences between measured and predicted dose rates may be taken as indicative of the facility-generated dose rate.

4.3.2 Effect of Fuel Form

Table 4-17 shows the computed gamma ray spectra at 8 feet from the fuel capsule center both radially and axially as well as the expected spectra 8 feet from a tandem SNAP-19 for both microsphere and solid solution cermet fuel. The SNAP-19 computations include the effects of thermoelectric modules and graphite.

4.3.3 Effect of Age

The growth of plutonium-236 and its daughters with increasing time from fuel fabrication is important for missions extending over several years. Of primary interest are the 2.6 Mev gamma rays. The growth of the total and 2.6 Mev gamma flux with time is shown in Figure 4-14. The relative importance of the 2.6 Mev gamma ray is dependent upon the initial plutonium-236 concentration as well as on the self-shielding of the heat source and the

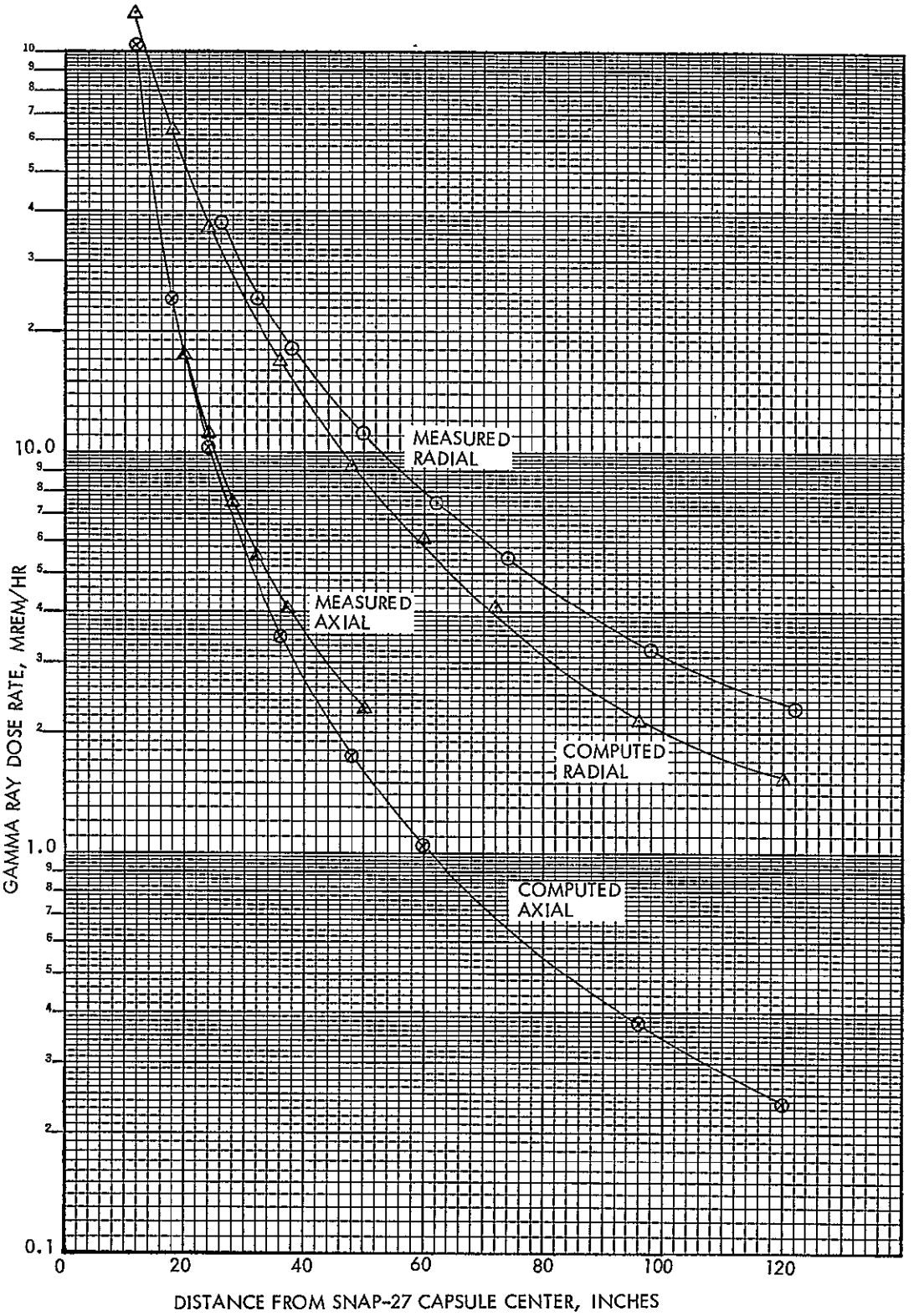

Figure 4-13. Gamma Ray Dose Rates as a Function of Distance from the Center of a SNAP-27.

Table 4-17. Computed Gamma Ray Flux at 8 Feet on the Axis of SNAP-27 and SNAP-19 (Microsphere and SSC Fuel) Assuming 2-year Old Fuel and 1.2 ppm Pu-236, Photons/cm^2-sec.

		One SNAP-19 Tandem (Axis)				SNAP-27 (Axis)		SNAP-27 (Midplane)	
Energy (Mev)	Group	Flux (Microsphere)	% in Group	Flux (SSC Fuel)	% in Group	Flux (Microsphere)	% in Group	Flux (Microsphere)	% in Group
0.05	1	4.51/-18*	0.00	5.78/-24	0.00	3.38/-18	0.00	2.61/1	1.0
0.10	2	6.20/-1	0.62	7.97/-2	0.12	2.70/-1	0.31	1.38/3	55.0
0.15	3	1.61/-1	0.16	1/61/-2	0.02	1.34/-2	0.02	2.97/2	11.9
0.2	4	2.90/-1	0.29	9.15/-2	0.14	1.08/-1	0.13	2.78/1	1.2
0.8	5	5.94/+1	59.4	3.99/+1	59.6	5.29/1	61.11	5.85/2	23.4
1.0	6	5.69/0	5.69	3.80/0	5.68	4.98/0	5.75	4.36/1	1.7
1.5	7	1.69/0	1.69	1.13/0	1.69	1.43/0	1.65	9.05/0	0.4
2.0	8	1.25/0	1.25	8.39/-1	1.25	1.04/0	1.21	5.66/0	0.2
2.6	9	3.07/1	30.7	2.08/+1	31.1	2.55/1	29.45	1.32/2	5.2
3.0	10	3.06/-1	0.31	2.08/-1	0.31	2.53/-1	0.29	1.25/0	0.05
4.0	11	5.73/-2	0.06	3.89/-2	0.06	4.65/-2	0.054	2.29/-1	0.01
5.0	12	2.83/-2	0.03	1.93/-2	0.03	2.29/-2	0.03	1.14/-1	0.00
6.0	13	1.36/-2	0.01	9.21/-3	0.01	1.09/-2	0.01	5.49/-2	0.00
	Total	1.00/2	100.	6.69/+1	100.	8.66/1	100.	2.51/3	100.

4.51/-18 = 4.51×10^{-18}

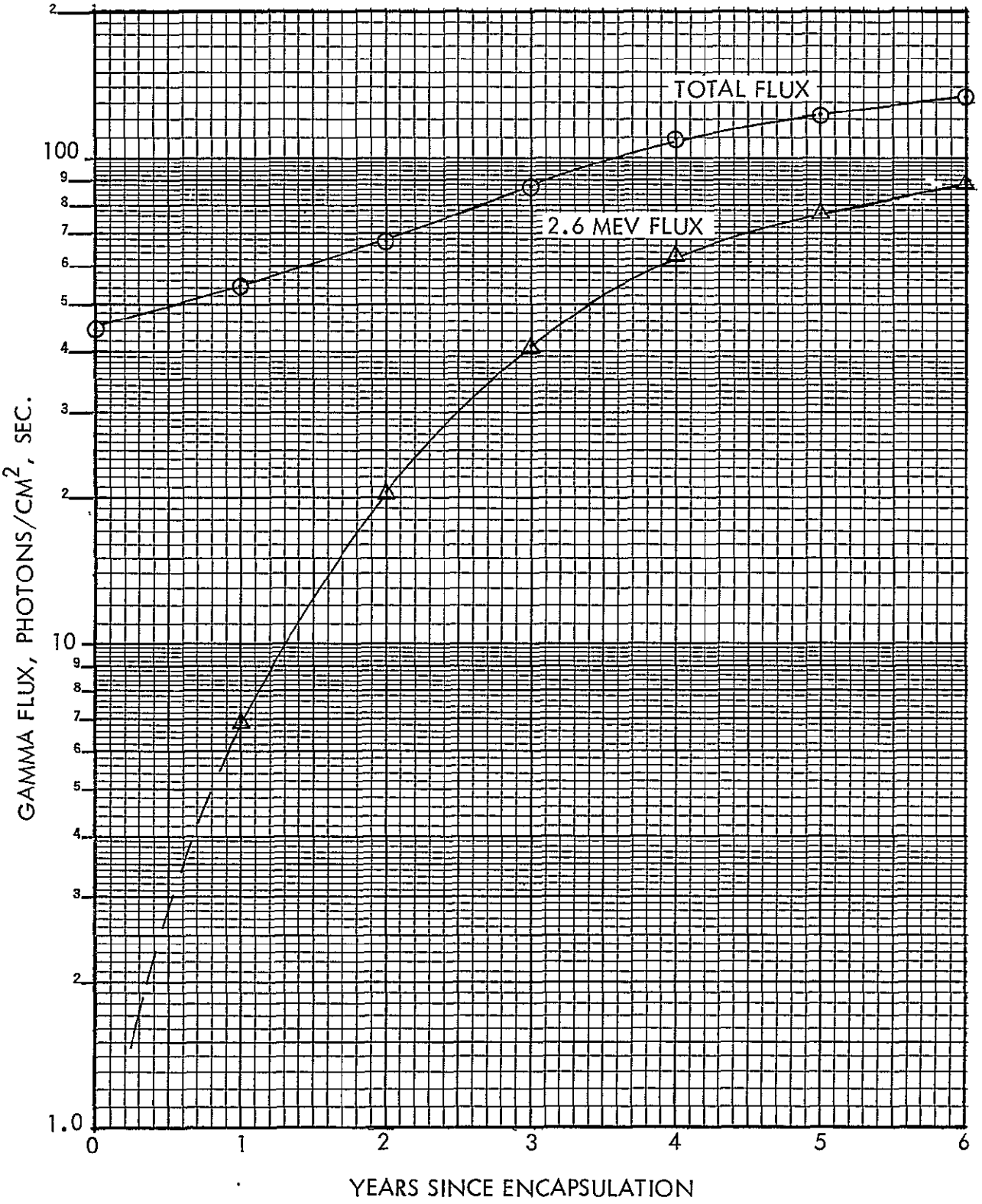

Figure 4-14. Calculated Change in Gamma Flux vs. Time

time since encapsulation. The calculations assume a value of 1.2 ppm for the initial plutonium-236 concentration.

The gamma ray spectrum at locations within the Pioneer instrument compartment varies less than ±20%. This is the result of there being two pairs of RTG's 120° apart; as one gets father from one pair one usually gets closer to the other. Mean values in the Pioneer instrument compartment for the 0.8 Mev, 2.6 Mev, and total flux at 2 years after fuel fabrication are 53, 27, and 88 photons/cm^2-sec., respectively.

The instrument compartment spectrum is very similar to that found on the SNAP-27 axis but much "harder" (and with a considerably lower magnitude) than that found in the SNAP-27 midplane. Thus most spacecraft radiation interference values would be expected to be substantially less than those derived by distance-only corrections of measurements made on the SNAP-27 midplane. More than 90% of the gamma rays have energies above 700 kev with 30% (at two years) being at 2.6 Mev.

The SNAP-19 thermoelectric modules and graphite reentry shielding reduce the instrument compartment gamma fluxes by about 40%. The reduction is partially offset by the scattering of radiation towards the instruments which would otherwise have gone into space.

The gamma ray output of the RTG's increases with time. Almost all of the increase in the gamma ray leakage is accounted for by the 2.6 Mev gamma ray from the decay of the thallium-208. Between two years and five years after fabrication the total flux increases by a factor of 1.8 while the 2.6 Mev gamma ray intensity increases by a factor of 3.7.

Geometric attenuation around SNAP-27 does not in general vary as $1/r^2$ from the fuel capsule center, and, on the axis is also energy dependent.

The walls and floors of the Building 84 test facility provide a contribution to gamma ray measurements around SNAP-27. This facility-induced background can be separated and evaluated by proper use of shadow shielding to block out the direct radiation. Its importance relative to the direct radiation is directly proportional to the distance from the source and to the amount of shielding placed between the fuel capsule and the detectors. It also depends upon the location within the facility of both

the fuel capsule and the detector.

4.4 Measured Radiation Fields

The radiation spectra at the midplane of the SNAP-27 fuel capsule was measured using a germanium-semiconductor detector. The detector was 20 cubic centimeter coaxial device with a calibrated gamma ray efficiency(ε) of

$$\varepsilon = \frac{0.441}{A} \quad E^{-1.32}$$

where A is the projected area of the detector and E is gamma ray energy in Mev (calibrated in the range of 0.1 to 2.5 Mev).

The results, shown in Figures 4-15 to 4-22, represent the most complete and accurate measurements of the SNAP-27 fuel capsule gamma ray spectrum performed during the course of this study.

4.5 Summary of Radiation Effects on Science Instruments

In summary the following statements can be made about the effects of the RTG radiation on the Science Instruments on board the Pioneer spacecraft.

- Gamma radiation from the RTG's is the predominant cause of radiation interference.
- Neutrons contribute a negligible amount to the interference (but are responsible for majority of the radiation damage as discussed in Section 7.).
- RHU's will contribute on the order of 10% of the interference.
- The gamma radiation resulting from plutonium fuel which contains 1.2 ppm ^{236}Pu impurity appears to be low enough to permit meeting the majority of the scientific objectives of the Pioneer F/G mission as they are presently defined. However, some of the experiments concerned with measurements of space radiation have been curtailed, including measurements of low energy electrons. Any decrease in the radiation level would improve the quality of the data.
- Conversations with the experimenters indicate that it would take a factor of ten reduction in gamma ray emission from the RTG's and RHU's to permit measurement of low energy electrons . At present, this is not feasible to accomplish.

- Instruments designed to measure low (<2 Mev) energy electrons are most significantly affected by the RTG radiation.
- Gamma ray photons with energy of 2.62 Mev and several gamma ray lines concentrated around 0.8 Mev are the most significant sources of interference.
- The magnitude of interference will vary with fuel age and will be much more severe at or near Jupiter encounter than in the beginning of the mission.
- Interference produced by (n,α) and (n,p) reactions in silicon semiconductor detectors is very small as compared to the interference caused by the gamma radiation.

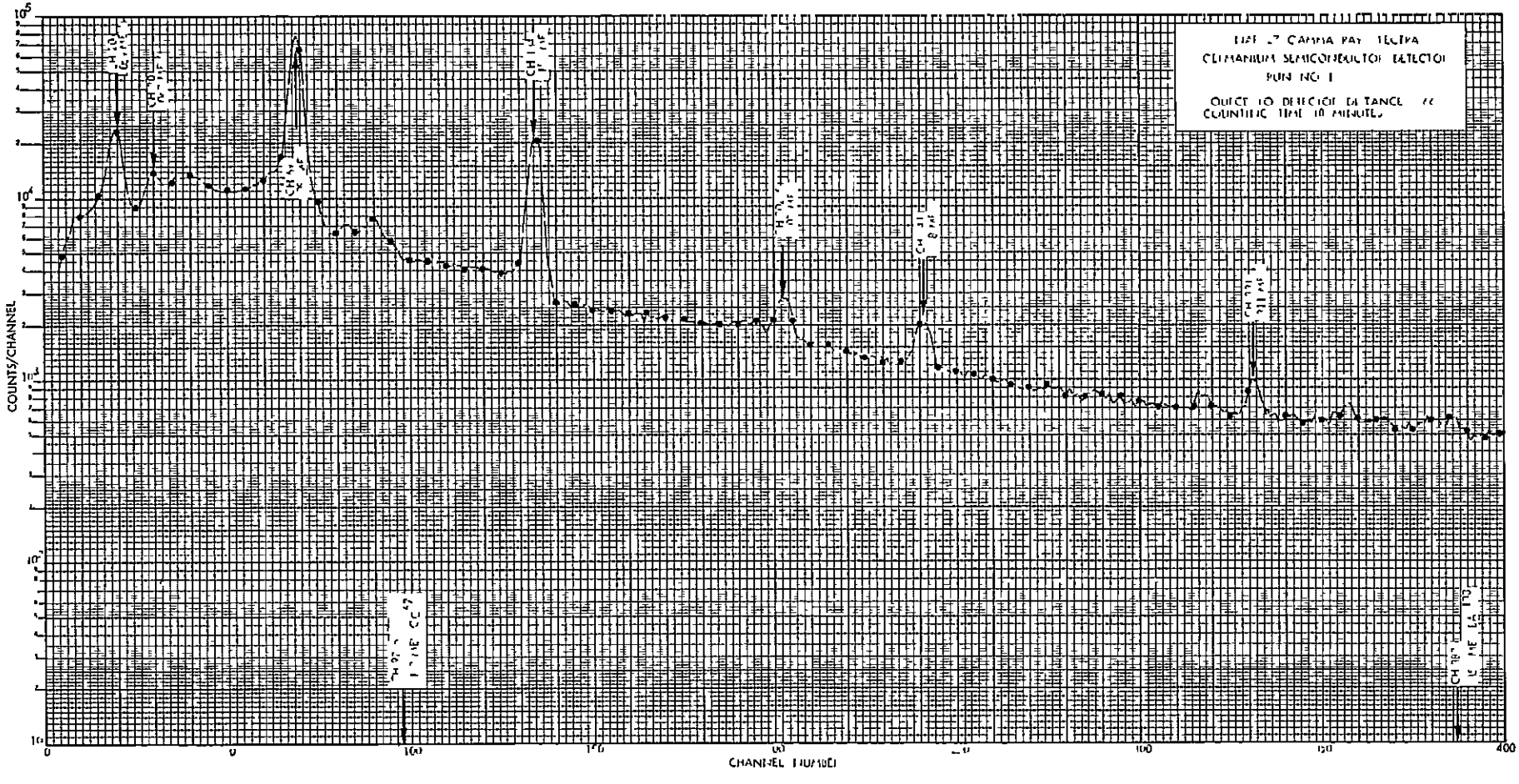

Figure 4-15. SNAP-27 Fuel Capsule Gamma Ray Radiation Spectrum

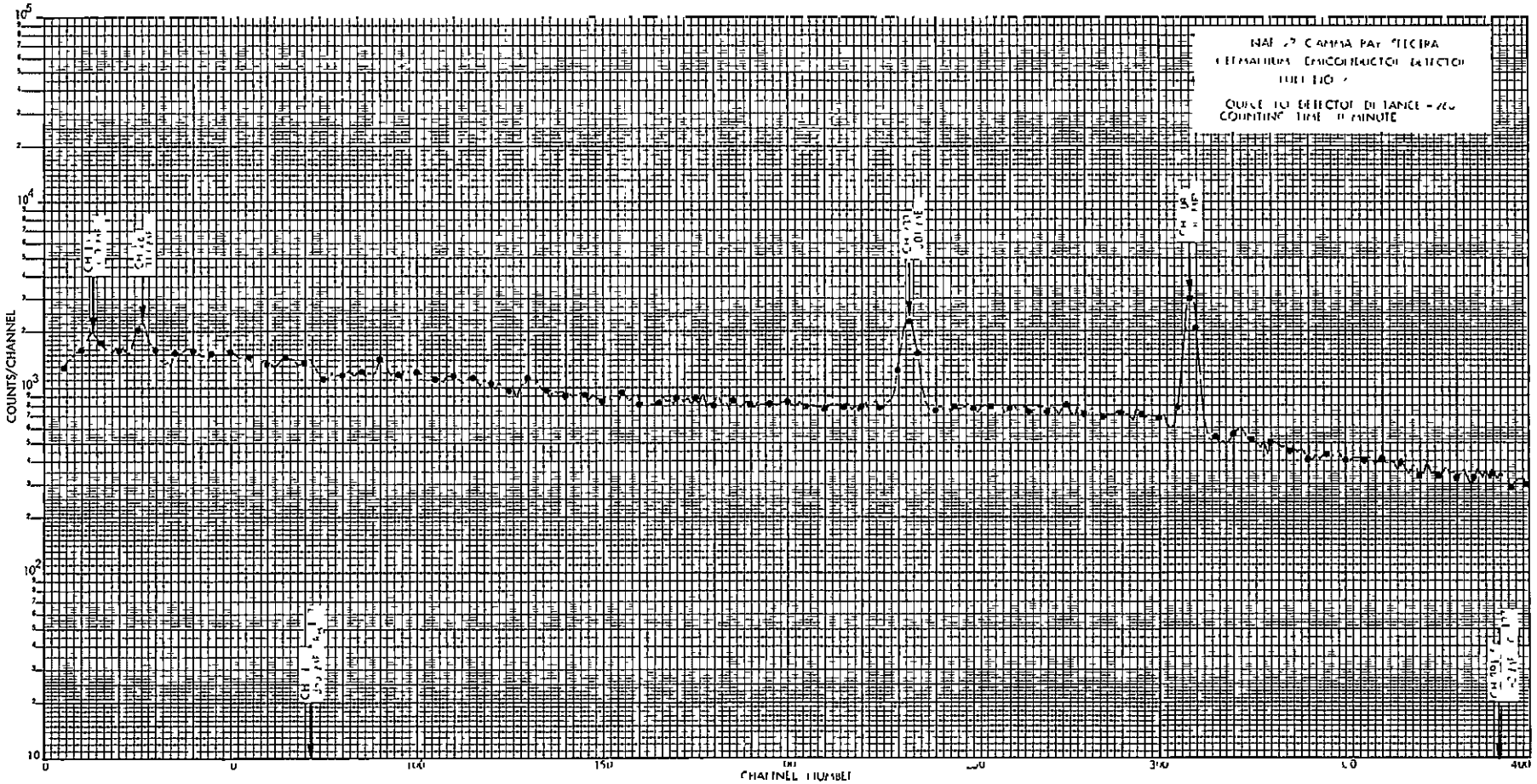

Figure 4-16. SNAP-27 Fuel Capsule Gamma Ray Radiation Spectrum

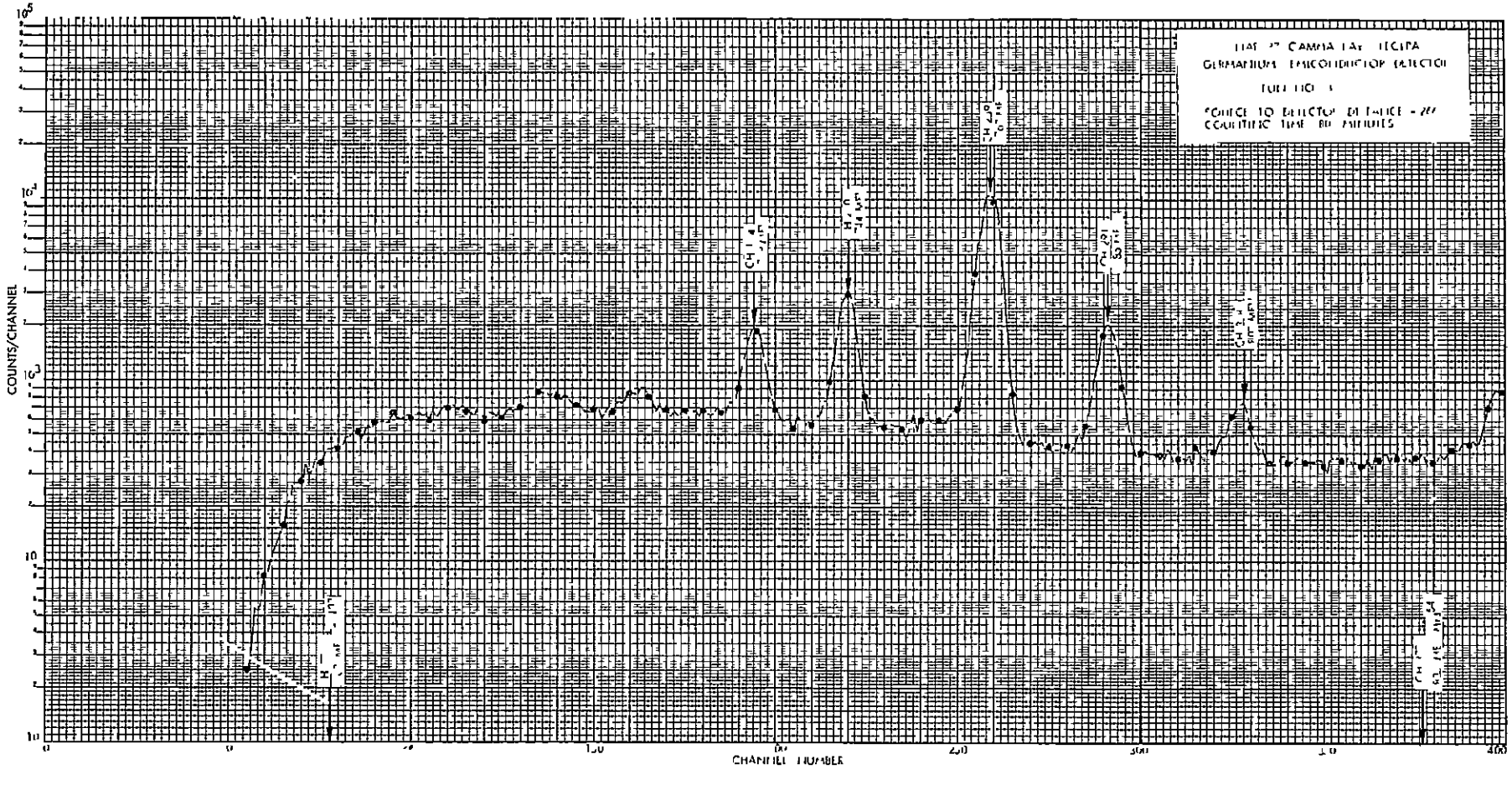

Figure 4-17. SNAP-27 Fuel Capsule Gamma Ray Radiation Spectrum

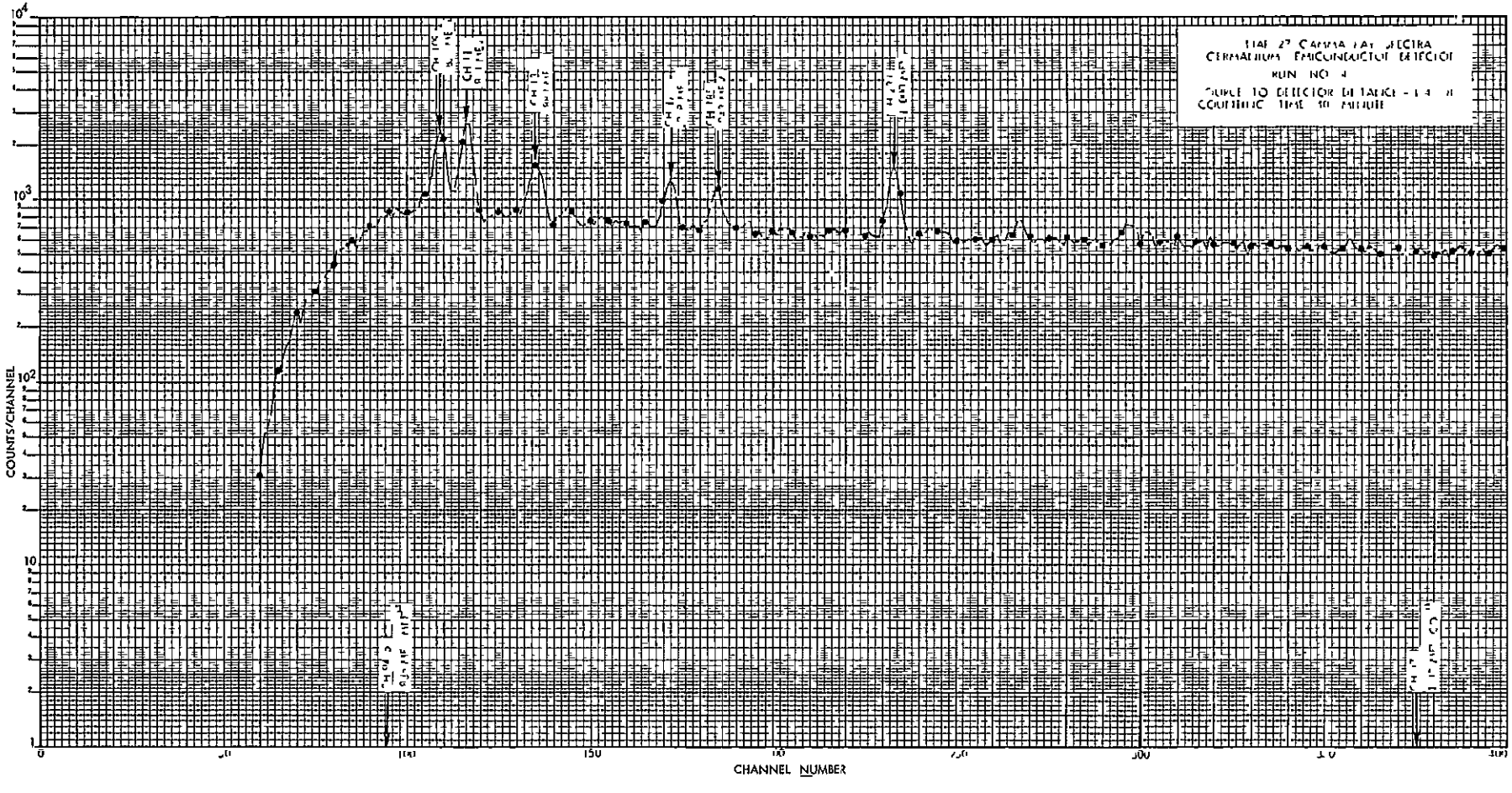

Figure 4-18. SNAP-27 Fuel Capsule Gamma Ray Radiation Spectrum

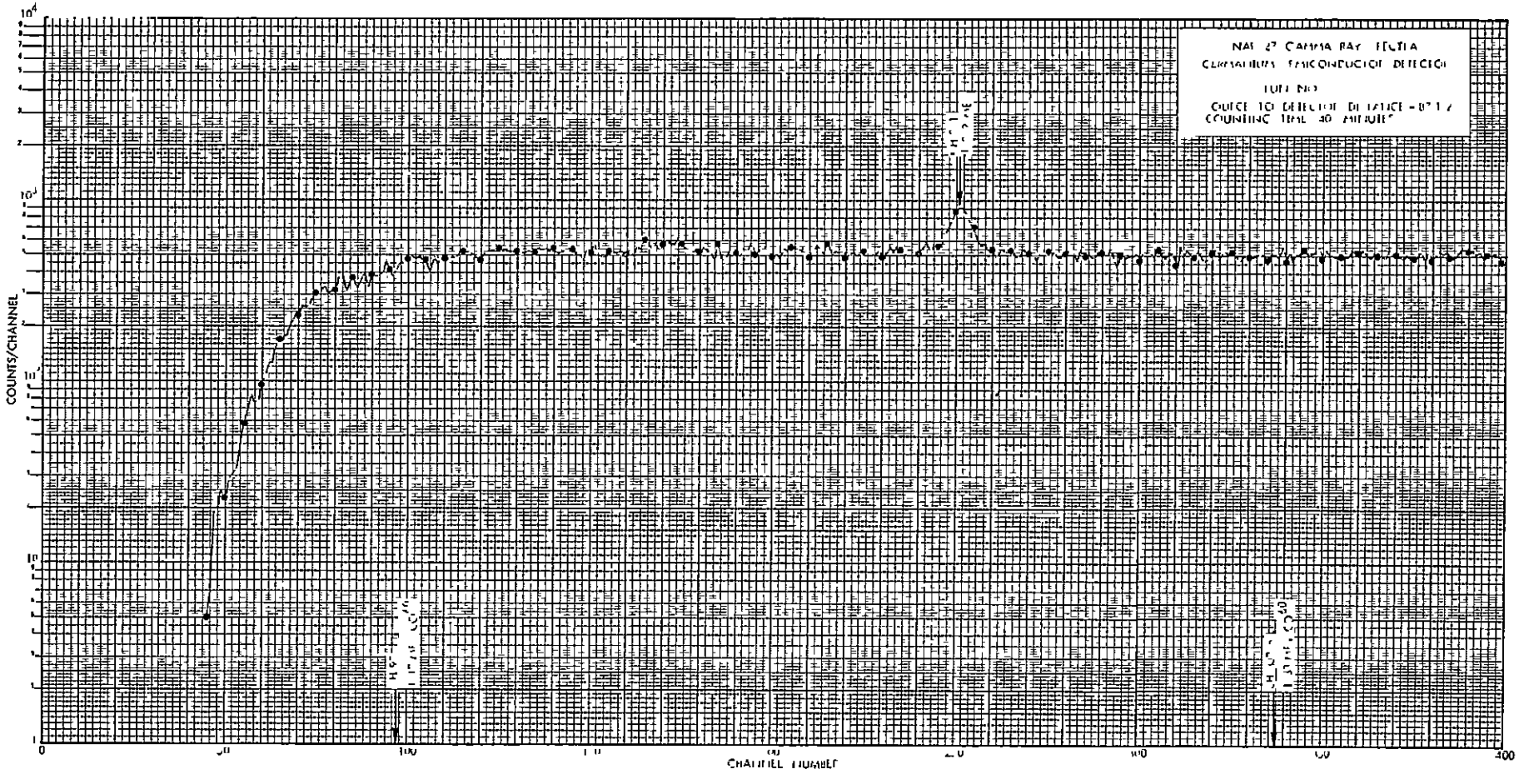

Figure 4-19. SNAP-27 Fuel Capsule Gamma Ray Radiation Spectrum

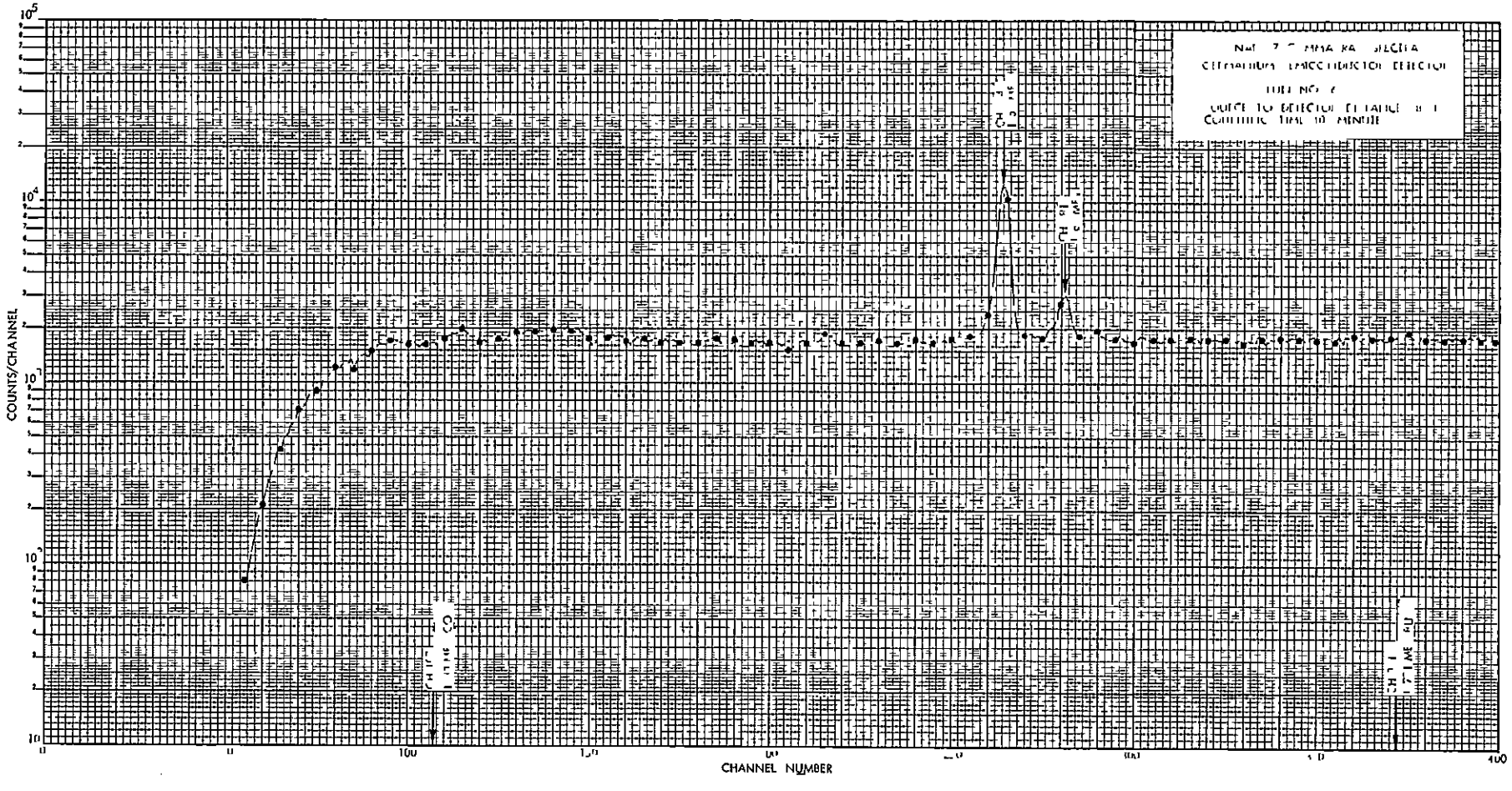

Figure 4-20. SNAP-27 Fuel Capsule Gamma Ray Radiation Spectrum

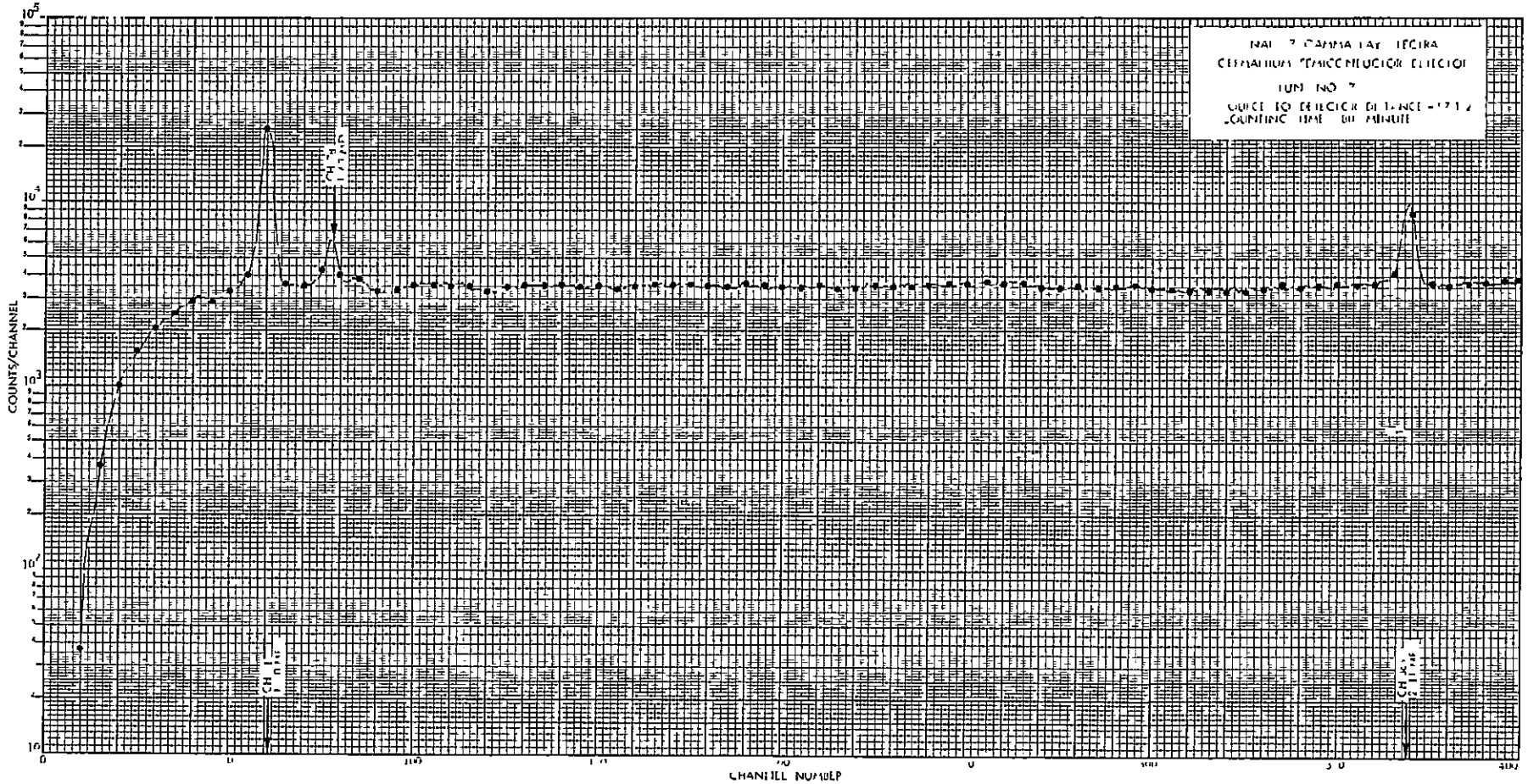

Figure 4-21. SNAP-27 Fuel Capsule Gamma Ray Radiation Spectrum

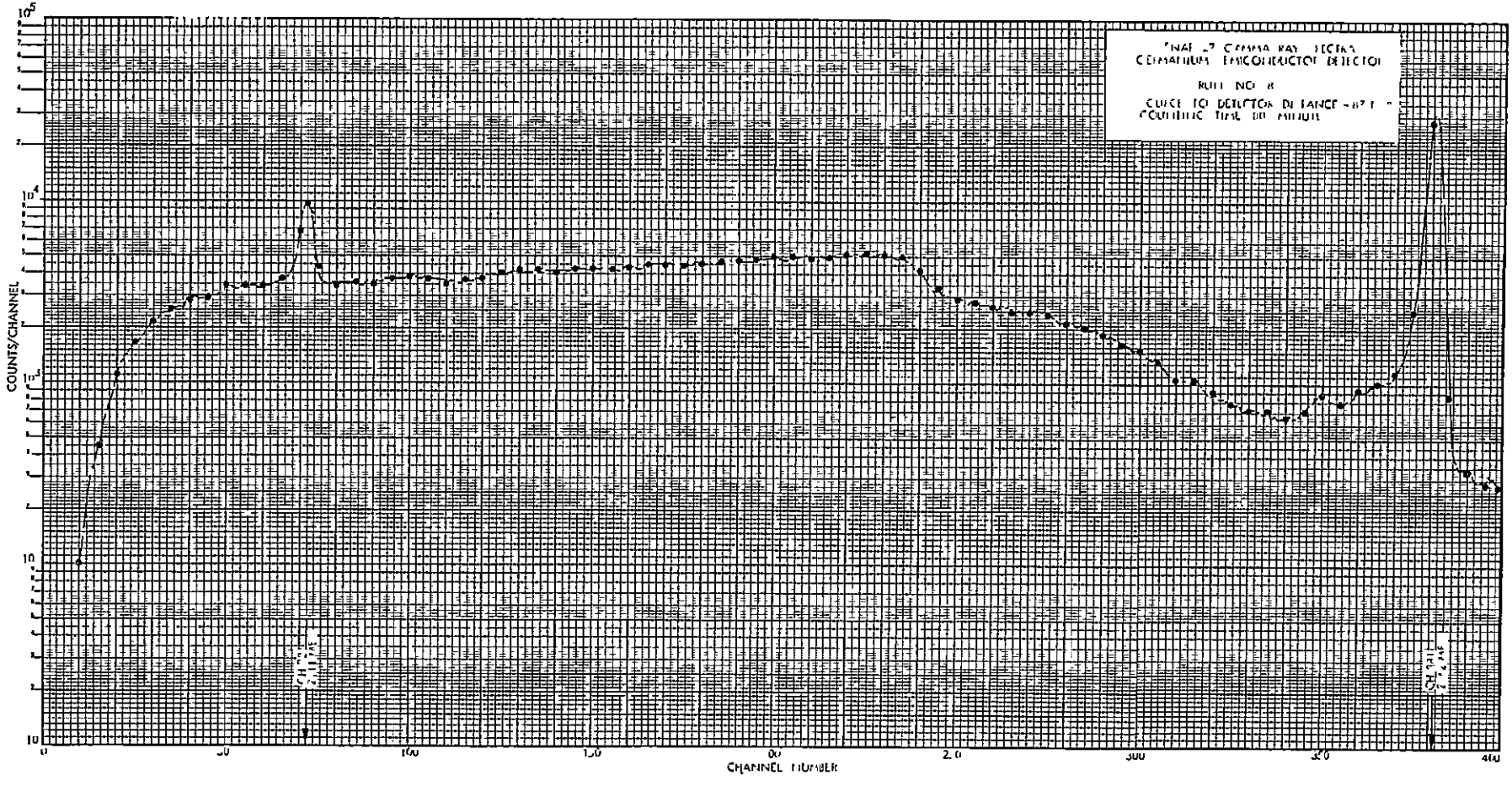

Figure 4-22. SNAP-27 Fuel Capsule Gamma Ray Radiation Spectrum

REFERENCES

(4-1) R. A. Kaminskas, et al., "RTG/Science Instrument Radiation Interactions for Deep Space Probes, Phase I Final Technical Report," Contract NAS-25222 (July 31, 1969).

(4-2) T. R. Herold, "Neutron Spectrum of $^{238}PuO_2$, "Nuclear Applications, 4, (1), 19-22 (January, 1968).

(4-3) R. A. Wolfe, "The Nuclear Criticality Safety Aspects of Plutonium-238," Nuclear Applications and Technology, 9, (August, 1970).

(4-4) E. J. Hennelly, Trans Am Nucl Soc, 11, 456 (1968).

(4-5) W. J. Lindsey, et al., "Production of ^{238}Pu with Minimum ^{236}Pu Contamination," Trans Am Nucl Soc, 13, (2), 496 (November, 1970).

(4-6) RSIC Code Package CCC-48 "QAD Point Kernel General Purpose Shielding Codes QAD IV, P-5, B, V, INT, HD, 5K, BR, P5A", (July, 1967).

(4-7) M. A. Capo "Polynomial Approximation of Gamma Ray Buildup Factors for a Point Isotropic Source" GE-ANP Report APEX-510, (1959).

5.0 PIONEER RADIATION MODEL

5.1 Spacecraft Mockup

A mockup of the Pioneer F/G Spacecraft was fabricated for the purpose of simulating the radiation scattering and absorption characteristics of the real spacecraft. The mockup was of the same physical size as the actual Pioneer F/G Spacecraft and consisted of an equipment platform, antenna, RTG booms, a propellant tank, and various electronic packages. Virtually all spacecraft parts with a design weight of 2 pounds or more were represented by an individual mockup.

A drawing of the Pioneer F/G mockup structure is given in Figure 5-1. Figure 5-2 is a drawing of the actual spacecraft showing the electronic hardware and science instrument package locations.

The three most significant parameters which influence the propagation of gamma radiation through a heterogeneous medium are the atomic weight of the material, density, and the geometric shape and size. To simulate the average atomic weight of various components in the Pioneer spacecraft, the mockup was constructed mostly of aluminum and fiberglass. The mockup structure was constructed from aluminum sheets having the same weight per unit area as the aluminum honeycomb used for the actual spacecraft. The aluminum sheets were reinforced with aluminum angles to provide rigidity. The antenna was constructed from trapezoidal sections of aluminum sheets approximating the mass per unit area of the actual aluminum honeycomb antenna. The center of the antenna was left out for accessibility. The antenna supports were fiberglass of the same diameter and thickness as on the real spacecraft.

Pioneer's 16.5 inch I.D. titanium propellant tank was simulated using a stainless steel tank of approximately the same dimensions. Hydrazine fuel was simulated with water.

The electronic boxes were constructed from flat aluminum plates held together with aluminum tape. The contents of the boxes were simulated by aluminum plates and epoxy fiberglass boards to duplicate printed circuit cards. The total weight of each box and, where possible, the ratio of

aluminum to epoxy corresponded to the actual spacecraft component. Some of the boxes, such as power supplies containing large and heavy transformers, were constructed by placing pieces of copper or other appropriate material within the aluminum box.

The scientific instruments were simulated similarly to the electronic boxes except that even greater care was taken to duplicate the mass, average atomic weight, and mass distribution of each instrument. All the electronic boxes in the instrument compartment were constructed so that they could easily be removed and replaced with prototype instruments. The weights and sizes of the various electronic boxes and science instruments used for the mockup are listed in Table 5-1.

Figure 5-3 shows the completed spacecraft mockup. The support booms for the simulated RTG's are seen in their extended positions to the left and front center. Support lines were attached to the triangular RTG mounting frames to prevent the booms from sagging from the weight of the RTG source mockups. The propellant tank and several electronic packages are visible in the electronics compartment.

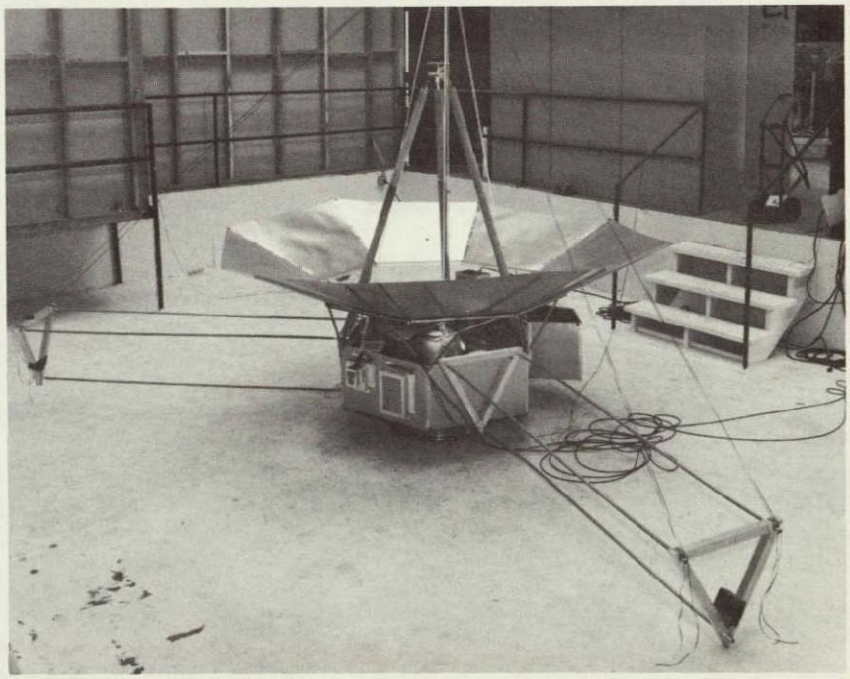

Figure 5-3 Pioneer F/G Spacecraft Radiation Mockup

Table 5-1. Dimensions and Weights of Electronic Gear and Science Instruments for Pioneer F/G Spacecraft Mockup.

Subsystem	Unit	Length, inch	Width, inch	Height, inch	Weight, pounds
Electrical Power	Battery	9.8	7.0	2.5	7.35
	Central TRF Assembly	10	6	8	
	Power Inverters (2)	4.0	6.0	7.0	5.2 ea
	Power Control Unit	6	8.5	10	15
Communications	Conical Scan Signal Processor	8.5	7.0	3.0	2.8
	Receivers (2)	8.4	3.0	6.2	4.2
	Power Supplies (2)	5.0	11.0	3.0	3.8 ea
	TWT's (2)	9.0	1.6	1.6	
	Transmitter Drivers (2)	5.2	2.3	3.6	1.5 ea
Antennas	Coupler	2.7	2.7	1.0	0.7
	Duplexers (2)	6.8	3.43	2.0	2.0 ea
	Switches (2)	3.0	1.53	0.66	1.0 ea
Data Handling	Digital Telemetry Unit	11.0	7.0	5.3	7.5
	Data Storage Unit	9.0	6.0	3.5	4.1
	Digital Decoder Unit	9.0	6.0	1.3	1.9
Electrical Distribution	Command Distribution Unit	6.2	8.6	8.0	12
Attitude Control	Stellar Reference Assembly	4.0	4.1	9	2.5
	Control Electronics Assembly	10.0	6.7	7.8	10

Continued on next page.

Table 5-1. (continued)

Subsystem	Unit	Length, inch	Width, inch	Height, inch	Weight, pounds
Attitude Control	Sun Sensor Assembly	6.0	4.0	3.5	1
	Design Sensor Assembly	2.5	1.5	1.5	0.5
Propul-sion	Propellant Tank	18.0 dia			
	Pressure Trans-ducer	3.0	0.99 dia		
	Temperature Trans-ducer	2.2	0.688 hex		20
	Filter	6.25	1.25 dia		
Science Instrument	1. ARC/Wolfe	11	11.54	6	9.5
	2. JPL/Smith	5	7.2	4	5
	3. Univ. of Chicago/Simpson	7	9	7	5.6
	4. Univ. of Iowa/Van Allen	3.8	6	5.3	3.2
	5. GSFC/McDonald	6	8	6.5	4.3
	6. UCSD/Fillius	5	6	6	3.3
	7. USC/Judge	5	4	4	1.5
	8. Univ. of Arizona/Gehrels	7.5	7.4	7	8.5
	9. CIT/Munch	3.5	7.5	9	4.9
	10. GE/Soberman 4 Telescopes	7.5	8.0 dia	--	3
	11. LRC/Kinard Electronic	3	3	3	2
	Sensor	7.6	12.5	1	2

The total weight of the spacecraft mockup exclusive of RTG's and the fuel was 302 lbs. This compares to a design weight of 324 lbs for the real spacecraft. The difference in weight is due in part to omission of cabling, plumbing, and other small items in the mockup. In October, 1969, the allowable spacecraft weight was increased to 360 lbs.

Figure 5-4 shows a close-up view of the electronics compartment showing the relative positions of the electronic packages and propellant tank. Each electronic package was labeled with its originator's name, affiliation, and an identification number.

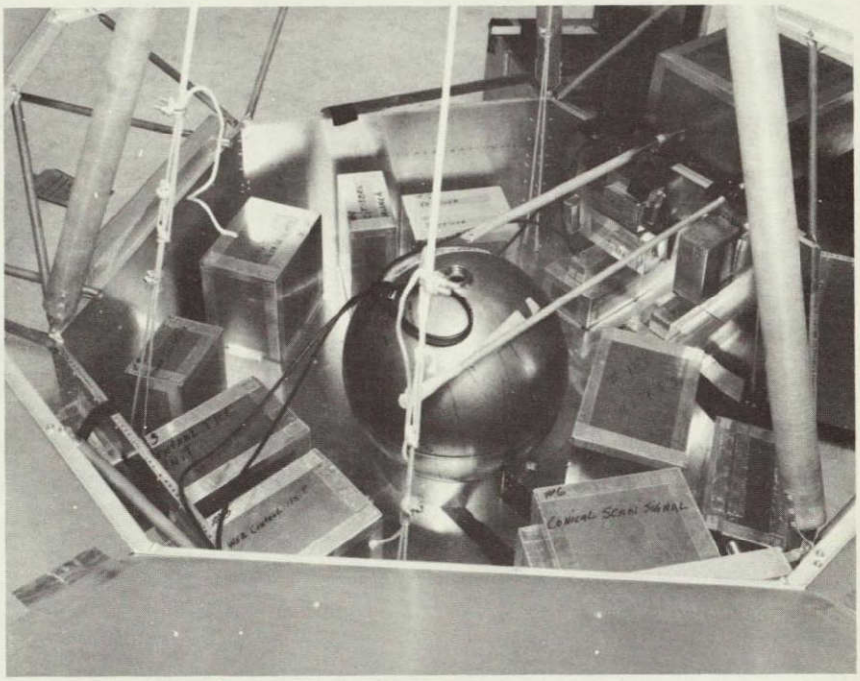

Figure 5-4 Pioneer F/G Spacecraft Mockup Equipment Compartment

The science instrument compartment with the aluminum cover removed is shown in Figure 5-5. The JPL/Smith and University of Chicago/Simpson instruments are visible under boxes representing the ARC/Wolfe and GSFC/McDonnald instruments. A detector used for radiation mapping of the spacecraft can be seen positioned between the ARC/Wolfe instrument and the rear wall.

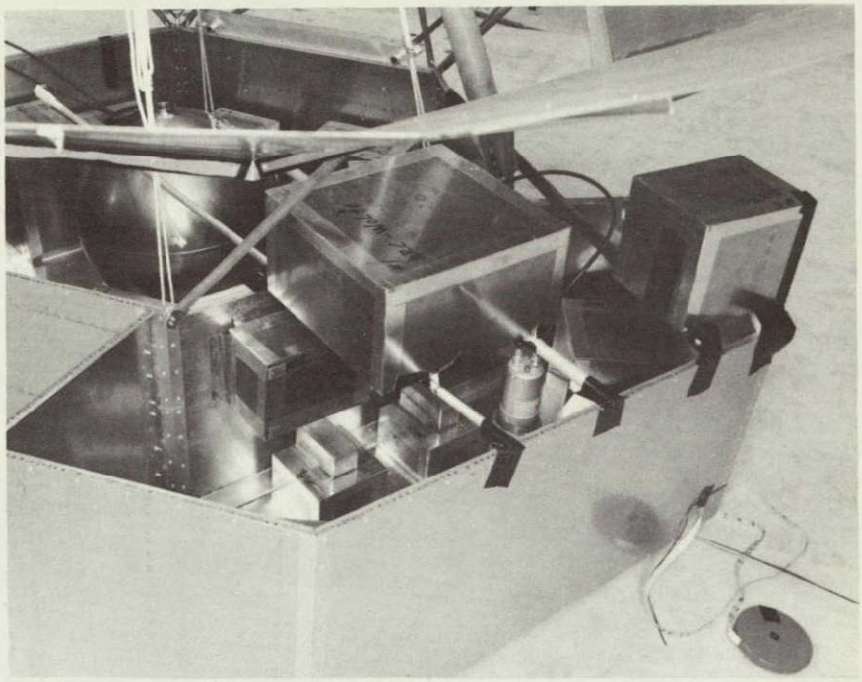

Figure 5-5 Pioneer F/G Spacecraft Mockup Science Instrument Compartment

In order to reduce test facility scattered radiation, the radiation interference tests were made in a high bay test facility. The facility was 32 feet wide, 48 feet long and 28 feet high and contained a pit 2.6 feet deep and 28 feet on a side. The test area was surrounded on three sides by corrugated steel walls. The fourth side was open. The floor and pit were concrete. A crane was used to lift the spacecraft into its test position above the floor. Figure 5-6 shows the spacecraft mockup suspended in the test facility.

5.2 RTG Radiation Source Mockups

To simulate the radiation environment in the Pioneer F/G mockup, the SNAP-19 RTG and RHU radiation was mocked up using a combination of radioisotope sources. The RTG source mockups were designed to duplicate the radiation flux and spectrum emitted by a pair of SNAP-19 RTG's including the effects of the graphite heat shield and thermoelectrics. The fuel was assumed to be in the form of plutonium-238 solid solution cermet containing 1.2 ppm plutonium-236. The apparent age of the fuel could be varied from 1 year to 4 years by selectively shielding the various radioisotope sources. RHU mockups were designed using the same fuel parameters.

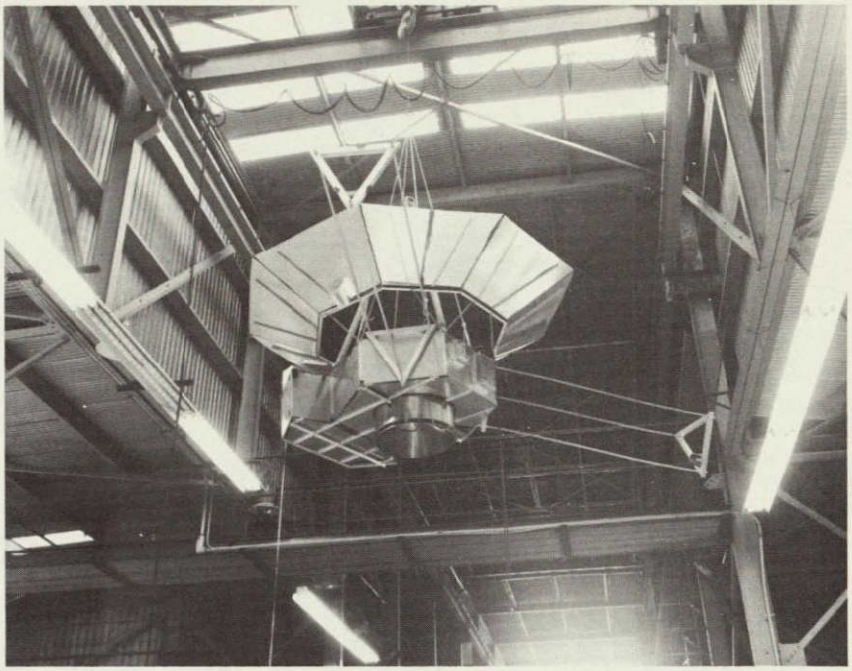

Figure 5-6 Pioneer F/G Spacecraft Mockup Suspended in the Test Facility

Source mockups were constructed for two tandem SNAP-19 RTG's, three 3-watt RHU's for the spacecraft thrusters, and one 2-watt RHU for the hydrazine tank. Each mockup was packaged as a separate unit.

The source mockup consisted of a composite source using three radioisotopes and absorbers so that the gamma ray emission could be adjusted to be the same as a SNAP-19 reference spectrum. The radiation from the mockup and the reference spectrum were then compared by measuring with a scintillation detector and a multichannel pulse height analyzer. A 1-1/2" x 1-1/2" diameter CsI(Na) scintillator was used as the radiation detector for most of the tests.

5.2.1 SNAP-19 Reference Spectrum

The SNAP-19 reference spectrum and gamma ray flux were obtained in the following way: The radiation emission from a complete tandem SNAP-19 pair of RTG's was computed using a QAD computer program (see Section 4.2.1). Then the radiation emission from a SNAP-27 fuel capsule was computed using the same program. Comparison between the two sets of data indicated that the gamma ray spectrum and flux for a pair of SNAP-19's at an angle of 20 degrees to the longitudinal axis was almost identical to the spectrum and flux

produced by the SNAP-27 fuel capsule at an angle of approximately 0 to 5 degrees to the longitudinal axis. The SNAP-27 fuel capsule spectrum was measured at that angle with a scintillation detector and used as the reference spectrum for the SNAP-19 at a fuel age of 3.3 years. For other ages the spectrum was corrected by multiplying it with the correction factor for several energy ranges.

The resultant SNAP-19 reference scintillation spectrum at a fuel age of 3.3 years is shown in Figure 5-7 along with the SNAP-27 spectrum.

5.2.2 Source Mockup Design

The first step in the design of the SNAP-19 radiation mockup involved choosing a set of radioisotopes which emit gamma radiation of the proper energy and calculating the amount of radioactive materials needed to simulate the radiation produced by plutonium-238. The next step was to determine how to shield the radioisotope sources in order to modify their spectra in the same way as occurs in the actual fuel capsule and structure. Simulating the ratio of Compton scattered photons to primary photons was of prime importance.

The approach selected was to start with the same acount of total gamma ray activity as is present in the SNAP-19 fuel capsules at that age and attenuate the radiation to the desired levels.

Source selections for the RTG and RHU were based on S. Block's work* at Lawrence Radiation Laboratory. Information on the gamma photon intensities for the plutonium-238 fuel was obtained from the Atomic Energy Commission during a Pioneer Experimenters' Coordination Meeting at NASA/Ames Research Center in November, 1969. The photon emission rates that were used to select the necessary activities of the radioisotopes are shown in Table 5-2. The gamma photon output per gram of plutonium-238 was multiplied by the total weight of the plutonium-238 in the heat source to obtain the total gamma photon output of the heat source.

---

*Block, S., "Radiation Dosimetry and Spectral Distribution of the SNAP", UCRL-50539.

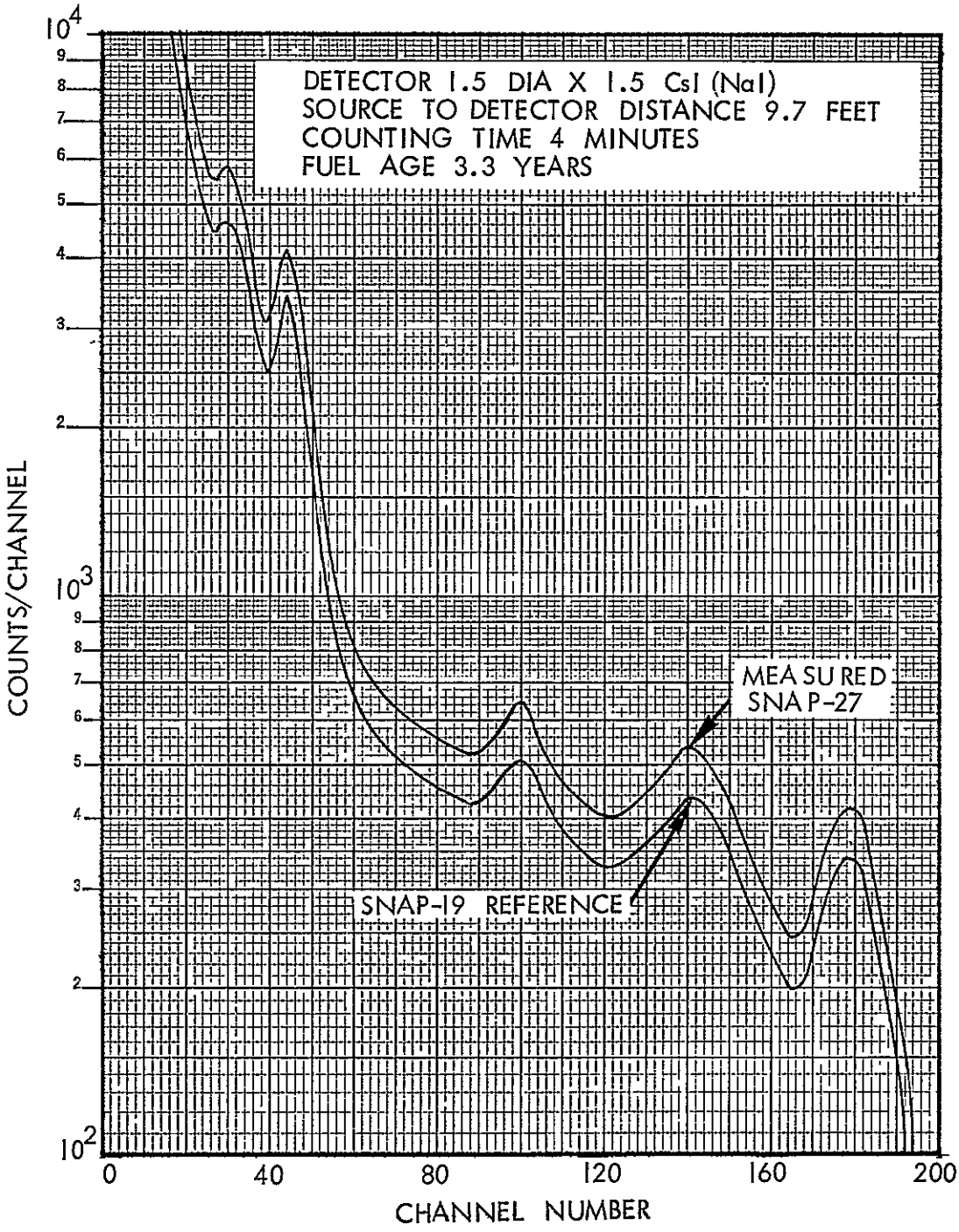

Figure 5-7 SNAP-19 Reference Gamma Ray Spectrum

Table 5-2 Calculated Gamma Photon Intensities In ^{238}Pu Decay

Energy (kev)	Origin	Photons/sec-gm ^{238}Pu						Mockup Source
		0 yrs.	1 yr.	4 yrs.	5 yrs.	6 yrs.	10 yrs.	
17	^{234}U x-ray	8.3×10^{10}	8.2×10^{10}	8.0×10^{10}	7.9×10^{10}	7.8×10^{10}	7.7×10^{10}	Not mocked up
43	^{238}Pu	2.4×10^{8}	2.4×10^{8}	2.3×10^{8}	2.3×10^{8}	2.3×10^{8}	2.2×10^{8}	Not mocked up
99.8	^{238}Pu	5.1×10^{7}	5.0×10^{7}	4.9×10^{7}	4.9×10^{7}	4.8×10^{7}	4.7×10^{7}	Not mocked up
115	^{212}Pb	---	2.1×10^{3}	1.9×10^{4}	2.5×10^{4}	3.1×10^{4}	4.4×10^{4}	^{228}Th
153	^{238}Pu	6.4×10^{6}	6.3×10^{6}	6.1×10^{6}	6.1×10^{6}	6.0×10^{6}	5.9×10^{6}	Not mocked up
203	^{238}Pu	2.5×10^{4}	2.5×10^{4}	2.4×10^{6}	2.4×10^{4}	2.4×10^{4}	2.3×10^{4}	Not mocked up
239	^{212}Pb	---	1.4×10^{4}	1.3×10^{5}	1.7×10^{5}	2.1×10^{5}	3.0×10^{5}	^{228}Th
241	^{224}Ra	---	1.1×10^{4}	1.0×10^{5}	1.4×10^{6}	1.7×10^{5}	2.4×10^{5}	^{228}Th
277	^{208}Tl	---	7.8×10^{2}	8.5×10^{3}	9.2×10^{3}	1.1×0^{4}	1.6×10^{4}	^{228}Th
300	^{212}Pb	---	9.8×10^{2}	9×10^{3}	1.2×10^{4}	1.5×10^{4}	2.1×10^{4}	^{228}Th
511	^{208}Tl	---	2.5×10^{3}	2.3×10^{4}	3.0×10^{4}	3.7×10^{4}	5.3×10^{4}	^{228}Th
583	^{208}Tl	---	9.4×10^{3}	8.2×10^{4}	1.1×10^{5}	1.4×10^{5}	2.0×10^{5}	^{228}Th
727	^{212}Bi	---	1.4×10^{3}	1.2×10^{6}	1.6×10^{4}	2.0×10^{4}	2.9×10^{4}	^{228}Th
743	^{238}Pu	5.7×10^{4}	5.7×10^{4}	5.5×10^{4}	5.5×10^{4}	5.4×10^{4}	5.3×10^{4}	$^{95}Zr/^{95}Nb$
767	^{236}Pu	2.2×10^{5}	2.2×10^{5}	2.1×10^{5}	2.1×10^{5}	2.1×10^{5}	2.0×10^{5}	$^{95}Zr/^{95}Nb$
785	^{212}Bi	---	2.2×10^{2}	1.9×10^{3}	2.6×10^{3}	3.2×10^{3}	4.6×10^{3}	^{228}Th
810	^{238}Pu	$<6\times10^{3}$	$<6\times10^{3}$	$<6\times10^{3}$	$<6\times10^{3}$	$<6\times10^{3}$	$<6\times10^{3}$	^{54}Mn
860	^{208}Tl	---	1.3×10^{3}	1.2×10^{4}	1.6×10^{4}	2.0×10^{4}	2.8×10^{4}	^{228}Th
865	$^{16}N(\alpha,p)$	variable - depends on nitrogen content.						
1075	^{212}Bi	---	1.2×10^{2}	1.1×10^{3}	1.5×10^{3}	2.2×10^{3}	2.6×10^{3}	^{228}Th
1620	^{212}Bi	---	3.5×10^{2}	3.2×10^{3}	4.2×10^{3}	5.3×10^{3}	7.4×10^{3}	^{228}Th
2614	^{208}Tl	---	1.1×10^{4}	1.0×10^{5}	1.3×10^{5}	1.6×10^{5}	2.3×10^{5}	^{228}Th

Higher energy fission gammas are present, but are very faint.

The change in the gamma photon spectrum and flux as a function of time, shown in Table 5-2, is due to accumulation of plutonium-236 decay products. As described in Section 4.1.4.2, thorium-228 is a part of this decay chain and it, together with its daughters, is the major contributor to the gamma emission from the fuel capsule. Therefore, the apparent age of the mockup can be changed by altering the amount of thorium-228 in the source. Buildup of thorium-228 from plutonium-236 as a function of time is given in Figure 5-8.

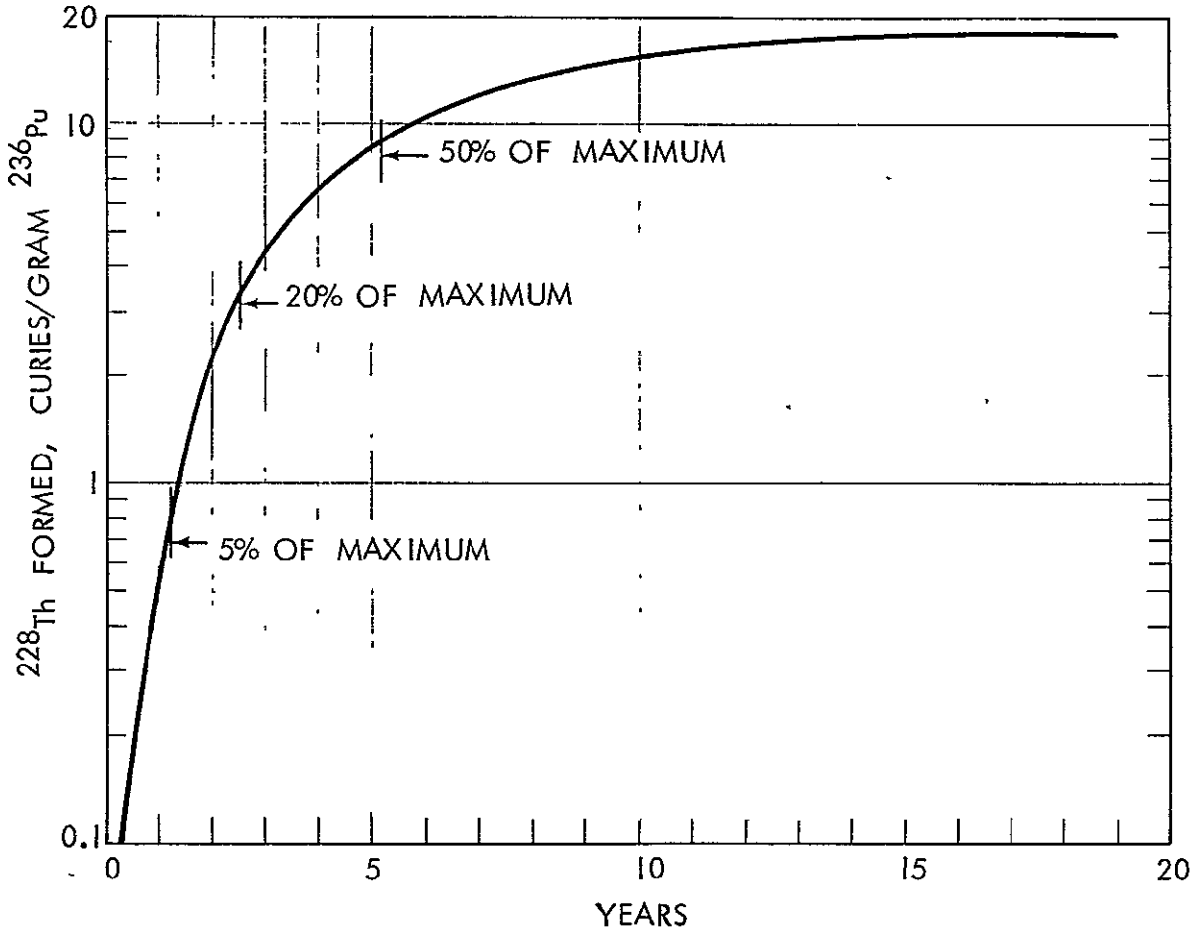

Fig. 5-8 Ingrowth of ^{228}Th from ^{236}Pu

Thorium-228, zirconium-95/niobium-95 and manganese-54 radionuclides were used to mock up the SNAP-19 RTG and RHU spectra. How the three radioisotopes were used to duplicate the plutonium-236 spectrum is shown in Table 5.2. The amounts of each radioisotope used in the RTG and RHU source mockups are given in Table 5-3. The SNAP-19 mockup simulates the output of two SNAP-19's referred to as tandem SNAP-19.

Table 5-3. Radioisotope Sources Used for SNAP-19 RTG and RHU Radiation Source Mockups

Isotope	Source Activity*, mCi		Gamma Energy, kev
	Tandem SNAP-19	2-watt RHU's	
^{54}Mn	0.40	0.22×10^{-3}	835
$^{95}Zr/^{95}Nb$	4.14	2.28×10^{-3}	724,765,766
^{228}Th (1 yr)	2.0	2.2×10^{-3}	2615
(4 yrs)	18.0	20.0×10^{-3}	2615
Am-Be	2.0×10^{7} neutrons/sec		

*At the time of purchase

The amounts of radioisotopes required to mock up the SNAP-19 RTG's and RHU's were calculated as follows:

SNAP-19 RTG

(A) Thorium-228. The thorium-228 activity is calculated from the 2615 kev photon output requirement in Table 5-2 for one year old SNAP-19 fuel as follows:

$$^{228}Th \text{ activity} = \frac{\phi(E) \times G}{3.7 \times 10^{7} \times f} \text{ in mCi}$$

Where $\phi(E)$ = is the number of photons emitted per second per gm of ^{236}Pu (1.1×10^{4} photons/second-gram)

G = Weight of ^{238}Pu in a pair of SNAP-19 ($\sim$2300 gms)

f = Number of photons at this energy per disintegration of the isotope (0.34 photons 2615 kev ^{208}Tl gamma/disintegration of ^{228}Th.)

3.7×10^{7} = Number of disintegration/second per millicurie.

Substitution of these values into the equation gives approximately 2 millicuries of thorium-228 for a pair of one year old SNAP-19's. The thorium-228 activity needed to simulate a pair of 4 year old SNAP-19's is found to be 18 mCi by proportionally adjusting the 2615 kev intensity.

(B) Zirconium-95/Niobium-95. The zirconium-95/niobium-95 activity was calculated from its major photons in the 700 kev range. A comparison of the gamma ray energies and abundances for zirconium-95/niobium-95 and the corresponding gamma ray energies and intensities from the SNAP-19 are given in Table 5-4.

Table 5-4. Gamma Ray Energies for SNAP-19 and Mockup Sources

	Mockup Source		SNAP-19	
Isotope	Energy, kev	Abundance, %	Energy, kev	Intensity, $\frac{\text{photons}}{\text{sec-gm-Pu238}}$
^{95}Zr	724	49	743	5.5×10^4
	765	49		
^{95}Nb	766	100	767	2.1×10^5

Zirconium-95 exists in equilibrium with its decay product niobium-95. Therefore, there will be $2 \times 3.7 \times 10^7$ photons/second emitted per 1 mCi of zirconium-95. The emission rate of 743 and 767 kev gamma radiation from a pair of SNAP-19's is 2.9×10^8 photons/second. The amount of zirconium-95/niobium-95 required by the mockup was 4.0 mCi of zirconium-95.

(C) Manganese-54. The manganese-54 activity was calculated by equating its 100% abundant 835 kev gamma photon intensity to the 810 kev SNAP-19 photon intensity. This yields 0.4 mCi of manganese-54 for a pair of SNAP-19 RTG's.

(D) Neutrons. The neutron source strength was based upon an average neutron output of 9×10^3 neutrons/sec-gm of plutonium-238. This emission rate for a pair of SNAP-19's is 2.3×10^7 neutrons/second. This is equivalent to the neutron yield of a 10-curie americium-beryllium source.

Radioisotope Heater Unit

The source activity for the RHU mockup was determined by reducing the SNAP-19 mockup source by the ratio of plutonium-238 in the RHU to that in the RTG. The mockups were designed to duplicate heater unit groups of two and three. These groups contain 5 and 7.5 grams of plutonium-238, respectively. The source activities used to mock up the 2-watt heater groups are given in Table 5-3.

The radiation spectrum of the RHU was expected to be different that that of the SNAP-19 because of less absorption caused by the smaller size of the RHU. This was verified experimentally after the mockups were constructed, tested, and compared with an actual RHU. A discussion of the RHU gamma ray spectrum is included in Section 5.2.5.

5.2.3 Construction of the SNAP-19 Radiation Source Mockup

The SNAP-19 radiation source mockup consisted of three radioisotope sources, a source holder assembly and various absorbers. Figure 5-9 is a disassembled view of the RTG source mockup assembly showing source holder, base and several absorbers. Figure 5-10 is a rear view of the source block showing the three recessess used to mount the manganese-54, niobium-95 and thorium-228 sources. The source block was a cast cylinder of Cerrobend, a low-melting bismuth-tin alloy. The shield guides were brass tubes cast into the source block and slit down the sides to facilitate the insertion and removal of the cylindrical shields used to attenuate the radiation. This arrangement provided considerable flexibility in the shielding of each source separately and allowed easy modification of their relative intensities. A lead rear plate was attached to the source block by means of the attachment holes shown in Figure 5-9. The source block and rear plate are slip fitted into a 4 x 4 x 2-inch lead block base. Figure 5-11 shows the assembled unit with several typical shields located in the shield guides. To simulate the attenuation and scattering of the RTG typically, 1.5 inch thick lead absorber was used for the thorium-228 source, a 0.75 inch thich absorber was used for the zirconium-95/niobium-95 source, and no absorber for the manganese-54 source. The mounting holes in the base of the source mockup were used to position the source holder on the spacecraft mockup. Figure 5-12 shows the radioisotope source capsules used for the SNAP-19 RTG and RHU source mockups.

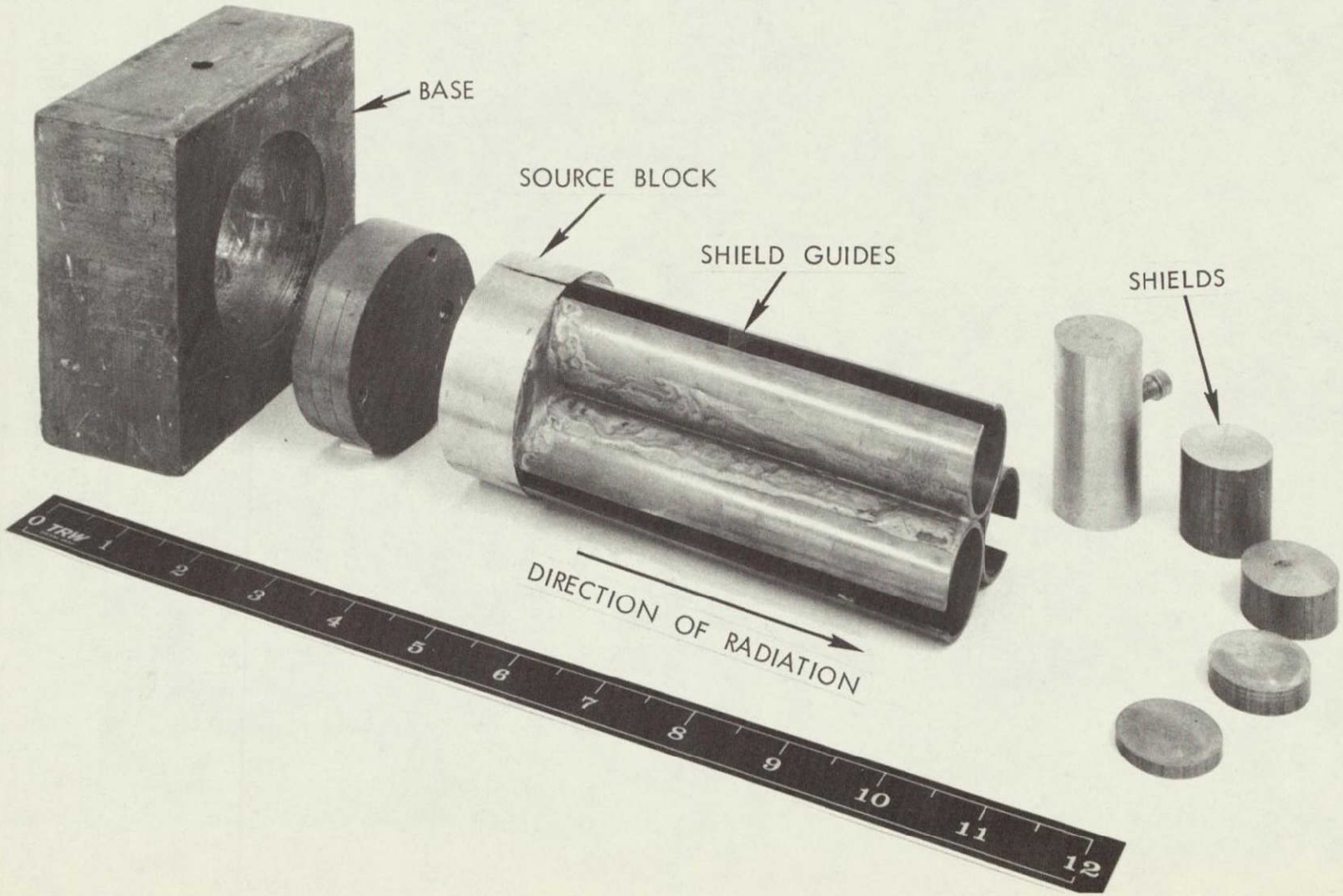

Figure 5-9 Disassembled RTG Radiation Source Mockup

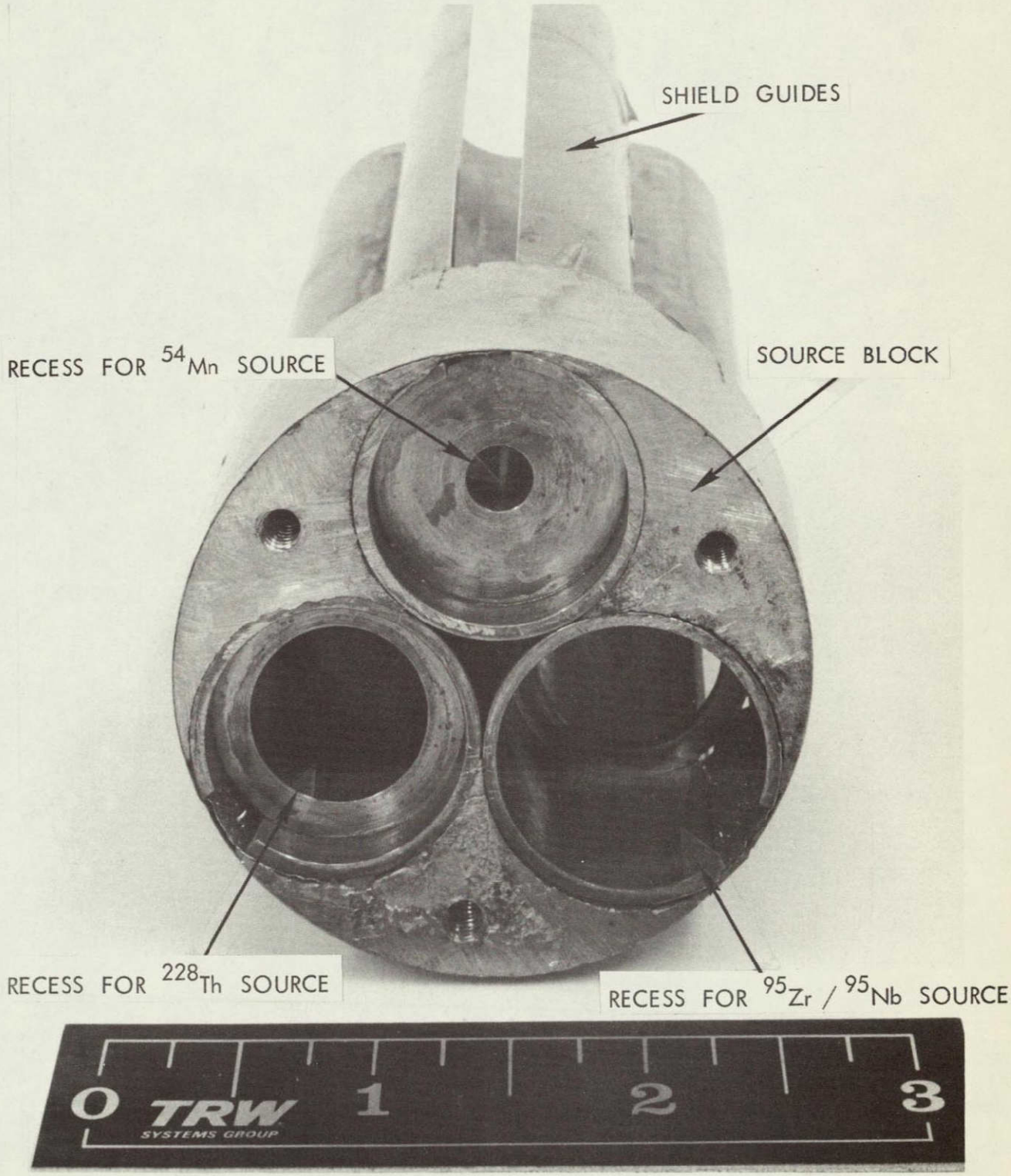

Figure 5-10. Rear View of Holder for RTG Source Mockup

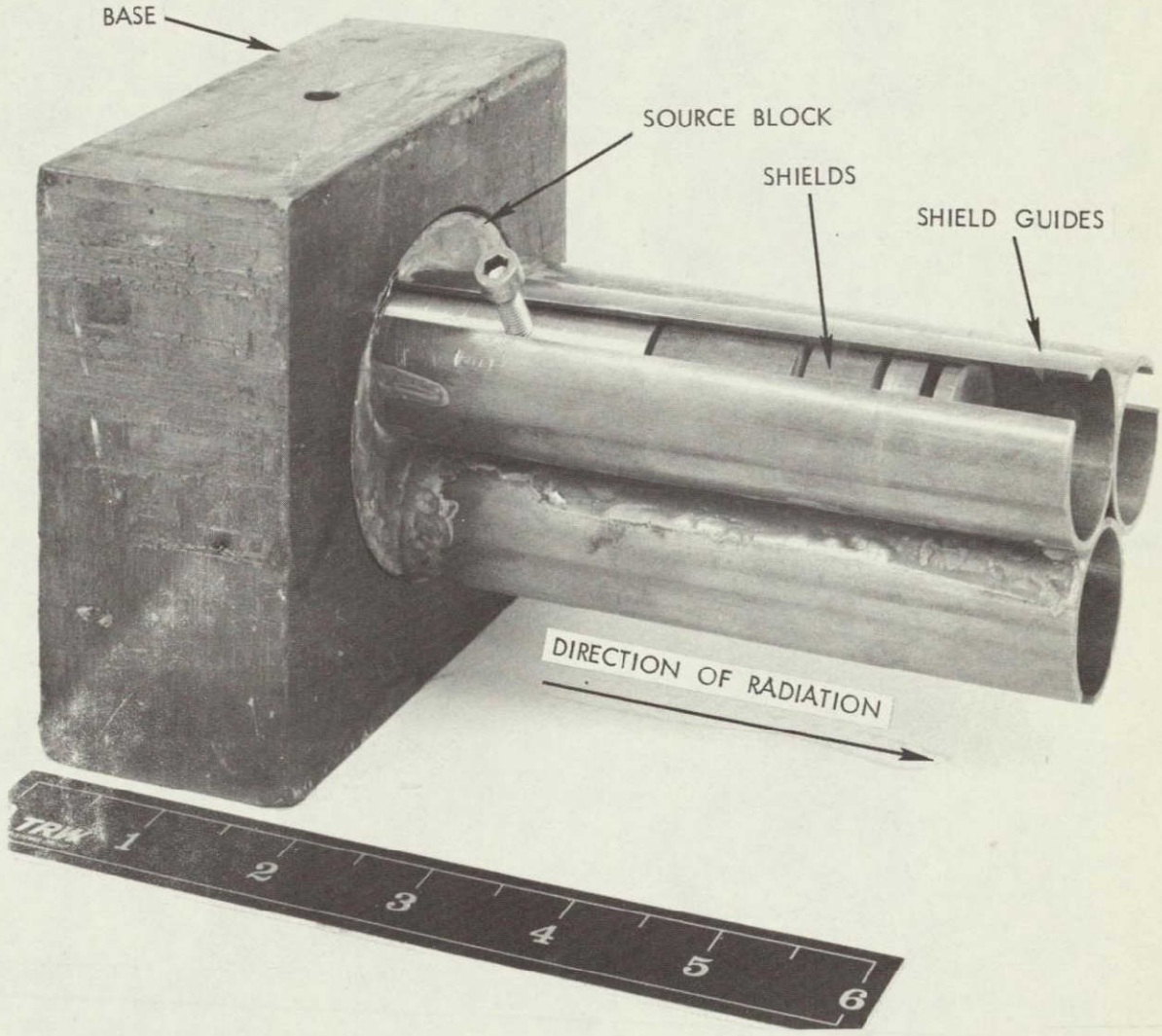

Figure 5-11. RTG Source Mockup Holder

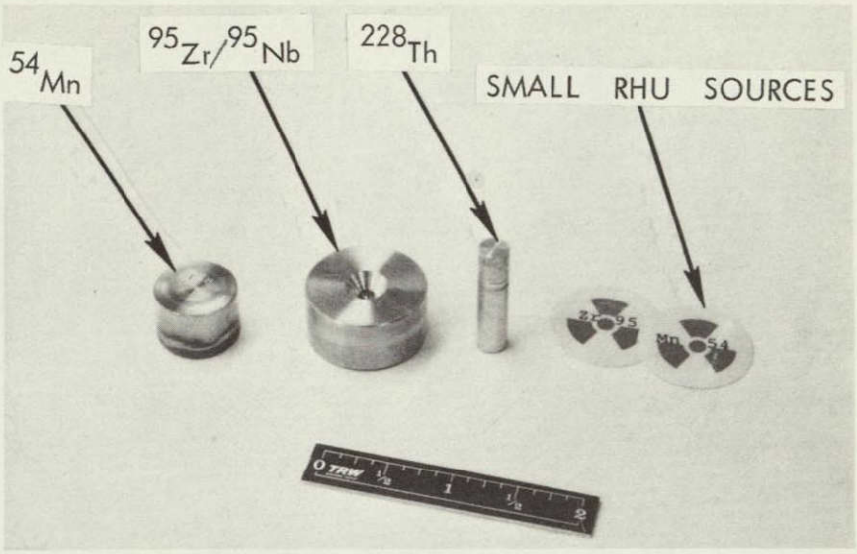

Fig. 5-12 Radioisotope Sources Used for SNAP-19 RTG & RHU Radiation Mockups

The RHU mockup consisted of 1.5 x 1.5 inch square, 0.25-inch thick lead absorbers and microcurie quantities of manganese-54, zirconium-95/niobium-95, and thorium-228. Leading shielding thicknesses necessary for the proper attenuation of emitted gamma radiation from the thorium-228, manganese-54, zirconium-95, and niobium-95 sources were experimentally determined to be 1-1/2, 3/4 and 0 inch, respectively. An exploded view of the assembly is shown in Figure 5-13. The sources and lead attenuators were held together with tape and installed in the spacecraft mockup at the desired location.

5.2.4 SNAP-19 Mockup Radiation Spectra

Figure 5-14 shows the response of a CsI scintillator to the SNAP-19 radiation source mockup. It represents the spectrum recorded by a scintillator placed 9.7 feet along the logitudiual axis from the centerline of a tandem SNAP-19 containing 3.3 year old plutonium-238 solid solution cermet fuel with 1.2 ppm plutonium-236. For most of the radiation measurements which were performed with the spacecraft mockup, the radiation mockup was adjusted to produce the same spectrum as the SNAP-19 reference spectrum but at a somewhat higher intensity for the purpose of reducing counting times and expediting data acquisition. The ratio of the mockup to the SNAP-19 reference count rate at 2.6 Mev was 3.13. The overall count rate ratio was 3.0. Peaks appeared in the spectrum at 2.6 Mev (Ch 180), 1.98 Mev (Ch 132), 1.58 Mev (Ch 100), 0.765 Mev (Ch45)and 0.540 Mev (Ch 30). The peaks at

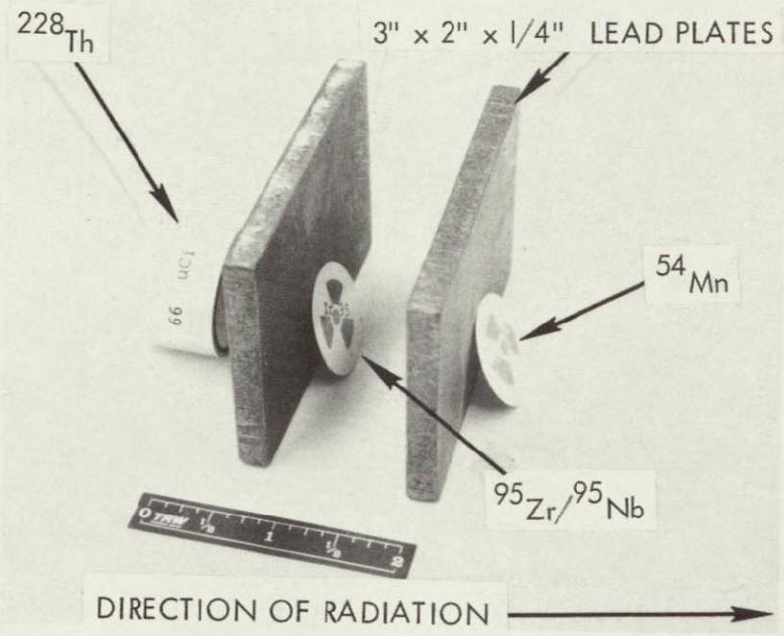

Fig. 5-13 Exploded View of RHU Source Mockup

channels 90, 132, 100, and 30 were from the bismuth-212 and thallium-208 decay products of thorium-228. The peak at channel 45 was caused by manganese-54 and zirconium-95/niobium-95.

For the purpose of comparing the reference and mockup spectrum shapes, the mockup source spectrum normalized to the SNAP-19 reference at 1.58 Mev (channel 100) is illustrated in Figure 5-15. A very close agreement between the two spectra can be seen. The spectra differ by no more than 10% throughout their range. Between channels 40 and 200 the difference is less than 0.7%. Because the SNAP-19 source mockup did not produce secondary gamma rays from neutron interactions in the fuel and structure of the RTG, nor contributions from fission fragments, the close fit between the two spectra indicates that the neutrons and fission fragments do not contribute significantly to gamma radiation from the SNAP-19 RTG.

Figure 5-16 shows the SNAP-19 mockup spectrum and the separate components used to mock it up. The general spectrum shape is that of thorium-228 and its decay products. The zirconium-95/niobium-95 source forms the peak at 760 kev and adds to the Compton spectrum below 500 kev. Manganese-54

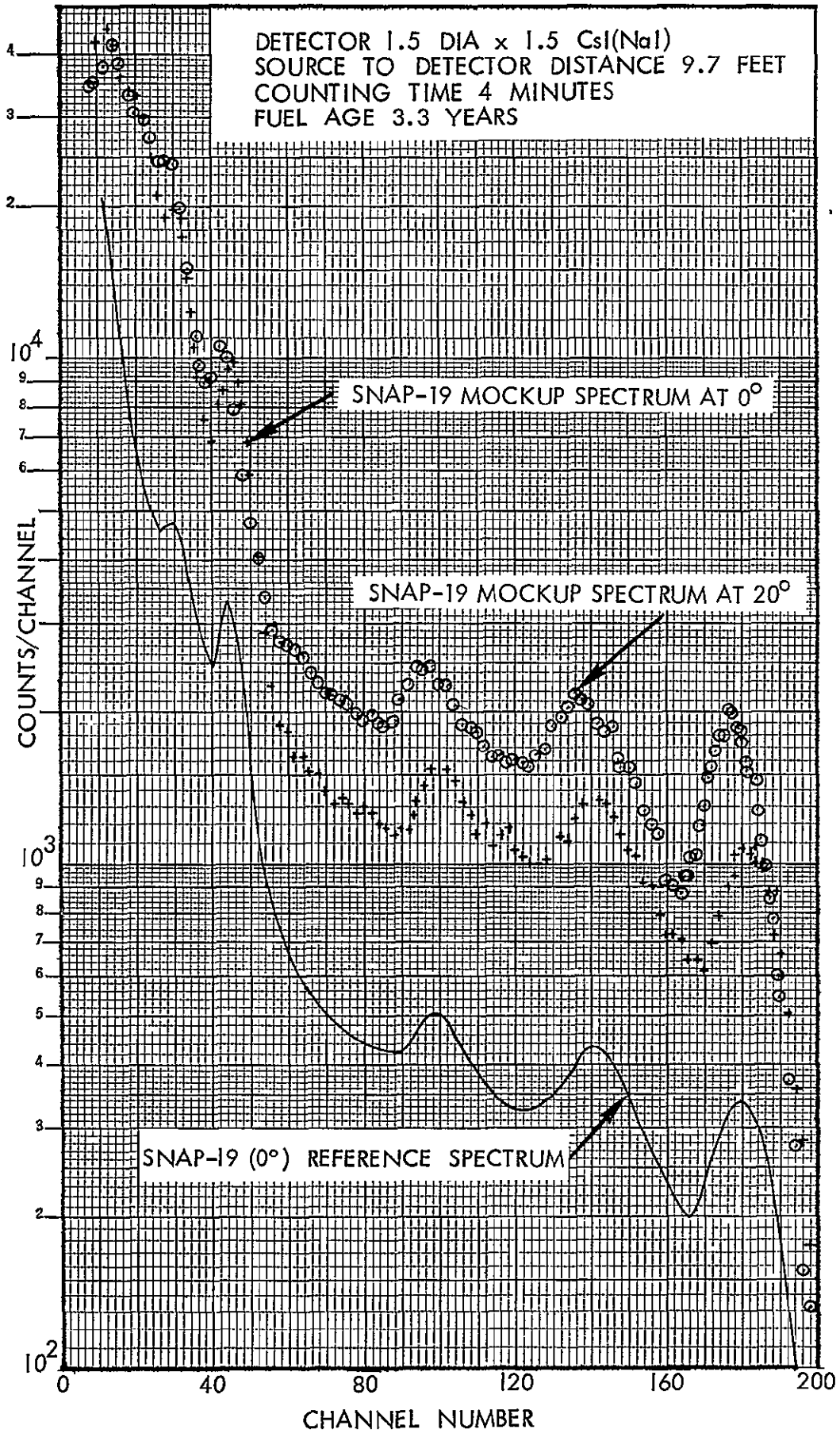

Figure 5-14. SNAP-19 Mockup Spectrum

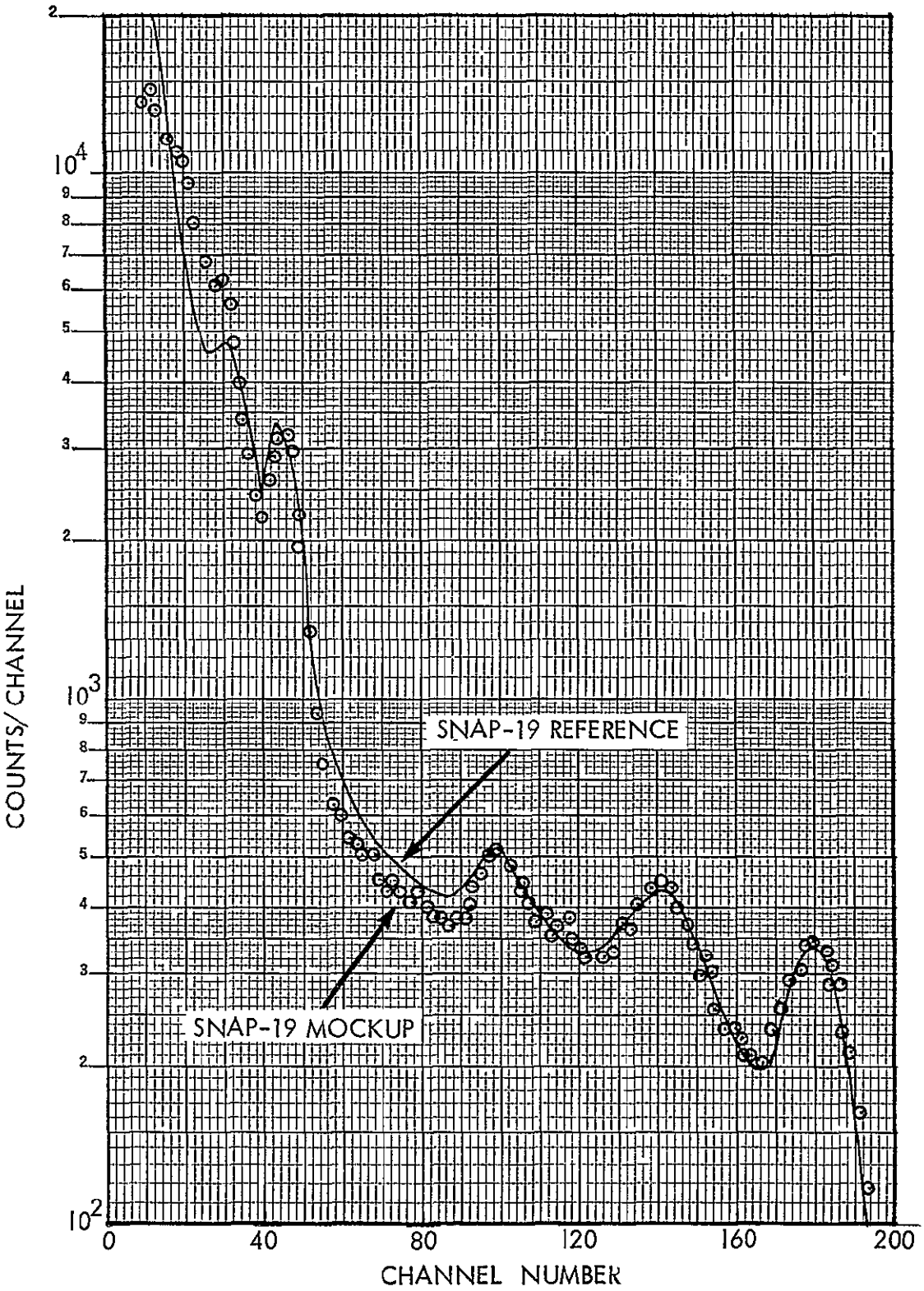

Figure 5-15. SNAP-19 Mockup Gamma Radiation Spectrum Normalized to SNAP-19 Reference Spectrum at 158 Mev (Channel 100)

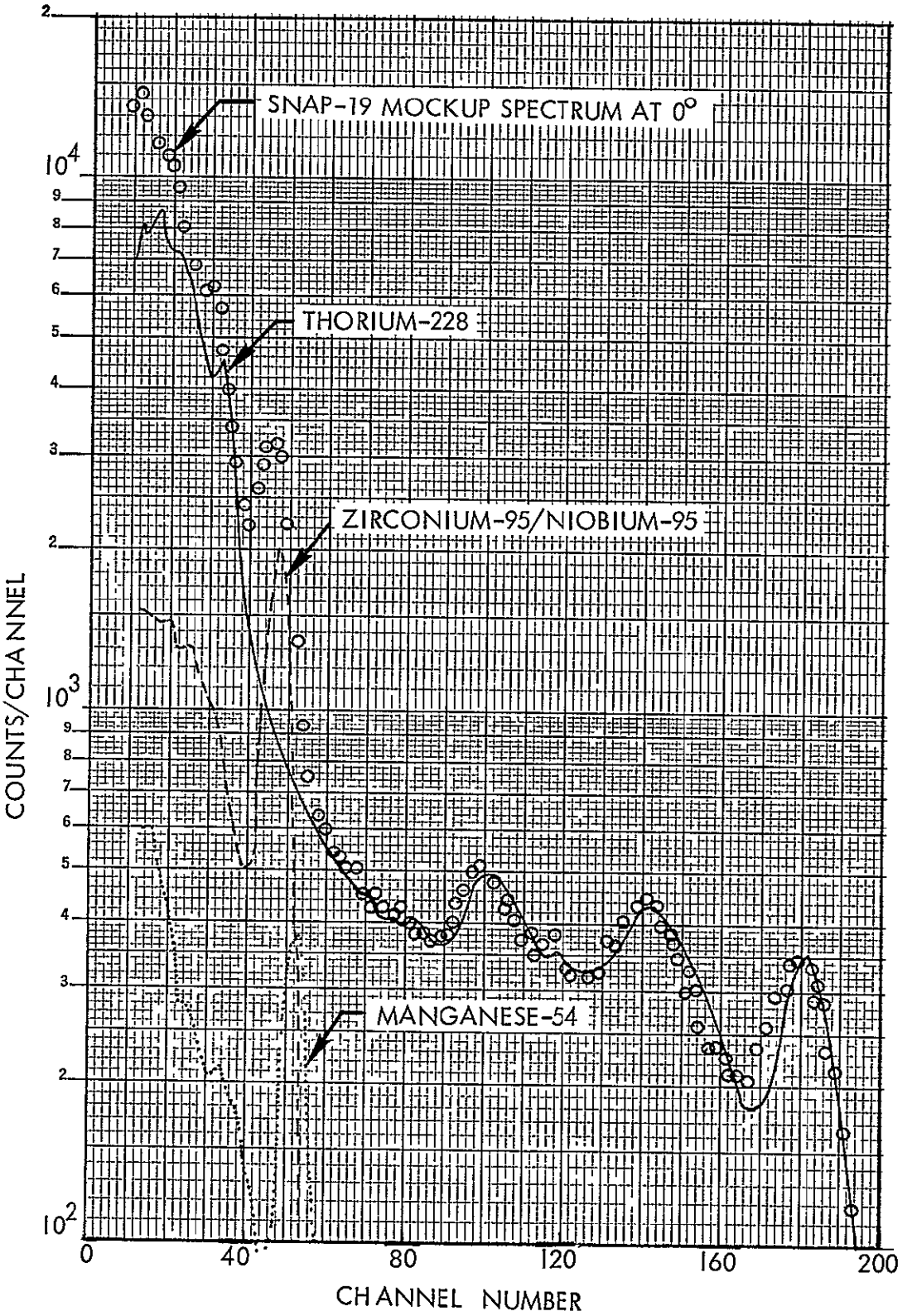

Figure 5-16 Composition of SNAP-19 Source Mockup Gamma Spectrum (Normalized to the Referenced Spectrum)

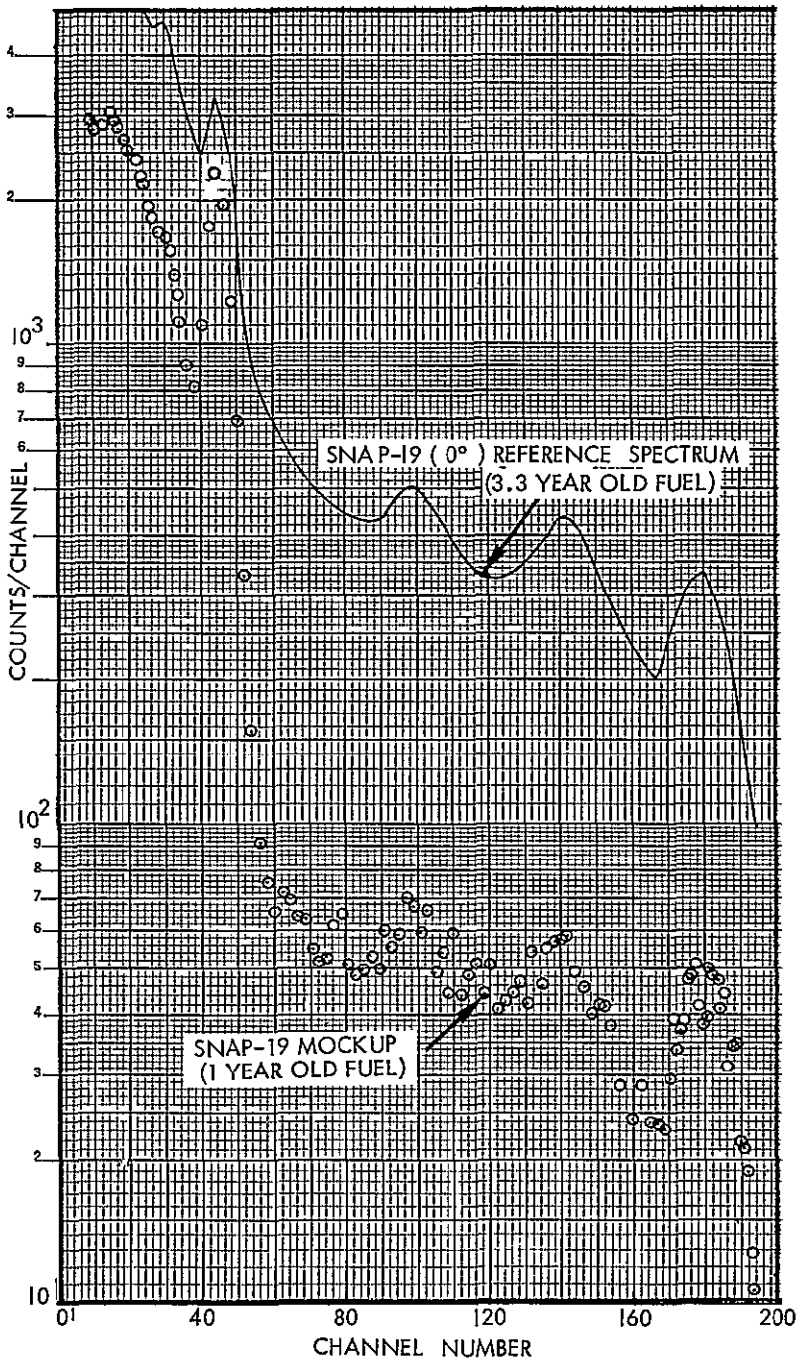

Figure 5-17. SNAP-19 Radiation Mockup Spectrum at 1 Year Age (Normalized to the Referenced Spectrum)

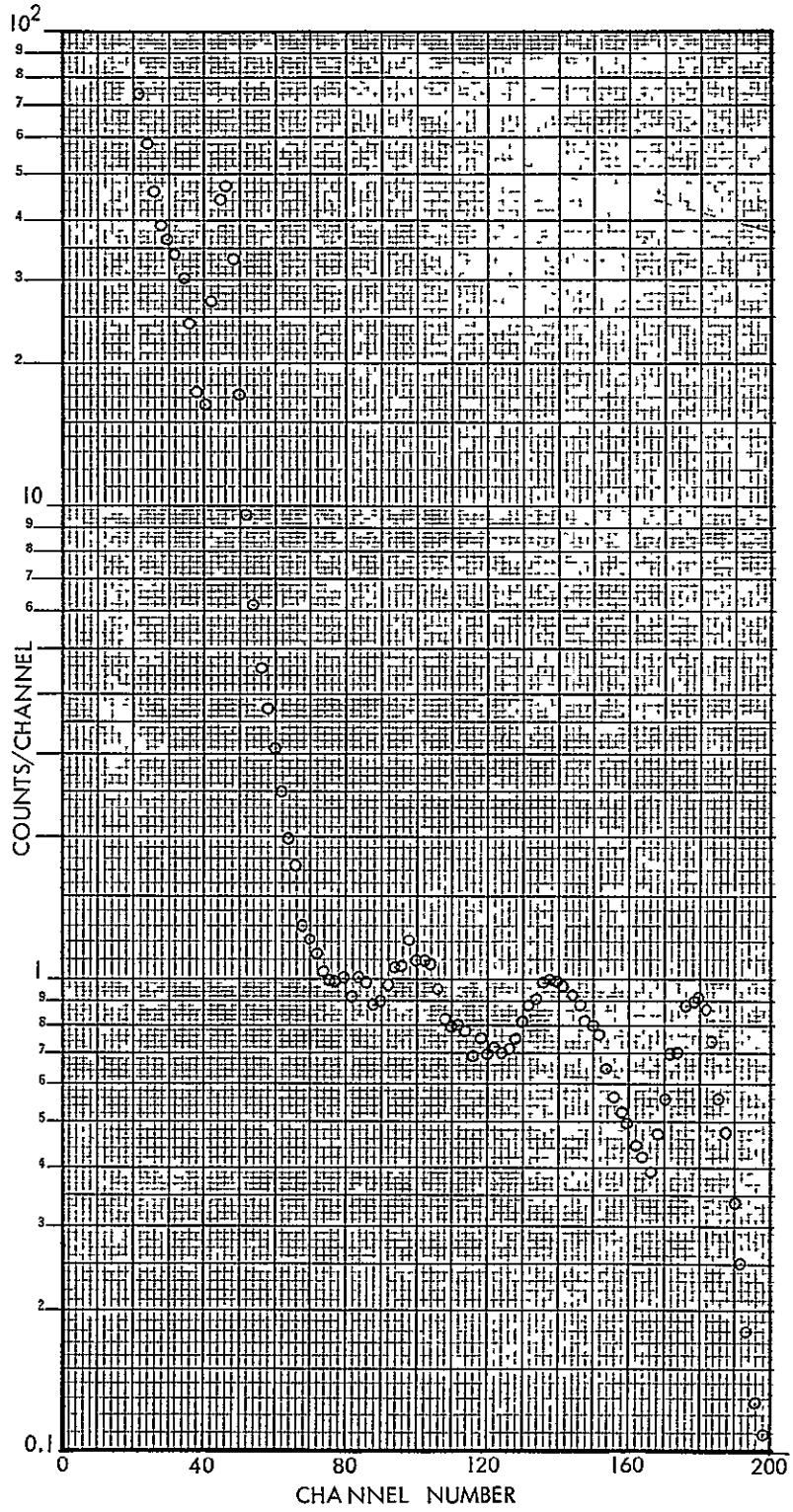

Figure 5-18. RHU Stand-in Radiation Spectrum

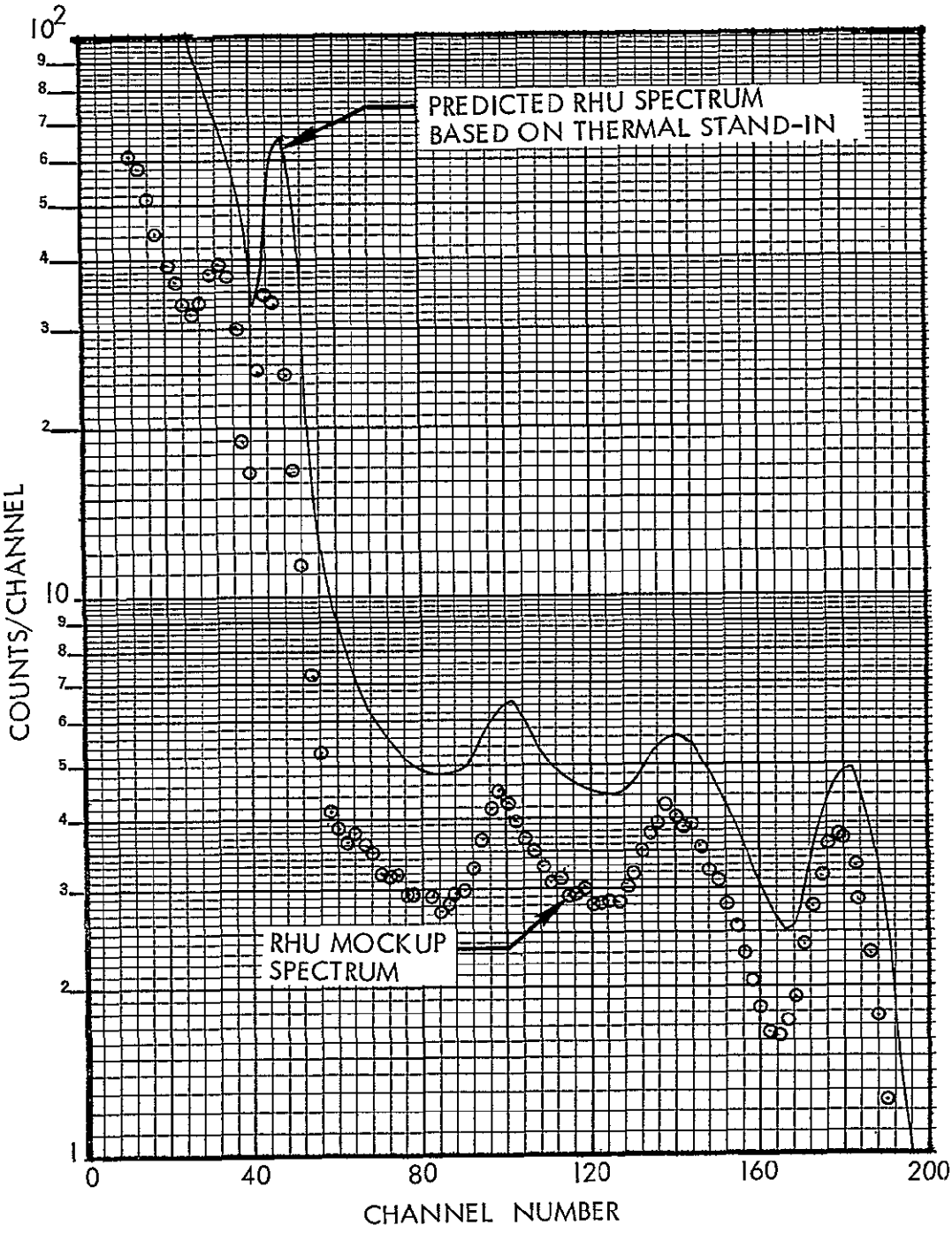

Figure 5-19 RHU Mockup Spectrum Compared to Predicted RHU Spectrum for 3.3 Year Old Fuel.

6.0 SHIELDING THE RTG RADIATION

6.1 DIRECTIONAL RADIATION MAPPING

In order to design minimum weight gamma radiation shields for shielding radiation sensitive detector elements from the RTG radiation it is important to know the relative radiation flux and spectrum incident on the detector as a function of direction. Because the radiation comes from several sources on the spacecraft, the radiation flux passing through a given location in the Pioneer F/G instrument compartment varies considerably with direction. The structure itself scatters and attenuates the radiation, thus modifying the radiation spectrum and flux. For example, the radiation flux from the direction of one RTG is more than ten times greater to the University of Chicago charged particle telescope than from the direction of the other RTG or the RHU's.

The required weight and thickness of radiation shields depend upon the radiation intensity and energy. It can be lessened and optimized by lowering the shield thickness in the direction of lower radiation intensity and concentrating the shield mass in the directions of the more intense radiation.

6.1.1 Radiation Detector Telescope

To measure the directional gamma radiation flux and spectrum at the instrument compartment, a special radiation detector telescope was constructed. It consisted of a 1-1/2 inch diameter by 1-1/2 inch long CsI(Na) Harshaw intergral line scintillation detector mounted in a lead collimator, which restricted the field of view of the detector to 0.087 steradian. Figure 6-1 shows the geometrical characteristics of the telescope assembly. The telescope assembly was designed so it could be rotated about two pivot points in the vertical and horizontal planes in 15° increments to form a matrix of angular directions covering the hemisphere in the direction of the spacecraft body. It was found, however, that considerable counts were caused by radiation leakage through the walls of the collimator and rear of the detector. To compensate for this leakage radiation, a measurement was first made with the collimator hole closed with a 4-inch lead plug and then a measurement was made without the lead plug. Subtracting the first measurement from the second gave the net

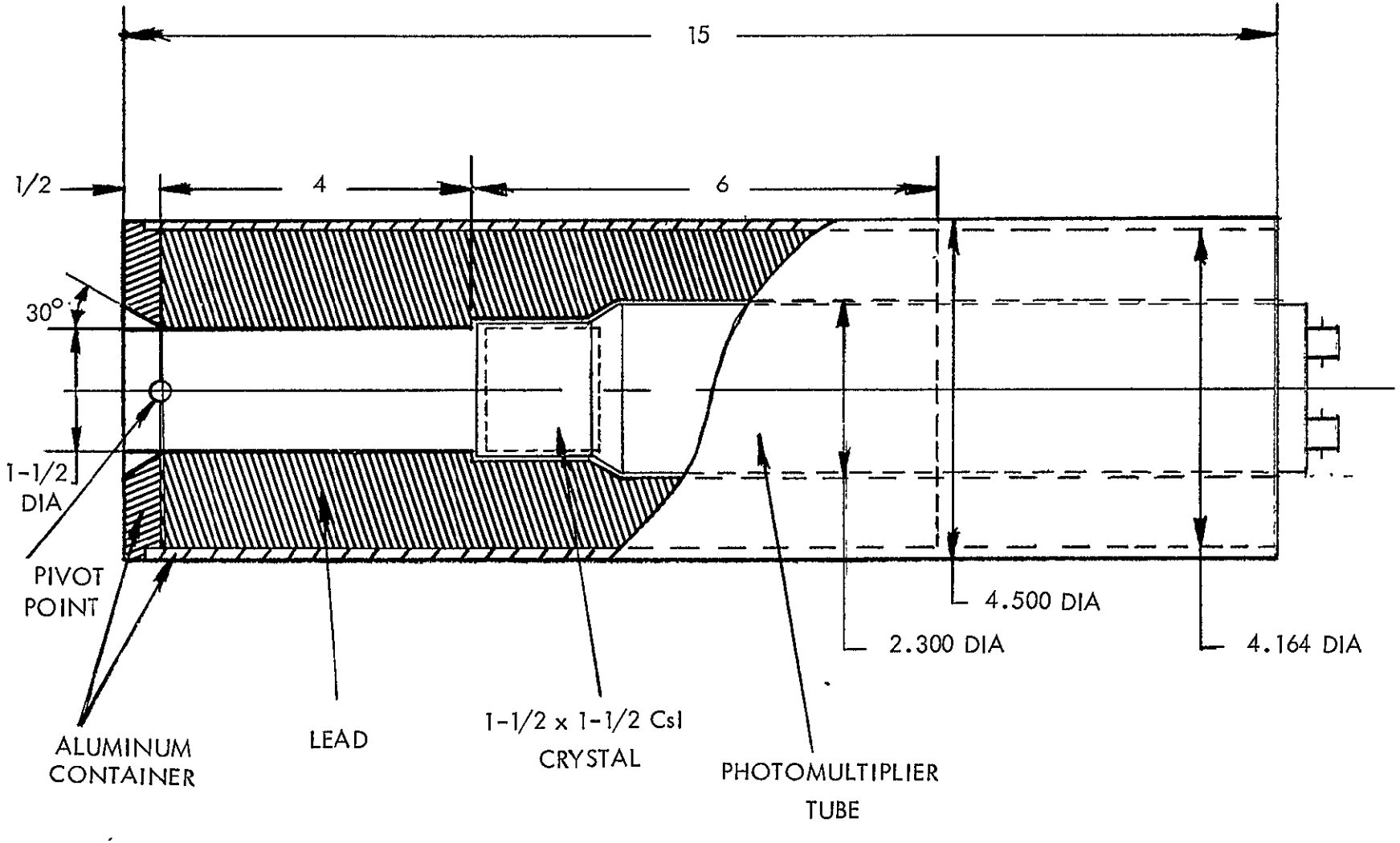

Figure 6-1. Cross Section of Collimated Detector Assembly for Directional Radiation Mapping

counts which entered the detector through the collimator hole. This method compensated for background counts as well as the counts due to scattered radiation entering the sides and the rear of the detector.

Measurements were made in three energy ranges: high, medium, and low. Figure 6-2 shows the energy spectrum of the RTG mockup sources together with the predicted SNAP-19 spectrum. The three energy ranges used for data acquisition and corresponding channel numbers to the spectrum of Figure 6-2 are as follows:

High Range - 1.30 to 5.00 Mev - channels 80 up
Middle Range - 0.67 to 1.30 Mev - channels 40 to 80
Low Range - 0.20 to 0.67 Mev - channels 10 to 40

The high range represents primarily direct radiation from the sources. Scattered radiation becomes more significant in the middle range and is most significant in the low range.

The block diagram of the electronic system used for data acquisition during the directional radiation mapping of the spacecraft mockup and instrument compartment is shown in Figure 6-3. The scintillation detector was coupled to two spectrometer systems, a booster amplifier, and a single channel analyzer and scaler. Also, a multichannel analyzer and a pulse generator were included in the system to facilitate the calibration of the single channel analyzers. Each spectrometer was calibrated to accumulate counts over a fixed energy range, one for the low range, one for the middle range, and one for the high range. The amplifier was used to boost the signal and shape it for the Hamner single channel analyzer, which was operated in the integral mode to accumulate pulses in the high range from 1.30 Mev up to the saturation level of the amplifier (5.00 Mev). The multichannel pulse height analyzer and the pulse generator were used for calibration of the spectrometer window locations.

6.1.2 Angular Efficiency of Collimator

The angular efficiency of the collimator was measured by aligning one of the RTG mockup sources with the center line of the collimator and then moving the source in an arc. Data were taken with and without the collimator

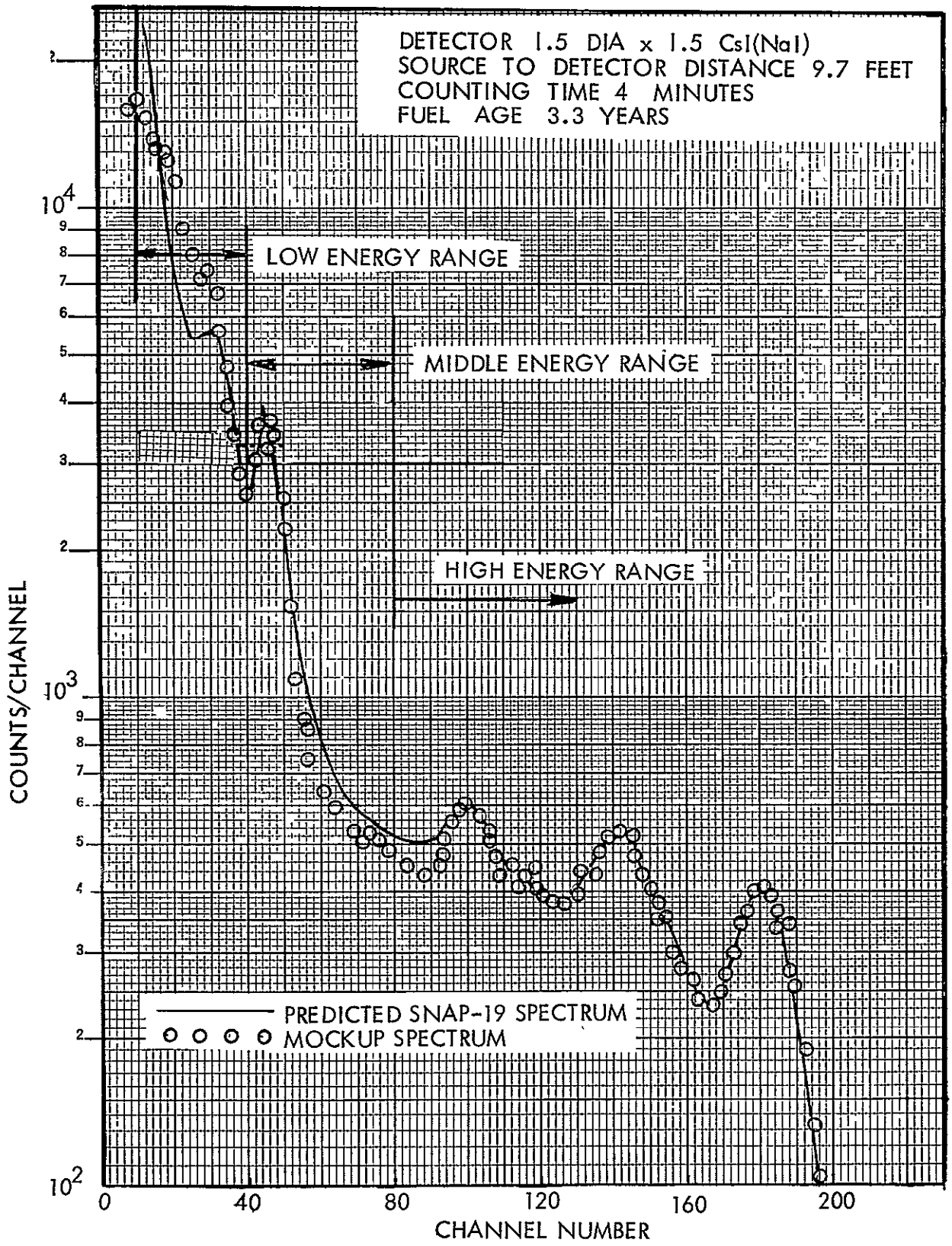

Figure 6-2. Gamma Radiation Spectrum of RTG Mockup Source Normalized to Predicted SNAP-19 Spectrum

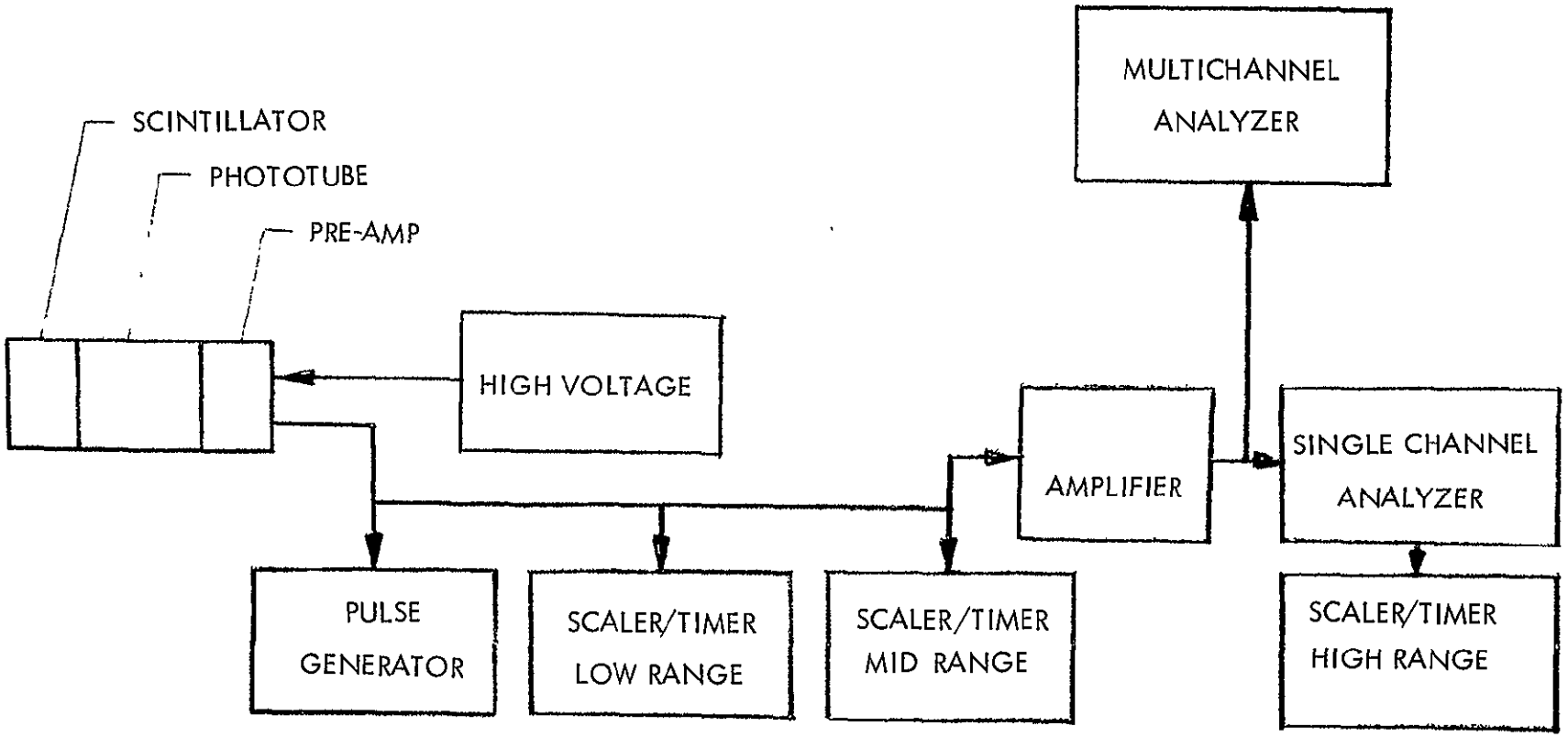

Figure 6-3. Block Diagram of Detection System Used For Directional Radiation Mapping

plug to compensate for the facility scatter of radiation as described above. Count rates were recorded over three energy ranges. The results for the high energy range are given in Figure 6-4 and show the response of the detector as a function of the angular displacement of the source. The angular response of the system in the middle and low energy ranges was essentially identical to that shown in Figure 6-4.

6.1.3 Mapping of the Spacecraft Mockup

The telescope system was located next to the spacecraft mockup as shown in Figure 6-5. The horizontal and vertical pivot points for movement of the telescope are indicated. Additional shielding to reduce the radiation entering the side of the detector from one of the RTG's is also seen. Mockups of the instrument boxes of the GFSC/McDonald and ARC/Wolfe experiments are shown just to upper right of the collimator support.

Figure 6-6 shows the overall view of the facility and the experimental setup. The spacecraft mockup was held by a hoist at a height of 9-1/2-feet from the bottom of a 4-foot deep pit and 7-feet from the near edge of the pit. The opening of the collimator was positioned just outside the location of the University of Chicago charged particle telescope. The RTG and RHU mockup sources were installed in their proper location. As described above, the counts were taken for three energy ranges. The setup is shown schematically in Figure 6-7, illustrating the orientations of the collimated detector. At the coordinate of 90° horizontal and 0° vertical, the collimator is directed straight up toward the antenna. At 90° horizontal, 180° vertical, the collimator is directed straight down at the facility floor. Counts were only taken in the direction of the spacecraft.

The location of the sources relative to the collimator are given in Table 6-1.

The count rates as a function of azimuth and elevation angles in 15° increments for the three energy ranges are given in Table 6-2. The horizontal angle positions are listed in Table 6-2 along the top and the vertical angle positions along the side. The count rates, in counts per second for each energy group, are listed in the appropriate spaces.

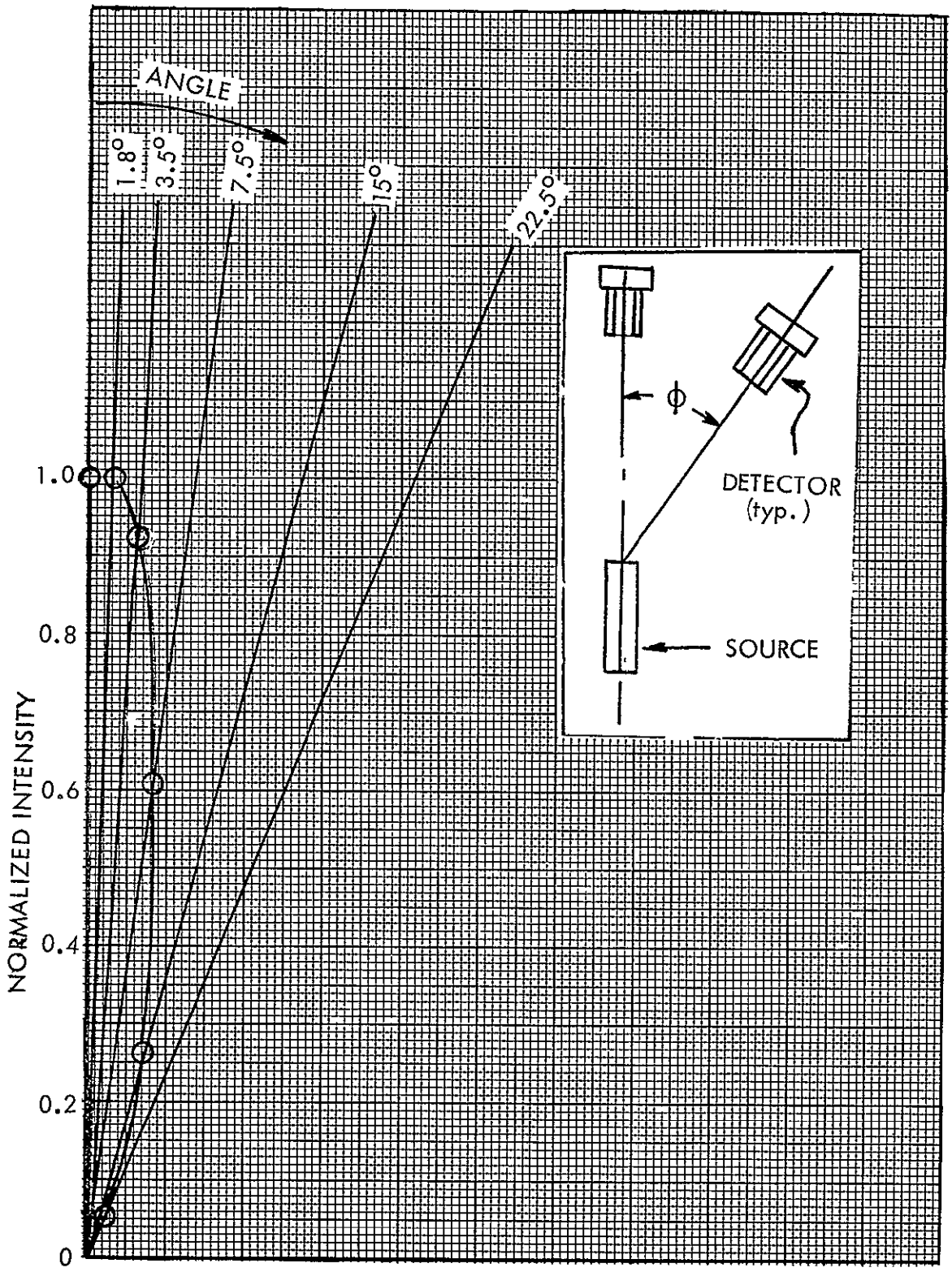

Figure 6-4. Angular Response of Collimated Detector for Pioneer F/G Mockup Directional Radiation Map

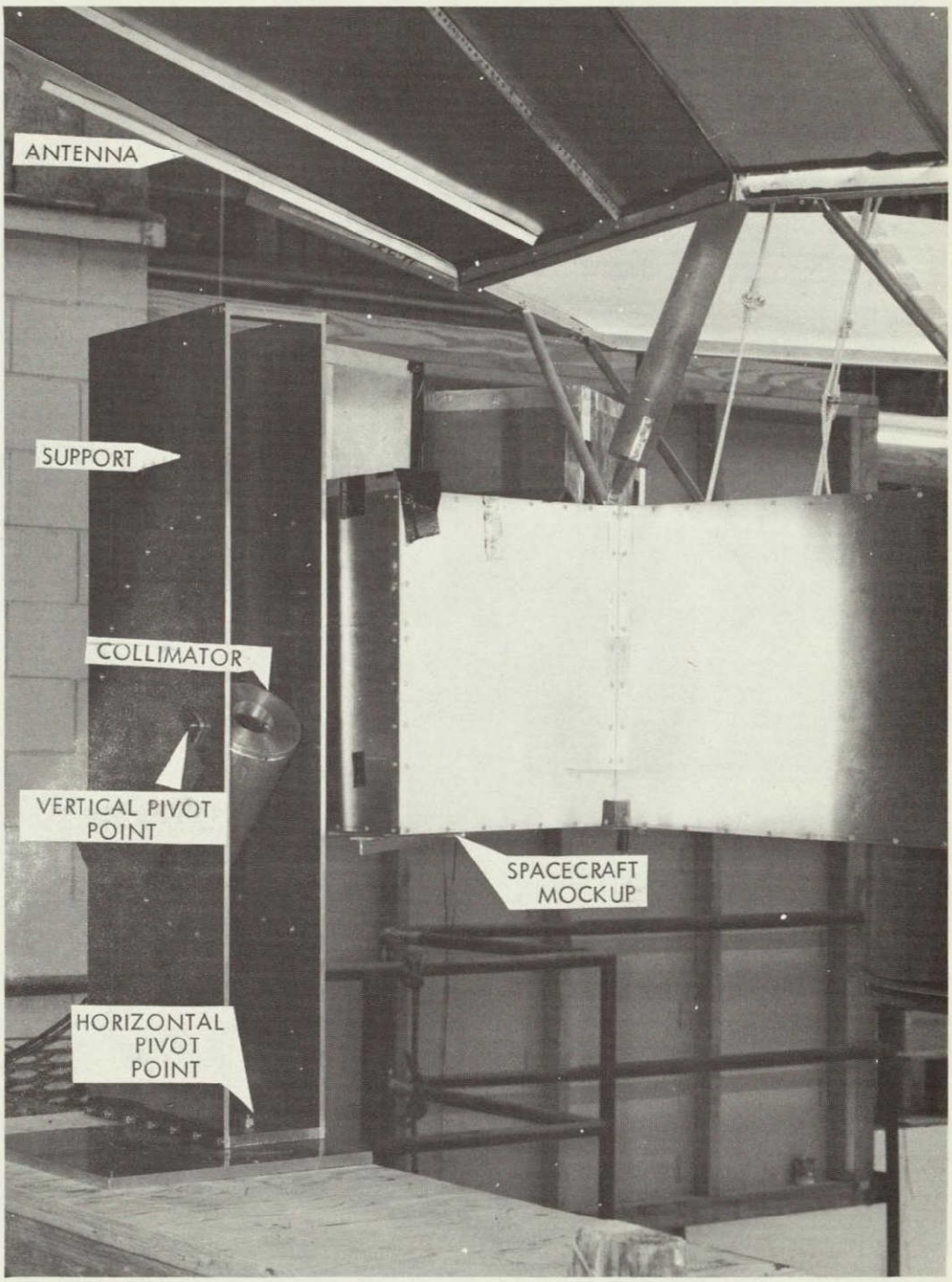

Figure 6-5. Collimator used for Directional Radiation Mapping of Pioneer F/G Spacecraft Mockup

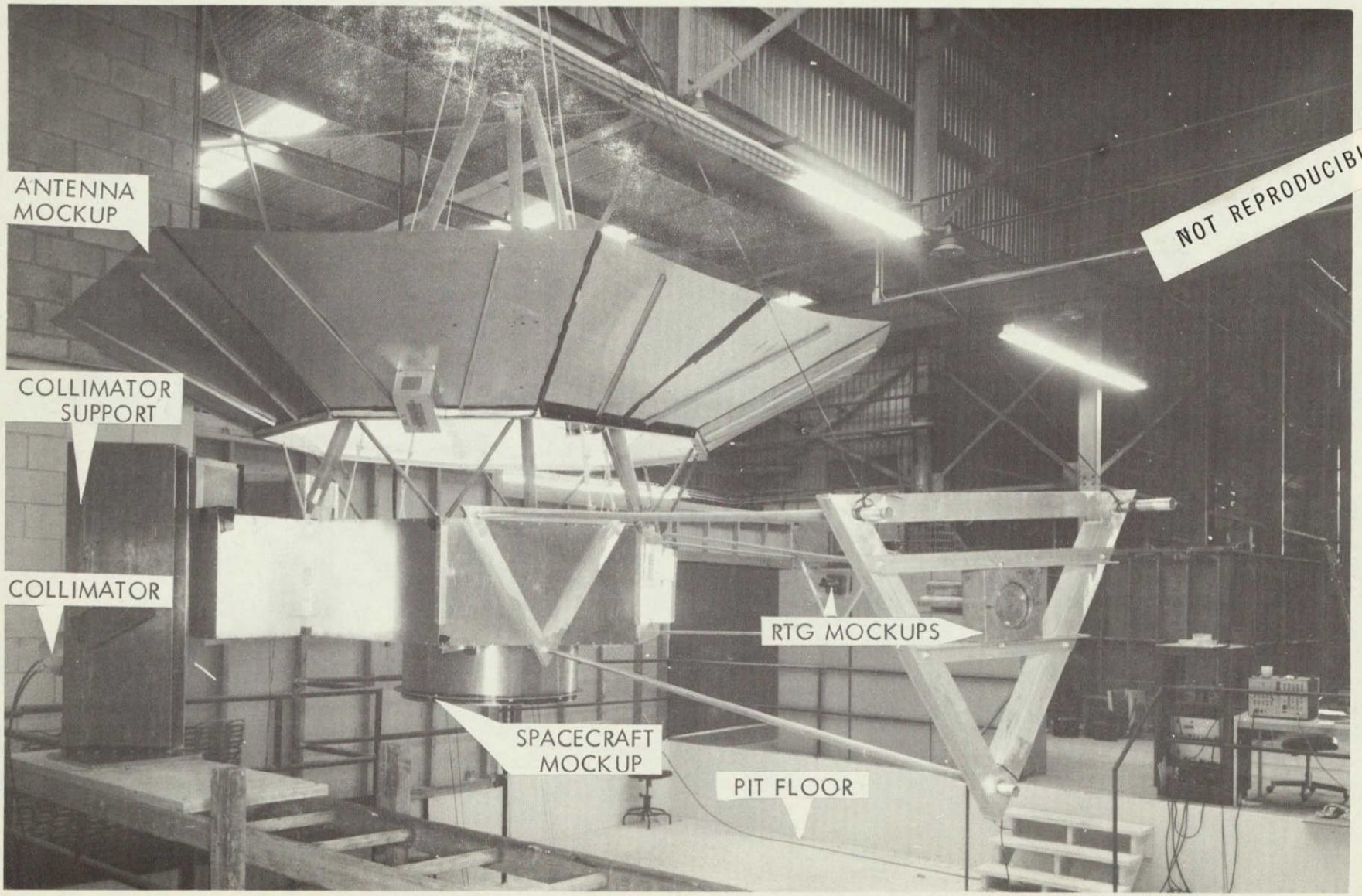

Figure 6-6. Test Setup for Directional Radiation Mapping

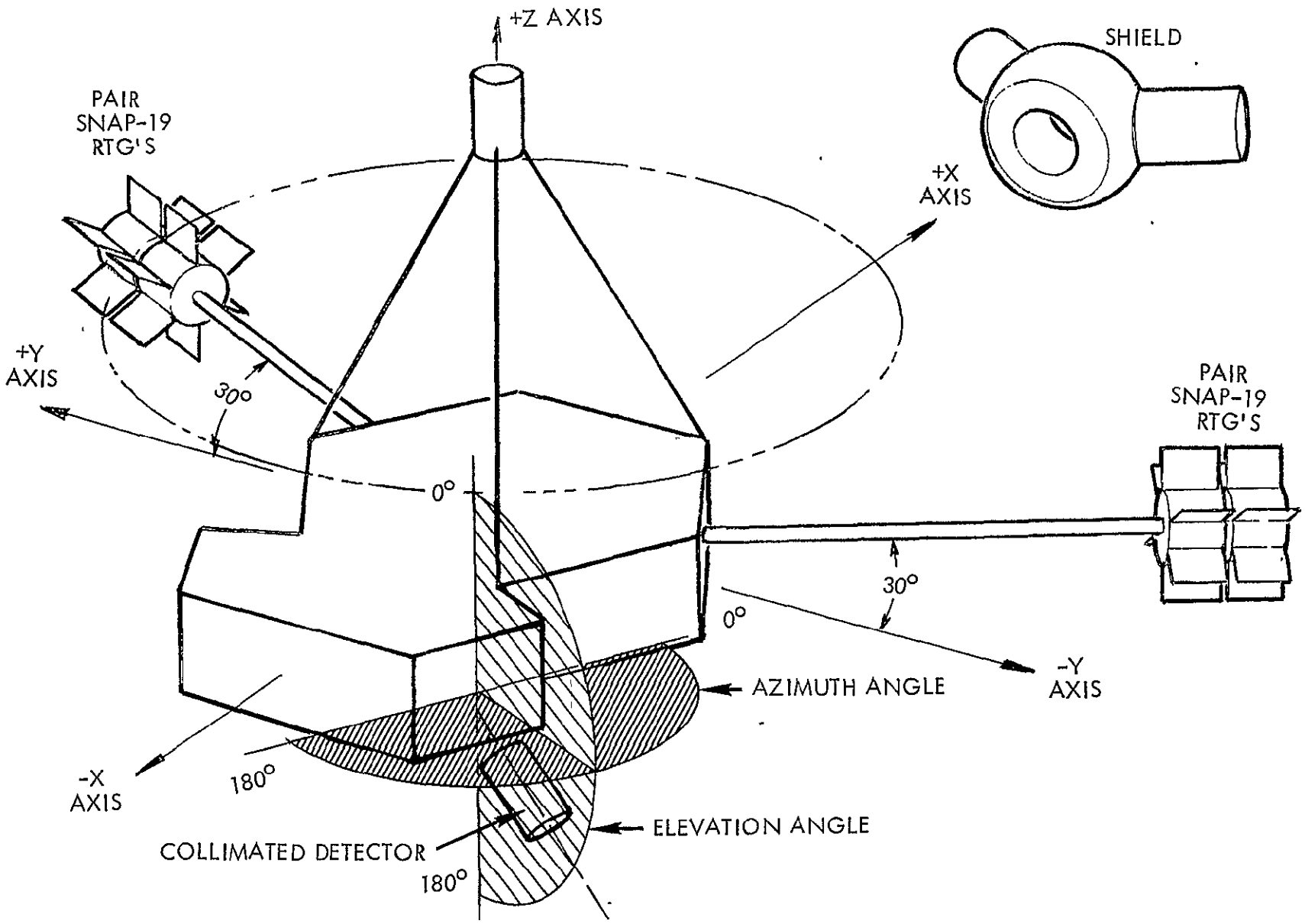

Figure 6-7. Pioneer F/G Spacecraft Radiation Mapping Test Set-up

Table 6-1. Location of Pioneer F/G Gamma Ray Sources Relative to Collimator

	Horizontal Angle	Vertical Angle
+Y Axis RTG	0°	90°
Propellant Tank RHU	75°	90°
Thruster RHU's	0°	60°
Sun Sensor and Thruster RHU's	105°	75°
-Y Axis RTG	90°	90°

Table 6-2. Directional Radiation Count Rate Data for Pioneer F/G Mockup at the University of Chicago Telescope Location, Counts per Second (3.3 Year RTG and RHU Fuel).

Energy Group, Mev	Horizontal Angle													Vertical Angle
	0°	15°	30°	45°	60°	75°	90°	105°	120°	135°	150°	165°	180°	
1 30-5 0 0 67-1 30 0 20-0.67							1 - 6	3 4 12	- 2 7	- 2 2	- - 4			0°
			- 1 3	- 1 3	- 1 4	- 1 5	- 1 4	- - 4	- 1 3					15°
			4 6 11	- - 5	- - -	- 1 4	1 - 4	1 - 4	- - 5	- 1 6				30°
		11 9 15	- 1 4	- - 4	1 1 4	1 1 4	- 1 4	1 1 5	- 1 5	- - 5	- - 4			45°
	17 20 41	- 1 5	1 2 4	- 1 4	1 2 6	1 2 6	1 2 5	1 2 6	- 1 6	- 1 4	- - 3			60°
	100 142 390	26 34 105	2 2 4	- 2 7	6 2 8	3 5 13	28 22 43	3 4 12	- 1 6	- 1 4	- 4 4			75°
	306 494 1120	44 72 374	10 14 23	1 3 10	1 3 12	11 10 23	38 31 42	6 6 18	1 2 10	- 1 7	- - 5	- - 6	1 - 8	90°
	69 119 340	16 29 90	1 1 7	1 2 10	1 2 10	3 4 18	9 7 20	4 3 15	1 1 9	- 1 7	- 1 6	1 - 8		105°
	6 15 56	7 11 43	- 1 10	- 1 12	1 2 13	1 1 13	- 1 13	1 1 12	1 1 9	- 1 7	- - 6			120°
			- 1 13	- 1 15	- 1 16	1 1 16	1 1 17	1 1 14	- 1 11	1 1 11				135°
							- 1 18							150°

Figure 6-8 shows polar plots at 90° vertical angle for the three energy ranges. Higher count rates are visible in the directions of the RTG mockups, as would be expected. However, the attenuation of radiation from the RTG mockup located on -Y axis is somewhat greater than was anticipated. Figure 6-9 shows a polar plot at 0° horizontal angle for gamma radiation of 0.20 to 0.67 Mev. Some indication is seen of the RHU mockup at 60° vertical. No readily discernible radiation was detected from the RHU mockup installed on the tank.

As described above, the count rates in Table 6-2 should be high by about 10 to 20 percent because of the contributions of facility scattered radiation. Facility scatter can be seen in the low energy range in the measurements made at 120°, 135° and 150° vertical angle, and at 0° vertical angle. The scatter at 120°, 135° and 150° vertical angles is from the florr of the facility.

The data of Table 6-2 can be used to design a minimum weight shield, such as illustrated in the upper right corner of Figure 6-7, for a radiation detector at that location.

6.1.4 Mapping of the Instrument Compartment

Radiation mapping of the Pioneer F/G instrument compartment was performed by placing an unshielded 1.5 x 1.5 dia. CsI scintillation detector at selected locations and accumulating counts over the same three energy ranges as described previously. Due to limitations of space it was not practical to perform directional mapping in the instrument compartment.

The contribution of facility-scattered radiation was measured by placing the detector and two sources on the low mass boom described in Section 5.1, shielding the detector from direct radiation from the sources, and measuring the remaining radiation. During the measurements of unshielded radiation the RTG and RHU mockup sources were installed in their normal locations. For the measurements of facility scatter the RHU mockups were not included because their contribution to facility scatter is negligible. The facility-scattered radiation contributed from 10 to 20 percent of the radiation observed at the spacecraft in the low energy range, from 1 to 6 percent in the middle energy range, and from 0.1 to 0.5 percent in the high energy range, depending on the location.

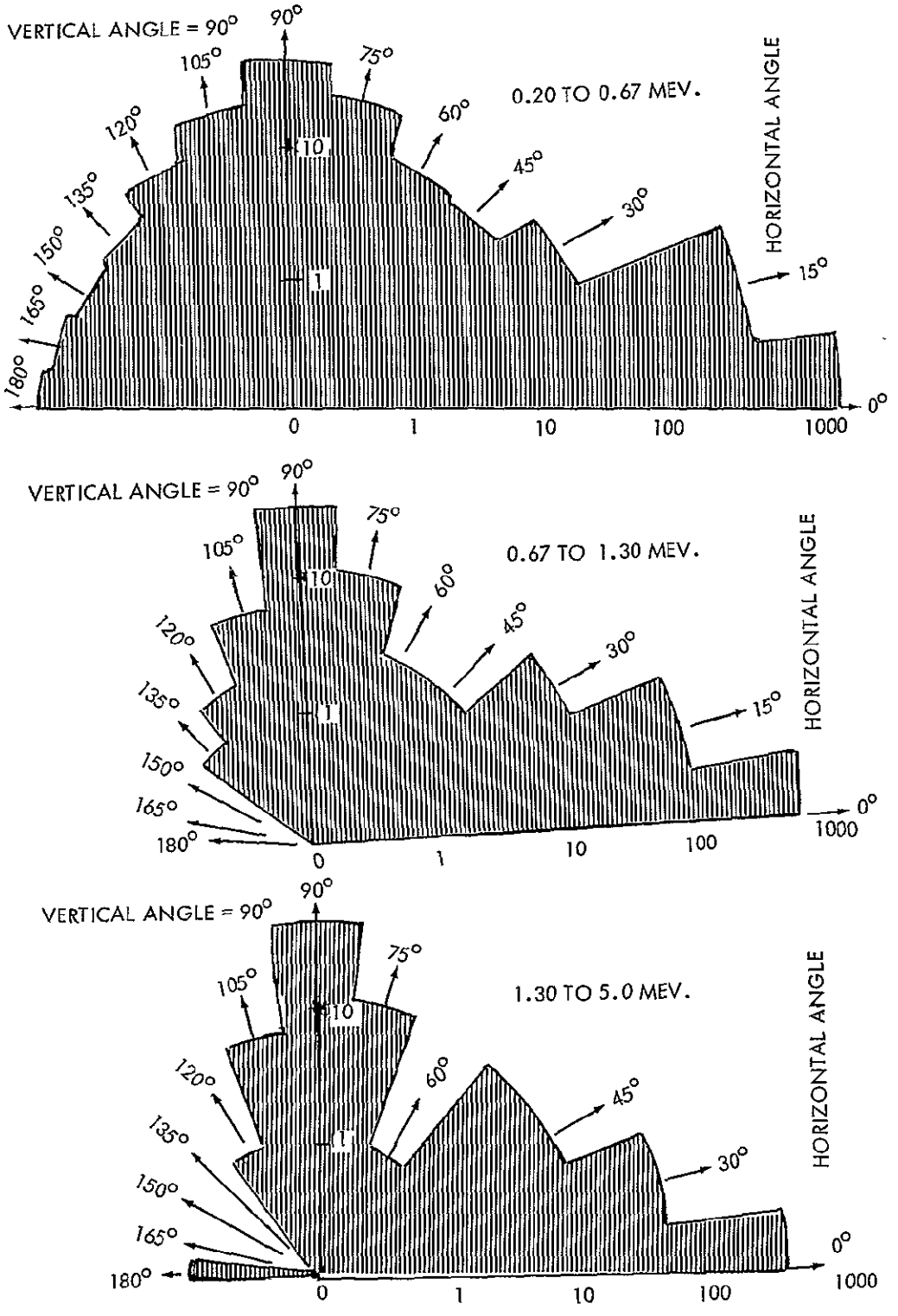

Figure 6-8. Polar Plots of Gamma Radiation at University of Chicago Telescope Location for Three Energy Levels, Counts per Second

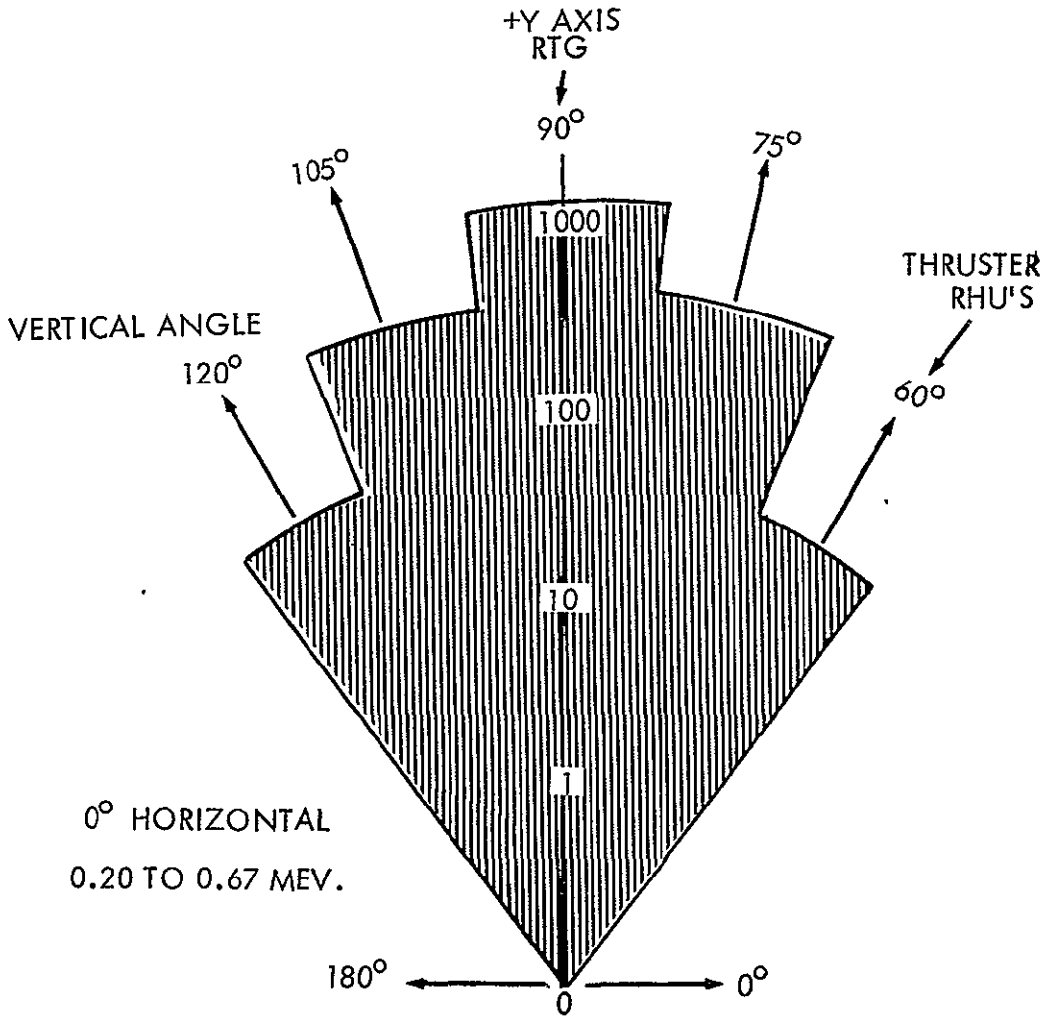

Figure 6-9. Polar Plot of Gamma Radiation in Pioneer F/G Mockup at the University of California Telescope Location, counts per second

The eleven locations of measurement are shown in Figure 6-10 and the results of the radiation mapping points, corrected for facility scattered radiation, are given in Table 6-3.

Table 6-3. Measured Relative Radiation Intensity of Mockup of Pioneer F/G Spacecraft, Counts per Second

Location	Experiment	Energy Range, Mev		
		0.200 to 0.670	0.670 to 1.30	1.30 to 5.00
1	Simpson	3090	920	690
2	Fillius	2400	830	690
3	Fillius	3790	1215	785
4	Smith-Judge	2940	900	660
5	Van Allen	2200	750	690
6	Gehrels-Kinard	4370	1460	1030
7	-	2210	460	310
8	Munch	3690	1030	700
9	Wolfe	4070	1200	780
10	McDonald	3210	1090	820
11	Soberman	7360	3370	2790

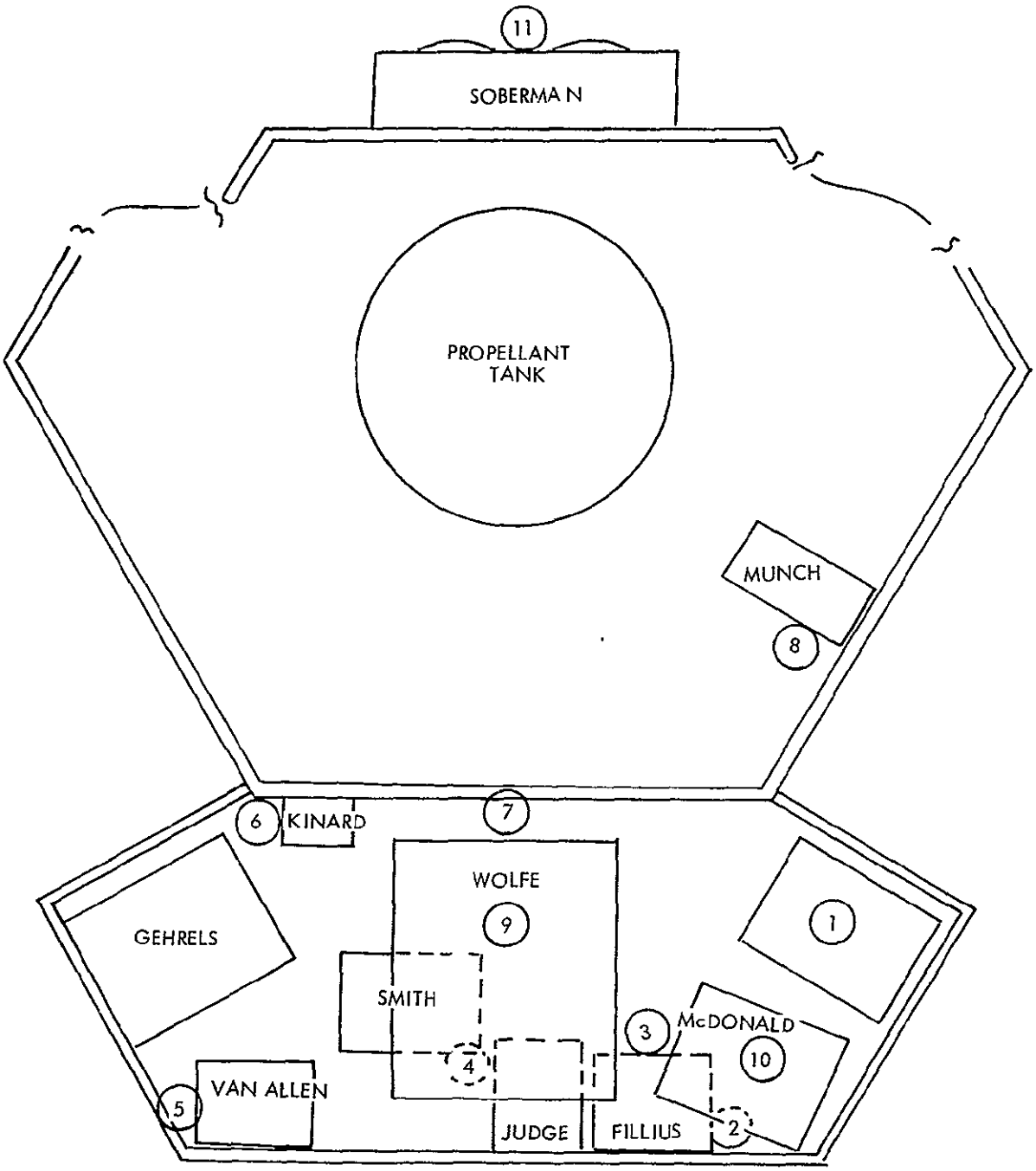

Figure 6-10. Radiation Intensity Map of Pioneer F/G Spacecraft Mockup

6.2 ABSORPTION DATA

The absorption of SNAP-27 fuel capsule radiation by Pb, Cu, W, and depleted U was measured as part of the Countermeasure Investigation (Section 2.2. of the Phase II Revised Statement of Work). The purpose of these measurements was to evaluate the effectiveness of these materials as radiation shields for use on the Pioneer F/G spacecraft. A 1.5- by 1.5-inch diameter CsI(Na) scintillation crystal and a 2-mm thick by 0.8-cm^2 semiconductor detector were used as the detectors. The absorption and scattering data for the CsI(Na) detectors are presented below.

6.2.1 Scattered Radiation Determination

Prior to conducting the absorption tests, the effects of scattered radiation from the facility were investigated in detail. The significance of the scattered radiation is that it enters from the sides and the rear of the detector and reduces the effectiveness of the absorbers. In space, scattered radiation will be much lower than in the laboratory, so that the effective absorption of a shield material will be closer to the ideal narrow-beam absorption.

In order to measure the magnitude of the scattered radiation, the CsI crystal was placed 135 cm from the end of the SNAP-27 fuel capsule and shielded on the sides and top by 2- by 4- by 8-inch lead bricks and on the bottom by a 1/2-inch-thick lead plate. A 1-inch diameter hole was drilled in the top brick to form a collimator and the 3- by 3-inch square absorber discs were placed over the hole to attenuate the direct radiation from the SNAP-27 fuel capsule to the detector. The fuel capsule was oriented with the long axis pointing towards the detector as shown in Figure 6-11 to approximate the SNAP-19 radiation spectrum. To minimize scatter the entire detector and shielding assembly was located on the low mass floor in the Radiation Research Facility above a 20 by 20 by 10-ft deep pit.

The electronics system used with the CsI(Na) crystal consisted of a Technical Measurements DS-13 preamplifier, a Hamner Na-11 RC clipped amplifier, a Victoreen PIP-400 multichannel pulse height analyzer, and a

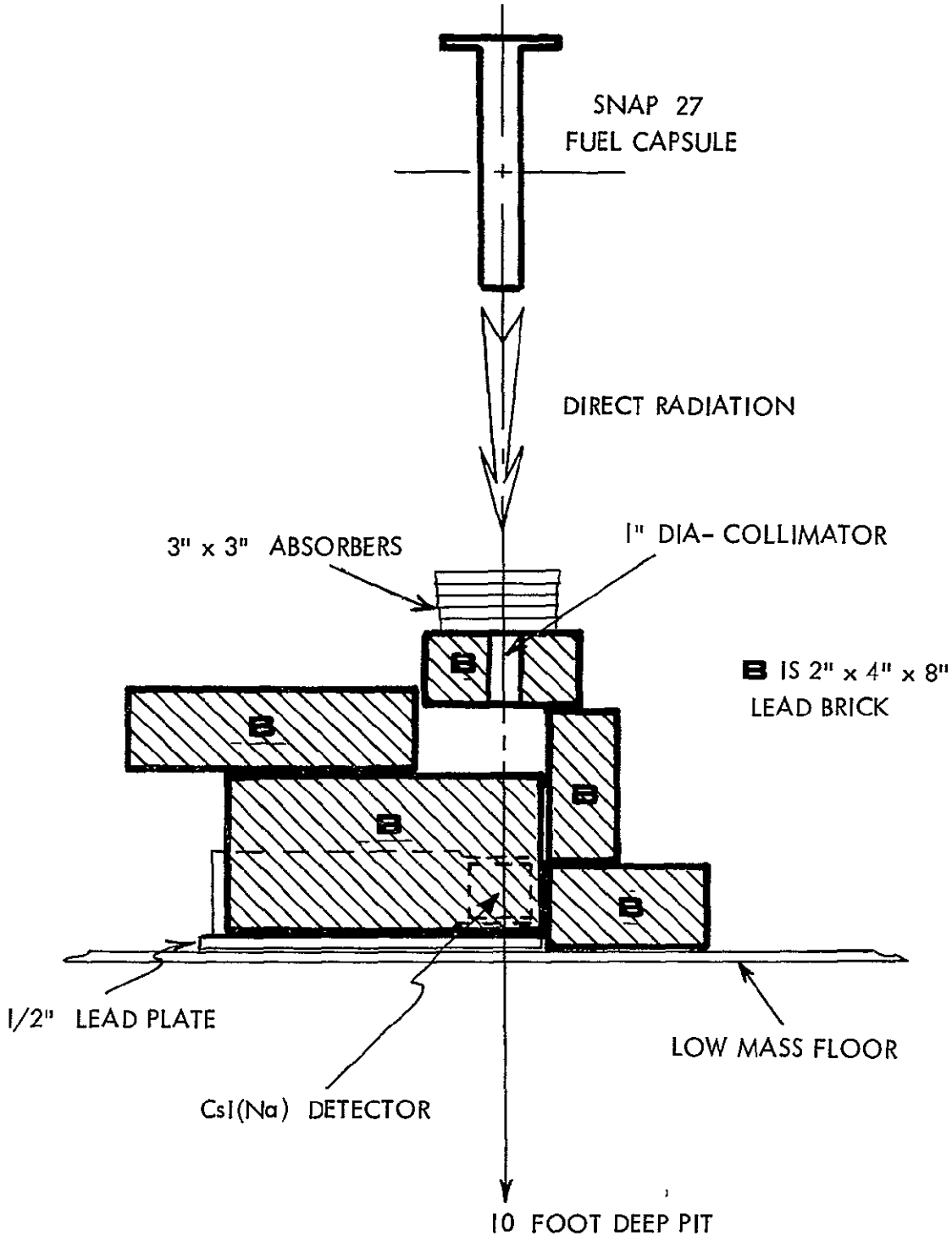

Figure 6-11. Schematic Diagram of Radiation Absorption Experimental Setup

Fluke high voltage power supply. Calibration was accomplished using the SNAP-27 fuel capsule radiation peaks whose energy values had been previously established.

The scattered radiation was measured by covering the 1-inch collimator hole and increasing the thicknesses of lead absorber until the addition of more lead had no appreciable effect on the signal. A lead thickness of 8.8-inches was found to be adequate. At this thickness it was assumed that all the count rate seen by the detector was no longer from direct radiation passing through the absorber, but was produced by scattered radiation from the sides and rear of the detector. The scattered radiation component percentage of the signal at zero absorber thickness for each energy range is given in Table 6-4.

Table 6-4. Scattered Radiation Component of Total Radiation Measured by CsI(Na) Scintillator

Energy Range	Percent
2600 ± 100 Kev	8
787 ± 100 Kev	11
200 to 3250 Kev	16

6.2.2 Absorber Effectiveness

The effectiveness of lead, copper, depleted uranium and tungsten for shielding the SNAP-27 fuel capsule radiation was measured. Lead, copper, and uranium absorbers of thickness ranging from 1/8 inch to 1/2 inch were cut into 3- by 3-inch square plates. The tungsten alloy absorbers were 2- by 3-inch rectangular plates of thicknesses ranging from 1/8 inch to 1/2 inch. The area weight of each piece was found by measuring the area and weighing each absorber. The lead was 100 percent natural lead with a density of 11.3 g/cc; the tungsten alloy was 90 percent W, 6 percent Ni, and 4 percent Cu, with a density of 16.7 g/cc; the copper was unalloyed copper with a density of 8.9 g/cc; and the uranium was uranium-238 depleted to less than 0.22 percent uranium-235 with a density of 18.8 g/cc.

6.2.2.1 Measurements with CsI Detector

The absorption data were obtained by recording the spectrum using a pulse height analyzer for each absorber thickness. The absorption data were analyzed at 2600 kev, 810 kev, and over the energy interval from 200 to 3250 kev. The detector was located 135 cm from the midplane of the SNAP-27 fuel capsule with the detector aligned along the axis of the fuel capsule as shown in Figure 6-11. Since the scattering was shown to be a significant fraction of the count rate, the data for the absorption curves were obtained by recording the count rate and spectrum as a function of absorber thickness and subtracting the scattered radiation component.

The data for Pb, W, and Cu absorption of the RTG radiation are presented in Figures 6-12 through 6-13. Agreement between theoretical absorption and the measured values is quite good.

The absorption measurements of depleted uranium were complicated by the presence of natural radiation which contributed a significant amount to the count rate. The radiation contributed by the depleted uranium was measured by first counting the uranium absorbers. This radiation was then subtracted from the measurements made with the SNAP-27 fuel capsule. Figure 6-14 shows the absorption characteristic of depleted uranium with and without its natural radiation. In a theoretical sense, depleted uranium is an excellent absorber because of its high atomic number and high density, but in practice its natural radiation acts to reduce its effectiveness.

The explanation for the curvature of the uranium slope in Figure 6-14 is the natural radiation. The natural radiation acts as a source located in the absorber that increases its percentage contribution to the total signal as the direct radiation from the fuel capsule is reduced by the increasing absorber thickness.

A similar effect may explain the W absorption data where the source of gamma radiation may be due to neutron collisions in the tungsten. Gamma rays produced by such neutron reactions would act very similarly to the naturally occurring radiation of uranium discussed above.

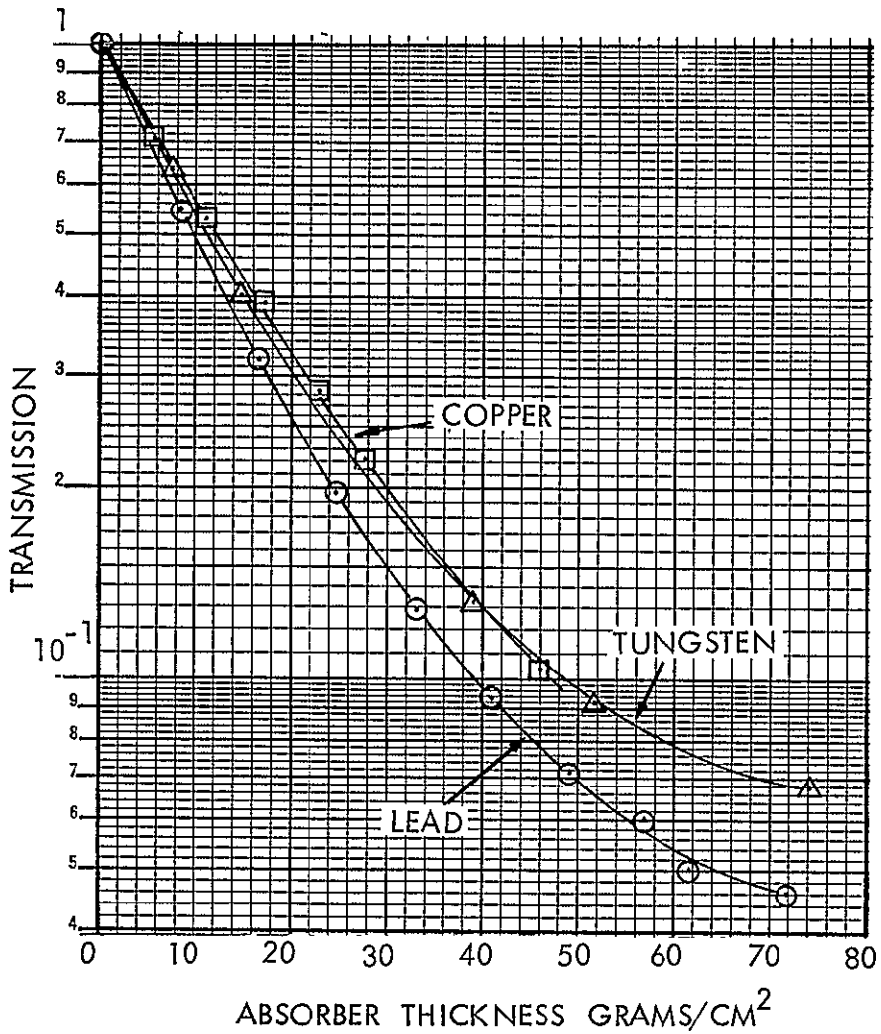

Figure 6-12. Attenuation of SNAP-27 Radiation Energy Range 767 ± 100 kev.

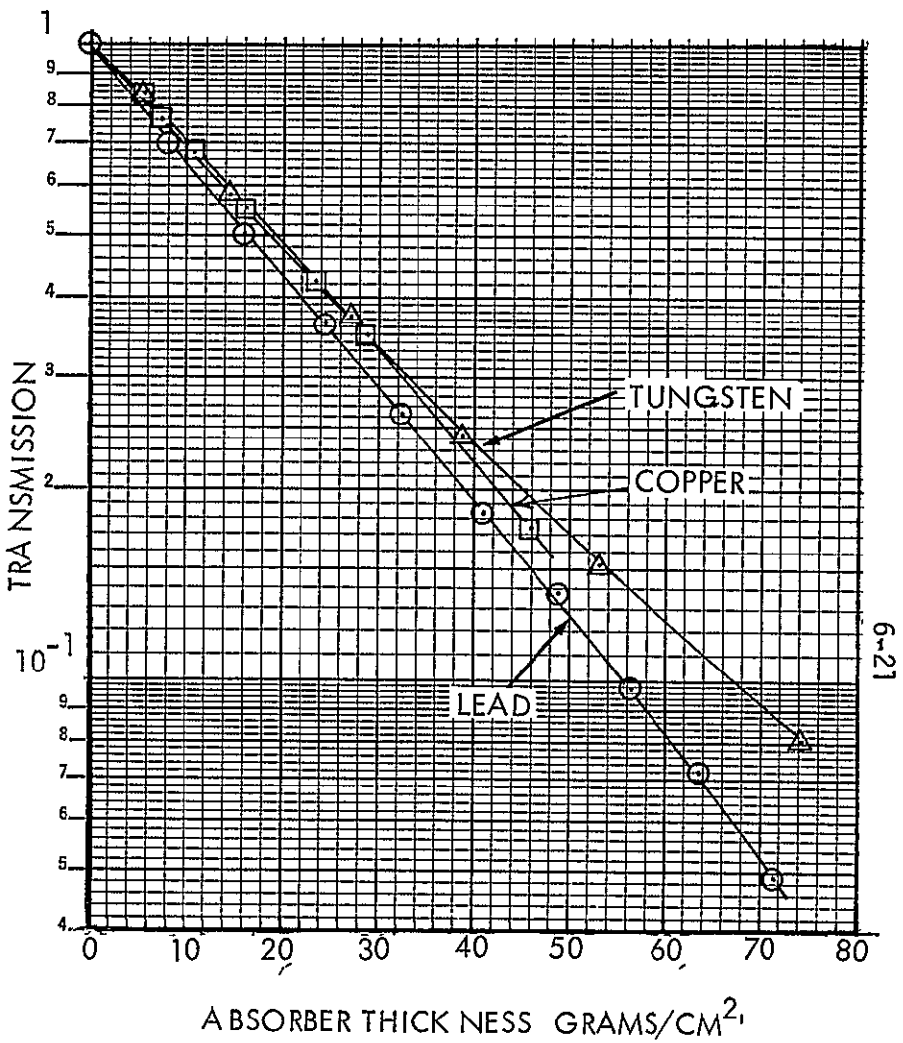

Figure 6-13. Attenuation of SNAP-27 Radiation Energy Range 2600 ± 100 kev.

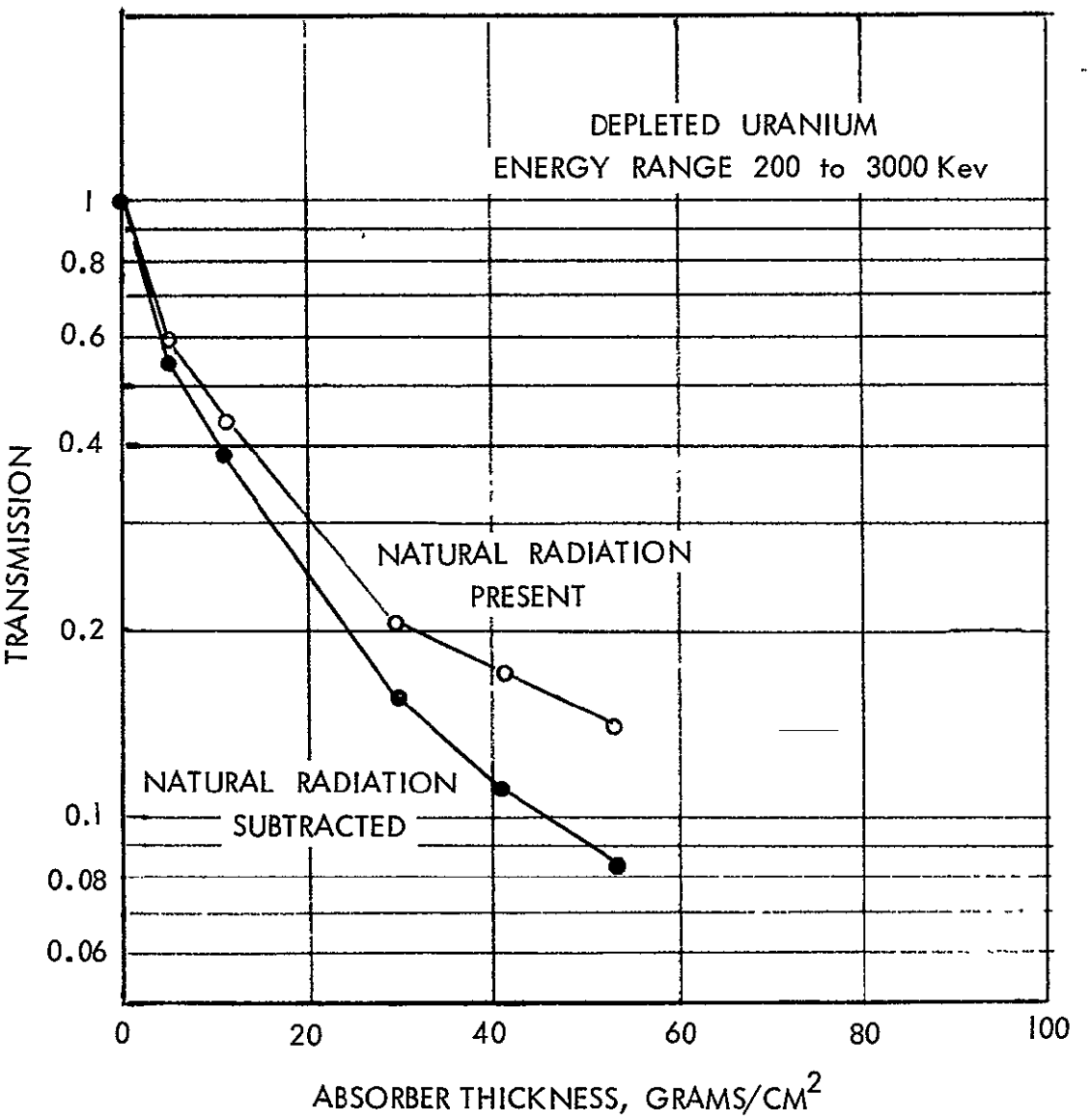

Figure 6-14. Attenuation of SNAP-27 Radiation by Depleted Uranium.

If the absorber is located far from the detector, U is the best absorber on a unit weight basis, as well as on a thickness basis. If the absorbers are located close to the detector, then lead is the most effective absorber.

6.2.2.2 Measurements with Silicon Semiconductor Detector

SNAP-27 radiation absorption measurements were performed using a 2 mm thick by 0.8 cm^2 area silicon semiconductor detector. The same absorbers and similar experimental setup was used as for measurements with the CsI detector described in Section 6.2.2.1. The detector output was recorded using a pulse height analyser. The resultant spectra without absorber and with 1" thick absorber is shown in Figure 6-15. The spectra was integrated between energy ranges of 70 to 300, 300 to 700, and 700 to 3000 kev. The resultant absorption plots for tungsten, lead and copper absorbers is given in Figures 6-16, 6-17, 6-18, and 6-19. The data obtained with semiconductor detectors was in relatively good agreement with data obtained with CsI scintillator described in Section 6.2.2.1.

6.2.3 Correction of Phase I Results for Facility Scattering

Since the absorption measurements taken during Phase I of this program did not consider scattering from the facility, additional tests were performed to evaluate this effect and provide data so that the Phase I results could be corrected. In these tests, the CsI (Na) crystal was placed at 106 inches from the midplane of the fuel capsule with the fuel capsule oriented vertically and measurements were taken with the radiation detector in the shielded and unshielded conditions. Figure 6-20 shows the results of integral counts as a function of lead absorber thickness in the energy range from 200 Kev to 3250 Kev. The ratio between the two curves can be used to correct the Phase I absorption data to compensate for the effects of facility scattering.

Figure 6-21 shows the SNAP-27 fuel capsule radiation spectra taken with a 1.5 by 1.5-in diameter CsI (Na) detector in the geometry as shown in Figure 6-11 (fuel capsule horizontal 135 cm from the detector). Counting time was four minutes. Curves (a) and (c) are with scatter included, curves (b) and (d) with scatter subtracted.

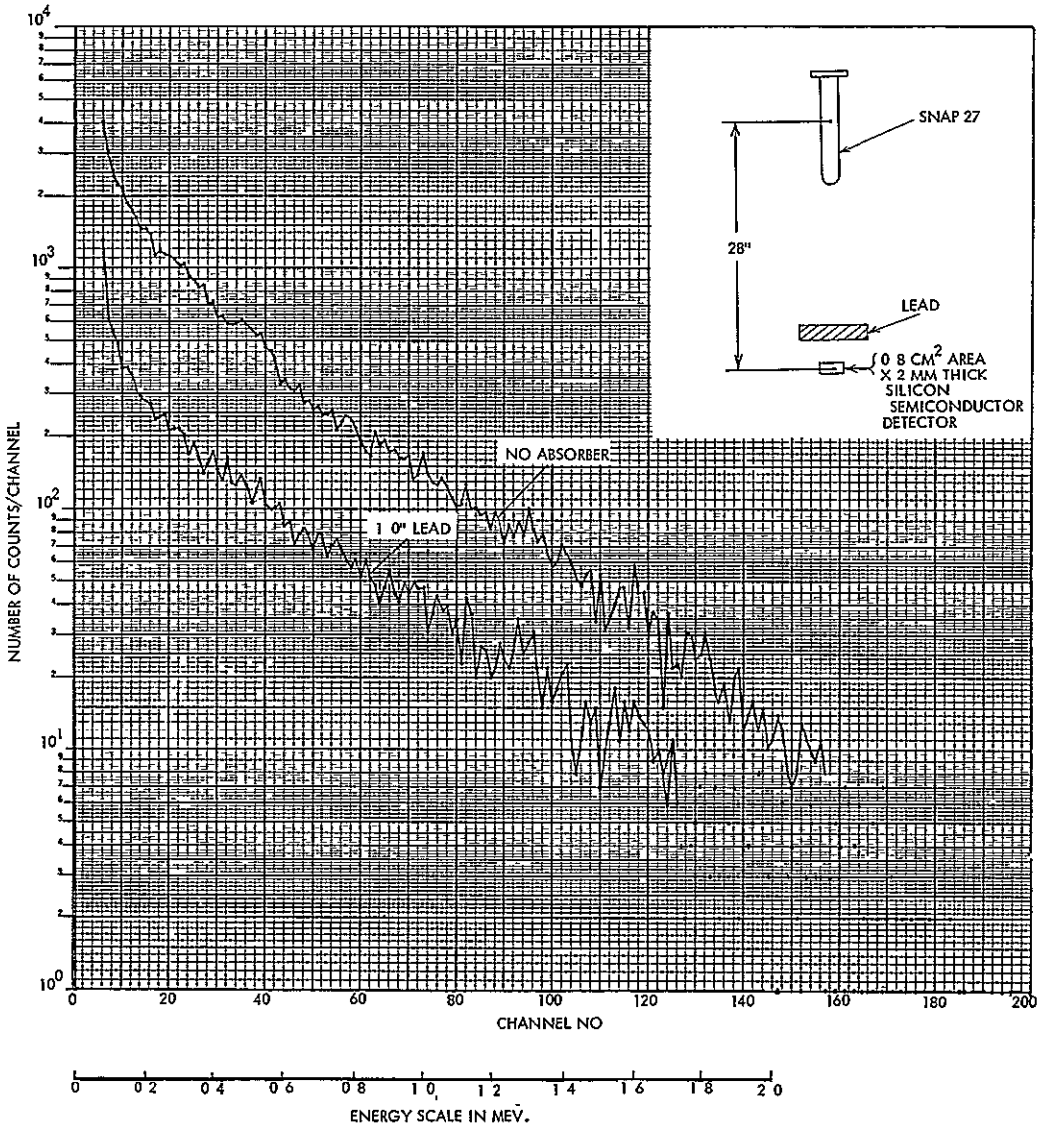

Figure 6-15. The Effect of Lead Absorber on Semiconductor Detector Spectrum

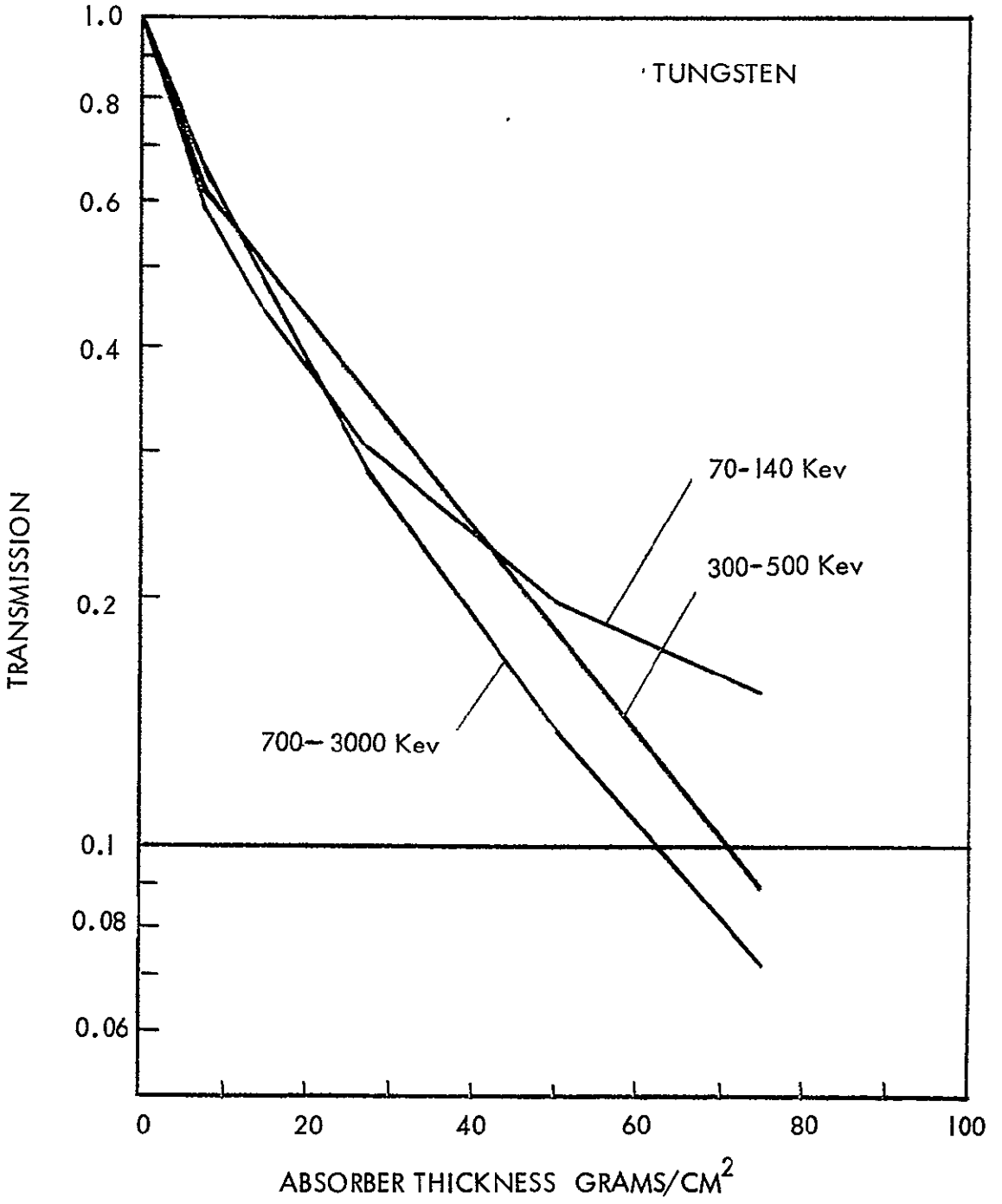

Figure 6-16. Absorption of SNAP-27 Fuel Capsule Radiation by Tungsten.

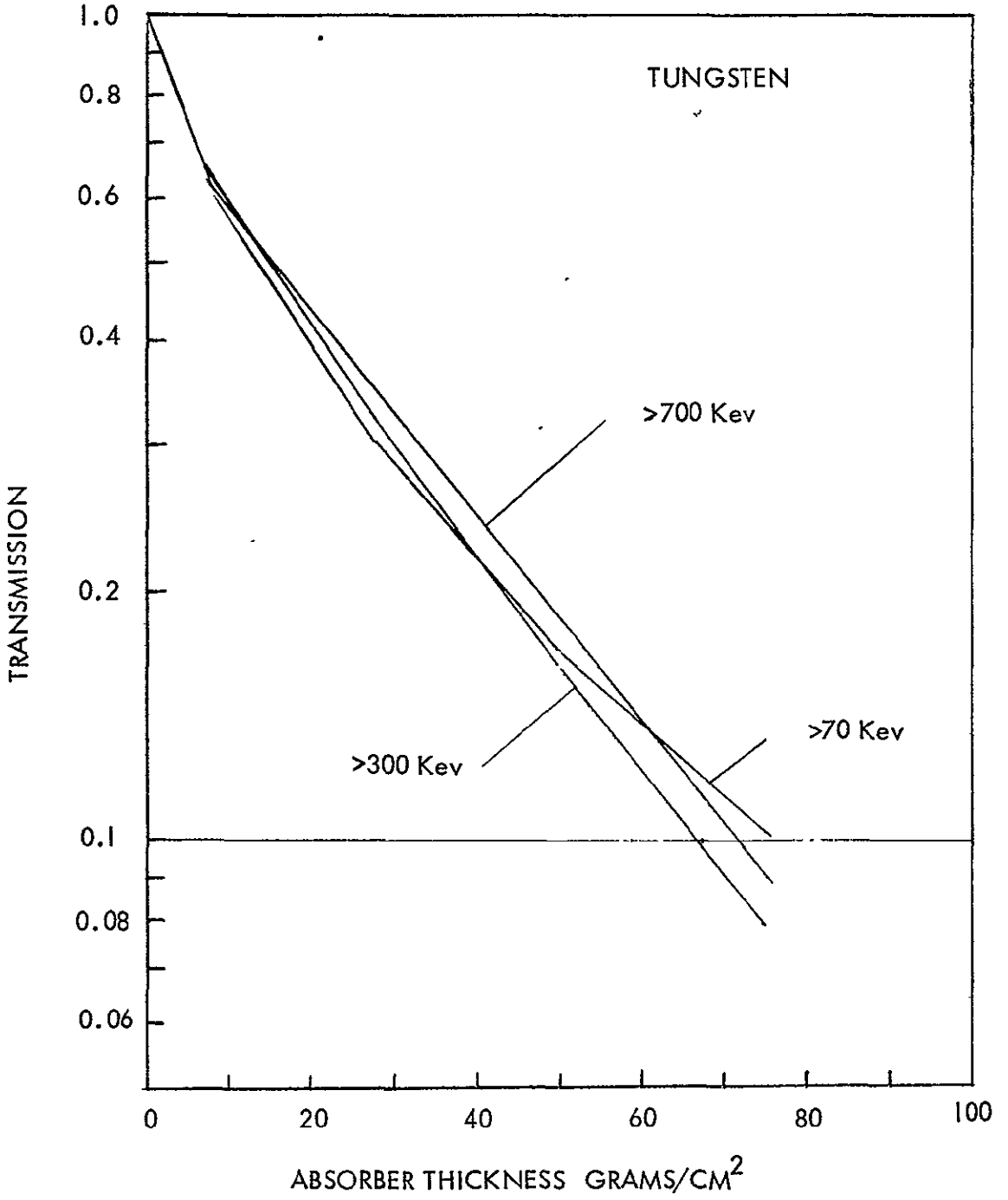

Figure 6-17. Absorption of SNAP-27 Fuel Capsule Radiation by Tungsten.

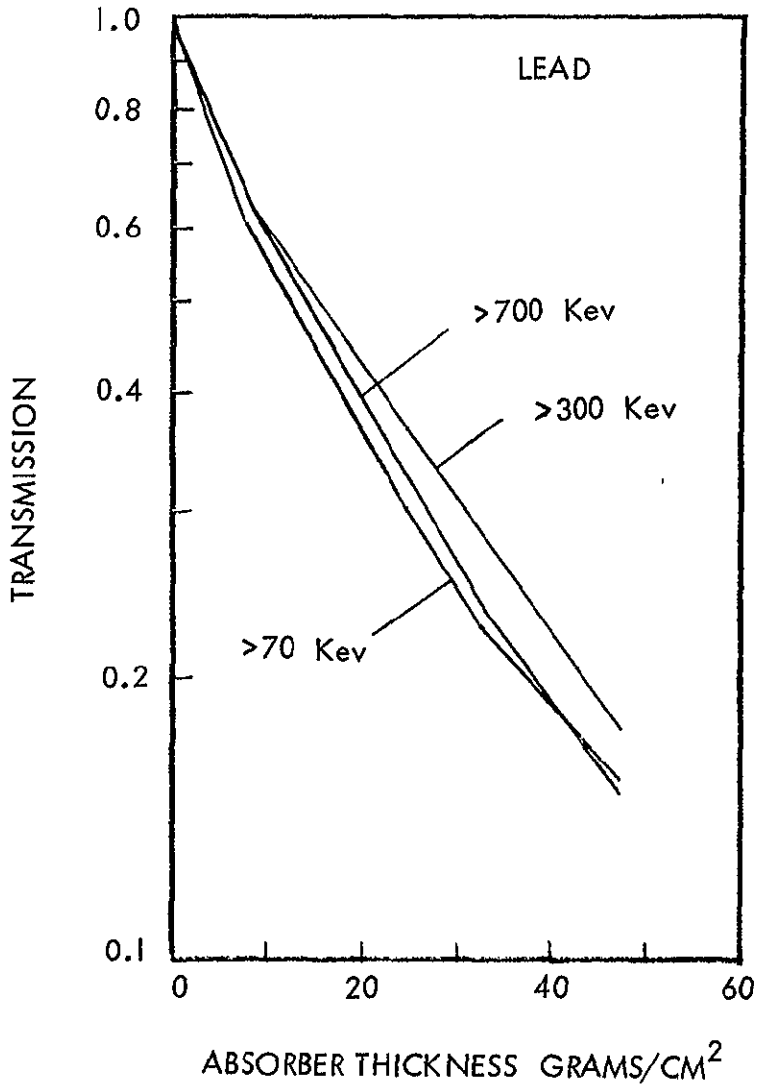

Figure 6-18. Absorption of SNAP-27 Fuel Capsule Radiation by Lead.

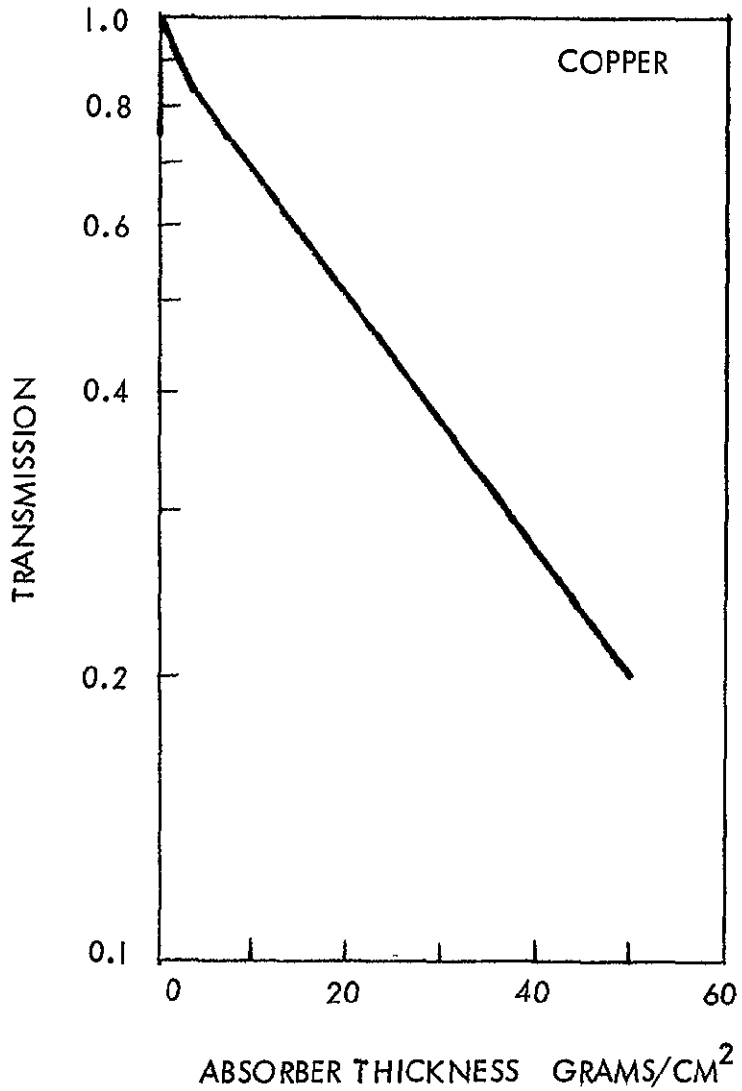

Figure 6-19. Absorption of SNAP-27 Fuel Capsule Radiation by Copper.

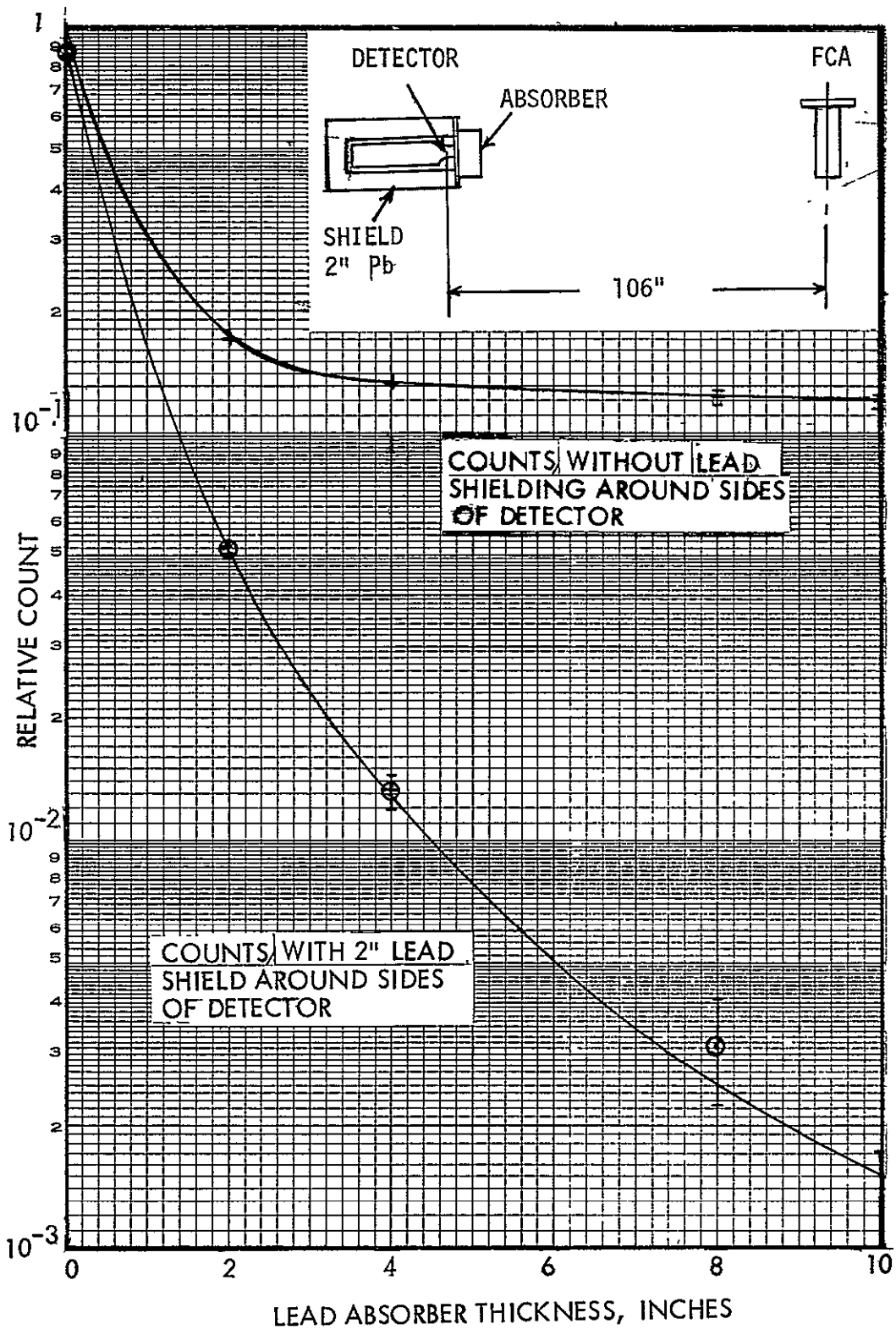

Figure 6-20. Effect of Facility Scattering on Attenuation of SNAP-27 200 to 3250 kev Radiation by Lead

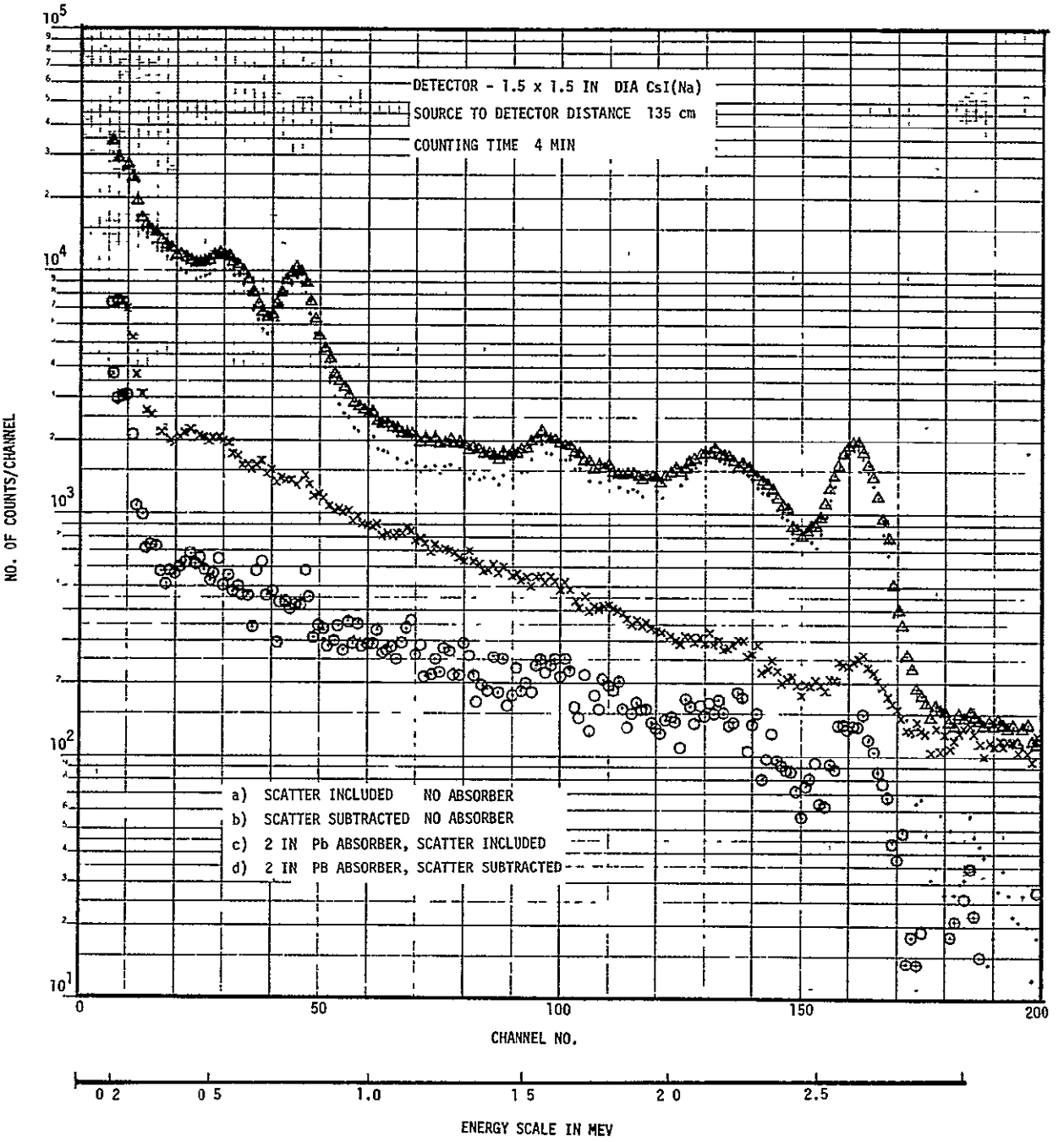

Figure 6-21. Response of CsI(Na) to SNAP-27 FCA Radiation

6.3 COINCIDENCE EFFECTS BETWEEN TWO SEMICONDUCTOR DETECTORS

Semiconductor radiation detectors are frequently used in spacecraft instrumentation in sets of two or more as telescopes and operate in coincidence or anticoincidence modes for charged-particle spectroscopy. RTG radiation will cause a certain amount of coincidence counts due to the statistical probability of nuclear interactions occurring simultaneously in the two detectors.

The coincidence counts due to this effect are statisitically independent and could be predicted by knowing certain electronic parameters and the response of each detector to the RTG radiation separately. However, a certain amount of statistically dependent coincidence counts is also anticipated as a result of Compton scattering of gammas occurring in one detector and one component of radiation escaping from the first detector and entering the other.

During Phase 1 of this contract, the coincidence spectrum representing the SNAP-27 fuel capsule radiation interference that would be superimposed on the spectrum of coincidence charged particles detected by the semiconductor telescope was measured under given parameters of geometry, resolving time, and gating threshold energy. Two semiconductor detectors were arranged in a charged particle telescope configuration and instrumented to measure the spectra of coincidence counts. The spectra of statistically independent components of radiation was measured by physically separating the two detectors with a shield. Both statistically dependent and independent components were measured by removing the shield and placing the detectors next to each other.

Presented below are data taken during Phase II. These measurements extended the data to include the effects of discriminator threshold level setting for the gating detector, shielding, distance, and orientation in coincidence and anticoincidence modes of operation. The telescope and electronics were identical to those described in reference 6-1 and are illustrated in Figure 6-22. The telescope consisted of a 2000μ thick 0.8 cm^2 area lithium drifted detector gated by a 200μ thick, 1 cm^2 area surface barrier detector. The two detectors were 0.47 cm apart and were operated either in coincidence or anticoincidence modes. The entire detector

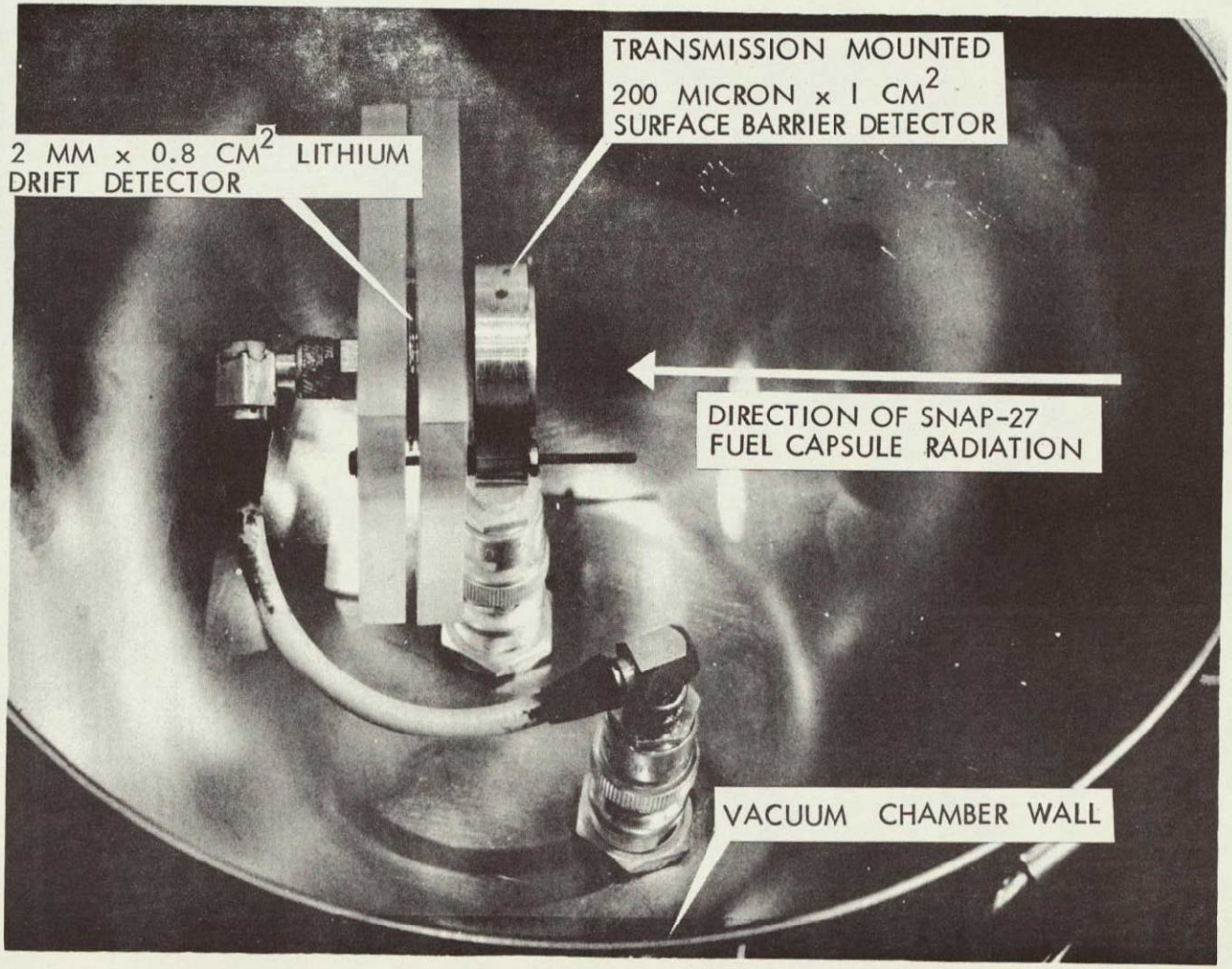

Figure 6-22. Photograph of Semiconductor Detector Telescope

assembly was mounted in a vacuum chamber to reduce air scattering and absorption of Compton electrons, thus more closely simulating space conditions. Figure 6-23 shows the block diagram of the electronics used for the coincidence measurements. The transmission mounted detector signals were amplified by a low-noise, charge-sensitive preamplifier and amplifier system and passed through a single channel analyzer to provide a gating pulse to a Hamner NG-11 gate. The 2000-micron-thick-detector signals were amplified and routed to the gated input. The resolving time of the gate was measured to be 2.5 microseconds. The output of the gate was recorded by a multi-channel pulse height analyzer. The FWHM noise levels of the 200-micron detector was 25 kev and of the 2000-micron detector was 24 kev. The integrating and differentiating time constants of both amplifier systems were set at 1 microsecond.

A bismuth-207 source was used to obtain an energy calibration of the single channel analyzer threshold settings. Measurements of SNAP-27 radiation spectra as a function of distance (R) were taken from 3/4 to 3 feet. Total count rates integrated from 0.25 to 2.5 Mev are shown as a function of $1/R^2$ in Figure 6-24 for anticoincidence and Figure 6-25 for coincidence, respectively. Note that the counts decrease almost linearly with $1/R^2$ indicating that the coincidence is real. For statistically independent random coincidences the count rate would decrease with $1/R^4$. All other measurements were taken at 1 foot from the centerline of the capsule to the center of the 2000-micron detector.

Figure 6-26 shows the coincidence spectra at various gating detector threshold levels with the capsule at 1 foot distance. Variation of threshold energy had no measureable effect on the anticoincidence count.

The effect of orientation of the detector face to the direction of the radiation is shown in Figure 6-27 for anticoincidence and Figure 6-28 for coincidence modes. The count rates integrated from 0.250 to 2.5 Mev for coincidence and anticoincidence operating modes expressed in counts/sec/cm^2 are given in Table 6-4.

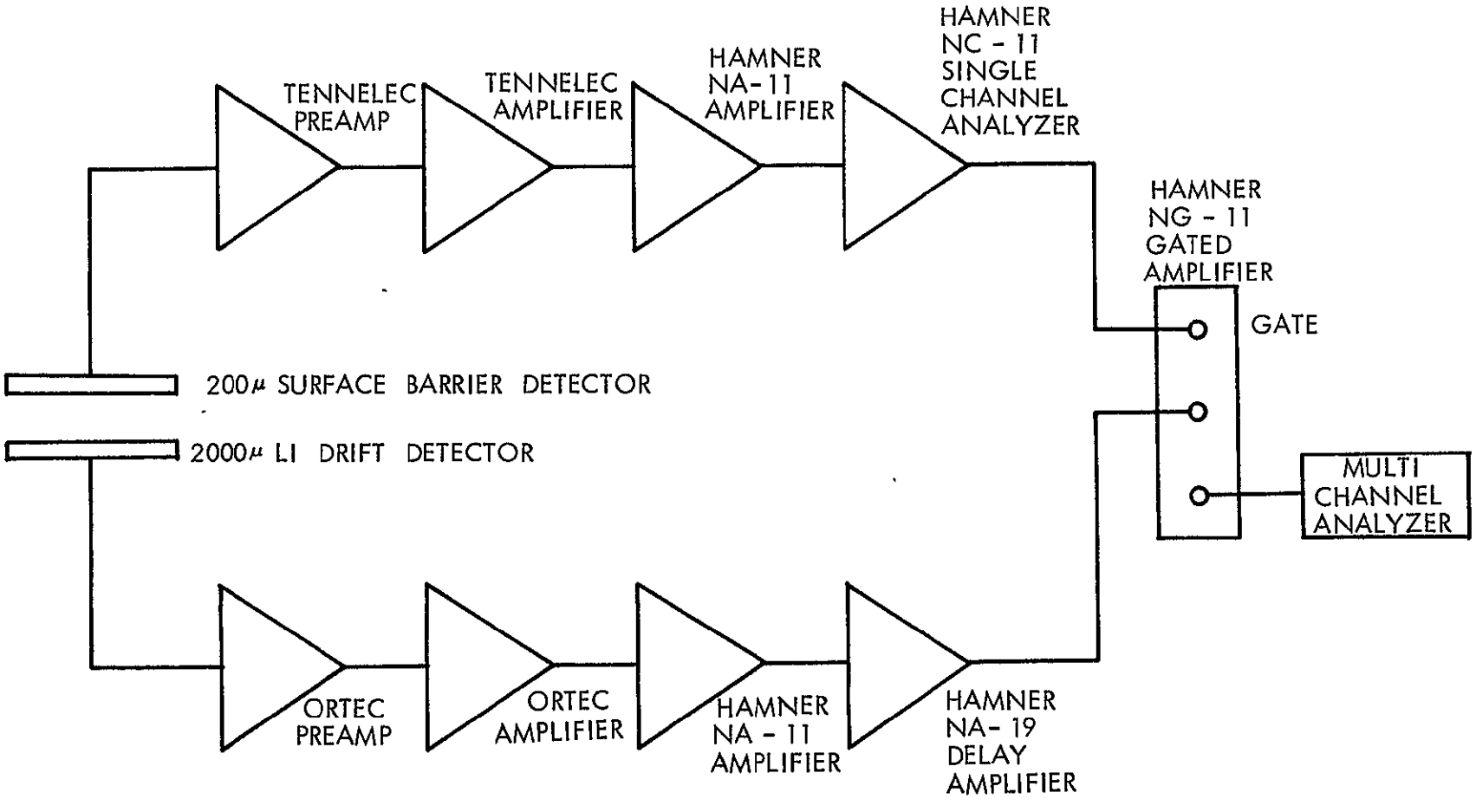

Figure 6-23. Block Diagram of Semiconductor Detector Telescope and Electronics.

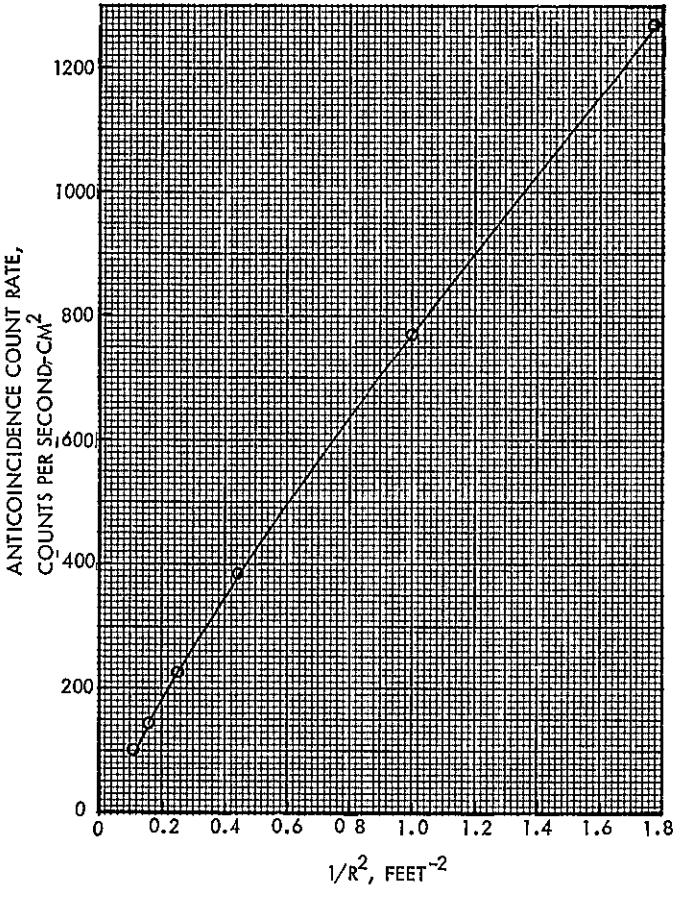

Figure 6-24. Semiconductor Telescope Anticoincidence Countrate as a Function of Radial Distance From SNAP-27 Fuel Capsule (Threshold 75 kev)

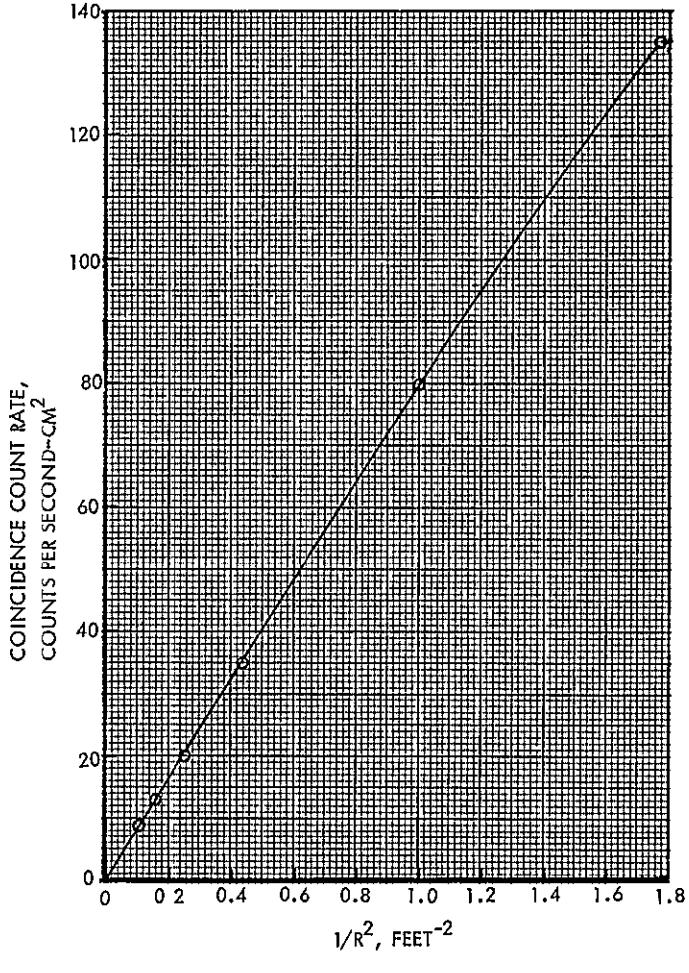

Figure 6-25. Semiconductor Telescope Coincidence Countrate as a Function of Distance from SNAP-27 Fuel Capsule (Threshold 75 kev)

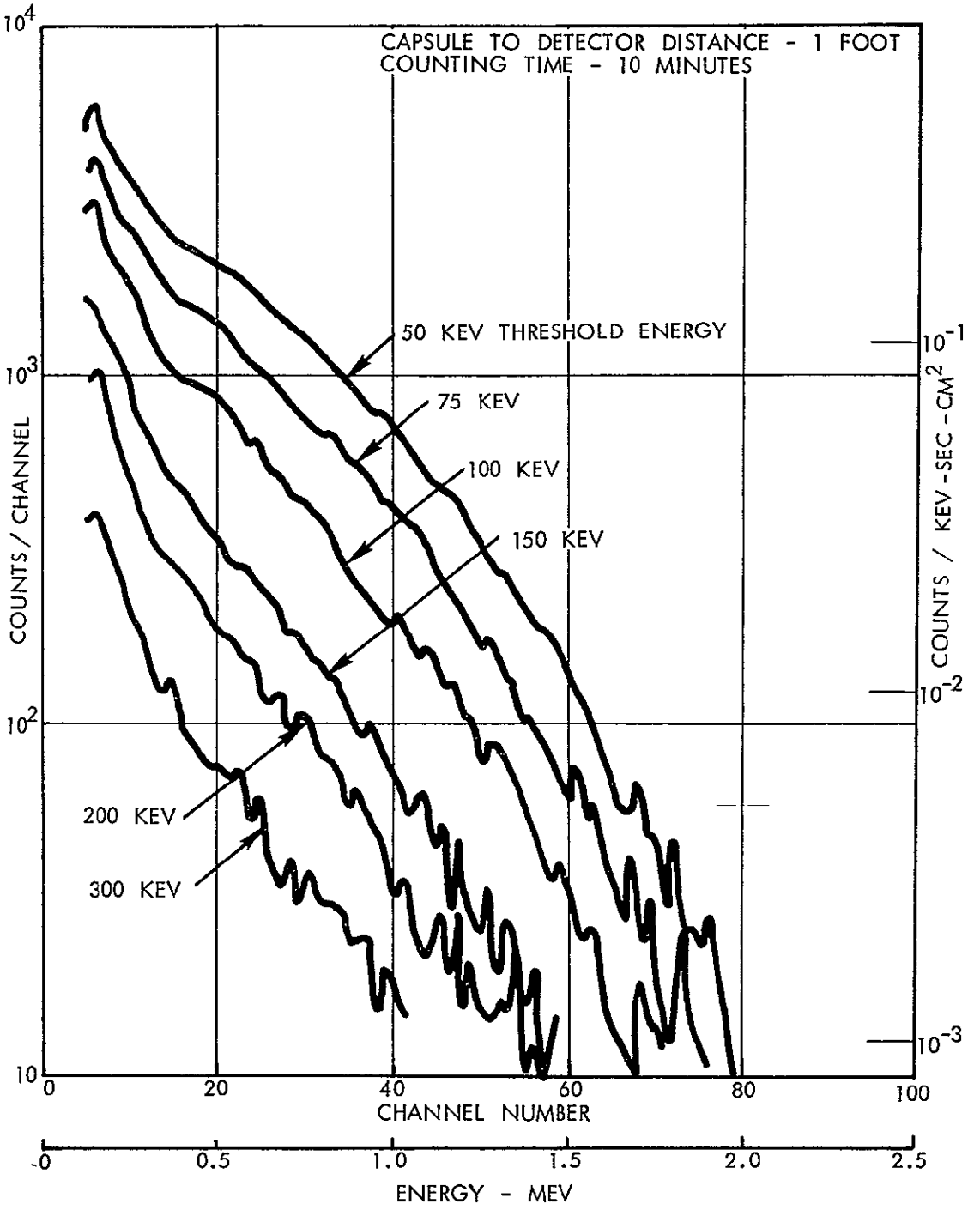

Figure 6-26. Semiconductor Telescope Response to SNAP-27 Fuel Capsule Radiation in the Coincidence Mode at Various Gating Threshold Levels.

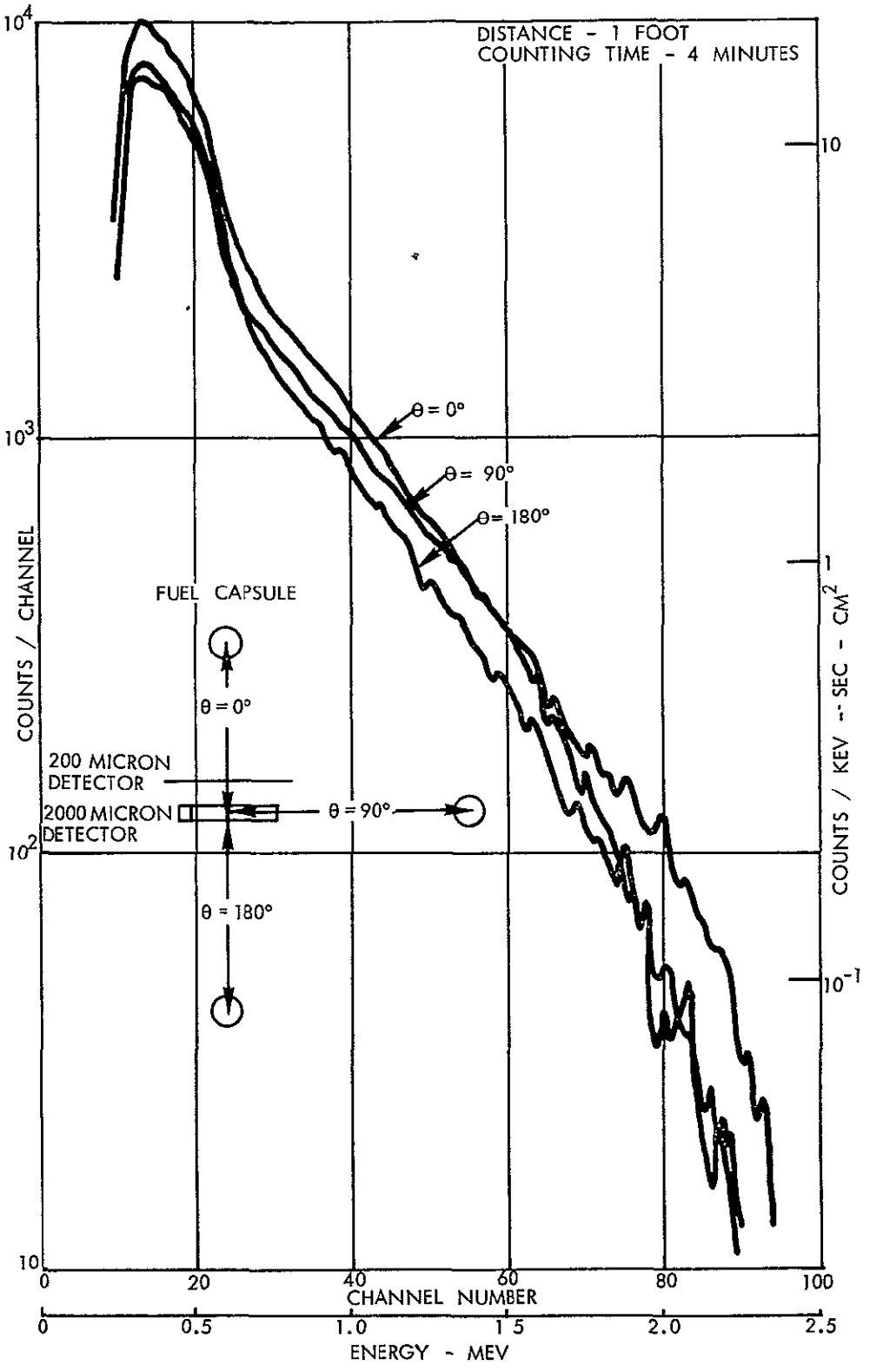

Figure 6-27. Effect of Orientation of Semiconductor Telescope on Anticoincidence Response to SNAP-27 Fuel Capsule Radiation.

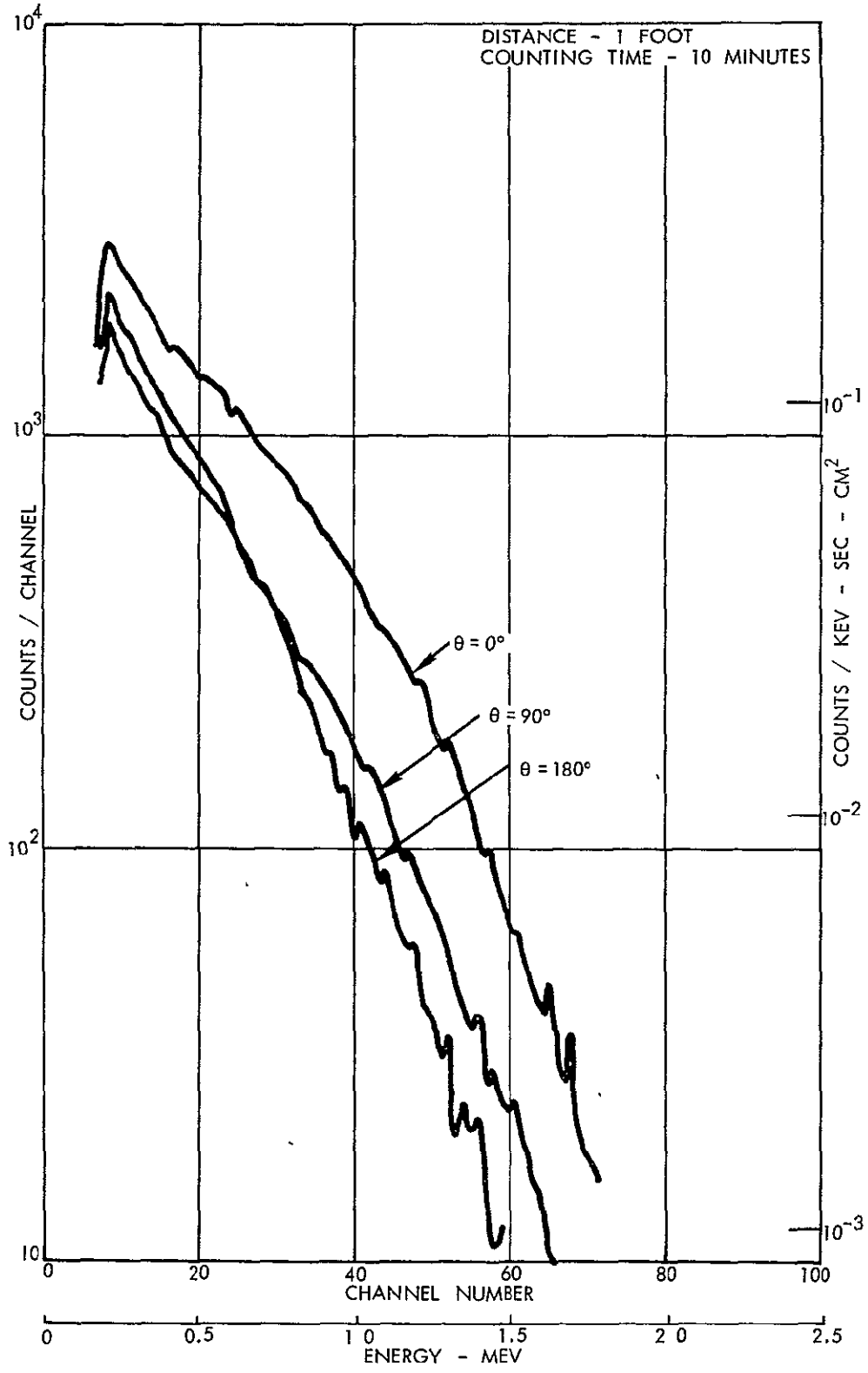

Figure 6-28. Effect of Orientation of Semiconductor Telescope on Coincidence Response to SNAP-27 Fuel Capsule Radiation.

Table 6-4. Effect of Orientation of the SNAP-27 Fuel Capsule Relative to the Semiconductor Telescope Detector Face on the Count Rate

Orientation*	Coincidence Count Rate, Counts per Second	Anticoincidence Count Rate, Counts per Second
0°	108	810
90°	56	675
180°	61	620

In order to measure the accidental coincidence rate, a 2-mm thick aluminum shield was placed between the two detectors. The shield prevented coincidence events by absorbing all beta particles with energy less than 1.2 Mev. Beta particles with energies greater than 1.2 Mev could not exceed the threshold of the single channel analyzer (set at 75 kev for this test) because the dE/dX energy loss when penetrating the gating detector is more than 75 kev. The coincidence rates taken at various single channel analyzer threshold levels with and without the internal aluminum shield is shown in Figure 6-29. The lower curve is the accidental coincidence count rate and the upper curve is the coincidence count rate caused by the fuel capsule radiation.

The direct count rates of the individual detectors were measured independently by a scalar and a theoretical accidental coincidence rate was calculated by the equation

$$C_a = 2\tau C_\tau C_g$$

where:

C_a is the accidental coincidence count rate from the thick detector,

τ is the resolving time of the system,

C_τ is the independent count rate of the thick detector,

and C_a is the independent count rate of the single channel gating pulse.

*See Figure 6-34.

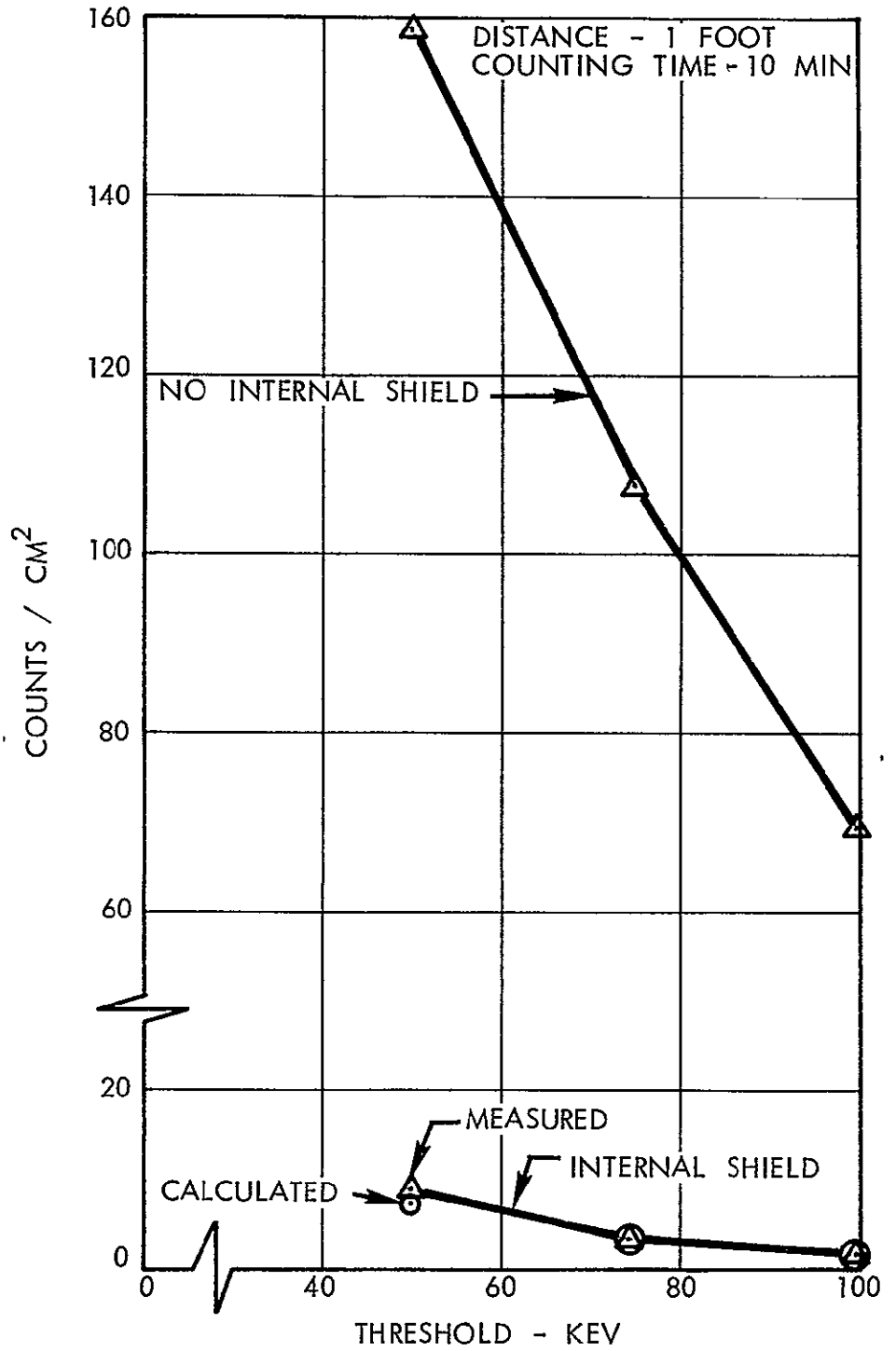

Figure 6-29. Effect of Internal Shield on Semiconductor Telescope Coincidence Countrate Response to SNAP-27 Fuel Capsule Radiation.

The calculated values of accidental coincidence rates are shown in Table 6-5. The measured value at 50 kev is slightly high probably due to a small contribution of true coincidence caused by Compton electrons from the 2.6 Mev gamma photons which are able to trigger the 50 kev threshold.

Table 6-5. The Accidental Coincidence Rate of a Semiconductor Telescope at Several Threshold Energies, Counts per Second per Square Centimeter

Threshold Energy, Kev	Measured	Calculated
50	8.8	7.5
75	3.4	3.4
100	2.0	2.2

REFERENCE

6-1 R. A. Kaminskas, et al., "RTG/Science Instrument Radiation Interactions for Deep Space Probes, Phase I Final Technical Report" Contract NAS 2-5222 (July 31, 1979).

7.0 RADIATION DAMAGE TO SCIENCE INSTRUMENTS

The radiation from the RTG's and RHU's, interplanetary radiation, and the Jovian trapped radiation belts have been analyzed and the integrated dose for an 850-day mission determined. The mechanisms and extent of damage to science instrument components identified on the Pioneer F/G materials list were then analysed.

7.1 RADIATION ENVIRONMENT

The radiation environment in the Pioneer F/G spacecraft is caused by the radioisotope fuel in the RTG's and RHU's, the interplanetary (galactic) radiation,and the Jovian trapped radiation belts. This section describes the radiation sources which affect the Pioneer spacecraft environment, assumed source models, and their individual contributions to the total radiation environment.

The radiation environment that the experiments on the Pioneer F/G spacecraft are expected to experience as a function of time during their missions to Jupiter is presented in Figures 7-1 and 7-2. Figure 7-1 presents the accumulated neutron fluence and Figure 7-2 the accumulated ionizing dose. The fluxes were converted to dose rates by using the conversion factor 1×10^{-10} rads(c)-cm^2/n (reference 7-1) Table 7-1 presents a summary of the accumulated neutron fluence and accumulated ionizing dose at the time of Jupiter encounter for an 850-day mission and includes a breakdown of the environment by radiation source. The same fluence and dose valu are used to characterize the experiments as a whole since the variation in the radiation environment over the experiments sector of the spacecraft is small in relation to the total.

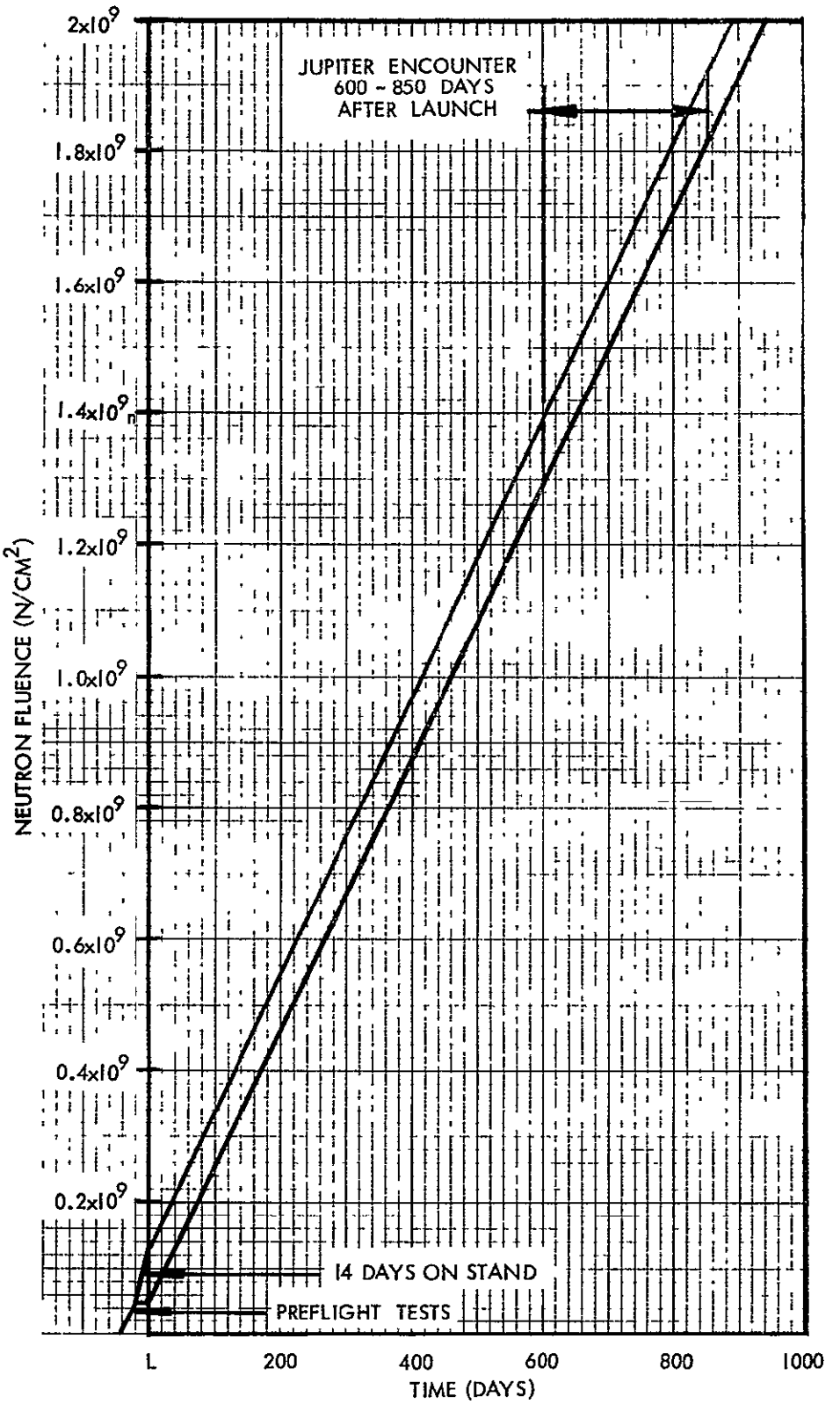

Figure 7-1. Neutron Fluence As A Function of Time for the Pioneer F/G Experiments

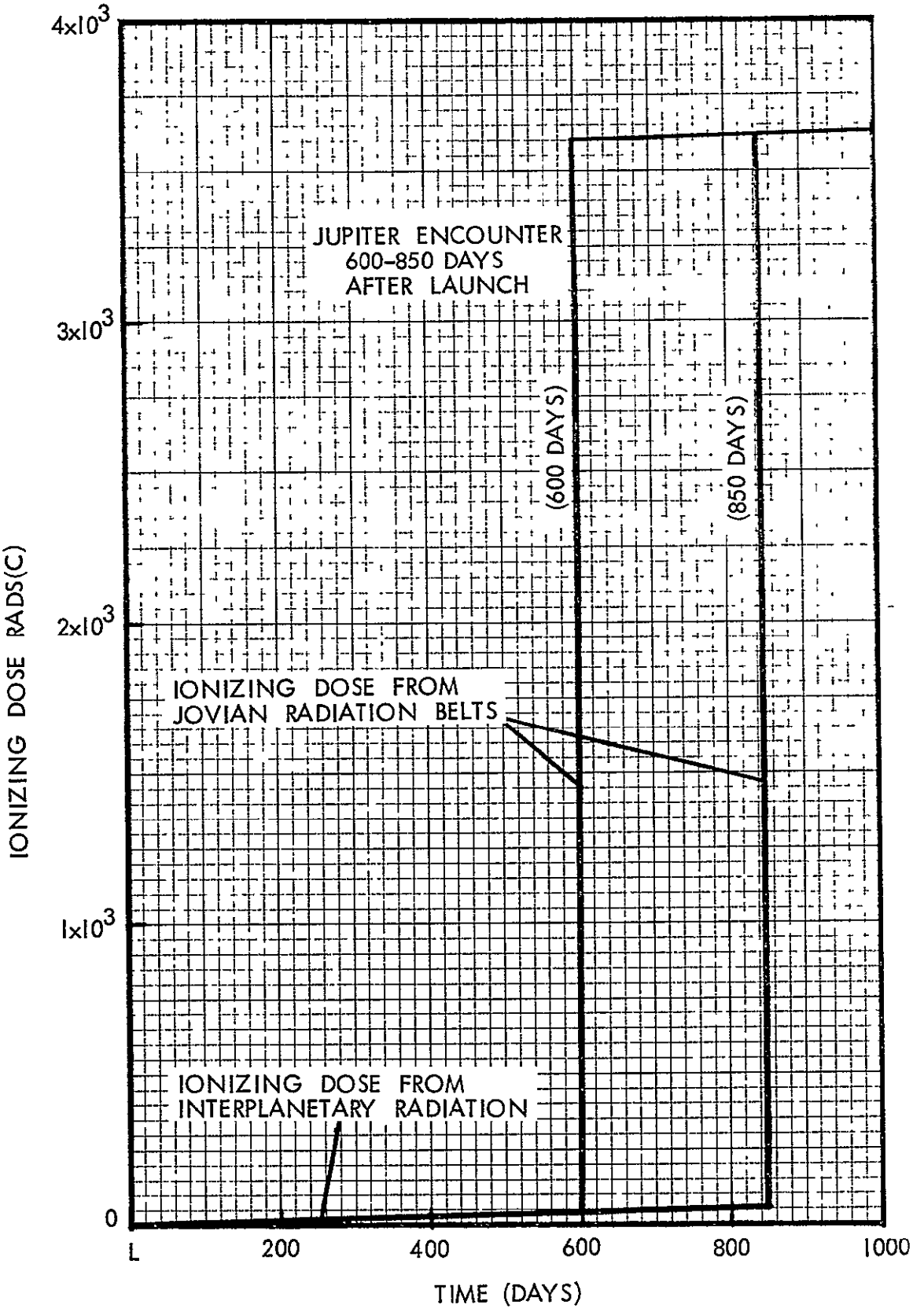

Figure 7-2. Total Ionizing Dose as a Function of Time for the Pioneer F/G Experiments

Table 7-1. Cumulative Radiation at the Instrument Compartment for a 850 Day Mission

Radiation Source	Ionizing Radiation, rads (C)	Neutron Fluence, n/cm^2
1. Jovian Radiation Belts		
Electrons	3.2×10^3	
Protons	0.4×10^3	
2. Interplanetary Radiation	40	
3. RTG and RHU Fuel	0.2*	1.8×10^9**
4. Total	3.6×10^3	1.8×10^9**

*Gamma radiation not included
**Based on 5×10^3 n/sec/gram of Pu

7.1.1 RTG and RHU Fuel Contribution

The model assumed for the radioisotope fuel sources neglects the gamma-ray component of the radiation and considers only the neutron component. The neutron component is specified as a point source with $1/R^2$ attenuation emitting 5×10^3 n/sec-gm Pu-238. Under these assumptions and taking into account the minimum shielding afforded by the RTG and RHU structural materials, the neutron fields of a pair of RTG sources as a function of radial distance are given by:

$$N = 1.8 \times 10^5/R^2 \qquad (7\text{-}1)$$

where

N = neutron flux ($n/s\text{-}cm^2$)
R = radial distance (inches)

Similarly, the neutron field for a 1 watt RHU is given in equation (7-2).

$$N = 133/R^2 \qquad (7\text{-}2)$$

where

N = neutron flux (n/s-cm^2)

R = radial distance (inches)

Combining the contributions from each RTG pair and RHU source for the spacecraft geometry described in Section 3.1, the total neutron flux was determined over the spacecraft volume for the RTG's in both the deployed and stowed positions. The resulting flux maps are presented in Figures 7-3 and 7-4, respectively.

7.1.2 Interplanetary Radiation Contribution

The high energy particle flux of the interplanetary radiation is given in Figure 3.5.3 of reference 7-2. This flux was converted to a dose rate by using the methods of reference 7-3. The technique used was the graphical integration of the integral:

$$D = \int_0^\infty \phi(E)\ \ c(E)\ \ dE \qquad (7\text{-}3)$$

where:

D = dose rate (rads(c)/day)

$\phi(E)$ = flux of particles (P/cm^2-day)

c(E) = dose conversion factor rads(c)-cm^2/n

E = energy of particles (Mev)

While the conversion factor c(E), is known to apply for 1-1000 Mev protons, it was assumed that the dose conversion function held above that. The result was 50 mrad(c)/day and compares favorably with the measured value of 45 mrad/day during periods of minimum solar activity (reference 7-4).

7.1.3 Jovian Radiation Belt Contribution

The Jovian radiation belts are defined in reference 7-5 as producing a fluence of 4×10^{10} P/cm^2 and 4×10^{10} e/cm^2 in the time that the spacecraft encounters Jupiter. The electrons and protons under the stated model

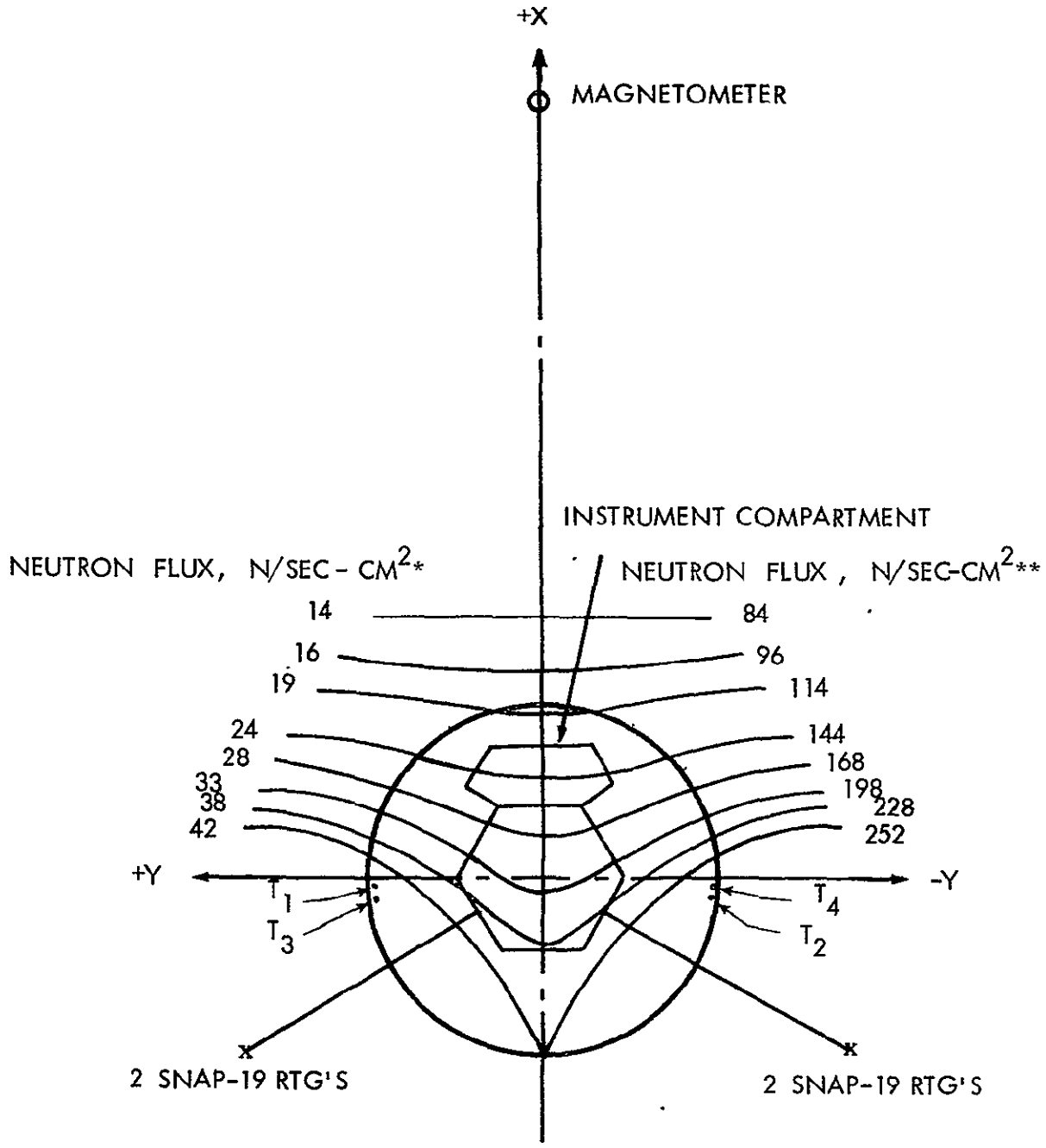

* BASED ON 5×10^3 NEUTRONS/SEC-GRAM OF PU-238.

** BASED ON 3×10^4 NEUTRONS/SEC-GRAM OF PU-238.

Figure 7-3. Neutron Isoflux Plot for Pioneer F/G Spacecraft

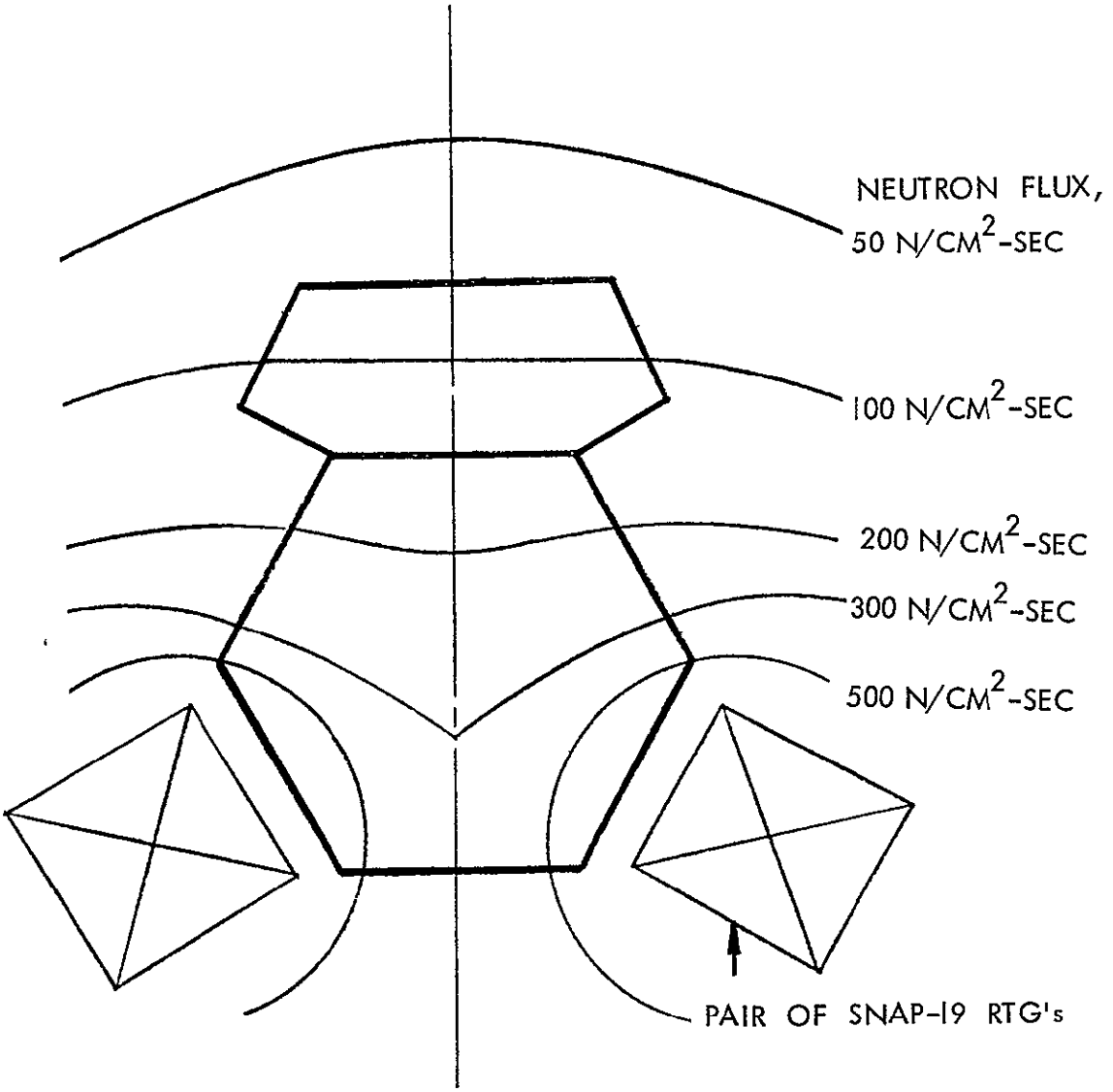

BASED ON 5×10^3 NEUTRONS/SEC-GRAM OF Pu-238.

Figure 7-4. Isoflux Plot for Pioneer F/G Spacecraft With RTG's in Stowed Position

have energies between 5 and 100 Mev with the differential spectrum:

$$\frac{dN}{dE} = 2 \times 10^{11} \; E^{-2}$$

where: N = fluence (particles/cm^2)
E = particle energy (Mev)

It is assumed that the spacecraft provides 0.4 gm/cm^2 of inherent shielding. More than 80% of the electrons of 5 Mev and greater will traverse this amount of shielding and be degraded in energy only slightly. The collision cross-section for electrons in the range of 5 to 100 Mev is relatively constant and is approximately 1.8 Mev-cm^2/g over this range for carbon. This gives a conservative total ionizing dose of 3.2×10^3 rads(c) for the electron component of the Jovian radiation belts for the total encounter period.

The attenuation, emergent spectrum, and ionizing dose of the protons behind 0.4 gm/cm^2 of shielding were determined using the calculational techniques in reference 7-6. These calculational techniques are based on the extensive results presented by Berger and Seltzer (reference 7-7 on the transmission of electrons through aluminum.) The calculated results show that the proton fluence is reduced by a factor of ten and that the shielded ionizing dose is about 400 rads(c) for the proton component of the Jovian radiation belts.

7.2 RADIATION EFFECTS ON ELECTRONIC COMPONENTS

A parts list of the Pioneer F/G experiments was obtained from NASA/ARC and the effect of radiation on the various electronic parts was assessed. The paragraphs below discuss the nature of radiation effects on components of the Pioneer F/G scientific instruments. Paragraph 7.2.4 summarizes the results of the analyses.

7.2.1 General Considerations

It is important to distinguish between two characteristically different physical effects in discussing the behavior of high energy radiation on electronic parts. The first, associated predominantly with the neutron component, is the production of lattice disorder by elastic collisions between incident high energy neutrons and the atoms of the lattice. The

displaced atoms and vacancies produced in this way in a semiconductor are active electrically and will reduce the lifetime of minority carriers and correspondingly the gain of a bipolar transistor. The second characteristic effect is associated primarily with the incident ionizing component. The primary effect in this instance results from the production of atomic ionization which, in an electronic conductor, will produce free charge that can migrate in the presence of an electric field. This second effect is also responsible for degraded semiconductor device performance but is localized in the device surface in contrast to the predominantly bulk effect from neutrons.

The passive electronic part is also degraded by both lattice displacements and ionization, but generally with higher thresholds for measurable effects than for the active semiconductor.

7.2.2 Semiconductor Devices

7.2.2.1 Discrete Transistors

The decrease in bipolar transistor gain, β, from high energy neutrons has been found generally to obey the following equation:

$$1/\beta\ (\Phi) = 1/\beta_0 + (0.2K/f_T)\Phi \qquad (7\text{-}5)$$

where:

- $\beta\ (\Phi)$ is the transistor gain as a function of neutron fluence
- Φ, β_0 is the unirradiated gain
- K is a damage constand that characterizes life-time degradation for a particular material
- f_T is the device gain-bandwidth product

For an npn silicon device, K will be determined by the p-base material. An experimentally determined average value (7-9) is $K = 8 \times 10^{-7}$ cm^2/sec. This number will be dependent on the device operating point and will decrease emitter current (7-10). Equation (7-5) above is plotted in Figure 7-5 for various values of f_T and an assumed value of 200 for β_0

It can be seen that for a transistor with an f_T of 1 MHz that the gain will be down by about 5% at a fluence of 1.8×10^9 nvt. For transistors with gain bandwidth products in the 10-100 MHz range, accordingly, the gain degradation will be negligible at the estimated fluence of 1.8×10^9 nvt. Of the discrete bipolar transistors listed for the payload, the lowest

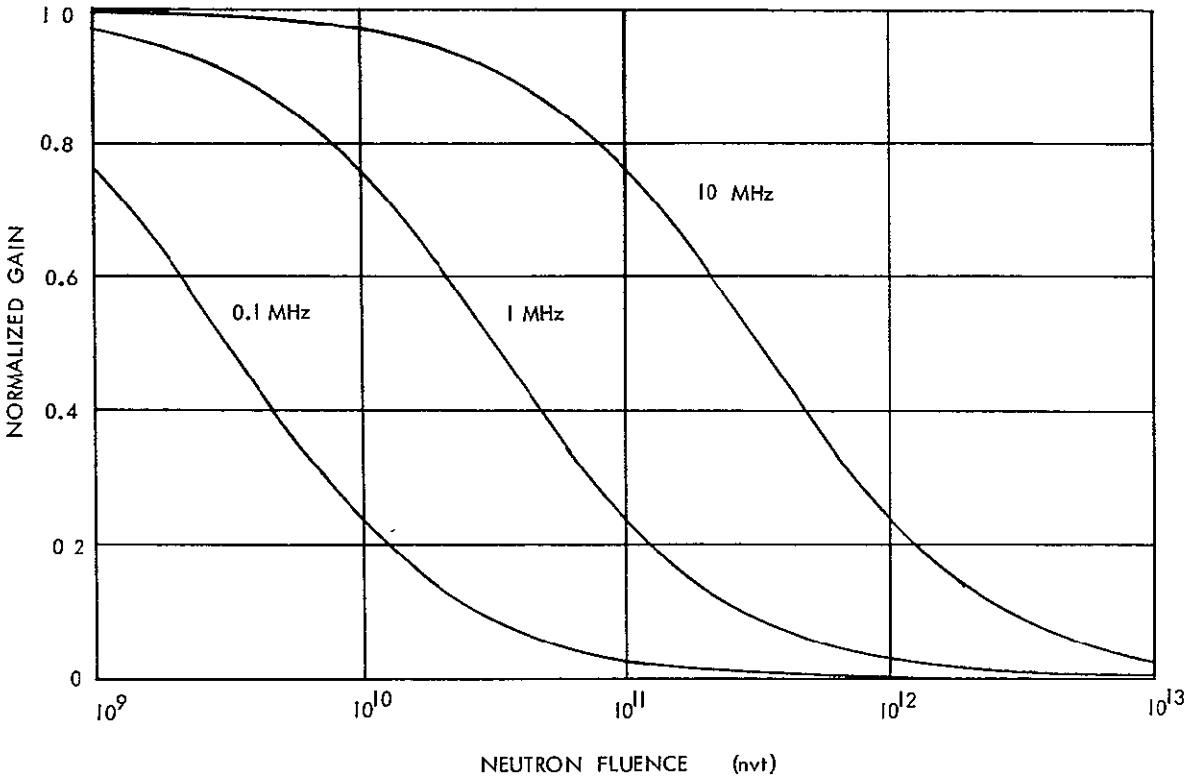

Figure 7-5. Dependence of Normalized Gain on Neutron Fluence and Transistor Gain Bandwidth Product Assuming $K = 8 \times 10^{-7}$ cm^2/sec and $\beta_o = 200$

rated f_T value is 5 MHz for a 2N2946A, pnp silicon low power device in the Geiger tube telescope. For n-type base material, the damage constant is essentially the same. It can be concluded, therefore, that the gain degradation will be less than 5% for the device from the neutron component.

Gain degradation for the discrete device must also be considered with respect to the ionizing component of the environment. As indicated previously, reference must be made to empirical device data. In a particular study (7-11, 7-13), a selection of silicon npn and pnp planar transistors were exposed to ionizing radiation from an X-ray source at a dose rate of 8×10^3 r/min. An important aspect of the ionizing radiation effect is a dependence on device bias, and in this study various conditions of bias were used. Some results for a 2N1613, a low power npn silicon device, are shown in Figure 7-6, which is taken from reference (7-11). It is seen that a rapid change in β occurs during the initial stage of exposure with a tendency to saturation with increasing exposure. If it is assumed that the effect is dose rate independent, then the estimated mission dose of 3.6×10^3 rad corresponds to a time interval of less than a minute. It is

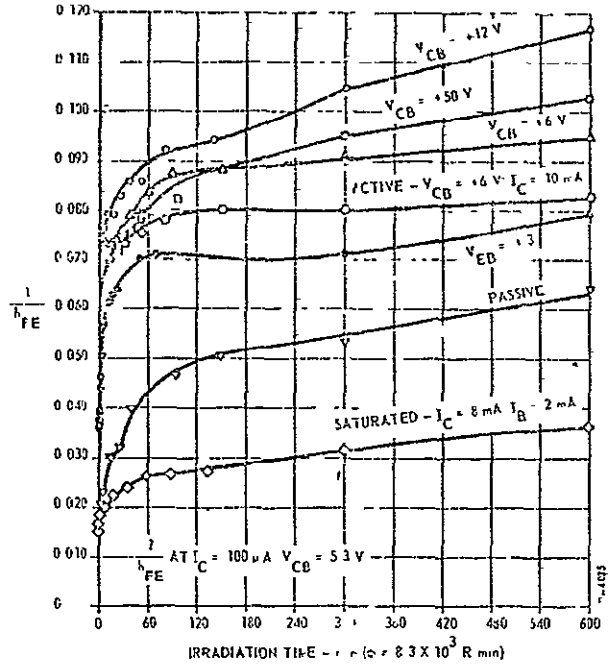

Figure 7-6. Effect of Ionizing Radiation on a 2N1613 Silicon Planar Transistor for Various Conditions of Applied Bias (Ref. 7-13)

difficult to determine the magnitude of the effect from the curves in Figure 7-6 because of the time scale; for the case of V_{CB} = 12V, it is estimated that β has changed from a value of about 67 to a value of 13 during this period. The decrease in gain is accompanied also by an increase of I_{CBO} in the device; this occurs largely in the first few minutes of exposure. The extent of the increase varied between devices with the leakage current increasing to as much as a microamp in one device for V_{CB} = 5.3V. Similar data on the increase in leakage current has been obtained in a 2N2222 and a 2N2801, with I_{CBO} increasing from values of less than a nanoamp to values of the order of one tenth microamp at about 10^4 r.

In a more recent paper, Poch and Holmes-Siedle (7-12) studied gain degradation in a series of silicon npn planar devices using ionizing radiation from a cobalt-60 source. The results for a Fairchild 2N1711 low power device with an f_T of about 70 MHz showed similar gain degradation with absorbed dose, with extent of degradation depending on the bias state of the device. With collector-base bias applied, a 10% decrease in β was observed at 10^4 rad. A predicted worst case, based on tests on a number

of devices, of a 10% degradation at 10^3 rad. is made for the 2N1711. Data are also presented on a Motorola 2N2222A pnp after an exposure of 10^4 rad. A decrease of about 10% in β was again observed. An "anomalously sensitive" unit of this type showed a decrease in gain from a value of 100 to less than 20 at 10^4 rad. This result illustrates the nature of the range of variation for the surface effect.

7.2.2.2 Diodes

The effect of neutrons on diodes is to cause an increase in forward current at constant voltage, and an increase in reverse saturation current. Thresholds for measurable effects are in the range of 10^{15} nvt (7-13, 7-15), which is a comfortable safety margin for the neutron component.

With respect to the ionizing component, a decrease of 9% in breakdown voltage was observed in a switching diode at about 4×10^6 rad(C). A 1N547 rectifier was not significantly affected in a combined environment of 4.8×10^{12} nvt and 2.3×10^6 rad(C). Zener diodes are similarly unaffected. A Zener voltage change of about 3% was observed in a 1N749A for 4.8×10^{12} nvt and 7×10^5 rad(C).

It can be concluded that semiconductor diodes will not be measurably affected in the Pioneer radiation environment.

7.2.2.3 Field Effect Transistors

A number of junction gate field effect transistors are called out for the experiments. This device is inherently hard to neutrons since current flow is by drift of majority carrier rather than by diffusion of minority carriers as in a polar transistor. There will be no detectable effect from the neutron component for the mission. This device is also inherently stable with respect to ionizing radiation effects. A good margin of safety for this device accordingly will result in the Pioneer radiation environment.

7.2.2.4 Integrated Circuits

7.2.2.4.1 Bipolar

The integrated circuit transistor can be expected to have generally the same degree of radiation susceptibility as its discrete counterpart.

In a linear amplifier, for example, high β devices are used in order to reduce input bias currents. High β is usually achieved by minimizing the base width which, in turn, increases f_T. This leads, correspondingly, to good tolerance to the neutron component.

Radiation tests on digital integrated circuits (7-14, 7-16) have been carried out up to 5×10^{14} nvt. TTL gates and flip-flops from four manufacturers were tested in a combined neutron-gamma ray environment. It was concluded that fast neutron exposure approaching 5×10^{14} nvt can be tolerated in low noise systems. Additionally, exposure to cobalt-60 radiation indicated no significant effect up to 10^7 rad. It can be concluded that payload bipolar logic digital microcircuits should not be affected by the radiation environment.

Neutron radiation tests have been carried out on bipolar linear microcircuits (7-15). Test data were obtained in two operational amplifiers and two comparators. No significant effects in voltage gain occur up to 10^{13} nvt. It can be concluded that no measureable effect will occur, with a good safety factor, in the bipolar linear circuit for the neutron component of the radiation environment.

As in the case of the discrete bipolar transistor, the possibility of radiation induced surface effects from the ionizing component must also be considered in the linear integrated circuit transistor. A recent report (7-16) describes the radiation response of a selection of integrated and hybrid operational amplifiers. These are listed in Table 7-2.

Table 7-2. Operational Amplifier Radiation Test

Type	Construction	Manufacturer	No. of Units Tested
LM101	Monolithic	National Semiconductor	4
LM101	"	Siliconix	4
μA714	"	Fairchild	5
RA909	Dielectric Isolation	Radiation, Inc.	8
NH0001	Hybrid	National Semiconductor	3

The devices were irradiated under bias at an initial exposure dose rate of 4×10^4 r/hr, which was increased to 4×10^5 r/hr after the first exposure increments. The total exposure dose was 3.4×10^7 r.

A number of circuit characteristics were studies as a function of dose. The threshold for significant change in DC offset voltage occurred between 10^4 and 10^5 rad(Si) after which the offset voltage varied in an unpredictable and erratic fashion. This was attributed to lack of matching in transconductances of the two after 10^4 rad(Si). For one unit the degradation knee (-3 db point) was as low as 3×10^3 rad(Si); however, for most units it was between 10^4 and 10^5 rad(Si). The data for a selection of units are given in Figure 7-7. Input bias current and input offset current were also observed to change and this was attributed to gain degradation in the low current h_{FE} of the input transistors. These bias current data are plotted in Figure 7-8 which is taken from reference 7-16. It can be seen that two RA909 units showed current variations in the 10^3 rad(Si) range. Offset current data are shown in Figure 7-9. Experiments were carried out to determine if changes in I_{CBO} in the input transistors could account for these current deviations. These measurements were inconclusive, however, since they were made several days after the units had been removed from the radiation source, and it was not certain that any excessive leakage current would not have recovered during this time.

Noise measurements were also made on all units. Data are presented, however, for only post-3.4×10^7 rad(Si) exposure. At this exposure dose noise referred to input was as high as 40μv (rms) in units exhibiting noise levels of the order of 1μv(rms) prior to irradiation.

The above data relate directly to payload components in several experiments. These are the plasma analyzer and the charged particle experiment in which "LM100 Series" circuits are called out. Additionally, an NH0001 operational amplifier is listed for the helium vector magnetometer, plasma analyzer, trapped radiation detector, and asteroid/meteoroid detector. An NH0003, a type of the same series, is also listed for the A/M detector experiment.

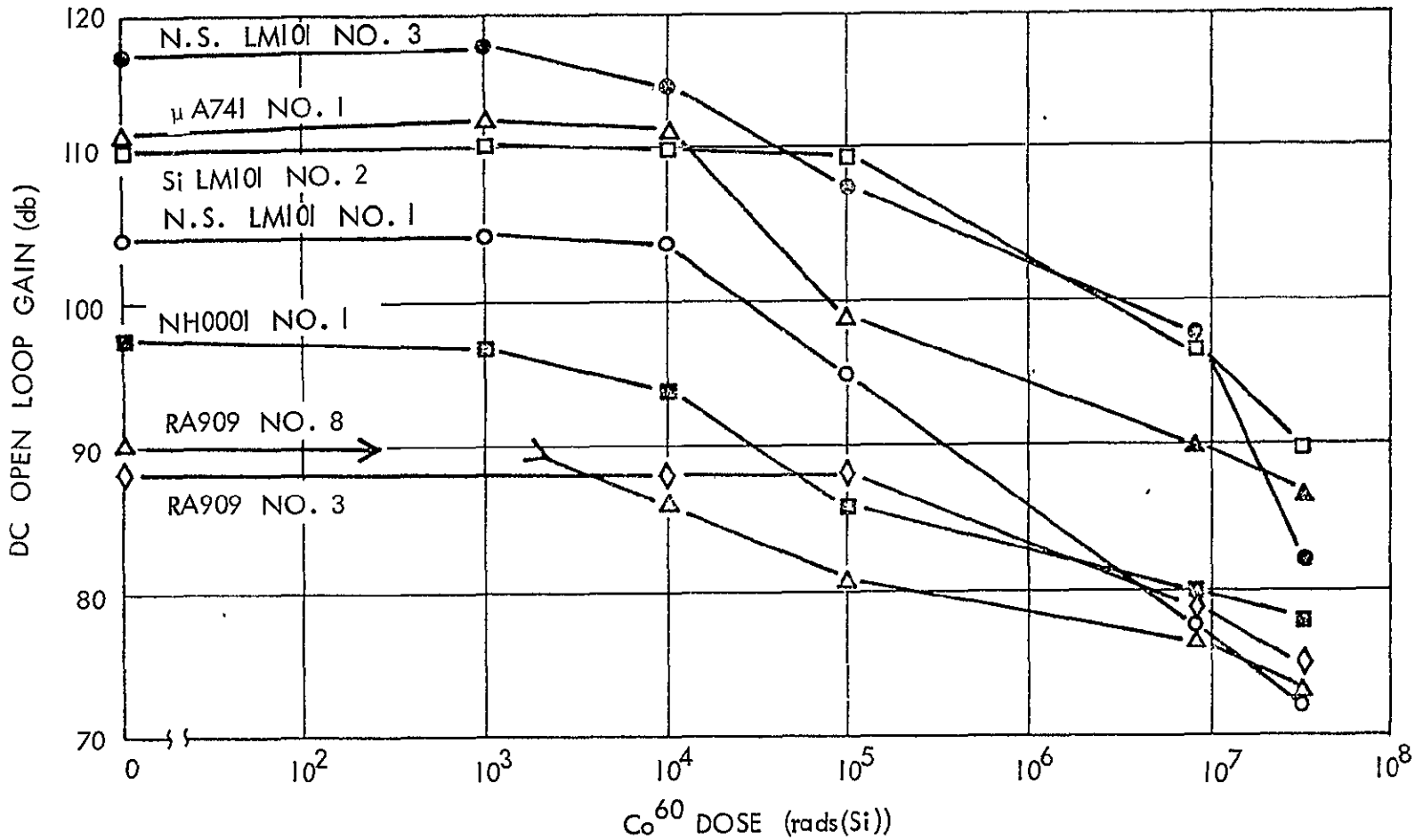

Figure 7-7. Illustrative Gain Degradation vs. Co^{60} Dose

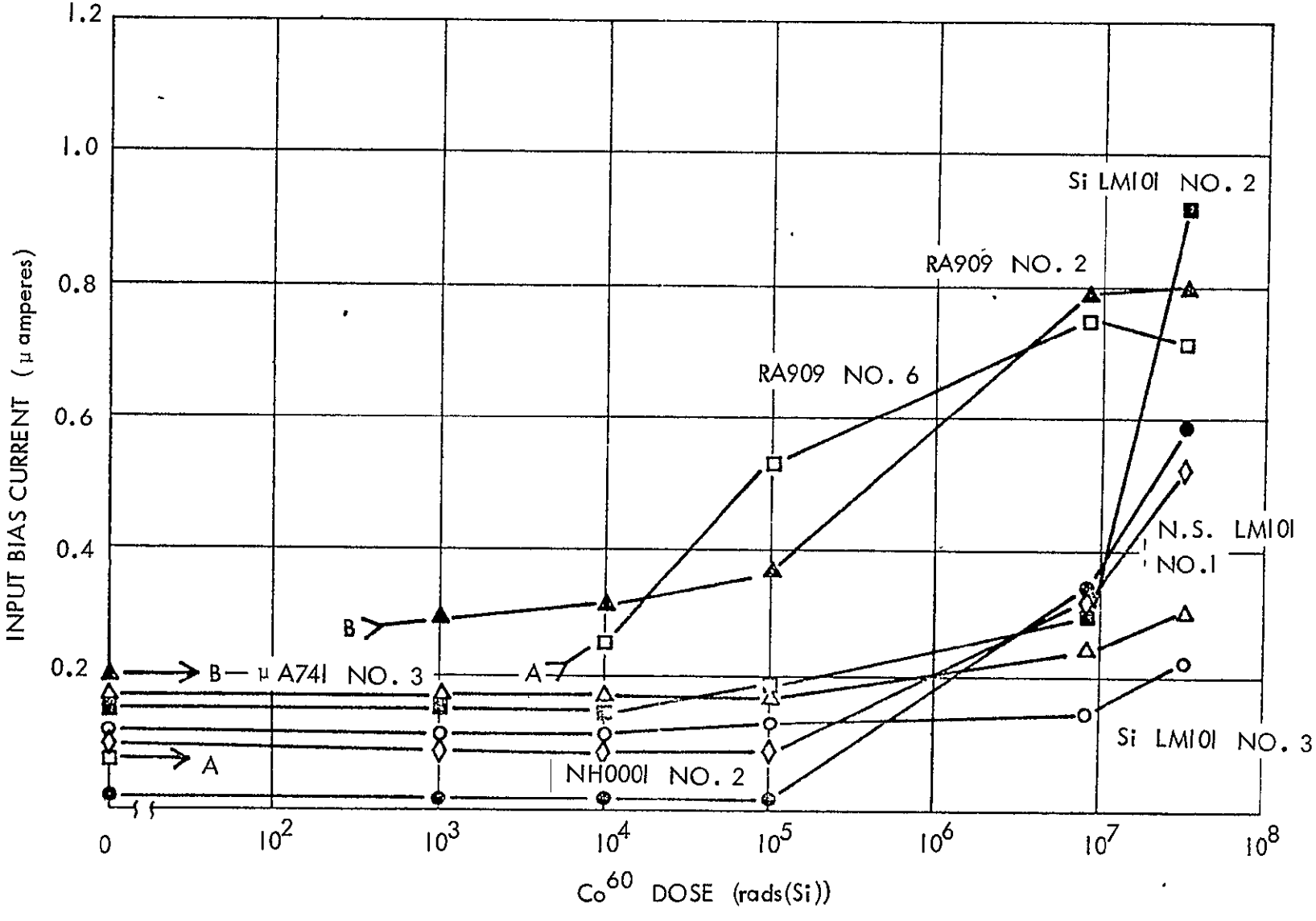

Figure 7-8. Illustrative Input Bias Current Variations vs. Co^{60} Dose

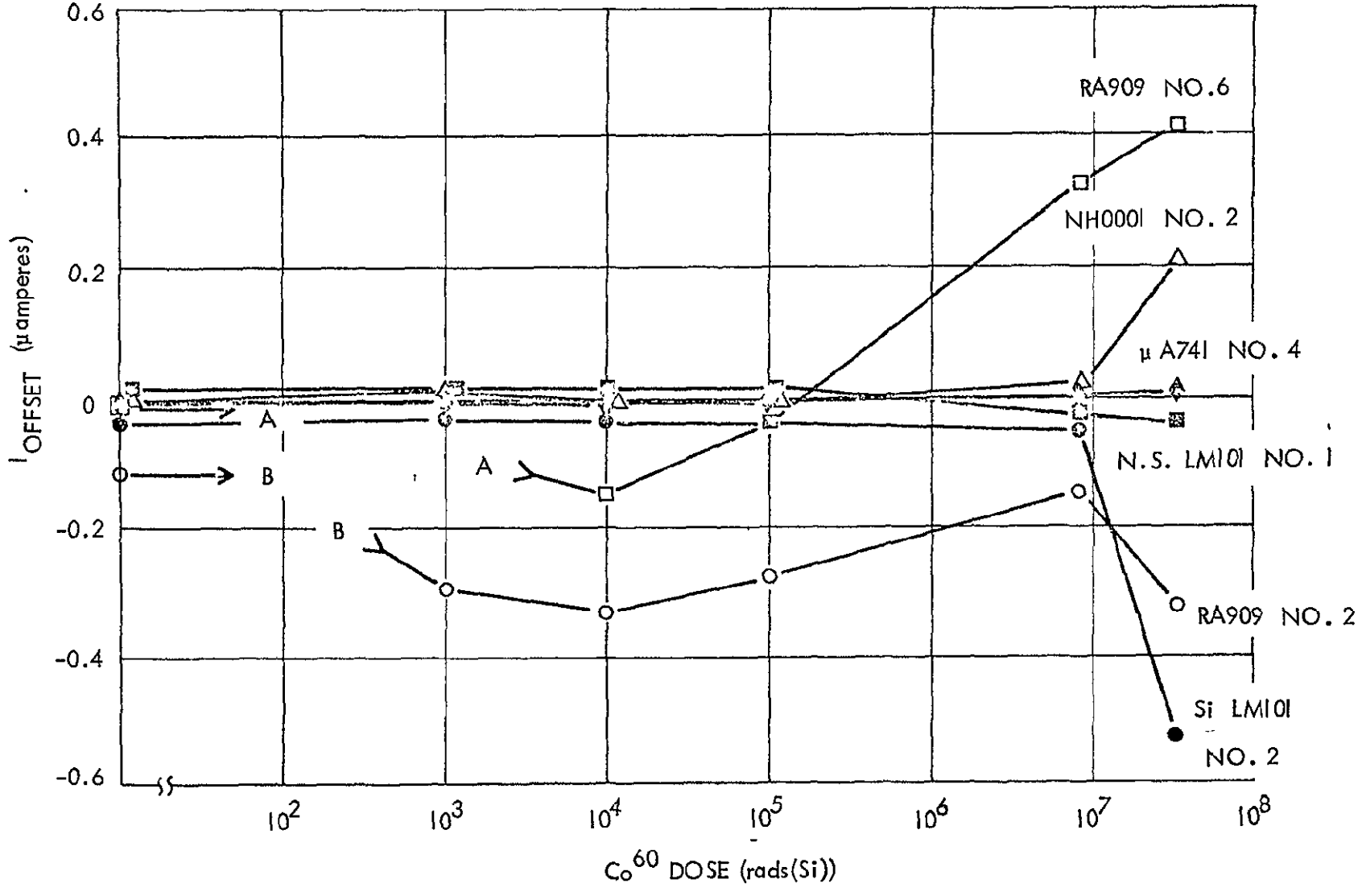

Figure 7-9. Illustrative I_{Offset} Current Variations vs. Co^{60} Dose

7.2.2.4.2 Radiation Effects in the COS/MOS Microcircuits

The Pioneer F/G payload will utilize a number of MOS digital microcircuits. These consists of the RCA series CD4000-4004, CD4007, CD4009, CD4009 (TA5660), CD4010 (TA5668), CD4012 (TA5675) and a number of other types with the TA designation that are still in the developmental stage. This group of circuits will be utilized in the meteoroid detector, the trapped radiation detector, and the charged particle experiment. Solid State Scientific MOS logic circuits SCL-5101-5106, SCL-5111, 5132, 5401 and 5402 are also used in the trapped radiation detector and meteoroid detector.

It has been indicated (7-17, 7-18) that the MOSFET is susceptible to ionizing radiation. The effect consists of a shift in threshold voltage to more negative values. Generally the magnitude of the effect depends upon the ionizing radiation dose, the gate bias polarity, and on the particular structure of the gate insulator material. Experimental data on discrete devices, although not very consistent, shows generally a larger shift in threshold voltage for devices irradiated under positive as compared to negative bias. This means that the effect will tend to be larger in p-channel depletion and in n-channel enhancement devices. The effect will be less, for example, in a p-channel enhancement negative logic device which operates with a negative gate bias.

The RCA and Solid State Scientific microcircuits listed previously are unique in that they are complementary/symmetry MOS (COS/MOS) circuits that utilize both p- and n-channel enhancement devices fabricated on the same chip.

A paper by Poch and Holmes-Siedle (7-12) discusses radiation effects in COS/MOS circuits of the RCA type listed above. The results for a type CD4007, "Dual Complementary Pair Plus Inverter", indicate a shift in threshold voltage, for an individual device on the chip, of about three volts for an applied gate bias of ±9 volts at 10^5 Rad(Si). For developmental types TA5361 and TA5388, the observed shifts were about 3 volts at +9 volts in the gate for an n-channel device, and about 5.4 volts at -9 volts for a p-channel device at 5×10^4 rad. This type of device, it is indicated, has a "sandwich" insulator structure consisting of a thermally grown oxide,

covered by a pyrolytically-deposited phosphosilicate glass layer. This probably accounts for the superior behavior at positive gate bias over the usual pure silicon dioxide layer, and favors the use of the RCA types as positive logic circuits. Data were also obtained on devices under irradiation and intermittent bias conditions characteristic of logic operation. Preliminary data are presented in the paper for a type CD4000D, "Dual 3-input Gate and Inverter," in which the threshold voltage shift is compared in similar devices for continuous and intermittent bias. The results indicate that, under conditions of cycled bias, the shifts observed fall between upper and lower limits formed by the continuous bias curves. These are a 0.3 volt shift for zero bias and a 1 volt shift for -9 volts continuous bias at 10^4 rad.

In a conversation with R. Painter of RCA, Somerville, New Jersey, the manufacturer, it was stated that the gate insulator structure for their off-the-shelf circuits is essentially the same as that employed in the above experiments. For the ionizing radiation exposure of 3.6×10^3 rad for the mission, then, the expected gate voltage shift is less than a volt for cycled bias conditions characteristic of logic circuit operation. There is, however, a question of the variability of the results between forthcoming lots. Poch and Holmes-Siedle (7-12) show data on the range of threshold voltage shifts with radiation for ten p-channel types with SiO_2 insulation from a range of different production lines between 1965 and 1968. For a continuous bias of -10 volts the measured shifts varied from a lower limit of 0.5 volts to an upper limit of 4 volts at 10^4 rad. For more recent microcircuit types the variability was about a volt at -9 volts for a p-channel type and less than half a volt at +9 volts for an n-channel device at 5×10^4 rad.

Similar experimental radiation effects data are not available on the Solid State Scientific units. Because the extent of gate voltage shift is critically dependent upon the exact structure of the insulator, a worst case, based on Poch and Holmes-Siedle's result for a standard oxide, will be assumed. An unidentified, "Type F", unit shows an extrapolated gate shift of 15 volts for a continuous positive bias of +9 volts at 10^5 rad. Data at intermediate radiation levels are not shown and it is necessary to resort to extrapolation. If this is done, utilizing the slope obtained from the

RCA units, a figure for the shift of about 1 volt is obtained at 10^3 rad. This will be the case, it should be noted, for positive logic operation, i.e., with positive gate bias.

7.2.3 Passive Parts

Passive electronic parts and structural materials have generally considerably higher thresholds for measurable effects of radiation than do active electronic devices. These thresholds are given in Tables 7-3 and 7-4. Paper dielectric capacitors and oil-impregnated paper types are somewhat more susceptible to radiation than inorganic capacitors, but thresholds for measurable effects will be in the range 10^6 to 10^7 rad(c) (7-13), which is well above exposure estimates for the mission. Variable capacitors also will be affected to the extent that the insulation present will exhibit a measurable loss. This will be negligible at the indicated exposure dose. Leakage currents, proportional to the radiation flux will likewise be negligibly small.

Fixed and variable resistors will also not be affected to any reasonable extent by the radiation environment. The microcircuit resistor whether diffused or thin film will be similarly unaffected.

Quartz crystals are utilized in the helium vector magnetometer, the plasma analyzer, the charged particle experiment, the asteroid/meteroid detector, and the University of Chicago charged particle experiment. These devices are subject to shifts in frequency when exposed to ionizing radiation. A figure of 2 parts in 10^{11} per rad is quoted for natural crystals. For the estimated radiation exposure for the mission of 3.6×10^3 rad, this gives, for example, for a 10 MHz crystal, a shift in frequency of 0.9 Hz.

Conversation with Murray Perkins and Bob Sauer of the University of Chicago revealed that the crystal used for the University of Chicago cosmic ray experiment is a 2 MH , AT cut quartz crystal with a stability requirement of ±500 Hz over the mission lifetime. The crystal will be exposed to approximately 2000 rad(c) over the mission lifetime. Ref. (7-23) states that natural quartz crystals, operating in the vicinity of 5 MHz, will undergo a radiation-induced frequency shift of about 2 parts in 10^{11} per rad up to

Table 7-3. Radiation Damage Thresholds for Electronic Components

Component Type	Component Description	Neutron Fluence, Threshold, n/cm^2	Gamma Dose Threshold, rad(c)
Capacitors	Solid Tantalum	1×10^{15}	*
	Ceramic	4×10^{14}	2×10^{8}
	Tantalum Foil	*	*
	Glass	3×10^{16}	4×10^{6}
	Variable	*	*
	Mylar	1×10^{15}	1×10^{7}
Resistors	Wirewound	3×10^{16}	$> 10^{7}$
	Composition	1×10^{14}	
	Variable	3×10^{16}	
	Film - Metal	1×10^{16}	
	- Carbon	1×10^{15}	
	Network	*	*
	Thermistor	1×10^{14}	$> 10^{8}$
Magnetic	RF Coil	1×10^{15}	$> 10^{7}$
Fuse	Current Limiter	*	*
Filters	Feedthrough	*	*
	Arc Supression	*	*
Connectors		1×10^{16}	2×10^{6}
Crystals	Rqmt. not defined	$\sim 10^{12}$	$\sim 10^{3}$

*No information immediately available.

Table 7-4. Radiation Damage Thresholds For Structural and Mechanical Materials

Material	Typical Use	Neutron Fluence Threshold (n/cm^2)	Gamma Dose Threshold (rads(c))
Aluminum	Structure Hardware	$\sim 10^{19}$	$>10^8$
Silicone Elastomers	Adhesive	10^{16}	2×10^6
Epoxy Resin	Encapsulant Adhesive Sealant	5×10^{18}	10^9
Polyester	Light Absorbing Coating	1×10^{15}	2×10^5
Polyurethane	Adhesive Coating for PC Boards	5×10^{18}	10^9
Polyvinyl	Coating for PC Boards	3×10^{18}	5×10^8
Silicone	Escapsulating Coating for PC Boards	3×10^{18}	5×10^8
Solder	Electrical Connections	$\sim 10^{19}$	$>10^8$
Fiberglass	Structural Hardware Insulation	1×10^{16}	2×10^6
Silver	Filler for Electrically Conductive Bonding	$\sim 10^{19}$	$>10^8$
Polysulfide Compound	Potting Material	2×10^{16}	3×10^6
Urethane Compound	Potting Material	5×10^{18}	10^9
Epoxy - Glass Laminate	Printed Wiring Boards	1×10^{16}	2×10^6

Table 7-4 (Continued)

Material	Typical Use	Neutron Fluence Threshold (n/cm^2)	Gamma Dose Threshold (rads(c))
Polyolefin	Striplines and Waveguides	5×10^{16}	10^7
Phenolic Reinforced Glass Fabric	Structural Laminate	3×10^{19}	6×10^9
Titanium	Pressure Vessels Screws	$\sim 10^{19}$	$>10^8$
Beryllium Copper	Spring Pin	$\sim 10^{19}$	$>10^8$
Copper	Wiring and Printed Circuit Boards	$\sim 10^{19}$	$>10^8$
Steel	Structural Hardware	$\sim 10^{19}$	$>10^8$
Graphite	Dry Film Lubricant	5×10^{16}	10^7
Oil	Lubricant	5×10^{16}	10^7
Grease	Lubricant	5×10^{14}	10^5
Acetal	Molding Compound	5×10^{14}	10^5
Tin Plated Brass	Nuts Washers	$\sim 10^{19}$	$>10^8$
Teflon	Electrical Insulation and Sleeving	10^{14}	2×10^4 (TFE in air) 2×10^6 (FEP or TFE in vacuum)
Mylar	Electrical Insulator	2×10^{16}	3×10^6
Black Opaque Polyester	Electrical Insulator	1×10^{15}	2×10^{15}

Table 7-4 (Continued)

Material	Typical Use	Neutron Fluence Threshold (n/cm^2)	Gamma Dose Threshold (rads(c)
Aluminized Plastic Film	Thermal Control	5×10^{16}	10^7
Silicate Compount	Thermal Control Coating	$\sim 10^{19}$	$>10^8$
Silicone, Aluminum Pigmented	Thermal Control Coating	3×10^{18}	5×10^8
Polyester, Black or White	Thermal Control Coating	1×10^{15}	2×10^5
Brass	Terminal Lugs	$\sim 10^{19}$	$>10^8$
Electroless Nickel	Metal Plating	$\sim 10^{19}$	$>10^8$
Nylon	Nut Insert Screw	2×10^{15}	4×10^5

doses on the order of 300,000 rads. Thus, the expected frequency shift will be

$$\frac{2}{10^{11}} \left(\frac{1}{\text{rad}}\right) \times 2000 \text{ rads} \times 2 \times 10^{6} \text{ Hz} = \cong 0.1 \text{ Hz}$$

A shift of 0.1 Hz is less than three orders of magnitude below the allowed shift. In addition, ref. (7-8) states that irradiation of general purpose quartz crystal units (allowed frequency change, $|\Delta f/f| \leq 5 \times 10^{-6}$/month) has shown that these devices are not permanently affected by a neutron fluence of 10^{13} n/cm^2 and gamma exposure of 10^3 rads.

The rest of the listed parts can be classified as miscellaneous. Included are inductors, electrical connectors, a computer and recording core stack, delay line, electron tubes, transformer relays, and fuses.

Radiation effects in inductors will be caused primarily by the presence of an insulator. Generally, thresholds for measurable effects in organic or inorganic insulating materials will exceed by several orders of magnitude the estimated radiation exposure for the mission. Thresholds for effects from neutrons in the remaining components are far above the estimated neutron fluence being in the range, for example, of 10^{15} -10^{18} nvt for vacuum tubes (7-13). The vacuum tube will also survive 4×10^{8} rad(c) of ionizing radiation. Thresholds for damage for these components correspong to those for any organic material present. The material with the lowest threshold dose is Teflon at about 4×10^{4} rad(C) (7-13).

7.2.4 Conclusions and Recommendations

The conclusions may be summarized as follows:

- Common emitter current gain degradation from the neutron fluence of 1.8×10^{9} nvt should be less than 5%.
- Gain degradation from the ionizing component from on-board and natural sources is difficult to estimate since published data are inconsistent in the range 10^{3} -10^{4} rad; depending on the state of bias, changes in gain varied from 10% at 10^{4} rad to an estimated 50% at about 3.6×10^{3} rad.

- Diodes and field effect transistors should not be measurably affected in the radiation environment.
- Bipolar micrologic should be unaffected by the radiation environment.
- Bipolar linear microcircuits should not be measurably affected by the neutron component; ionizing radiation tests of types that will be found in the payload showed less than a percent change in β in the range 10^3 -10^4 rad.
- P-channel MOS integrated circuits will be unaffected by the neutron component; effects of the ionizing component with respect to overall circuit performance are difficult to estimate since circuit data are lacking; some degree of performance degradation should be expected in the range 10^3 to 10^4 rad.
- The RCA complementary/symmetry MOS (COS/MOS) devices to be employed in the Pioneer F/G payload will experience estimated threshold voltage shifts of less than a volt, for cycled bias conditions characteristic of logic operation, at 3.6×10^3 rad assuming forthcoming device lot reproducibility.
- Lot variability data indicate that threshold voltage shifts with radiation exposure varied by about a volt between COS/MOS devices in different chips.
- Threshold voltage shifts in the Solid State Scientific COS/MOS circuits are estimated to be about a volt at 3.6×10^3 rad with the assumption of a standard oxide gate insulator material and positive logic operation.
- Passive electronic parts should not be measurably affected.
- Frequency shift of 0.9 Hz is estimated for a 10 MHz crystal in the radiation environment.
- The expected frequency shift of the University of Chicago cosmic ray experiment crystal oscillator over the Pioneer F/G mission ($\sim$0.1 Hz) is not predicted to have a significant effect on the accuracy of the unit.

Although the effect should not be significant for most circuits, some uncertainty exists with respect to the effect of ionizing radiation on bipolar discrete devices and microcircuits because of lack of consistency in published data in the range 10^3 -10^4 rad. A similar uncertainty exists for the p-channel MOS microcircuit with respect to overall circuit response for the same reason and because of difficulty in extrapolating from individual device response. It is recommended accordingly that where the radiation effects described will be critical for proper performance, radiation tests with a radioactive source be made to define the extent of the effect on the actual devices and circuits.

7.3 BIBLIOGRAPHY

A bibliography presenting pertinent radiation effects documentation was compiled. A very large number of papers and reports on radiation effects studies have been published, and it was not attempted to list all these. Instead, three preeminent publications were identified which present compilations and summaries of most of the available data in a manner which is usable for the engineer and designer. These publications are:

1) Kircher, J. F., and R. E. Bowman, Effects of Radiation on Materials and Components, Reinhold Publishing Corporation, New York, 1964.
This reference is a standard text on radiation effects. It presents an excellent overview of radiation effects together with many detailed data. Discussion is presented on basic concepts of radiation effects as well as radiation effects on polymers, fuels and lubricants, organic compounds, ceramics, structural metals and alloys, semiconductor devices and other electronic components. Each chapter is followed by an extensive list of references.

2) Transient Radiation Effects on Electronics (TREE) Handbook, Edition 2, Revision 1, R. K. Thatcher, ed., DASA 1420, August 1967.
This document is the standard text for nuclear weapon radiation effects on electronics. It should be noted that the word "transient" in the title modifies "radiation", not "effects", so that the permanent effects due to integrated exposure which are of interest to the Pioneer F/G program are also treated. The document discusses effects on discrete semiconductor devices, integrated circuits, capacitors, resistors, and

miscellaneous parts and devices, and circuit hardening and analysis techniques. Extensive lists of additional references are also presented. The document may be obtained from the Defense Documentation Center, Cameron Station, Alexandria,,Va., 22314.

3) Kingsland, R. H., et al, "Radiation Effects on Space Power Subsystems", SAMSO-TR-69-7, January 1969.
Although this document is primarily oriented toward space power subsystems, it provides a good general discussion of radiation effects on materials and components, including electronic components. Volume II, Part 1 presents a good summary of the most important data in 1) and 2), above. Also included are many references and a bibliography.

(It should be noted that in using documents 2) and 3), above, care should be taken in separating dose rate effects from total (integrated) dose effects. Since the dose rate of interest to Pioneer F/G instruments is so small, only total dose effects need be considered).

The three documents listed above are good compilations of available radiation effects data and the references and bibliographies obtained in them can be used for further investigations. Two other excellent sources may also be used for obtaining further information. These are the Radiation Effects Information Center (REIC) and the Defense Atomic Support Information and Analysis Center (DASIAC). REIC is located at Battelle Memorial Institute, Columbus, Ohio. Its purpose is to compile information and bibliographies on all radiation effects work done in the country. Accessions lists and bibliographies are published regularly. More specific information will be supplied on request. Generally, if information is requested on a particular subject, REIC will supply whatever data it has on hand together with a complete bibliography. DASIAC is primarily interested in nuclear weapon effects, which include general radiation effects. DASIAC bibliographies may be obtained by writing to DASIAC, 816 State Street, Santa Barbara, California.

In addition to the three general references listed above, a short bibliography was compiled of documents of particular interest to this program. This bibliography is presented below.

REFERENCES

7-1 Ritts, J. J., E. Solomits and P. N. Stevens, "Calculation of Neutron Fluence-to-Kerma Factors for the Human Body", Oak Ridge National Laboratory.

7-2 Pioneer F/G Spacecraft Specification, PC-210.

7-3 Haffner, J. W., Radiation and Shielding in Space, Academic Press, New York, 1967.

7-4 Saylor, W. P., D. E. Winen, C. J. Eiwen and A. W. Cariker, "Space Radiation Guide," Rept. AMRL-TDR-62-86, Biomed. Lab., USAF, Dayton, Ohio, 1962.

7-5 Personal Communication, Art Wilbur, NASA/AMES, Moffett Field, Calif. 13 January 1970.

7-6 Smith, C. A., "Ionizing Dose from Electrons and Protons (U)", TRW IOC 09670-6126-G1-00, 25 July 1969 (SRD).

7-7 Berger, M. J. and S. M. Seltzer, "Penetration of Electrons and Associated Bremsstrahlung Through Aluminum Targets", Protection Against Space Radiation, NASA SP-169, 1968.

7-8 "Transient Radiation Effects on Electronics Handbook", R. K. Thatcher, ed., DASA 1420, p. F-75, August 1967.

7-9 Loc Cit. p. F-76.

7-10 F. Larin, Radiation Effects in Semiconductor Devices, John Wiley and Sons, Inc., New York, 1968.

7-11 D. L. Nelson and R. J. Sweet, "Mechanisms of Ionizing Radiation Surface Effects on Transistors", IEEE Trans, Nuc. Sci. NS-13, 197(1966).

7-12 W. Poch and A. G. Holmer-Siedle, "A Prediction and Selection System for Radiation Effects in Planar Transistors". IEEE Trans. Nuc. Sci. NS-15, 213(1968).

7-13 R. K. Thatcher, et al., "The Effects of Nuclear Radiation on Electronic Components, Including Semiconductors", REIC Report No. 36, Battelle Memorial Institute, Columbus, Ohio, (1 October 1964).

7-14 E. S. Chambers, J. D. Kinder, and J. Tobolski, "Operation of Monolithic TTL Circuits During Fast Neuctron Exposure", GOMAC Conference, p. 105, October 1968.

7-15 J. D. Lieux, "Radiation Testing of Linear Microcircuits", Fairchild Technical Paper, TP-40, December 1966.

7-16 P. E. Partridge, "Irradiation of Several ICOAs and Other Selected Semiconductor Components by Cobalt-60", John Hopkins University Tech. Memo. TC-1048, January 1969.

7-17 Ridolphi, IOC to R. E. Loucks, "Radiation Damage - Pioneer F/G", 4334.1.69-106, 20 November 1969.

7-18 V. R. Honnold, IOC to R. B. Edgar, "Radiation Effects Assessment for Pioneer F/G Electronics", 70.4334.7-1, dated 4 March 1970.

7-19 Kircher, J. F. and R. E. Bosman, Effects of Radiation on Materials and Components, Reinhold Publishing Co., 1964.

7-20 Faelten, E. M., J. R. McDougall, and C. A. Smith, "Survivability of the 2 KW Battery Cell Block" (U), TRW No. 12502-6002-T1-00, 1 July 1969, (SRD).

7-21 Kingsland, R. H., et al, "Radiation Effects on Space Power Subsystems (Handbook), Volume II, Pat 2", SAMSO-TR-69-7, January 1969.

7-22 King, R. W., et al, Radiation Effects Information Center Report No. 21, Columbus, Ohio, September 1961.

7-23 R. A. Poll, & S. L. Ridgeway, "Effects of Pulsed Ionizing Radiation on Some Selected Quartz Crystal Oscillators", IEEE Trans. Nuc. Sci. NS-B #6, Dec. 1966.

8.0 CONCLUSIONS AND RECOMMENDATIONS

The Pioneer F/G is the first NASA spacecraft with the electrical power totally supplied by Radioisotope Thermoelectric Generators (RTG's). Since the RTG's emit gamma and neutron radiation, the use of these power supplies resulted in sumerous questions and concerns to the spacecraft designers and the scientists who have experimental hardware on board. In fact, at the time this program was started, it was not known for certain whether some experimental measurements could be performed in the presence of the RTG radiation. The results of this program not only answered these questions, but also provided valuable experience which can be applied to future RTG-powered spacecraft.

During the performance of the varied tasks on this program, some of the techniques were found particularly useful and helpful in evaluating the radiation fields and their effects on the spacecraft and scientific instruments. For instance, it became evident that the radiation mockups of the spacecraft and the RTG radiation sources which were constructed during the course of this program were very versatile and effective tools.

The construction of the radiation mockup of the spacecraft was a relatively simple task and became an accurate representation of the radiation scattering and absorption effects around the spacecraft. It would have been considerably more difficult and expensive to obtain the same results using a digital computer program of comparable detail. Also, the mockup provided great flexibility in changing the configuration of the spacecraft. If the position or mass of some components of the actual Pioneer spacecraft were changed, it was a simple matter to change the mockup to the new configuration. In addition, the mockup provided the flexibility of substituting prototype experiments in the mockup to obtain accurate radiation measurements.

The RTG source mockups also proved to be versatile tools. The radiation flux and spectrum from the RTG were simulated very accurately. In addition, the source mockups could be modified easily to change the radiation output to correspond to various RTG fuel ages. Also, the radioisotope sources for the mockup cost only a few thousand dollars while the cost of a real RTG fuel capsule is several hundred thousand dollars and requires

special handling and storage facilities.

From the work performed under this program, it is apparent that the problems of RTG radiation interference with most science instruments can be solved. This is especially true if the radiation sensitive instruments are identified before the spacecraft design is frozen and can be located in such a way as to take maximum advantage of the radiation absorption capabilities provided by adjacent equipment. In this way, the radiation interference may be greatly reduced with little or no weight penalty.

Much of the work was performed on the basis that the emission rate from the fuel would be 5×10^3 neutrons/second-gram of plutonium-238. However, as indicated in recent data reported in Section 4.1, the actual neutron emission rates for the flight SNAP-19 RTG fuel capsules is expected to be on the order of 4×10^4 neutrons/second-gram of plutonium-238, a factor of eight greater. Much of this higher emission rate is attributed to the fluorine present in the fuel. It is recommended that the effects of this higher emission rate on the operation of the key science instruments during the Pioneer F/G mission be analyzed. Further, reduction of neutron emission rates by altering fuel coating and processing techniques should be investigated.